PITHA 85/02

The Simulation of Hadronic Showers
- Physics and Applications -

by

H. Fesefeldt
III. Physikalisches Institut, RWTH Aachen, FRG

PITHA 85/02

The Simulation of Hadronic Showers
- Physics and Applications -

by

H. Fesefeldt
III. Physikalisches Institut, RWTH Aachen, FRG

ABSTRACT

In the last years high energy physicists have shown an increasing interest in the understanding of electromagnetic and hadronic cascades in matter, not only for purposes of shielding and dosimetry, but even more for the design and analysis of high energy physics experiments. In the present report the computer code GHEISHA is presented. The physical methods, which are used to describe the interactions of elementary particles with matter, are discussed in detail and compared with results from atomic and nuclear scattering experiments. The strengths and weaknesses of the computer code are demonstrated by various applications in detector design and detector analysis of medium and high energy physics experiments. It is the hope of the author that this presentation will enable the user to better understand the physics of hadronic cascades and will help him to run the computer code without serious difficulties.

CONTENTS

1.0 INTRODUCTION 1

2.0 THE PHYSICS OF SHOWER SIMULATION 3
2.1 General remarks 3
2.2 Relativistic theory of ionization energy loss 4
2.2.1 The continous slowing down approximation 4
2.2.2 δ-ray production in light materials 12
2.3 Multiple scattering 13
2.4 Tracking in magnetic fields 25
2.5 Electromagnetic Interactions 28
2.5.1 The discrete shower simulation 28
2.5.2 Shower parametrizations 39
2.6 Nuclear Interactions 48
2.6.1 General remarks 48
2.6.2 Elastic and inelastic cross sections 49
2.6.3 Optical model calculations 61
2.6.4 The cross section determination of compounds 66
2.6.5 Generation of secondary particles 69
2.6.6 Generation of four-momenta 89
2.6.7 Clustering invariant quantities 89
2.6.8 Quantum number flow in soft collisions 90
2.6.9 Comparison with recursive cascade models 97
2.6.10 Models based on overlapping quark jets 104
2.6.11 Comparison of quark- and hadron- fragmentation 107
2.6.12 Summary of inelastic hadron nucleon collisions 111
2.6.13 Elastic scattering and quasi-two-body reactions 112
2.6.14 Comparison with experimental data 114
2.6.15 The intra-nuclear cascade 121
2.6.16 Nuclear evaporation 123
2.6.17 Energy-momentum-balance 127
2.6.18 Coherent elastic scattering 130
2.6.19 Hadron nucleus interactions 131
2.6.20 Neutron capture and nuclear fission 147
2.6.21 Nuclear interactions for muons 149
2.6.22 The absorbtion of particles at rest 151
2.6.23 Final remark 153
2.7 Decays of stable particles 153

3.0 SHORT WRITE-UP OF THE GHEISHA-PROGRAM 158
3.1 The current version 158
3.1.1 General remarks 158
3.1.2 The initialization 160
3.1.3 The shower routine CALIM 169

3.1.4 The decay-routines 174
3.1.5 The cascading-routines 174
3.1.6 The tracking algorithm 174
3.1.7 Stopping tracks 178
3.1.8 The user routines 179
3.1.9 Hadron production by muons 183
3.1.10 The neutral kaon problem 185
3.1.11 Production of δ-rays 185
3.1.12 Use of the EGS package 187
3.2 Changes for the improved GHEISHA7 version 188
3.2.1 Materials 188
3.2.2 Geometry 190
3.2.3 Improved physics 191

4.0 MUONS IN TRACKING CALORIMETER 193
4.1 Momentum spread in tracking calorimeter 193
4.2 Measurement of coordinates 203
4.3 The method of sagittas 206
4.4 Inclusion of angle measurements 209
4.5 Momentum fitting under various conditions 212

5.0 CALORIMETRY 225
5.1 Introduction 225
5.2 Simulation of the scintilation process 225
5.3 Pulse heights and energy resolutions 247
5.4 Comparison with experimental data 266
5.4.1 Some selected test set-ups 266
5.4.2 Test run of the MARK J detector 275
5.4.3 The CDHS iron scintilator calorimeter 289
5.4.4 Calorimetric results of the MARK J detector at PETRA 296
5.5 Position reconstruction from the shower shape 309
5.6 Electron/pion shower separation 312
5.7 μ-identification 327
5.7.1 General remarks 327
5.7.2 The classic muon spectrometer 327
5.7.3 The TASSO spectrometer 334
5.7.4 The MARK J spectrometer 340
5.7.5 Optimization of μ-identification 352

6.0 ACKNOWLEDGEMENTS 363

7.0 REFERENCES 364

1.0 INTRODUCTION

There is a long history of computer simulations of the shower process for electrons and photons in matter. Before 1970 there existed three codes, namely from Zerby and Moran [1], Butcher and Messels [2] and Nagel [3], the last one extended to its final form by Ford and Nelson [4], the so called EGS program, which is today commonly accepted as the standard for electron-photon shower simulation.

On the other hand the situation of the cascade simulation initiated by hadrons is not so clear. There exist a lot of programs [5-8], only a part of which are available to outstanding users, the other ones are of rather limited use by various reasons. Experimental and theoretical work on strong interactions is by far not beeing finished. New results about the interactions of hadrons with nuclei filled up books and journals especially in 1970-1980. Up to now there is no theory, which describes all phenomena in a self-consistent way.

The task of the author of the present report was to implement a four-dimensional shower code for all particles including kaons and strange and nonstrange baryons into a detector simulation program for the Mark J experiment at PETRA. The computer time should not exceed 0.5 sec/GeV including the simulation of all active components like counters and drift-chambers. Very soon it was clear that none of the above mentioned programs could be used without serious problems in accuracy or computer time consumption. Therefore the problem of hadronic showers was attacked once more, the results of which are described in this report. Main emphasis was given to generality of particles and experimental set-ups, and a reasonable compromise between accuracy and computer time consumption was aspired.

Four comments must be added to the formal structure of this report:

1) References are given mostly to the works which have been really consulted. Very often these were review papers, the original work therefore not beeing mentioned explicitly.

2) As the reader will see, a lot of formulae are written down in this report. This lies in the nature of Monte Carlo simulations. Only what one can write down in a formula, can be translated to an efficient computer code. Whenever possible the author tried to understand and to explain the formulae and interpolations.

3) A lot of checks will be described too. This has two reasons. First we think that the results of these tests may be also useful for the design of

other set-ups, secondly they may indicate what accuracy for predictions other users can expect.

4) Most of the material of this report has been written originally as a private ducumentation for the author. Thus main emphasis was given to things which the author himself did not understand in detail when preparing the program.

The present report is organized in the following way : First we discuss in detail the fundamentals of the tracking, i.e. ionization energy loss, multiple scattering and the tracking in magnetic fields. The description of the electromagnetic shower simulation will be short, because we use the EGS as default. A detailed description of that program can be found elsewhere [4]. Some succesful shower parametrizations, already included in the program, are given. The physics of hadronic shower simulation is then discussed in great detail. Elastic and inelastic cross sections are parametrized from experimental data. Cross sections in the MeV region and below are calculated using the optical model. The multiplicity distribution is determined by a semiempirical formula. The generation of final state particles is similar to the nowadays commonly accepted iterative cascade model descriptions. This includes the simulation of the intranuclear cascade, Fermi-motion, nuclear evaporation and nuclear fission. Low multiplicity events at very low energy are treated seperately from the general scheme. This covers especially nuclear reactions in the MeV-region. The treatment of hadron production by leptons is done according to the quark parton model. Weak 2-,3- and 4-body decays are included for all particles. The physics description of the report ends with a short write-up of the program in chapter 3. In chapter 4 we continue with the discussion of muons in tracking calorimeter. A wide application of such devices will come up in future experiments. Comparisons with analytic calculations will be done for the correlations of various quantities connected with multiple scattering and also for the resolution of momentum measured from the bending of the tracks in magnetic fields. The discussion of applications continues with calorimetry, here especially the tuning of some input parameter, which could not be determined from nuclear scattering data. Comparisons with experimental test run results will be done. One of the main applications of this program in the past was the simulation of particle separation problems, especially electron/hadron and muon/hadron separation. One chapter is devoted to a discussion of the basic methods. Included are some comparisons of the Monte-Carlo program with the experimental results of the MARK J experiment at PETRA. Complete simulation programs for the MARK J experiment and for the L3 experiment at LEP have also been established. Detailed descriptions of these program versions will be published elsewhere.

2.0 THE PHYSICS OF SHOWER SIMULATION

2.1 GENERAL REMARKS

The computer program GHEISHA (Gamma- Hadron- Electron- Interaction SH(A)ower code) describes the development of a hadronic and/or electromagnetic shower within the materials which constitute the experimental set-up. All tracks are treated in detail, they are followed until they decay, interact, stop or leave the regions of the detector. Tracking involves multiple scattering and energy loss. The treatment of high energy interactions, nuclear excitation, Fermi-motion and the generation of secondary particles in nuclear cascades is based very strongly on experimentally measured results.

The program consists of three modules, which are described in turn. First a package of subroutines which handle the tracking through the given detector set-up, secondly the central part of the program which treats nuclear and electromagnetic interactions, and last a package of routines which digitize the energy deposits into ADC- and TDC- signals. These three packages can be used independently. The last package is certainly of limited value for other users.

The structure of the program is similar to that written by Grant [8]. This program has been used as a starting version. The reasons for updating Grant's old version were twofold. First the knowledge about strong interactions and nuclear cascades increased considerably since 1974, and secondly that program was written for very high particle momenta, whereas in the present time in storage ring experiments particles in the momentum range of 0-10 GeV/c have to be handled.

Writing a shower simulation program one is always confronted with the problem of accuracy and computer time consumption. The program described in this study has been tested and optimized for detector set-ups consisting of sandwiched metal calorimeters, interspaced by scintilators, liquid argon or chambers as active components, bombarded by incoming particles between 0.1 and 1000 GeV/c kinetic energy. Comparisons with experimental data have been done for photons, electrons, positrons, charged pions, charged and neutral kaons, protons and assemblies of particles as it happens in quark-jets. For quite different set-ups and incoming particles it may become necessary to include more detailed atomic- and nuclear interaction effects as those included in the present version.

There are a lot of older versions of this program around in various laboratories. We are thus somewhat in a dilemma in this respect. What is described in the physics part of this report refers only to the last version,

the GHEISHA7 code. The applications, on the other hand, have been performed with the previous version, the GHEISHA6. Due to limited computer time we were not able to repeat all the calorimetric calculations with the last version. Consequently we decided to report the write-up in chapter 3 for the GHEISHA6 version and to mention briefly only the changes done for the GHEISHA7 version. Both codes are available on the IBM at DESY (cataloge names "F13FES.GHEISH6.S" and "F13FES.GHEISH7.S"). Another supported version is that for the MARK J experiment. All other libraries include intermediate versions, which were not foreseen for general use.

2.2 RELATIVISTIC THEORY OF IONIZATION ENERGY LOSS

2.2.1 The continous slowing down approximation

For a detailed summary of experimental work and its theoretical interpretation of the ionization loss of fast charged particles in matter we refer to ref. [9]. The most-probable energy loss, which corresponds to the peak of the measured experimental distribution, can be calculated from the theory of Landau. In terms of the notation used by Sternheimer [10], we have for a particle of velocity β on traversing an absorber with atomic number, atomic weight and mean excitation potential Z, A and I respectively :

$$-\frac{dE}{dx} = \frac{D}{\beta^2}\left[G+2\cdot\ln\left(\frac{\beta^2}{1-\beta^2}\right) - 2\beta^2 - 2\delta(\beta)\right] \qquad (2.1)$$

$$D = 0.0001536\ \rho\ \frac{Z}{A} \qquad [\text{GeV cm}^{-1}\ \text{c}^{-1}] \qquad (2.2)$$

$$G = 2\ \ln(1.02\cdot 10^6/I) \qquad (2.3)$$

$$I = Z\ (9.76 + 58.8\ Z^{-1.19}) \qquad (2.4)$$

The saturation of the ionization energy loss for very energetic charged particles, as predicted by the last term in (2.1), is by now a well established experimental fact, and its origin in the polarization of the medium by the incident charged particle is at least qualitatively understood and known as density effect. The exact theory is rather complicated and requires detailed information on the photoionization cross sections and

form factors. Calculations have been performed so far only approximately for some drift chamber gases (see e.g. [9] and [11]). A best fit-formula to the experimental data is given by the semiemperical expression proposed by Sternheimer and Peierls [10] :

$$\begin{aligned} \delta &= 4.606\,x + c + a\,(x_1-x)^m && \text{for } x_0 \leq x < x_1 \\ &= 4.606\,x + c && \text{for } x > x_1 \\ &= 0 && \text{for } x \leq x_0 \end{aligned} \qquad (2.5)$$

$$x = \ln(\beta^2/(1-\beta^2))/4.606 \qquad (2.6)$$

$$a = (-c-4.606\,x_0)/(x_1-x_0)^m \quad , \qquad (2.7)$$

where the parameters x_0, x_1 and m can be expressed at least approximately as function of only parameter c for gases, liquids and solids respectively:

solids and liquids :

1) for I < 100 eV :

$x_1 = 2$

$m = 3$

$x_0 = 0.2$ for $c < 3.681$

$= 0.326\,c - 1.0$ for $c \geq 3.681$

2) for I ≥ 100 eV :

$x_1 = 3$

$m = 3$

$x_0 = 0.2$ for $c < 5.215$

$= 0.326\,c - 1.5$ for $c \geq 5.215$

gaseous materials :

1) for $c \leq 12.25$:

$x_1 = 4$

$m = 3$

$x_0 = 1.6$ for $0.00 < c \leq 10.0$

$= 1.7$ for $10.0 < c \leq 10.5$

$= 1.8$ for $10.5 < c \leq 11.0$

$= 1.9$ for $11.0 < c \leq 11.5$

$= 2.0$ for $11.5 < c \leq 12.25$

2) for $12.25 < c \leq 13.8$:

$x_1 = 5$

$m = 3$

$x_0 = 2$

3) for $13.8 < c$:

$x_1 = 5$

$m = 3$

$x_0 = 0.326\,c - 2.5$.

The parameter c has been chosen as to fit best the experimental data. Values at the minimum are given in table 1 for some selected materials:

Table 1

Material	density [g·cm^{-3}]	C	$(dE/dx)_{mp}/\rho$ [MeV·g^{-1}cm^{-2}] PDG	GHEISHA	$(dE/dx)_{mean}/\rho$ [MeV·g^{-1}cm^{-2}] PDG	GHEISHA
H	0.00009	9.11	2.11	2.09	4.12	4.10
HE	0.000178	10.19	0.90	0.92	1.94	1.96
Li	0.534	2.81	1.31	1.31	1.58	1.57
Be	1.848	2.7	1.41	1.42	1.61	1.59
C	2.265	2.82	1.58	1.57	1.78	1.79
N	0.00125	10.60	0.74	0.72	1.82	1.78
O	0.00143	10.80	0.92	0.93	1.82	1.88
Ne	0.0009	11.52	0.83	0.88	1.73	1.80
Al	2.70	4.06	1.41	1.40	1.62	1.62
Si	2.33	4.38	1.44	1.42	1.66	1.65
Ar	0.00178	11.92	0.73	0.69	1.55	1.50
Fe	7.87	3.97	1.36	1.36	1.48	1.48
Cu	8.96	4.43	1.32	1.33	1.44	1.44
Sn	7.31	5.49	1.14	1.15	1.26	1.27
Xe	0.00589	12.77	0.61	0.61	1.24	1.22
W	19.3	5.33	1.09	1.09	1.16	1.15
Pb	11.35	6.21	1.03	1.04	1.13	1.14
U	18.95	5.86	1.02	1.01	1.09	1.08

Material	density [g·cm^{-3}]	C	$(dE/dx)_{mp}/\rho$ [MeV·g^{-1}cm^{-2}] PDG	GHEISHA	$(dE/dx)_{mean}/\rho$ [MeV·g^{-1}cm^{-2}] PDG	GHEISHA
Air	0.00129	10.61	0.87	0.85	1.82	1.94
H_2O	1.00	3.30	1.72	1.65	2.03	2.04
Concrete	2.40	3.64	1.47	1.45	1.70	1.69
SiO_2	1.60	4.10	1.49	1.52	1.72	1.73
H_2(liquid)	0.063	2.91	3.17	3.02	4.12	4.13
D_2(liquid)	0.14	2.80	1.57	1.57	2.07	2.07
Ar(liquid)	1.40	5.43	1.38	1.39	1.69	1.69
Emulsion(G5)	3.815	5.10	1.26	1.26	1.44	1.43
NaI	3.67	3.40	1.13	1.13	1.32	1.29
BGO	7.13	3.20	1.14	1.10	1.27	1.31
$(CH)^k$	1.032	3.15	1.67	1.69	1.95	1.93
Plexiglass	1.18	3.10	1.68	1.71	1.95	1.92
Mylar	1.39	3.17	1.61	1.67	1.86	1.89
CO_2	0.00197	10.11	0.97	0.99	1.82	1.93
CH_4	0.000717	9.56	1.27	1.25	2.41	2.48
C_4H_{10}	0.00267	8.61	1.28	1.20	2.22	2.25

The corresponding energy loss for muons according to equ. (2.1) is shown in fig.1. In column 3 of table 1 we compare the results at the minimum with values given in the Particle Data Group (PDG) table. For other materials see e.g. ref. [9,10 and 4]. This treatment of the energy loss is sufficiently accurate for the shower development only, but is of course not sufficient for detailed simulations of dE/dx- counter performances (see e.g. [12]).

We use the same formula for electrons and for all charged hadrons. Experimental verification can be found in ref. [9,10]. Differences for electrons and positrons have been neglected. Another option in this program is the complete EGS-code for electromagnetic showers (see chapters 2.5 and 3.1.12). Here a very sophisticated dE/dx- calculation for positrons and electrons is used. For details see ref. [4].

A very important consideration is the precision attainable in the measurement of energy loss. We shall outline a simple treatment that gives the respective conditions for the two extreme cases, the Gaussian and the Landau approximation. The formula for the distribution of energy losses in a path x is given by [13] (see also equ. (2.1)) :

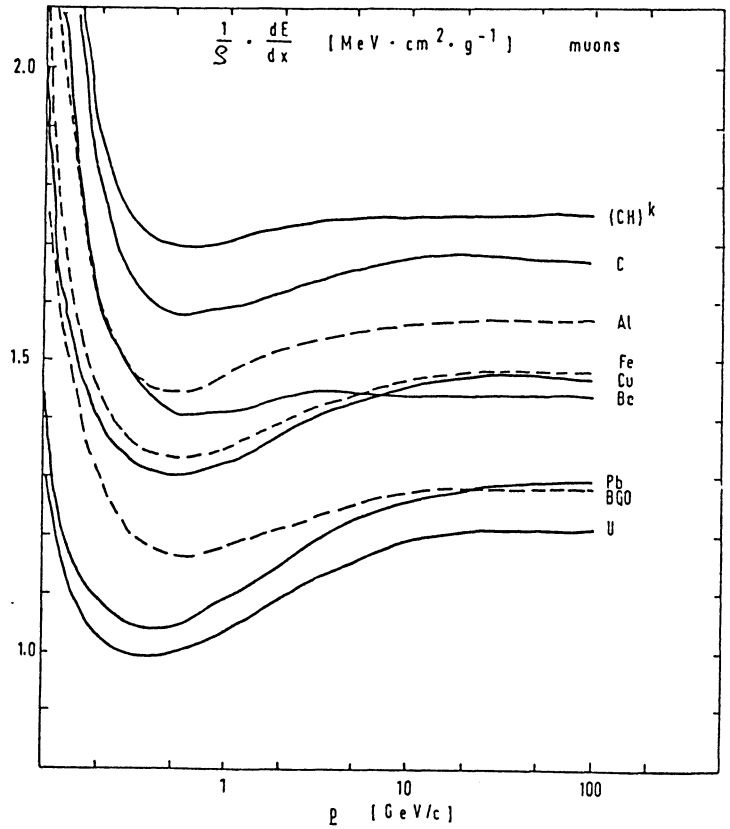

Figure 1. Most probable values of the specific ionisation energy loss as function of momentum for various materials.

$$p(E)\ dE = \frac{0.0001536}{\beta^2}\ \rho\ \frac{Z}{A}\ x\ \frac{dE}{E^2}\ . \qquad (2.8)$$

The probability for a collision of energy transfer greater than E to occur is given by

$$P(>E) = \int_E^{\infty} W\ \frac{dE}{E^2} = \frac{W}{E} \qquad (2.9)$$

with

$$W = \frac{0.0001536}{\beta^2}\ \rho\ \frac{Z}{A}\ x \quad . \qquad (2.10)$$

In the first case a large number of collisions involving maximum energy transfers occur during a traversal, and, as the total energy transfer is made up of a multiple of small energy losses, the fluctuations are Gaussian. Therefore the condition for Gaussian fluctuations is given by

$$W/E_{max} \gg 1 \quad , \qquad (2.11)$$

where E_{max} is the maximum energy transfer

$$E_{max} \approx \frac{2\beta^2}{1-\beta^2}\ m_e \quad , \qquad (2.12)$$

so that

$$\frac{W}{E_{max}} \approx 0.1506\ \rho\ \frac{Z}{A}\ x\ \frac{(1-\beta^2)}{\beta^4} \quad . \qquad (2.13)$$

On the other hand for Landau fluctuation to hold, we must have

$$W/E_{max} \ll 1 \quad . \qquad (2.14)$$

The momentum- vs x-diagram for $W/E_{max}=1$ is shown in fig.2 for various materials for muons (left scale) and protons (right scale). For typical

steplengths of 0.1-2 cm the second condition (2.14) is met for all gaseous materials. The first condition is only valid for solids and liquids and for particles with very low momenta ($\leq$0.1 GeV/c for muons and $\leq$ 1 GeV/c for protons). For typical momenta of 1-10 GeV/c one is just at the boarder between the Landau- and Gaussian fluctuation region.

What happens between these extreme cases is rather complicated for simulation purposes. We use for all liquids and plastics Landau fluctuation and for metals Gaussian fluctuation. This is of course a crude approximation, it does not take into account the dependence on steplength x and velocity β. In any case for each experimental set-up one has to decide this approximation to be valid. In previous versions we have chosen for the Gaussian fluctuatian

$$\sigma(dE) = \left(\frac{1}{\beta^2}\ 0.0001536\ \rho\ \frac{Z}{A}\right) dx \quad . \qquad (2.15)$$

This expression has the bad feature to be independent of the steplength, so that error propagation for finite steplengths is not correct. In the last version we use instead

$$\sigma(dE) = 2\ dE\ \left[\ \ln\left(\ 0.0001536 \cdot 1.333 \cdot 10^6\ \rho\ \frac{Z}{A}\ dx\ \right)\right]^{-1} \quad . \qquad (2.16)$$

For Landau fluctuation we took the phenomenological formula [14]

$$F(\Lambda)\ d\Lambda = \frac{0.762}{\sqrt{2\pi}}\ \exp\left[-0.5\ \left(\Lambda^{\alpha} + e^{-\Lambda}\right)\right]\ d\Lambda \quad , \qquad (2.17)$$

where α=1 (0.85) for $\Lambda \leq 0$ (>0). Λ is a parameter related to the momentum loss by

$$P = P_{mp} + \frac{\Lambda}{1.75}\ \sigma\left(\frac{dP}{dx}\right) \quad , \qquad (2.18)$$

where P and P_{mp} are the actual and most probable momentum loss respectively. The parameter 1.75 has been chosen as to fit best energy loss distributions for liquid argon .

The distributions obtained in this way seem to be too narrow for scintilators and gaseous materials. Because of the negligible energy loss,

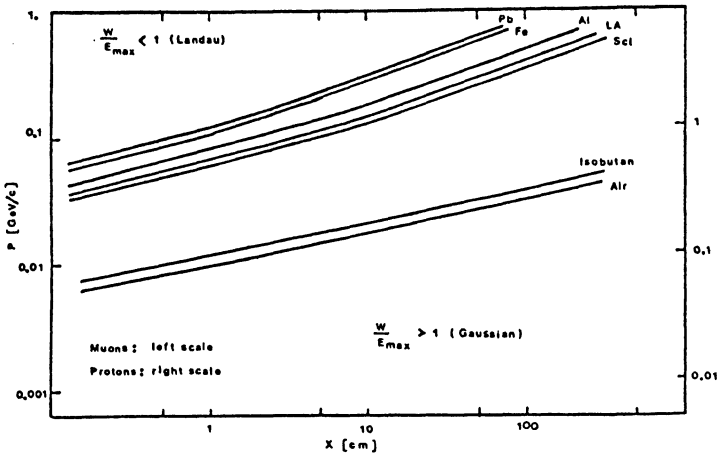

Figure 2. Momentum vs x diagram for $W/E_{max}=1$ for various materials. For muons use the left scale and for protons the right scale.

compared to the energy loss in metals, this does not influence the shower development itself. On the other hand one has in any case to calibrate a certain detector set-up with the response to muons (e.g. statistics of light-output, secondary electron emission, phototubes and electronics). Therefore we leave it to the digitization routines to do the final adjustment of the broadening of the energy loss distributions. For a discussion of detailed simulations of energy loss distributions in gas proportional chambers we refer to ref. [15].

In the latest version of the program (GHEISHA7) we use Landau fluctuations for all materials. Formula (2.17) is used to generate random numbers, folded with a width according to (2.16). The parameter in (2.18) has been adjusted for all materials. In this way we obtained mean values of the dE/dx distribution different from the most probable values, as shown in column 4 of table 1. A reasonable agreement with the values quoted by the Particle Data Group is observed.

2.2.2 δ-ray production in light materials

Depending on their energy, electrons ejected by the ionization process will cover a certain distance in the material. For energies up to a few hundred keV, a rather good approximation for the range is given by

$$R_e = 0.71\ E^{1.72}/\rho \qquad [cm] \quad , \tag{2.19}$$

where E in MeV and ρ in g/cm^3. From simple two-body kinematics, the maximum energy transfer to the electrons can be expressed by

$$E_{max} = \frac{2m_e\beta^2}{1-\beta^2} \quad , \tag{2.20}$$

β beeing the velocity of the traversing primary particle. E_{max} can in principle get any value for $\beta \to 1$. For a muon of p = 1 GeV/c momentum, we calculate E_{max} =91 MeV, for p = 10 GeV/c we get E_{max} = 9.1 GeV. The inverse square behaviour of the energy distribution (see equ. (2.8)) guarantees that electrons with such large energies are not rather abundant.

Electrons with a range exceeding a certain value, given in general by the resolution of the position measurement of the respective experimental device, are called δ-rays. Inspection to formula (2.19) shows that production of δ-rays is meaningful only for gaseous and fluid materials.

The simulation of δ-rays is done as follows. First we calculate the minimum energy E_{min} for δ-electrons from the minimum range requirement R_{min}, the value for the latter quantity has to be given by the user. Inverting equ. (2.19) we get

$$E_{min} = \left(\frac{R_{min}\,\rho}{0.71}\right)^{0.58} \qquad [MeV] \quad . \tag{2.21}$$

In case of magnetic fields, not the total path range but the diameter of the bending circle is the relevant range requirement, so that for B $\neq$ 0 equ. (2.21) has to be replaced by (see also the formulas in chapter 2.4)

$$E_{min} = \frac{R_{min}\,B}{6.67} \qquad [MeV] \quad , \tag{2.22}$$

B in kG.

The number of δ-rays leaving an energy E_{min} or larger in the present step is given by equ. (2.9),

$$\langle N \rangle_{E \geq E_{min}} = W/E_{min} \quad , \tag{2.23}$$

where W is already defined in equ.(2.10). The actual number N is Poisson-distributed around $\langle N \rangle$. The energies of the electrons are generated according to the inverse square behaviour and the emission angle Θ with respect to the primary particle direction is given by

$$\cos^2\theta = E/E_{max} \quad . \tag{2.24}$$

The δ-rays are followed through the detector until they stop or enter a heavy material. No cut-off energies are applied in the tracking algorithm. The energy of the δ-ray is subtracted from the energy deposit for the primary particle, as calculated by equ.(2.1).

The resulting effect of this procedure is 1) an increase of the Landau tail for light materials; 2) a more realistic space distribution of the ejected electrons in the ionization process. The programm GHEISHA is divided into a shower and a digitization simulation part. The generation of δ-rays lies just somewhere between these two parts. User who wants to simulate detectors with high spatial resolution wire chambers should make shure that the present δ-ray production scheme is compatible with their own digitization simulation. In any case the minimum range R_{min} has to be adjusted according to the resolution of the respective experiment.

2.3 MULTIPLE SCATTERING

In the design of a hadron filter for identification of muons a thick absorber is normally used, resulting in an increase of phase space both in angular divergence and lateral position. We shall discuss here a method, which allows to work out distribution functions of also other quantities connected with the passage of a particle through an absorber. The underlying mathematical theory can be found in ref. [16]. We repeat the main steps as a mathematical exercise.

Consider thus a passage of a particle through an absorber and denote the coordinates of the points in which collisions take place by $z_1, z_2, \ldots, z_k$ and the projected angles by $\vartheta_1, \vartheta_2, \ldots, \vartheta_k$. Consider now l quantities $F_1, F_2, \ldots, F_l$, which are related to z_ν and ϑ_ν by

$$F_\lambda = \sum_\nu f_\lambda(z_\nu, \vartheta_\nu) \quad , \tag{2.25}$$

where f_λ are arbitrary functions. Then one finds from purely statistical arguments for the logarithmic generating function

$$H_Q(v_1, v_2, \ldots, v_l) = \tag{2.26}$$
$$\iint a(z)\ \Phi(z,\vartheta)\ \left[\exp\left(\sum_{\nu=1}^{l} v_\nu f_\nu(z,\vartheta)\right) - 1\right] dz\ d\vartheta \quad ,$$

where H_Q is defined by

$$H_Q(v_1, v_2, \ldots, v_l) = \tag{2.27}$$
$$\ln \int \exp\left(\sum_{\nu=1}^{l} v_\nu F_\nu\right)\ Q(F_1, \ldots, F_l)\ dF_1 \ldots dF_l$$

and $Q(F_1,\ldots,F_l)$ is the simultaneous distribution function of all quantities $F_1, F_2, \ldots, F_l$. The right standing integral is the well known Laplace-transformed of Q. $\Phi(z,\vartheta)$ is the distribution in one collision and a(z) is defined as the probability density for a collision to take place at a depth z:

$$a(z) = N(z)\ \Phi(z) \tag{2.28}$$

$$\Phi(z) = \int \Phi(z,\vartheta)\ d\vartheta \quad . \tag{2.29}$$

a(z) depends on z because the energy of the particle is slewed down. In the following we shall normally assume that a(z) = a = constant and $\Phi(z,\vartheta) = \Phi(\vartheta)$.

The Gaussian approximation in multiple scattering is now introduced by expanding the integral in (2.26) and by taking the first two powers only :

$$H_Q(v_1, v_2, \ldots, v_l) =$$
$$\iint a(z)\ \Phi(z,\vartheta)\ \left[\sum_{\nu}^{l} v_\nu f_\nu + (1/2) \sum_{\nu\mu}^{l} v_\nu v_\mu f_\nu f_\mu + \ldots.\right] dz\ d\vartheta \quad . \tag{2.30}$$

This may be compared with the logarithmic generating function

$$H_G(v_1,\ldots,v_l) = \sum_{\nu}^{l} a_\nu v_\nu + (1/2)\sum_{\nu\mu}^{l} (A^+)_{\nu\mu} v_\nu v_\mu \qquad (2.31)$$

of the inhomogeneous Gaussian distribution

$$G(x_1,\ldots,x_l) = \qquad (2.32)$$

$$\frac{\Delta^{1/2}}{(2\pi)^{l/2}} \exp\left[-(1/2)\sum_{\nu\mu}^{l} A_{\nu\mu}(x_\nu - a_\nu)(x_\mu - a_\mu)\right]$$

to get the coefficients

$$a_\nu = \iint a(z)\Phi(z,\vartheta) f_\nu(z,\vartheta)\, dz\, d\vartheta \qquad (2.33)$$

$$(A^+)_{\nu\mu} = \iint a(z)\Phi(z,\vartheta) f_\nu(z,\vartheta) f_\mu(z,\vartheta)\, dz\, d\vartheta \quad . \qquad (2.34)$$

$(A^+)_{\nu\mu}$ are the elements of the Matrix A^{-1}.

We start with the calculation of the distribution of the projected angle and lateral spread. If we set

$$f_1(z,\vartheta) = \vartheta \qquad (2.35)$$

$$f_2(z,\vartheta) = (Z-z)\,\vartheta \quad , \qquad (2.36)$$

then F_1 is the total deflection angle Θ and F_2 the lateral spread X after passage of a step Z. By definition we denote

$$\sigma_\vartheta^2 = \int \vartheta^2\, \Phi(\vartheta)\, d\vartheta \qquad (2.37)$$

and set a(z) = constant and $\Phi(z,\vartheta) = \Phi(\vartheta)$. Because of symmetry it is evident that $\langle\vartheta\rangle = 0$ and therefore $a_1 = a_2 = 0$. A simple calculation shows that

$$\begin{aligned} (A^+)_{11} &= a\sigma_\vartheta^2 Z = \langle\theta_x^2\rangle \\ (A^+)_{12} = (A^+)_{21} &= (1/2)\, a\sigma_\vartheta^2 Z^2 = \langle\theta_x X\rangle \\ (A^+)_{22} &= (1/3)\, a\sigma_\vartheta^2 Z^3 = \langle X^2\rangle \quad . \end{aligned} \qquad (2.38)$$

According to classical theory of electrodynamic [17] we have

$$a\sigma_\vartheta^2 = \left(\frac{\alpha}{p\,\beta}\right)^2 \frac{1}{X_0} \quad , \qquad (2.39)$$

where α = 0.015 GeV and X_0 is the radiation length of the material. More accurate treatment of the problem leads to [18]

$$a\sigma_\vartheta^2 Z = \langle\theta_x^2\rangle = \left(\frac{\alpha}{p\,\beta}\right)^2 \frac{Z}{X_0}\left[1 + \frac{1}{9}\log_{10}\left(\frac{Z}{X_0}\right)\right]^2 . \qquad (2.40)$$

Then our basic formulae read:

$$Q(\theta_x, X) = \frac{\sqrt{3}}{\pi\langle\theta_x^2\rangle Z} \exp\left[-\frac{2}{\langle\theta_x^2\rangle}\left(\theta_x^2 - 3\theta_x\frac{X}{Z} + 3\frac{X^2}{Z^2}\right)\right] \qquad (2.41)$$

$$P(\theta_Y, Y) = \frac{\sqrt{3}}{\pi\langle\theta_Y^2\rangle Z} \exp\left[-\frac{2}{\langle\theta_Y^2\rangle}\left(\theta_Y^2 - 3\theta_Y\frac{Y}{Z} + 3\frac{Y^2}{Z^2}\right)\right] \quad , \qquad (2.42)$$

where $\langle\Theta_x^2\rangle$ and $\langle\Theta_Y^2\rangle$ are given by equ.(2.39) or (2.40). Equs. (2.41) and (2.42) are the well known formulae already given by Rossi [19].

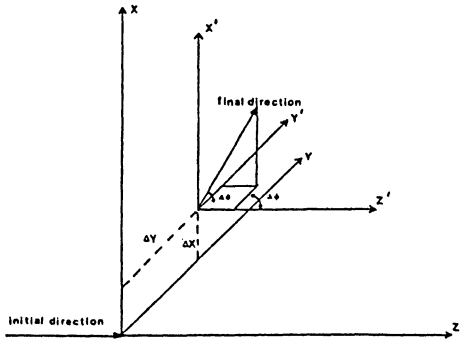

Figure 3. Definition of displacements and angles in multiple scattering.

The simulation of multiple scattering in a small step is then done as follows. We first generate two numbers A and B, which are distributed according to a two-dimensional Gaussian with a r.m.s. of 1 each. Then the two angles $\Delta\vartheta$ and $\Delta\varphi$ (see fig.3) with

$$\sin(\Delta\vartheta) = \sqrt{\langle\theta_x^2\rangle}\ B \tag{2.43}$$

$$\sin(\Delta\varphi) = \sqrt{\langle\theta_x^2\rangle}\ A \tag{2.44}$$

and the two displacements with

$$\Delta Y = \sin(\Delta\varphi)\ \Delta z/2 \tag{2.45}$$

$$\Delta X = \sin(\Delta\vartheta)\ \Delta z/2 \tag{2.46}$$

are calculated. The simulation according to equs. (2.43) to (2.46) is independent in both projections. The stepsize Δz in the tracking procedure is small ($\sim$ 0.1 - 0.2 cm, see chapter 4). Therefore the assumption that a(z) and $\Phi(z,\vartheta)$ do not depend on z is justified for each individual step. The decrease of momentum due to ionization energy loss is then applied after the step has been carried out. To check the multiple scattering simulation we have assumed a test set-up as shown in fig.4. A sphere of iron of a total of 200 cm radius is interspaced with 1 cm chambers at 50, 100, 150 and 200 cm radius. Muons of various momenta are generated along the z-axis and the deflection angles Θ_{Xi} and Θ_{Yi} and lateral displacements X_i and Y_i are measured in each chamber layer. X_i and Y_i are defined as the projected length on the sphere.

The second moments and correlation coefficients between measurements in the same layer and in two different layers according to equ. (2.34) are summarized in the following. X_1,Z_1 and X_2,Z_2 are given in fig 4. The Δ step function is defined as

$$\Delta(Z-z) = \begin{cases} 0 \text{ for } z > Z \\ 1 \text{ for } z < Z \end{cases} . \tag{2.47}$$

The moments of all odd orders vanish. There should be no correlations between quantities in different projections. All quantities are calculated for vanishing energy loss. $Z_2 > Z_1$ is always assumed.

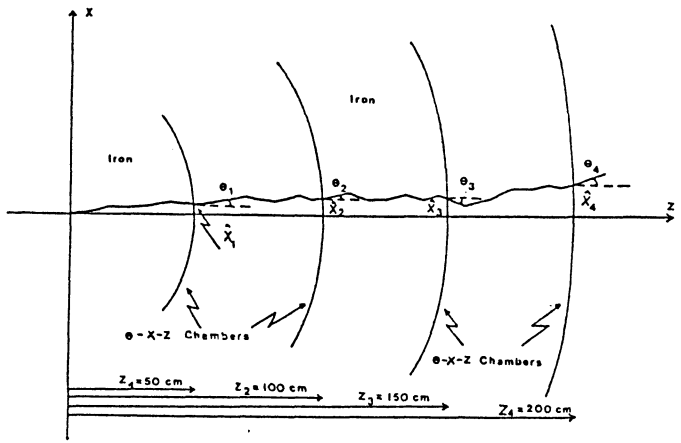

Figure 4. Experimental set-up used to check multiple scattering. For further details see text.

1) $f_1 = \vartheta$
$f_2 = (Z_1-z)\vartheta$

$$\Gamma = \frac{\sqrt{3}}{2}$$

$$\langle\theta_1\ X_1\rangle = (1/2)\ a\sigma_\vartheta^2 Z_1^2 \tag{2.48}$$

2) $f_1 = \Delta(Z_1-z)\vartheta$
$f_2 = \vartheta$

$$\Gamma = \frac{Z_1}{\sqrt{Z_1\ Z_2}} = \sqrt{\frac{Z_1}{Z_2}}$$

$$\langle\theta_1\ \theta_2\rangle = a\sigma_\vartheta^2 Z_1 \tag{2.49}$$

3) $f_1 = \Delta(Z_1-z)\ (Z_1-z)\ \vartheta$
$f_2 = (Z_2-z)\ \vartheta$

$$\Gamma = \frac{1}{2}\frac{Z_1[3Z_2-Z_1]}{Z_2\sqrt{Z_1Z_2}} = \frac{1}{2}\frac{[3Z_2-Z_1]}{Z_2}\sqrt{\frac{Z_1}{Z_2}}$$

$$\langle X_1\ X_2\rangle = (1/6)\ a\sigma_\vartheta^2 Z_1^2[3Z_2-Z_1] \qquad (2.50)$$

4) $f_1 = \Delta(Z_1-z)\ (Z_1-z)\ \vartheta$
$f_2 = \vartheta$

$$\Gamma = \frac{\sqrt{3}}{2}\frac{Z_1}{\sqrt{Z_1\ Z_2}} = \frac{\sqrt{3}}{2}\sqrt{\frac{Z_1}{Z_2}}$$

$$\langle X_1\ \theta_2\rangle = (1/2)\ a\sigma_\vartheta^2 Z_1^2 \qquad (2.51)$$

5) $f_1 = \Delta(Z_1-z)\ \vartheta$
$f_2 = (Z_2-z)\ \vartheta$

$$\Gamma = \frac{\sqrt{3}}{2}\frac{Z_1[2Z_2-Z_1]}{Z_2\sqrt{Z_1Z_2}} = \frac{\sqrt{3}}{2}\frac{[2Z_2-Z_1]}{Z_2}\sqrt{\frac{Z_1}{Z_2}}$$

$$\langle \theta_1\ X_2\rangle = a\sigma_\vartheta^2 Z_1[Z_2-(1/2)\ Z_1] \qquad (2.52)$$

6) $f_1 = \vartheta$
$f_2 = \vartheta$
$\Gamma = 1$
$\langle \theta_1^2\rangle = a\sigma_\vartheta^2 Z_1 \qquad (2.53)$

7) $f_1 = (Z_1-z)\ \vartheta$
$f_2 = (Z_1-z)\ \vartheta$
$\Gamma = 1$
$\langle X_1^2\rangle = (1/3)\ a\sigma_\vartheta^2 Z_1^3$. $\qquad (2.54)$

For a measurement of angle or displacement at fixed Z_2 = 100 cm Fe we have calculated the correlation coefficient for second measurements of angle or displacement at $Z_1 < Z_2$, as shown in fig.5. It is interesting to note

that $\Gamma(\Theta_1X_2)$ has a maximum at $Z_1 = (2/3)Z_2$. If one wants to measure the track outside the absorber and at one point inside, then often the question arises, what to measure, the angle or the displacement. From fig.5 the following answer is given: If momentum measurement using a magnetized absorber is required, then the most uncorrelated quantities have to be preferred, i.e. the deflection angle outside and the displacement inside the absorber. On the other hand for muon identification, in order to distinguish the μ-track from uncorrelated shower particles, it is much better to use the displacement outside the absorber and the angle or displacement inside. We come back to these questions in later sections of this report.

The behaviour of the correlations is changed somewhat if one includes ionization energy losses. For the following results use has been made of the detailed simulation program. In fig.6 we compare the r.m.s. deflection angles and displacements for various depths in iron with the curves expected without energy loss. It is seen that energy loss do not play an important role for p > 5 GeV/c, whereas for lower momenta the deflections and displacements rise if energy loss is taken into account. All correlations drop down for low momenta. This is shown in figs. 7 and 8. The numbers given on the right side in each figure have been calculated from the formulae (2.48)-(2.54), i.e. the corresponding values for no energy loss. The curves are only to guide the eye. As can be seen, any correlation involving measurement of displacement outside the absorber ($\Gamma(X_iX_k)$ and $\Gamma(\Theta_iX_k)$) is only weakly affected by energy loss, whereas on the other hand $\Gamma(\Theta_i\Theta_k)$ and $\Gamma(X_i\Theta_k)$ drop down very steeply approaching lower momenta. This favours additionally the use of displacement inside and angle outside for momentum measurement with magnetized absorbers and displacement or angle inside and displacement outside for μ-identification.

Our simulation procedure reproduces quite well what is expected from theory. This was demonstrated in the previous figures. The only parameter to adjust is the r.m.s. deflection angle $\sqrt{\langle\Theta_0^2\rangle}$ per unit length. The formula given in (2.40) is exact to a few percent depending on the material and stepsize. It is surprising that inspection to the literature shows, that this quantity has been measured accurately at very low momenta (< 1 GeV/c), but only for muons also at higher momenta. Just very recently a measurement for pions at higher momenta has been performed [20]. Another comment has to be made to the simulation procedure. The response of the simulation for $\sqrt{\langle\Theta_0^2\rangle}$ is in general slightly smaller compared to the input given by (2.40), due to various reasons (see chapter 4). Therefore for each detector set-up the multiple scattering canstant α has to be adjusted in order to get the right response for the r.m.s. deflection angle.

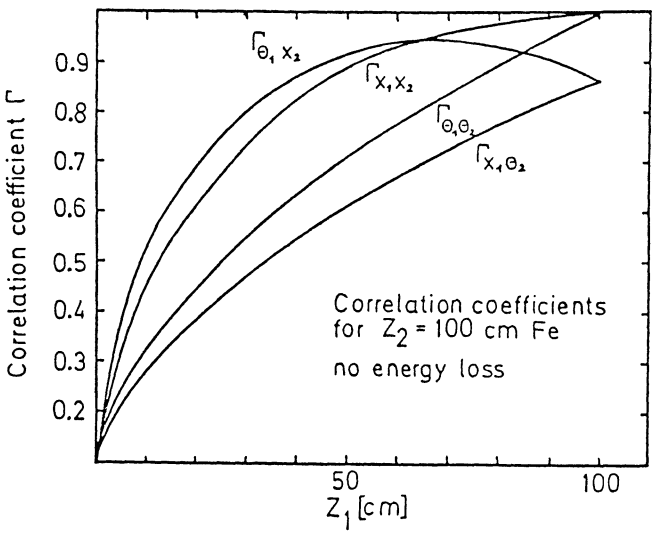

Figure 5. Correlation coefficients for multiple scattering. For further details see text.

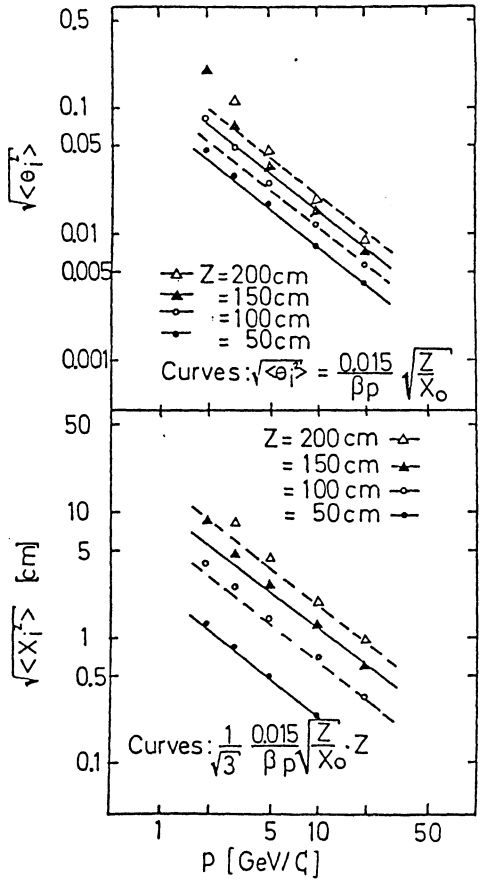

Figure 6. R.m.s. deflection angles and displacements for various depths in iron as function of momentum p. The curves represent expectations without ionization energy loss.

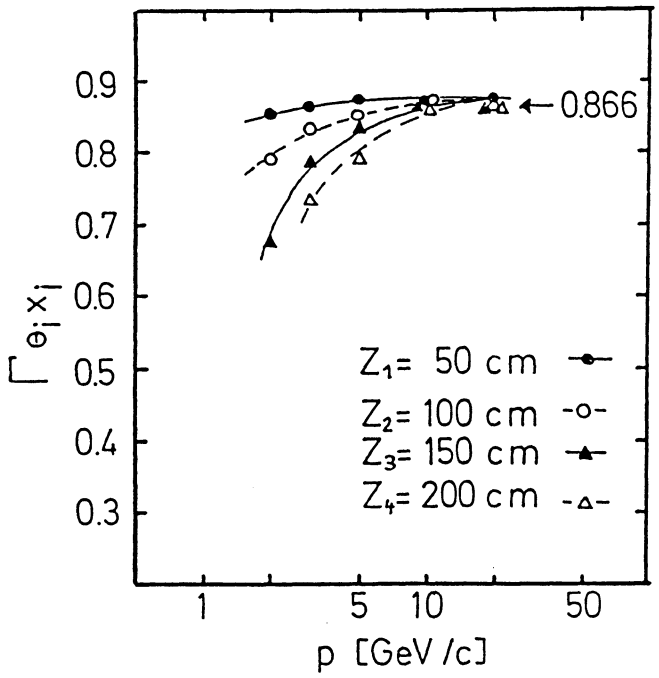

Figure 7. Correlation coefficient $\Gamma(\Theta_i X_i)$ for various depths of iron as function of momentum p. The curves are only to guide the eyes. The number 0.866 is the result without ionization energy loss.

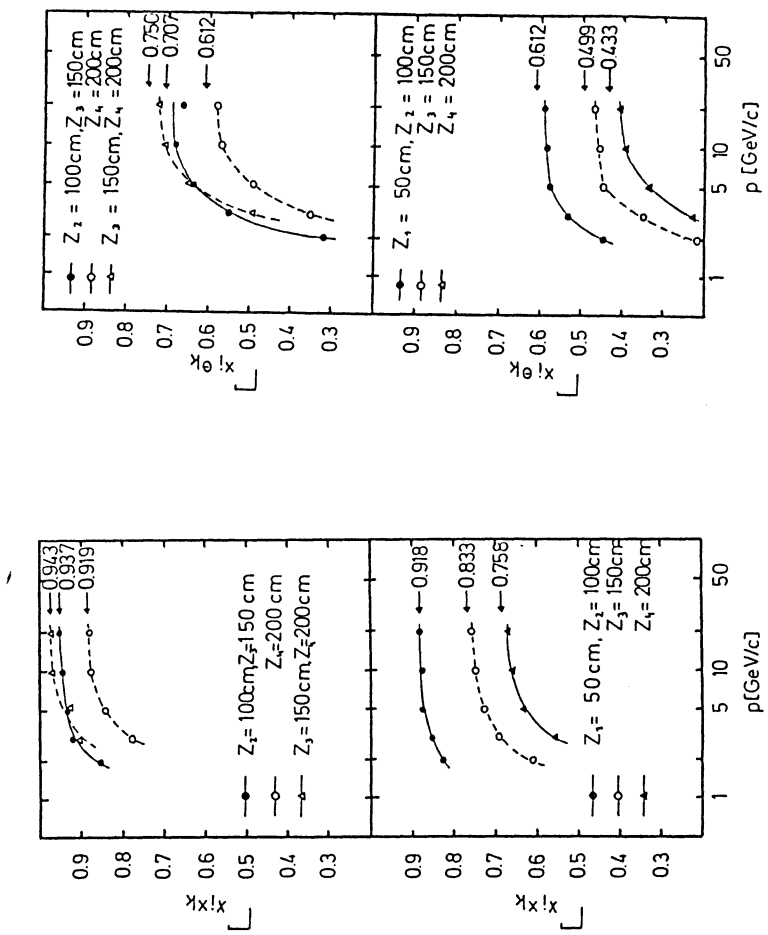

Figure 8. Correlation coefficients for various depths of iron as function of momentum p. The curves are only to guide the eyes. The numbers given on the right side in each figure have been calculated for no energy loss.

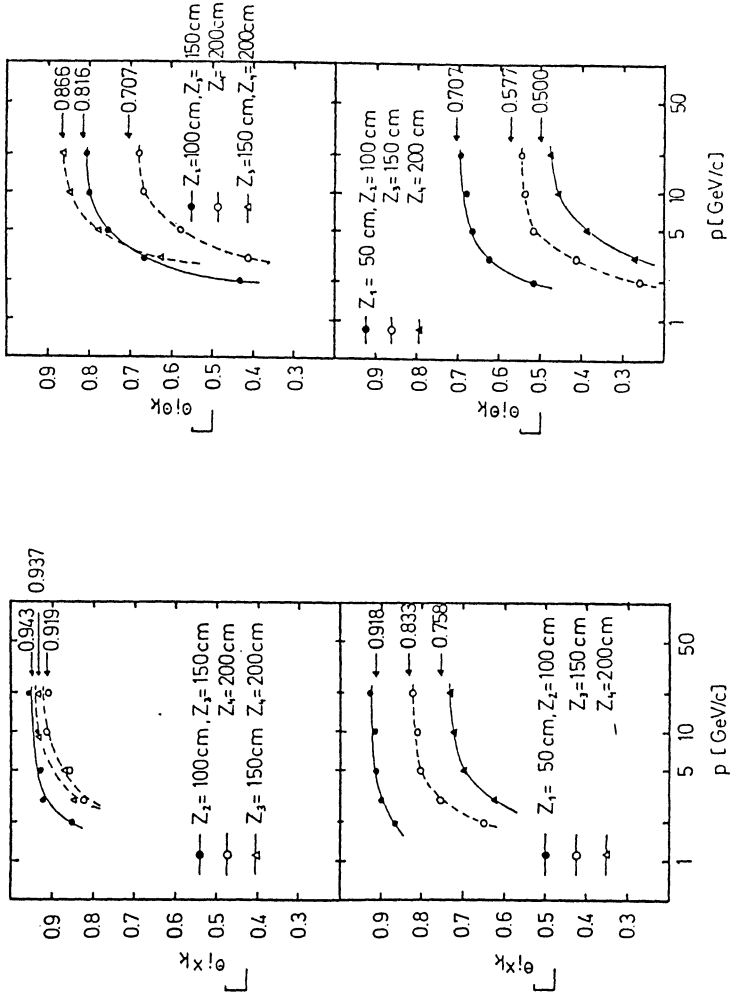

Figure 8. Correlation coefficients for various depths of iron as function of momentum p. The curves are only to guide the eyes. The numbers given on the right side in each figure have been calculated for no energy loss.

2.4 TRACKING IN MAGNETIC FIELDS

In this section we shall give the basic formulae for the path of particles through magnetized absorbers. We will continue this in chapter 4 with a discussion on the dependence on magnetic field strength, on multiple scattering, with the radiation length of the material as parameter, on setting errors of chambers as measuring devices and the dependence on the absorber layer thickness and the number of absorber layers.

We assume that the magnetic field has been measured in each point and is given in a form of a vector function $B_x(x,y,z)$, $B_y(x,y,z)$, $B_z(x,y,z)$. The angles λ and φ are defined as dip-angle with respect to the x-y plane and angle in the x-y plane with respect to the x- axis respectively, as shown in fig.9.

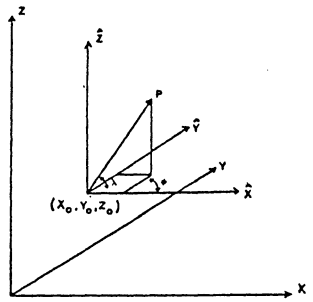

Figure 9. Definition of coordinates and angles used in the tracking in magnetic fields.

Without field ($B_x=B_y=B_z=0$) we have for a steplength S :

$$\begin{aligned} p_x &= p_{x0} = p \cos\lambda \cos\varphi \\ p_y &= p_{y0} = p \cos\lambda \sin\varphi \\ p_z &= p_{z0} = p \sin\lambda \end{aligned} \qquad (2.55)$$

$$\begin{aligned} x &= x_0 + S \cos\lambda \cos\varphi \\ y &= y_0 + S \cos\lambda \sin\varphi \\ z &= z_0 + S \sin\lambda \end{aligned} \qquad (2.56)$$

The momentum loss according to ionization energy loss and the changes of the angles according to multiple scattering are applied after the step has been carried out. We define the following quantities (B in kG, S in cm and P in GeV) :

$$\gamma = \frac{q\ B}{3336\ P} \tag{2.57}$$

$$\delta = B\ P \sqrt{1-\left(\frac{\vec{B}\cdot\vec{P}}{B\ P}\right)^2} \quad , \tag{2.58}$$

and the matrix R by

$$\begin{aligned}
R_{13} &= B_x/B \\
R_{23} &= B_y/B \\
R_{33} &= B_z/B \\
R_{12} &= (B_yP_z-B_zP_y)/\delta \\
R_{22} &= (B_zP_x-B_xP_z)/\delta \\
R_{32} &= (B_xP_y-B_yP_x)/\delta \\
R_{11} &= (R_{22}B_z-R_{32}B_y)/B \\
R_{21} &= (R_{32}B_x-R_{12}B_z)/B \\
R_{31} &= (R_{12}B_y-R_{22}B_x)/B \quad .
\end{aligned} \tag{2.59}$$

Then the transformations (2.55) and (2.56) have to be replaced by

$$\vec{P} = P_0\ (R\cdot\vec{b}) \tag{2.60}$$

with

$$b_1 = \sqrt{1-\left(\frac{\vec{B}\cdot\vec{P}_0}{B\ P_0}\right)^2}\ \cos(\gamma S) \tag{2.61}$$

$$b_2 = -\sqrt{1-\left(\frac{\vec{B}\cdot\vec{P}_0}{B\ P_0}\right)^2}\ \sin(\gamma S) \tag{2.62}$$

$$b_3 = \frac{\vec{B}\cdot\vec{P}_0}{B\ P_0} \tag{2.63}$$

and

$$|R\cdot\vec{b}| = 1 \tag{2.64}$$

and

$$(X,Y,Z) = (X_0,Y_0,Z_0) + S(R\cdot\vec{c}) \tag{2.65}$$

with

$$c_1 = \sqrt{1-\left(\frac{\vec{B}\cdot\vec{P}_0}{B\ P_0}\right)^2}\ \frac{\sin(\gamma S)}{(\gamma S)} \tag{2.66}$$

$$c_2 = -\sqrt{1-\left(\frac{\vec{B}\cdot\vec{P}_0}{B\ P_0}\right)^2}\ \left(\frac{1-\cos(\gamma S)}{(\gamma S)}\right) \tag{2.67}$$

$$c_3 = \frac{\vec{B}\cdot\vec{P}_0}{B\ P_0} \tag{2.68}$$

and

$$|R\cdot\vec{c}| = 1 \quad . \tag{2.69}$$

For later applications we specialize formulae (2.60) and (2.65) for $\vec{P}_0 = (0,0,P_0)$ and $\vec{B} = (0,B,0)$:

$$\begin{aligned}
x &= x_0 - S\left(\frac{1-\cos(\gamma S)}{(\gamma S)}\right) \\
y &= y_0 \\
z &= z_0 + S\,\frac{\sin(\gamma S)}{(\gamma S)}
\end{aligned} \tag{2.70}$$

$$\begin{aligned}
p_x &= -p_0\ \sin(\gamma S) \\
p_y &= 0 \\
p_z &= p_0\ \cos(\gamma S) \quad .
\end{aligned} \tag{2.71}$$

For $(\gamma S) \ll 1$ this can be expanded into a serie :

$$\begin{aligned} x &\approx -\tfrac{1}{c}\ \gamma S^2 \\ y &\approx 0 \\ z &\approx S \end{aligned} \qquad (2.72)$$

$$\begin{aligned} p_x &\approx -p_0 \gamma S \\ p_y &\approx 0 \\ p_z &\approx p_0 \left(1-\tfrac{1}{2}\ (\gamma S)^2\right) \end{aligned} \qquad (2.73)$$

This finishes the collection of transformation formulae which will be used in later paragraphs.

2.5 ELECTROMAGNETIC INTERACTIONS

2.5.1 The discrete shower simulation

A big part of the energy of initial hadrons is carried off by photons from neutral pion decay, which in turn start electromagnetic showers. Thus the electromagnetic cascade process of photons and electrons (positrons) is an essential problem also for hadronic cascades. In the hadronization process of quarks (jet-formation) initial electrons may be produced by the decay of heavy quarks. A widely used tag for exited $q\bar{q}$-systems is the decay into lower lying levels emitting one or more photons. All these processes call for a good simulation of electromagnetic showers for the analysis of storage ring experiments. A very sophisticated treatment of electromagnetic showers is included in the EGS-code (for a detailed description see ref. [4]), which is used as default in the present version of the GHEISHA program. But the reader should remember that we wanted to develop a program for a complete detector simulation of a storage ring experiment. Therefore approximations which reduce computer time consumption had to be applied whenever justified. This is described in the following. Clearly further simplications of electromagnetic showers will be one of the future developments of the GHEISHA-program. All users are invited to help.

We make the distinction between discrete and continous energy losses of electrons and positrons, and between shower parametrizations. In the discrete case secondary particles with energies above their cut-off energies E_c are created and subsequently transported as a real particle. The

continous loss is the result of interactions in which the energy transfer to the secondary particles is not sufficient to put them above the discrete transport energy threshhold. The cut-off energy E_c is given by the sensitivity of the detector. Processes which create particles with energies lower than E_c have to be integrated over to give the total ionization loss.

The dominant processes for the multiplication of secondary particles, bremsstrahlung and pair production, are discussed in detail in ref. [21] and [22] respectively. The Feynman graphs drawn in fig.10 show that they are closely related to each other and similar formulae may be expected. A lot of different approximations for various conditions have been calculated in ref. [21] and [22] for the cross sections as function of energies and angles of the particles and as function of the atomic number A and charge number Z (or equivalently radiation length X_0). According to the experiences of other authors ([2], [3], [4] and [23]) we have chosen the following formulae :

$$\frac{d\sigma_{brems}}{dk} = \frac{r_0^2 \alpha Z(Z+\xi(Z))}{k}\ f_{brems}(E_0,k,Z) \qquad (2.74)$$

$$\frac{d\sigma_{pair}}{dE_+} = \frac{r_0^2 \alpha Z(Z+\xi(Z))}{k^3}\ f_{pair}(E_+,k,Z) \qquad (2.75)$$

$$\xi(Z) = \ln(1440\ Z^{-2/3})/[\ln(183\ Z^{-1/3}) - f_c(Z)] \qquad (2.76)$$

$$f_c(Z) = x^2\left[\frac{1}{1+x^2} + 0.20206 - 0.0369x^2 + 0.0083x^4 - 0.0020x^6\right] \qquad \text{for } k > 50 \text{ MeV} \qquad (2.77)$$

$$f_c(Z) = 0 \qquad \text{for } k < 50 \text{ MeV}$$

$$x = \alpha Z$$

$$f_{brems}(E_0,k,Z) = \left[1+\left(\frac{E}{E_0}\right)^2\right]\Psi_1 - \frac{2}{3}\left(\frac{E}{E_0}\right)\Psi_2 \qquad (2.78)$$

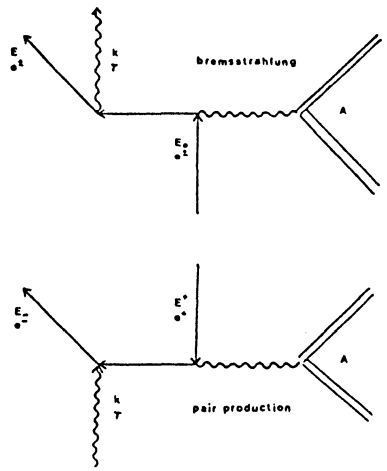

Figure 10. Feynman graphs for bremsstrahlung and pair production.

$$f_{pair}(E_+,k,Z) = (E_+^2+E_-^2)\Psi_1 + \frac{2}{3} E_+E_-\Psi_2 \qquad (2.79)$$

$$\Psi_i = \Phi_i - \frac{4}{3} \ln Z - 4f_c(Z) \qquad (2.80)$$

$$\Phi_1 = 20.867-3.424\cdot\delta+0.625\cdot\delta^2 \quad \text{for } \delta<1$$
$$= 21.12-4.184\ \ln(\delta+0.925) \quad \text{for } \delta>1 \qquad (2.81)$$

$$\Phi_2 = 20.029-1.930\cdot\delta-0.086\cdot\delta^2 \quad \text{for } \delta<1$$
$$= 21.12-4.184\ \ln(\delta+0.925) \quad \text{for } \delta>1 \qquad (2.82)$$

$$\delta = 272\ Z^{-1/3}\ \Delta \qquad (2.83)$$

$$\Delta = \frac{km}{2E_0E} \quad \text{for bremsstrahlung}$$
$$\Delta = \frac{km}{2E_+E_-} \quad \text{for pair-production.} \qquad (2.84)$$

All energies are given in MeV and the other constants are given by

$$\alpha = 1/137$$
$$r_0^2 = 7.9524\ 10^{-26}\ cm^2 = 79.524\ mb \qquad (2.85)$$
$$m = 0.511\ MeV\ .$$

The total cross sections are then given by numerical integration

$$\sigma_{brems}(E_0) = \int_{E_c}^{E_0-m} \frac{d\sigma_{brems}}{dk}\, dk \qquad (2.86)$$

$$\sigma_{pair}(k) = \int_{E_c}^{k-m} \frac{d\sigma_{pair}}{dE_+}\, dE_+ \ . \qquad (2.87)$$

In fig.11 we show the integrated cross sections as function of the energy of the initial particle for various cut-off energies E_c. In case of pair production the cut-off energies have essentially only an effect for very small energies, whereas for bremsstrahlung the E_c influences the total cross section over the whole energy range. The reason for that is quite simple and lies in the momentum spectra of the outgoing particles, as shown in fig.12. The probability to get a positron (or electron) with energy E_+(or E_-) does nearly not depend on E_+(or E_-) in case of pair production, i.e.

$$\frac{d\sigma_{pair}}{dE_+} \approx \text{constant } f(k). \qquad (2.88)$$

On the other hand for bremsstrahlung we observe the cross sections to become infinite as the energy approaches zero (infrared catastrophe). Therefore the integration is very sensitive to the choice for E_c.

The scaling law for electromagnetic processes is shown in fig.13, which shows that the mean free path divided by the radiation length is independent on the absorbing material, i.e.

$$\frac{\lambda}{X_0} = \frac{A}{X_0 N_a \rho \sigma} = \begin{cases} f_1(E_0) & \text{for bremsstrahlung} \\ f_2(k) & \text{for pair-production.} \end{cases} \tag{2.89}$$

Formula (2.74) can be quite good approximated by

$$\frac{d\sigma_{brems}}{dk} = \frac{A}{N_a \rho X_0} \frac{1}{k}, \tag{2.90}$$

which is shown for lead in fig.12 as dashed curves. From that we get by integration

$$\sigma_{brems} = \frac{A}{N_a \rho X_0} \ln(E_0/E_c) \tag{2.91}$$

or the mean free path

$$\lambda_{brems} = \frac{X_0}{\ln(E_0/E_c)}. \tag{2.92}$$

For pair production the mean free path approaches the value

$$\lambda_{pair} = \frac{9}{7} X_0 \qquad \text{for } k \to \infty. \tag{2.93}$$

The simulation procedure for pair production and bremsstrahlung may then be formulated as follows : In the default stepsize of $X_0/\ln(E_0/E_c)$ bremsstrahlung and pair production is tried according to formulas (2.92) and (2.93), where for pair production the mean free path for $k < 1$ GeV is calculated with formulas (2.87), (2.75) and the following ones. The energy of the photon and the positron is calculated according to equs. (2.90) and (2.88) respectively. The emission angle of the outgoing particle has been fixed in that way, so that the shower curves for incoming electrons fit best

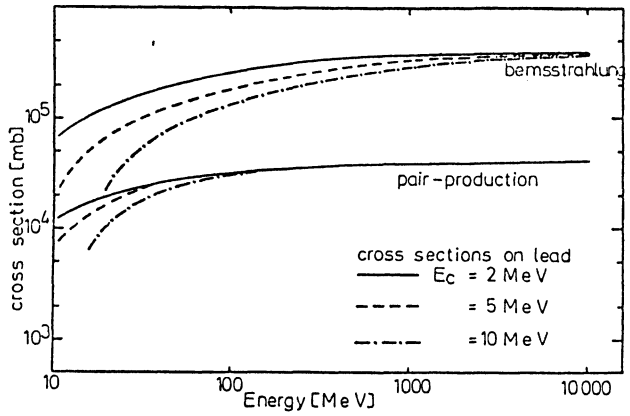

Figure 11. Cross sections for bremsstrahlung and pair production for various cut-off energies as function of the initial particle energy.

the lateral expansion in lead. A value of $18m_e/E_0$ and $18m_e/k$ had to be chosen for bremsstrahlung and pair production respectively.

Comparisons of the longitudinal and lateral shower expansion with experimental data [24] in lead, copper and alluminum are shown in fig.14. Plotted is the fraction of deposited energy per radiation length in fig.14a and the fraction of energy leaving a lateral radius r in fig.14b. Further comparisons will be shown later. The conclusion was that it seems not to be necessary to include other processes like Compton-scattering, Moller-scattering or Bhabha-scattering. These processes do not contribute to the multiplication process, but are only responsible for a steeper attenuation. The cross sections of these processes, shown in fig.15 in comparison with pair production, indicate that even at very low energies around 10 MeV they are negligible compared to the two dominating ones, bremsstrahlung and pair production. The energy absorption by ionization gives already a satisfactory attanuation.

For bremsstrahlung by muons we use the same formulae as for electrons, except of the different mass, so that the mean free path is given by

$$\lambda_{brems,\mu} = \left(\frac{m_\mu}{m_e}\right)^2 \frac{X_0}{\ln(E_0/E_c)} \qquad (2.94)$$

Values for Pb and Fe are 47 m and 120 m respectively. Therefore the effect of this process is expected to be very small. Fig.16 shows the energy spectrum of the produced photons by muons of 5 GeV in 1 m Fe. 2% of the muons produce a photon with $k > E_c = 6$ MeV in 1 m iron, only 0.8% with an energy larger than 10% of the muon energy.

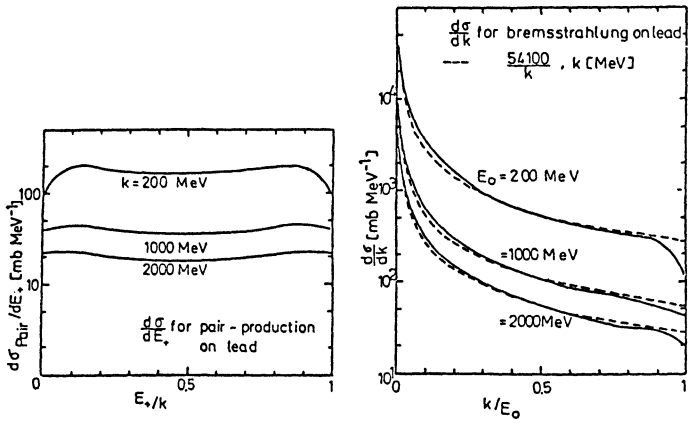

Figure 12. Energy spectra of outgoing particles for bremsstrahlung and pair production.

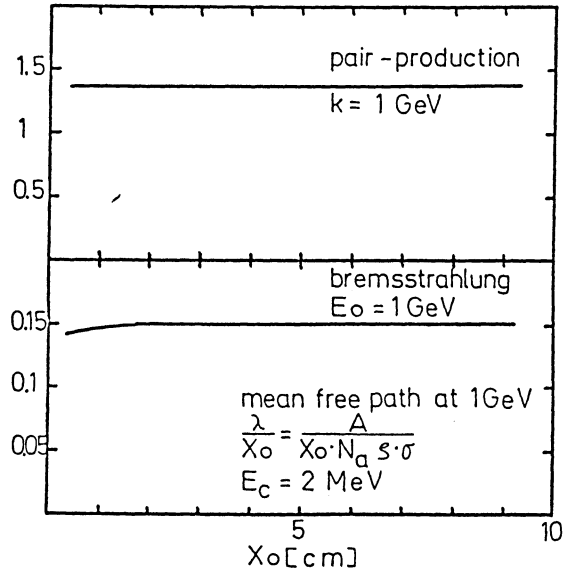

Figure 13. Mean free path for bremsstrahlung and pair production as function of the radiation length.

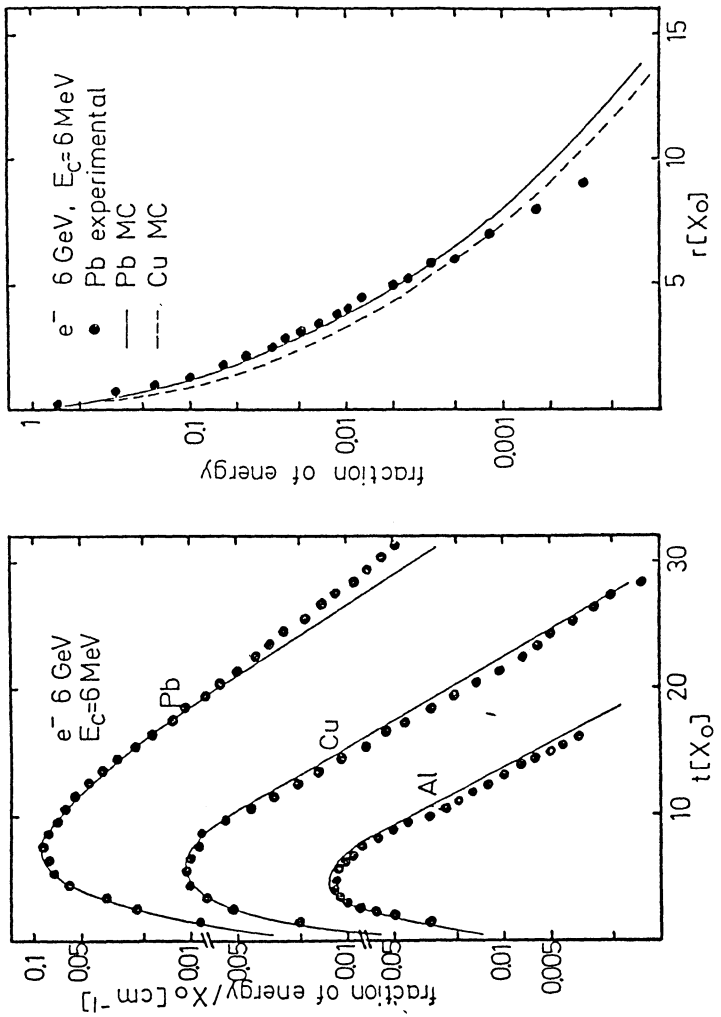

Figure 14. Fraction of deposited energy per radiation length (a) and fraction of energy leaving a lateral radius r (b) for e.m. showers in Pb, Cu and Al. The curves show the MC results.

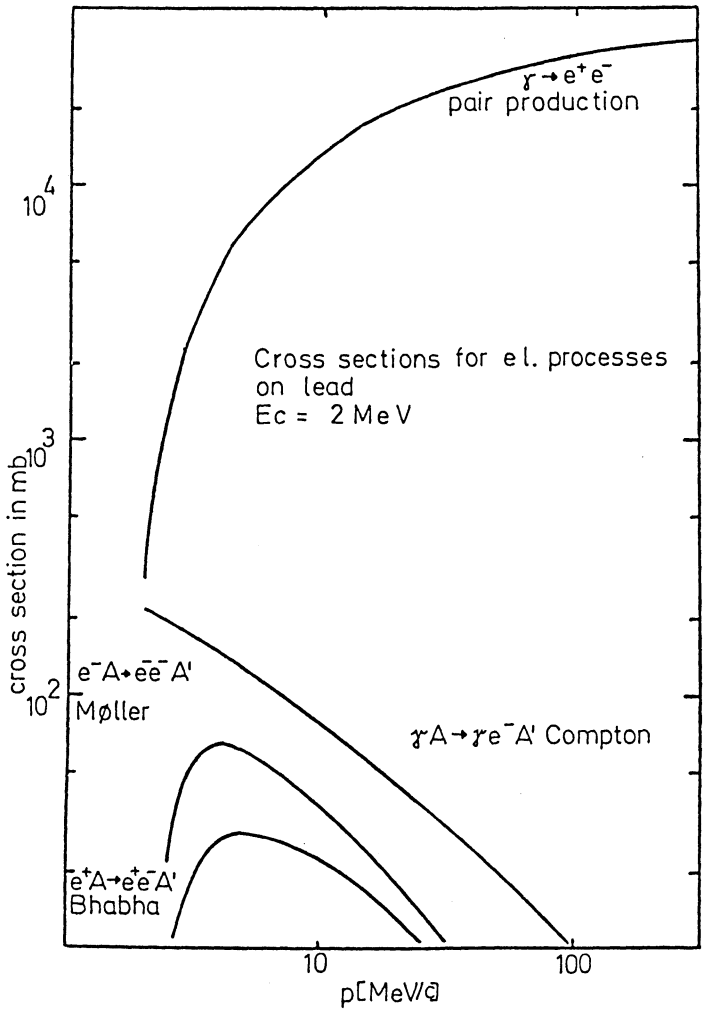

Figure 15. Cross sections for Compton scattering, Moller scattering and Bhabha scattering compared to pair production.

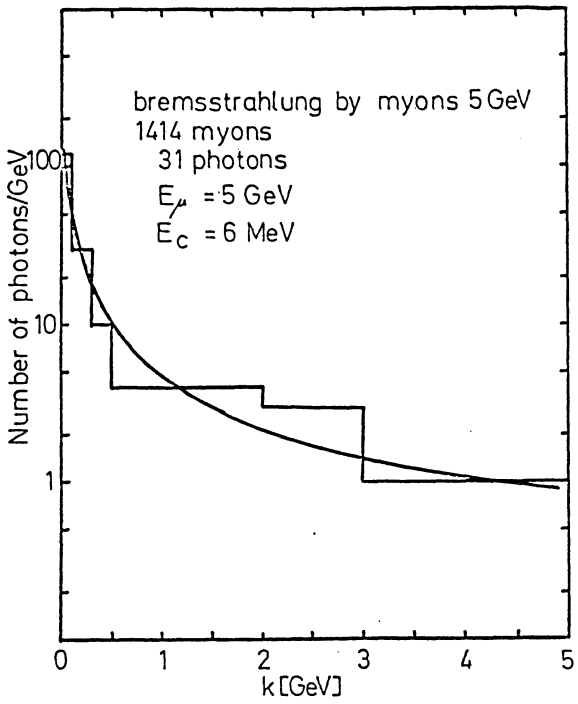

Figure 16. Energy spectrum of photons produced by muon bremsstrahlung at 5 GeV/c in Fe. The line is only to guide the eyes.

2.5.2 Shower parametrizations

For certain not too sophisticated detector set-ups it is not necessary to transport all electrons, positrons and photons until they reach the cut-off energy around 100 keV - 2 MeV. Use of parametrizations may be adequate below a relatively high cut-off energy of ,say, 100 - 500 MeV. But the experiences of the author have shown that a certain parametrization, worked out for a special detector, can not be taken over to any other detector. We can only give some hints here how to implement a parametrization into the program. Beside that the form of the parametrization depends highly on the problem in question. For electron/hadron separation by means of the lateral shower development it is certainly not sufficient to use an only one-dimensional parametrization. For acceptance studies in central track chambers any parametrization will be doubtful at all. As can be seen from this two examples, the use of parametrizations is limited to unsensitive detectors or detector parts.

Several types of parametrizations have been tried. The most frequently used ansatz for the longitudinal shower expansion is

$$\frac{dE}{dt} = E_0 \frac{b^{1+a}}{\Gamma(1+a)} t^a e^{-bt} \qquad (2.95)$$

t is the longitudinal coordinate in units of radiation lengths, E_0 the energy of the initial particle for a total absorbing device or the total pulse height for a sandwich calorimeter.

In a first attempt we have used only bremsstrahlung and pair production as multiplication processes and have chosen a cut-off energy of E_c = 200 MeV. This is clearly above the energies where all other reactions (Compton, Bhabha, ...) become important. For the bremsstrahlung and pair production we have not used the EGS-version, but the simplified treatments as discussed in the previous section. For all particles which have been slewed down below E_c, a longitudinal shower parametrization according to equ.(2.95) has been used. To this end the parameters a and b and their respective fluctuations, expressed by the r.m.s., have been determined as function of the energy of the incoming particle. For establishing the parametrization we used the EGS-code. This procedure has been carried out for a total absorbing copper block and also for a Cu-scintilator sandwich calorimeter of 0.5 cm sampling each. The results of this simple parametrization is shown in fig.17 for the total absorbing copper block.

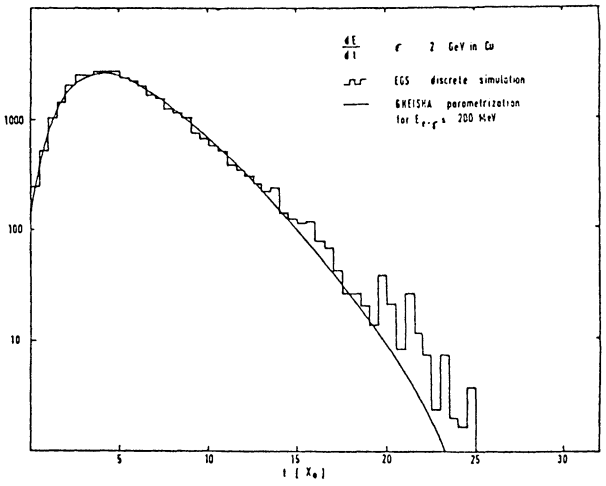

Figure 17. Longitudinal shower development in a copper block.The histogram represents the EGS simulation with cut-off energies 1.5 MeV and 100 keV for electrons (positrons) and photons respectively. The line is the GHEISHA result with simplified pair production and bremsstrahlung and parametrizations below E_C = 200 MeV.

In table 2 we give t_0 and $\langle t \rangle$, t_0 beeing the longitudinal position of the maximal energy deposit and $\langle t \rangle$ the radiation length averaged over the shower curve :

$$\langle t \rangle = \int_0^\infty t \frac{dE}{dt} dt \qquad (2.96)$$

Table 2 Shower parametrization in a copper block

t_0	1 GeV	5 GeV	10 GeV
EGS	3.45	5.00	5.60
GHEISHA	3.43	5.10	5.70
$\langle t \rangle$			
EGS	5.15	6.65	7.48
GHEISHA	5.23	6.63	7.27

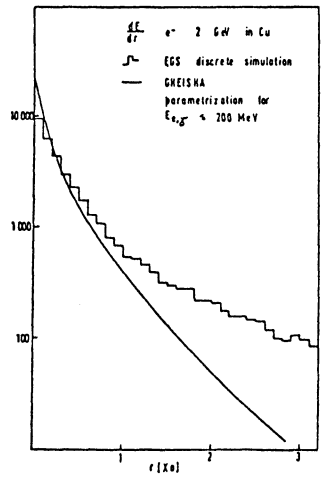

Figure 18. Same as fig.17, but transverse shower development.

Table 3 Shower parametrization in a copper scintilator sandwich calorimter

	EGS		CHEISHA	
p	⟨E⟩	σ_E	⟨E⟩	σ_E
1	124	8.3	125	8.5
2	250	11.6	250	11.9
3	380	17.6	375	15.1
5	631	21.3	626	18.0

A similar comparison is shown in table 3 for the Cu-scintilator sandwich. Here we give the total pulse-height and the r.m.s. We see that it is no problem to describe the longitudinal shower development by such a parametrization. It is clear that the transverse shower development can not be described by such a method, where the low energy processes have been integrated over. Just at low energies particles are produced with large emission angles. The disagreement of the lateral shower expansion in the copper block, shown in fig.18, is thus not surprising.

The shower parametrization, expressed in the form (2.95), does not describe the longitudinal fluctuations in a right way. The parameters a and b are correlated and not Gaussian distributed. This can be avoided by an ansatz of the form

$$\frac{dE}{dt} = E_0\, gc\, (gt)^{c-1} \exp[-(gt)^c] \quad . \tag{2.97}$$

We have used a lead-scintilator sandwich of 0.5 cm thickness each to get a throughout parametrization of photons and electrons of any energy. The parameters and their fluctuations as function of the primary energy are shown in fig.19. Due to leakage effects on both lateral sides of the calorimeter corrections had to be applied for inclination angles different from 90°. These are shown in fig.19g. Further corrections of the total pulse height turned out to be necessary. The correction factors given in fig.19h had to be applied for the first 3 radiation lengths (A-counter), the following 3 radiation lengths (B-counter) and the last 12 radiation lengths (C-counter) respectively. This experimental set-up is identical to the electromagnetic shower calorimeter of the Mark J experiment. The first 3 scintilator layers, then the following 3 and finally the last 12 layers are connected on both sides to one phototube each (A-, B- and C-counter). This experimental set-up will be described in more detail in chapter 5. In fig.20 we compare this parametrization with the complete discrete

EGS-simulation. Plotted is the avarage pulse height as function of the inclination angle of the primary photon. The electromagnetic calorimeter is followed by a hadron calorimeter, with a sequence of 2.5 cm iron and 1 cm scintilators. The leakage of the photon showers into the first two layers of this hadron calorimeter is shown in fig.21. As can be seen the parametrization gives a good overall description of the longitudinal shower shape.

For sandwich calorimeter a total other type of parametrization has been tried succesfully. The distribution of energy deposited in the various scintilators is given by

$$p(E;\Delta E_1,\ldots,\Delta E_n) \tag{2.98}$$

with the energy E of the primary particle. This can be expressed in terms of conditional probabilities as

$$\begin{aligned} p(E;\Delta E_1,\ldots,\Delta E_n) &= p(E;\Delta E_n \,|\, \Delta E_{n-1},\ldots,\Delta E_1) \\ &\cdot p(E;\Delta E_{n-1} \,|\, \Delta E_{n-2},\ldots,\Delta E_1) \\ &\cdots \\ &\cdot p(E;\Delta E_2 \,|\, \Delta E_1) \\ &\cdot p(E;\Delta E_1) \quad . \end{aligned} \tag{2.99}$$

The shower development can be treated as a Markov process, so

$$p(E;\Delta E_k|\Delta E_{k-1},\ldots,\Delta E_1) = p(E;\Delta E_k|\Delta E_{k-1}) \quad . \tag{2.100}$$

One gets

$$p(E;\Delta E_1,\ldots,\Delta E_n) = \prod_{i=1}^{n} p(E;\Delta E_i|\Delta E_{i-1}) \quad , \tag{2.101}$$

where $p(E;\Delta E_1|\Delta E_0)=p(E;\Delta E_1)$ by definition. For electromagnetic showers one can make a gaussian ansatz for $p(E;\Delta E_i|\Delta E_{i-1})$. This method has been used to describe electromagnetic showers in the Mark J calorimeter. A extremely good description of longitudinal shower fluctuations have been obtained (not shown). It can be used on the other hand also for the energy determination in the off-line analysis. The optimal estimation of the parameter E is given by the solution of the maximum likelihood equation

$$\frac{\partial}{\partial E} \ln p(E;\Delta E_1,\ldots,\Delta E_n) = 0 \quad , \tag{2.102}$$

where $\Delta E_1,\ldots,\Delta E_n$ are the experimental pulse heights in the various layers for one event. Using the Markov-expansion we get

$$\sum_{i=1}^{n} \frac{\dfrac{\partial}{\partial E}\, p(E;\Delta E_i \,|\, \Delta E_{i-1})}{p(E;\Delta E_i \,|\, \Delta E_{i-1})} = 0 \qquad (2.103)$$

Assuming again a Gaussian form for the conditional probabilities a nonlinear equation is obtained which can be simply solved numerically. This method generalizes the linear weighting procedure which has been applied in some experiments in the past. We can not go further into the details of this method, because it is away from the scope of this report.

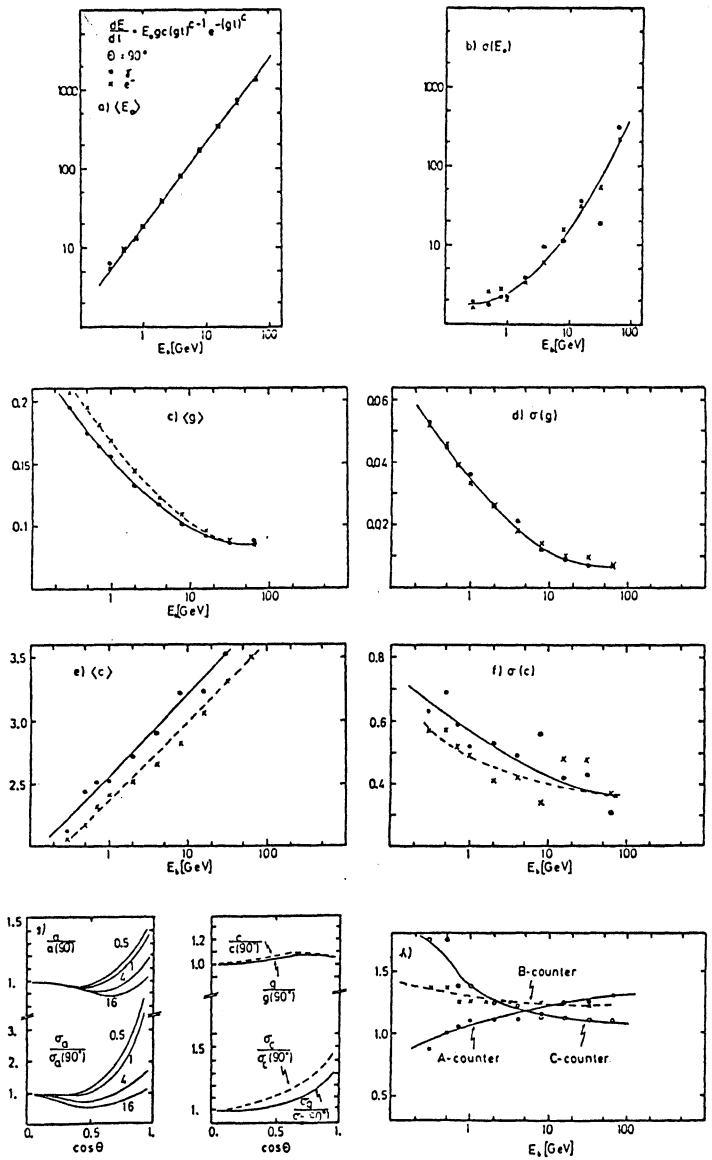

Figure 19. Parameters and their fluctuations as function of energy of the incoming photon for the parametrization (2.97). The experimental set-up is explained in the text. Parameter a in fig. g) is identical to E_0 in a) and b).

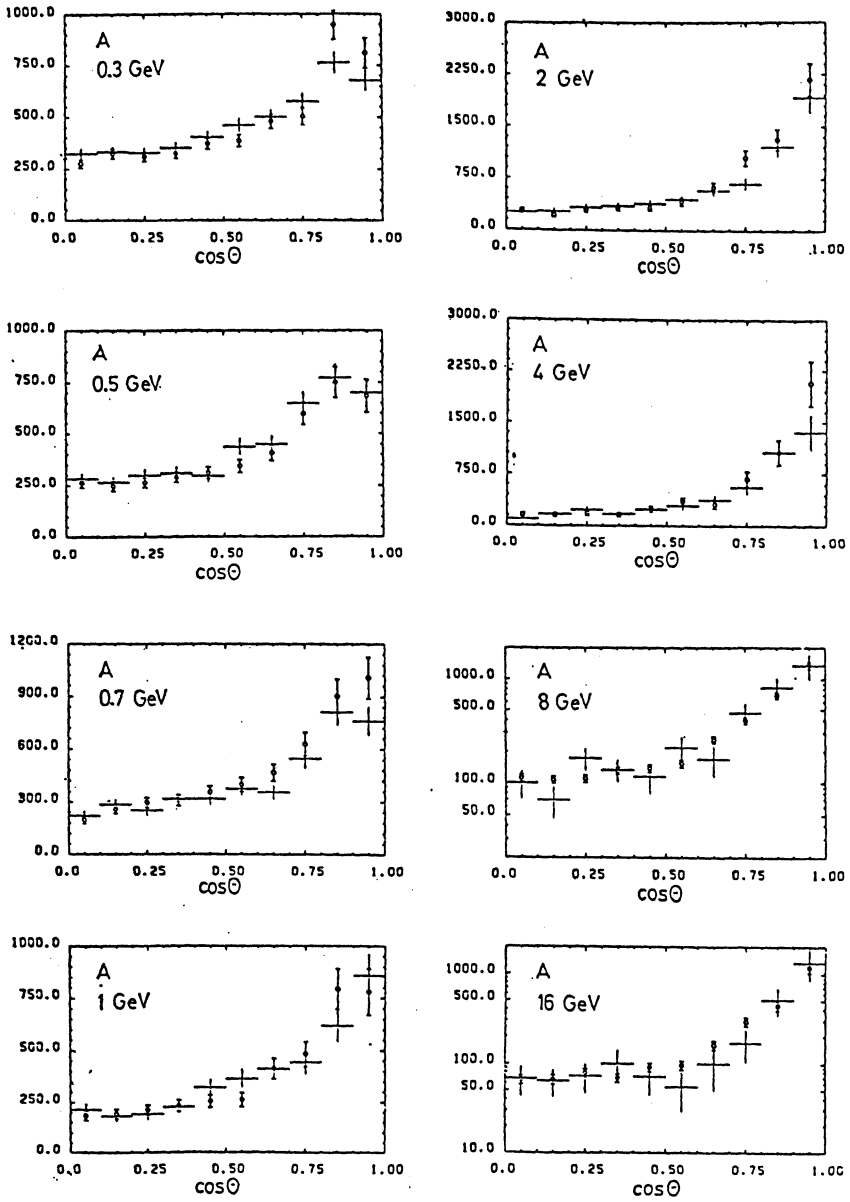

Figure 20. Average pulse height as function of the inclination angle, determined by the parametrization shown in fig.19 (+). For comparison we show also the results obtained with EGS (ϕ). The meaning of A, B and C is explained in the text.

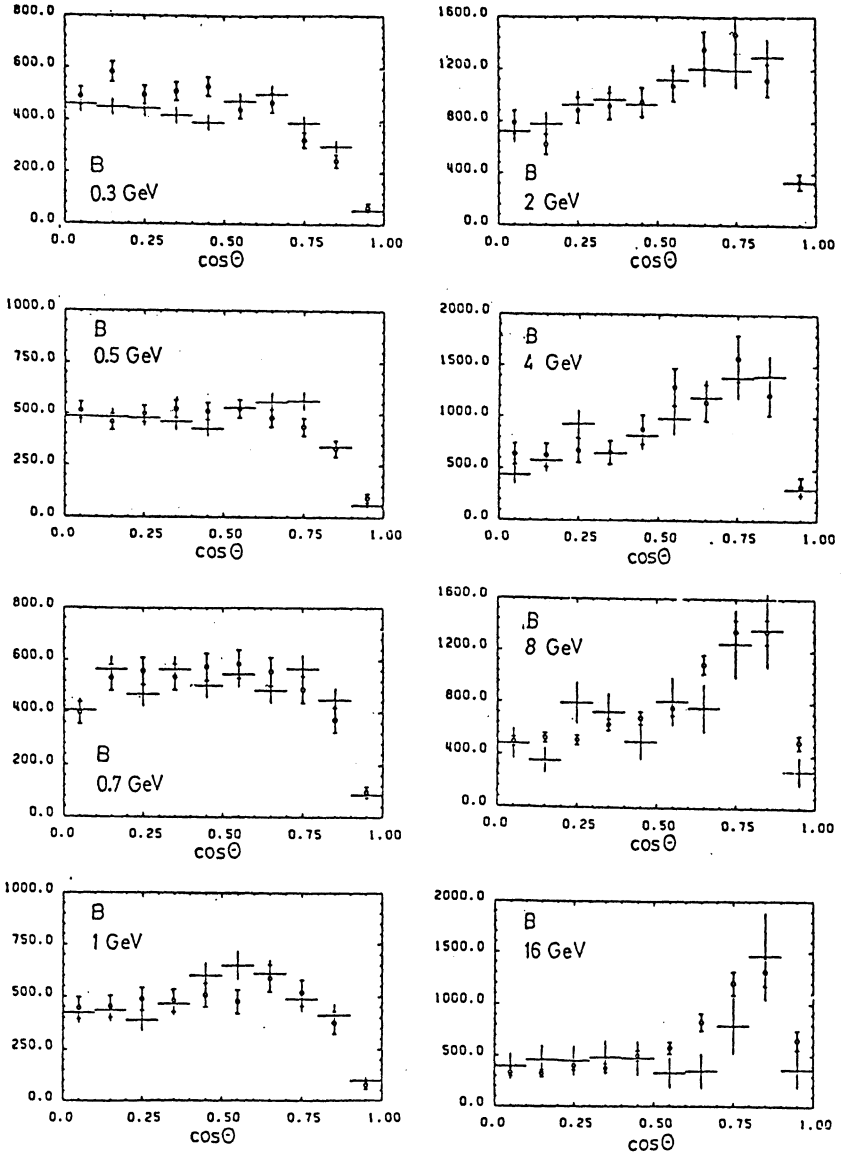

Figure 20. Average pulse height as function of the inclination angle, determined by the parametrization shown in fig.19 (+). For comparison we show also the results obtained with EGS (ϕ). The meaning of A, B and C is explained in the text.

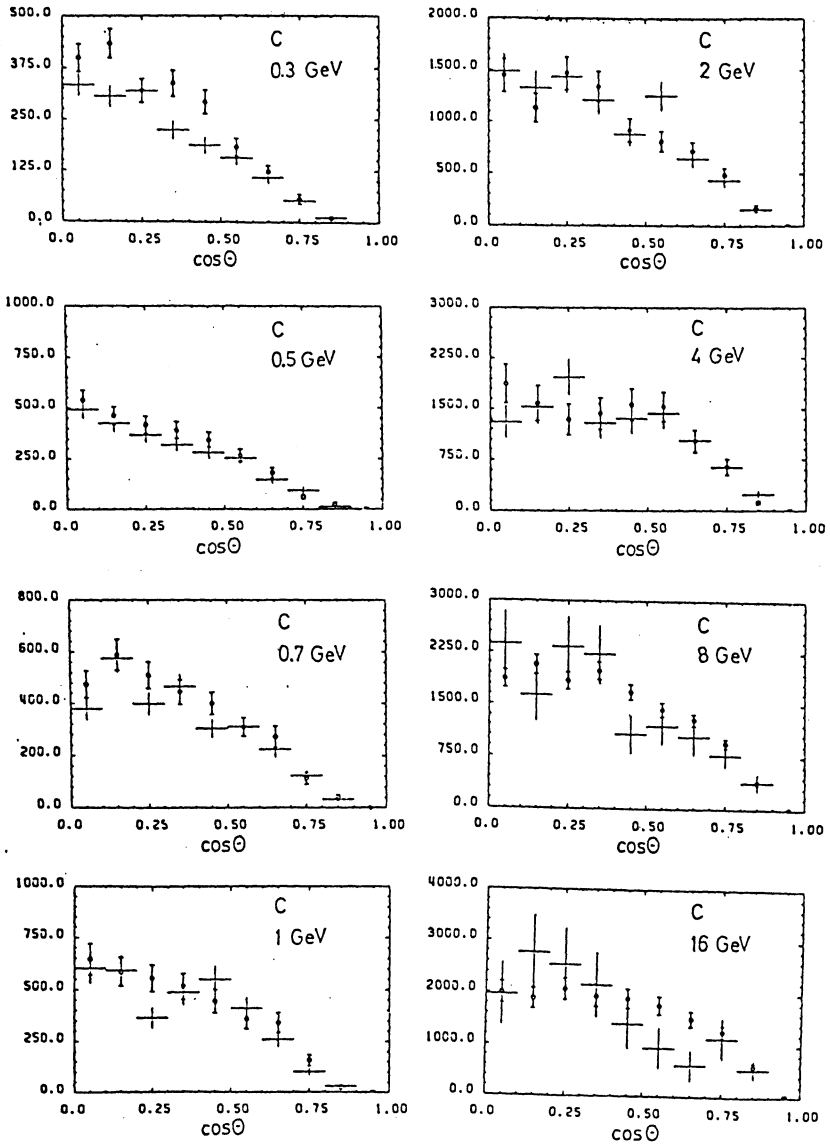

Figure 20. Average pulse height as function of the inclination angle, determined by the parametrization shown in fig.19 (+). For comparison we show also the results obtained with EGS (ϕ). The meaning of A, B and C is explained in the text.

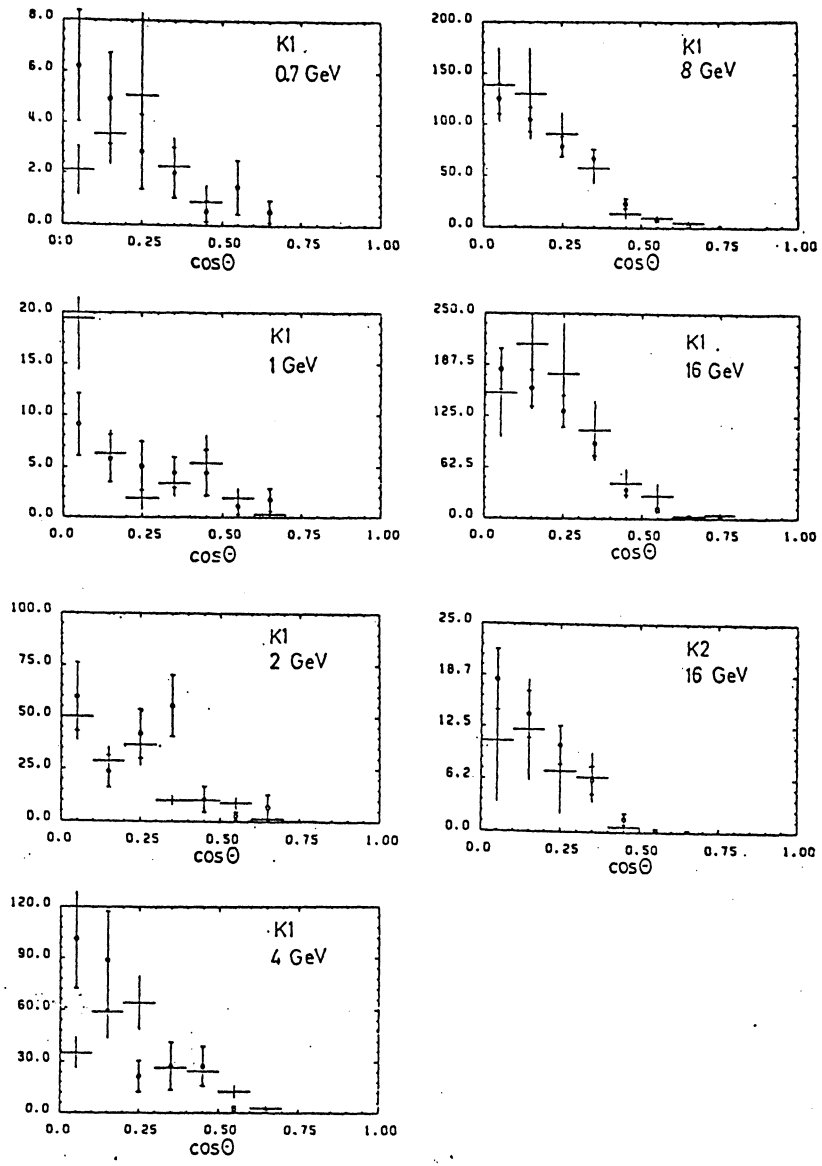

Figure 21. Average pulse height of photon showers after 17 r.l. Pb in the hadron calorimeter (+). The experimental set up is explained in the text. EGS results (ϕ) are shown for comparison.

2.6 NUCLEAR INTERACTIONS

2.6.1 General remarks

Dependent on the material, momentum and the type of incoming particle, an interaction probability is calculated according to

$$P(\Delta) = 1-\exp[-\Delta/\lambda_0] \quad . \tag{2.104}$$

where Δ is the length of the given step and λ_0 the nuclear collision length, the latter one calculated from the total cross sections

$$\lambda_0 = \frac{A}{N_{av}\ \rho\ \sigma(aA)} = \frac{A\ 10^4}{6.022045\ \rho\ \sigma(aA)}\ [cm] \quad . \tag{2.105}$$

A is the atomic number, ρ the density of the material in units of g/cm^3 and σ the cross section in [mb]. The reactions are divided into four main categories, coherent elastic scattering, coherent inelastic scattering, quasielastic incoherent scattering and inelastic incoherent scattering (see fig.22). Whereas the first two reactions are theoretically well understood in terms of the exchanged quanta, the last two reactions are very complicated to describe. Experimental data have been used to develop parametrizations for the cross sections, the multiplicity distributions and the four-momenta of final state particles. We use the ansatz of the intranuclear cascade development. The first interaction on a proton or neutron inside the nucleus is simulated according to the results of the scattering on free nucleons and the multiplication of particles due to further scatterings inside the nucleus is parametrized according to experimental nuclear scattering data.

We proceed as follows : First we discuss the total cross sections and the cross sections for all four reactions from fig.22. Then we concentrate on the scattering of particles on free nucleons. From that we get a simple extension to the generation of the secondary particles for coherent elastic and inelastic reactions. Formally the nucleon with A = 1 has to be replaced by A > 1. Finally the intranuclear cascade for incoherent scattering will be discussed. This includes in special chapters the treatment of stopping particles and nuclear fission. Hadron production by muon scattering does not really fit into this scheme, but is nevertheless described at the end of this chapter. It is without saying that we will justify all our doings by comparison with experimental data.

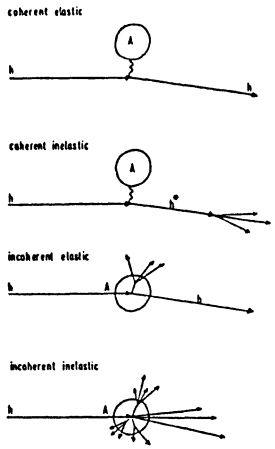

Figure 22. Schematic definition of the various types of nuclear scatterings.

2.6.2 Elastic and inelastic cross sections

The elastic and inelastic cross sections for interactions on protons were tabulated as function of momentum for π^-, π^+, K^-, K^+, K_L^0, p and $\bar{p}$ ([25] - [36]). For all other cross sections on protons we use the charge independent approximation for the forward elastic scattering amplitudes according to the naive quark parton model (see for example ref.[37]). These read :

$$\sigma(\pi^+ p) = 6P + A$$
$$\sigma(\pi^- p) = 6P + 2A$$

$$\sigma(K^+ p) = 6P - 3S$$
$$\sigma(K_S^0 p) = 6P + (1/2)\ A - 3S$$
$$\sigma(K_L^0 p) = 6P + (1/2)\ A - 3S$$
$$\sigma(K^- p) = 6P + 2A - 3S$$
$$\sigma(K^0 p) = 6P - 3S$$
$$\sigma(\bar{K}^0 p) = 6P + A - 3S$$

$$
\begin{aligned}
\sigma(p\ \ p) &= 9P \\
\sigma(\bar{p}\ \ p) &= 9P + 5A \\
\sigma(n\ \ p) &= 9P \\
\sigma(\bar{n}\ \ p) &= 9P + 4A
\end{aligned}
\qquad (2.106)
$$

$$
\begin{aligned}
\sigma(\Lambda\ \ p) &= 9P \quad -3S \\
\sigma(\bar{\Lambda}\ \ p) &= 9P + 2A \ -3S
\end{aligned}
$$

$$
\begin{aligned}
\sigma(\Sigma^-\ p) &= 9P \quad -3S \\
\sigma(\Sigma^+\ p) &= 9P \quad -3S
\end{aligned}
$$

$$
\begin{aligned}
\sigma(\bar{\Sigma}^-\ p) &= 9P + 2A \ -3S \\
\sigma(\bar{\Sigma}^+\ p) &= 9P + 4A \ -3S
\end{aligned}
$$

$$
\begin{aligned}
\sigma(\Xi^0\ p) &= 9P \quad -6S \\
\sigma(\Xi^-\ p) &= 9P \quad -6S
\end{aligned}
$$

$$
\begin{aligned}
\sigma(\bar{\Xi}^0\ p) &= 9P + 2A \ -6S \\
\sigma(\bar{\Xi}^-\ p) &= 9P + \ A \ -6S
\end{aligned}
$$

where the quark scattering amplitudes are defined by

$$
\begin{aligned}
\langle uu|uu\rangle &= \langle dd|dd\rangle = P \\
\langle ud|ud\rangle &= \langle du|du\rangle = P \\
\langle ud|du\rangle &= \langle du|ud\rangle = 0
\end{aligned}
$$

$$
\begin{aligned}
\langle us|us\rangle &= \langle ds|ds\rangle = P-S \\
\langle u\bar{s}|u\bar{s}\rangle &= \langle d\bar{s}|d\bar{s}\rangle = P-S \\
\langle us|su\rangle &= \langle ds|sd\rangle = 0
\end{aligned}
\qquad (2.107)
$$

$$
\begin{aligned}
\langle \bar{u}d|\bar{u}d\rangle &= \langle \bar{d}u|\bar{d}u\rangle = P \\
\langle \bar{u}u|\bar{u}u\rangle &= \langle \bar{d}d|\bar{d}d\rangle = P+A \\
\langle \bar{u}u|\bar{d}d\rangle &= \langle \bar{d}d|\bar{u}u\rangle = A
\end{aligned}
$$

$$
\begin{aligned}
\langle ss|ss\rangle &= (P-S)^2/P \\
\langle \bar{s}s|\bar{s}s\rangle &= (P+A)(P+S)^2/P^2 \\
\langle \bar{u}u|\bar{s}s\rangle &= \langle \bar{d}d|\bar{s}s\rangle = A(P-S)/P
\end{aligned}
$$

From the measured elastic and inelastic cross sections we have fitted the amplitudes P, A and S as function of the momentum and have determined the corresponding cross sections of all unmeasured or poor measured reactions. The cross sections for neutrons as target have assumed to be the same as for protons. All used elastic and inelastic cross sections on protons are shown in fig.23. The values for the strange baryons should not be taken too serious. The decay dominates, the cross sections are given only for completeness. For A = 1 (i.e. for simulation of bubble chamber experiments) exactly these cross sections are used in the program.

It is commonly accepted that the diffraction and absorption cross section for the scattering on a heavy nucleus can be parametrized as

$$
\sigma_d = \sigma_{d0}\, A^{\alpha_d} \qquad (2.108)
$$

$$
\sigma_a = \sigma_{a0}\, A^{\alpha_a}\ , \qquad (2.109)
$$

where A is the atomic number. The usual interpretation of nuclear cross sections at high energies has been made in terms of the optical model, which assumes that the detailed structure of the nucleus can be described approximately by an average potential. The real and imaginary part of this potential then gives the diffraction cross section σ_d and absorption cross section σ_a. For a total black disc one gets simply

$$
\sigma_d = \sigma_a = \pi R_A^2 = 49\ A^{2/3} \quad [\text{mb}]\ , \qquad (2.110)
$$

where R_A is the nuclear radius, for which we set

$$
R_A = 1.25\ 10^{-13}\ A^{1/3} \quad [\text{cm}] \qquad (2.111)
$$

The potential of a black disc is of course too simple and therefore σ_{d0}, σ_{a0}, α_a and α_d may depend on the momentum and of the type of the scattered particle. In our nomenclature we identify the diffraction cross section with the first reaction in fig.22, the coherent elastic scattering, whereas the absorption cross section is the sum of the cross sections of the last three reactions.

There exist mainly two different methods to measure the absorption cross sections. The first method is to measure the angular distribution of the most deflected secondary particle. At very small angles one observes the events from diffraction scattering and at nearly zero angles from Coulomb scattering. The three contributions can be separately determined by fits. Fig.24 gives an example [38]. This method has been applied mainly by counter-hodoscope experiments. On the other hand from bubble chamber exposures the following types of reactions may be accepted as absorptive events : a) all cases where the beam particle appears to suffer an energy loss in the target, as evidenced by the production of secondary particles (other than knock-on electrons), or by a change in ionization; b) large angle scatterings; c) disappearance of beam particles inside the target plate. A bubble chamber experiment will be described later.

The absorption cross sections, as measured by various groups for atomic numbers ranging from A = 9 (Be) to A = 207 (Pb) ([38] - [49]) have been fitted to equ. (2.109). The results for σ_{a0} are compared with the total cross sections of the corresponding scattering on free protons in fig.25, the slope parameters α are given in fig.26. Both figures are for positive and negative charged pions. There is evidently no difference between the particles of either charge, in contrary to the observation for the scattering on free protons (see fig.23 a,b,f and g). In the range from 0.5 Gev/c $\lesssim$ p

$$\sigma_{a0}{}^{\pi^-A} = \sigma_{a0}{}^{\pi^+A} = 1.25\ (\sigma_{tot}{}^{\pi^-p} + \sigma_{tot}{}^{\pi^+p})/2 \qquad (2.112)$$

seems to be a good approximation to the data. On the other hand for α_a one gets a function which is just conversely to σ_{a0}, i.e. if σ_{a0} becomes large then α_a becomes small. Any resonance structure is smeared out for high A values. This leads us to the handdrawn curve shown in fig.26. The same curve is also shown in fig. 27, but normalized to one for indefinite momentum. Equivalent plots are shown in figs. 28 and 29 for kaons, with the same functional dependence of the slope parameter vs momentum. Here no experimental verification is available for low momenta.

In proton scattering on free nucleons there is no resonance production in the s- channel. The shoulder in the total cross section at p $\approx$ 1 GeV/c comes from the opening of new inelastic channels. Therefore the slope parameter has been taken to be constant (see figs.30 and 31).

For all particles small corrections have been applied in order to describe

$$\sigma_{a0}(p) = c_a(p)\ \sigma_{tot}(p) \quad . \qquad (2.113)$$

The correction function $c_a(p)$ is slightly different for mesons and baryons.

For the elastic cross section we got by a similar procedure

$$\sigma_{d0}(p) = c_d(p)\ \sigma_{el}(p) \qquad (2.114)$$

$$c_d(p) = 0.36\ c_a(p) \quad . \qquad (2.115)$$

The slope parameter can be quite good approximated by a constant

$$\alpha_d = 1.17 \quad . \qquad (2.116)$$

The structure observed in the scattering on free protons are smoothed by the Fermi-motion of the nucleons inside the nucleus. A comparison of our final results with experimental data ([38] - [56]) for some of the most frequently used materials are shown in figs.32 for the total and absorption cross sections. A good agreement with experimental data is observed for charged pions, charged kaons, protons, neutrons and antiprotons. For neutral kaons only the scattering cross sections of the long-lived K_L^0 are experimentally available. In the Monte Carlo simulation these cross sections have been calculated by the average of the cross sections for the K^0 and $\bar{K}^0$ respectively. In order to have some independent estimates of the neutral kaon cross sections, we compare in fig.33 the K^0_S-K^0_L regeneration amplitudes $|f(0)-\bar{f}(0)|/P$ with experimental data [158]. For constant regeneration phases these amplitudes are given by the imaginary part of the forward scattering amplitudes, and are thus a direct test for the total cross sections for K^0 and $\bar{K}^0$ scattering. The neutron- and proton cross sections at very low energies have been obtained by an optical model calculation. This will be discussed in the next chapter.

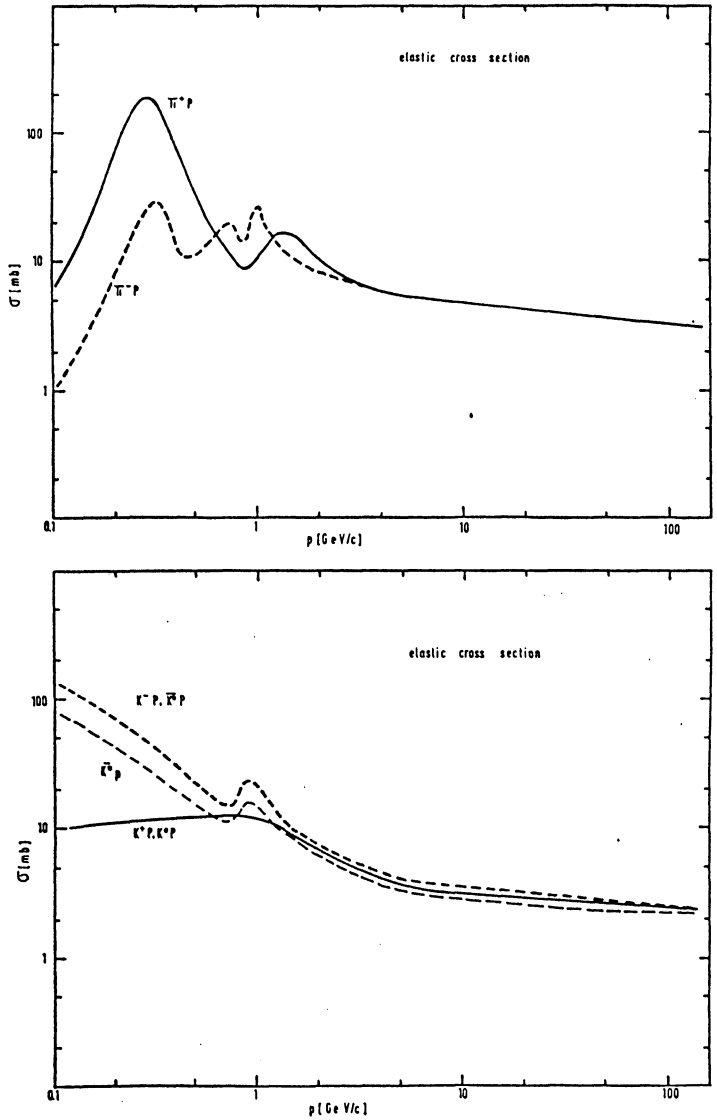

Figure 23. Elastic and inelastic cross sections on free protons for all stable particles as function of momentum p.

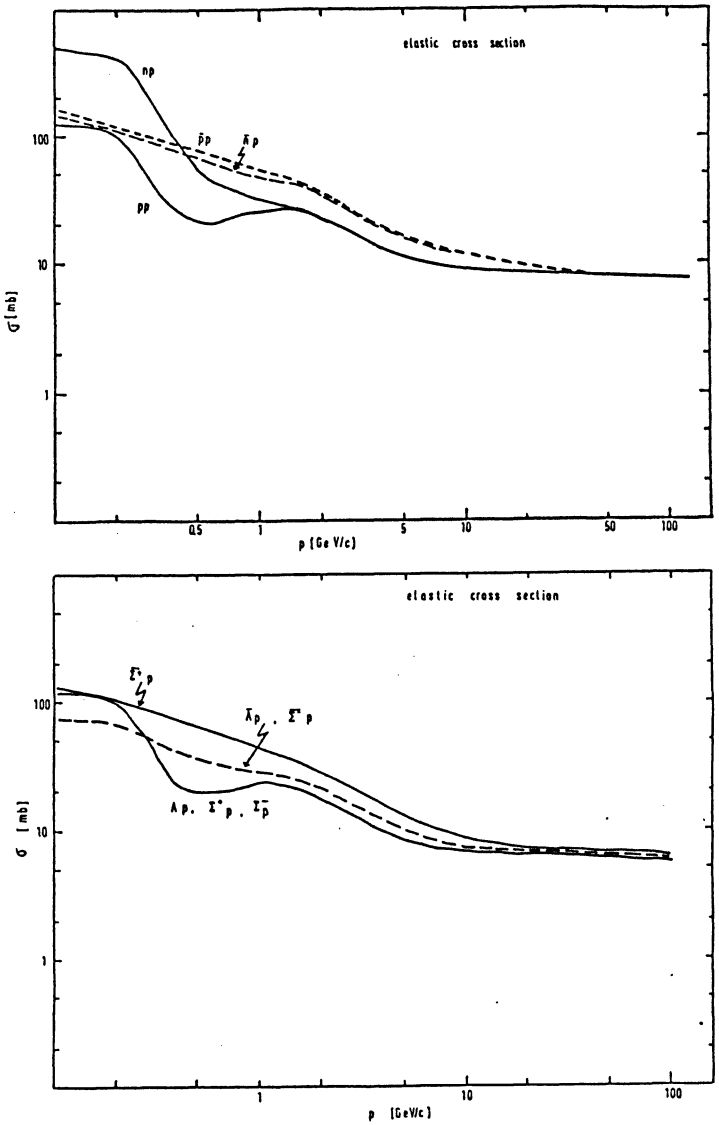

Figure 23. Elastic and inelastic cross sections on free protons for all stable particles as function of momentum p.

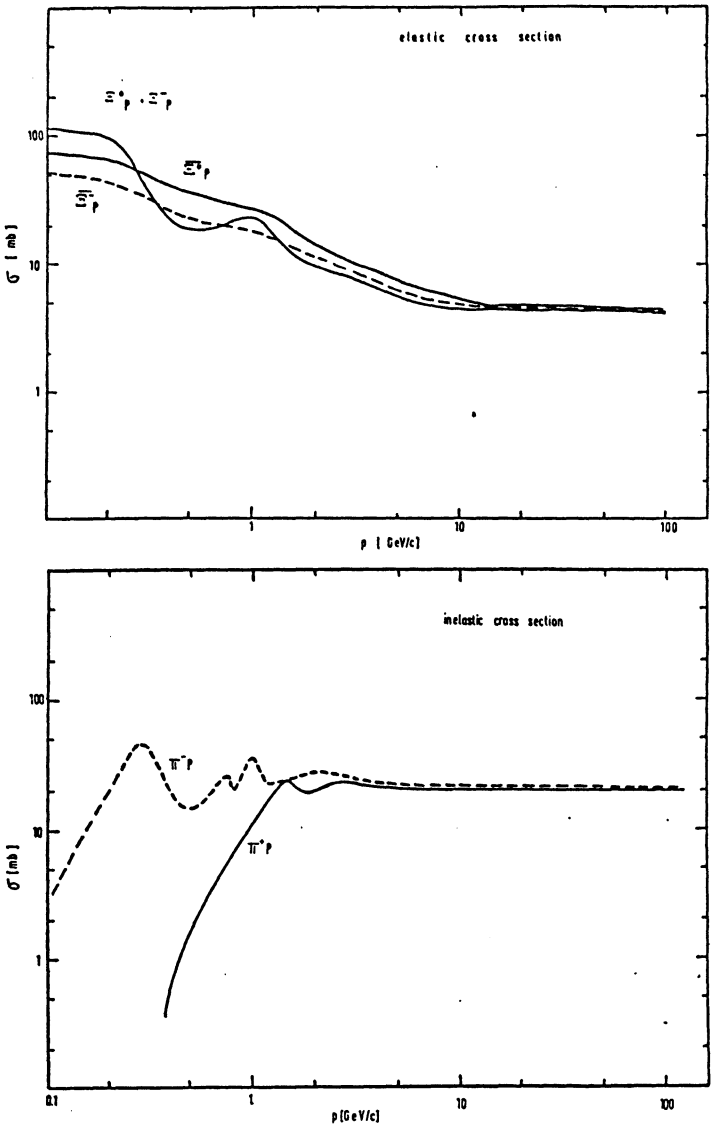

Figure 23. Elastic and inelastic cross sections on free protons for all stable particles as function of momentum p.

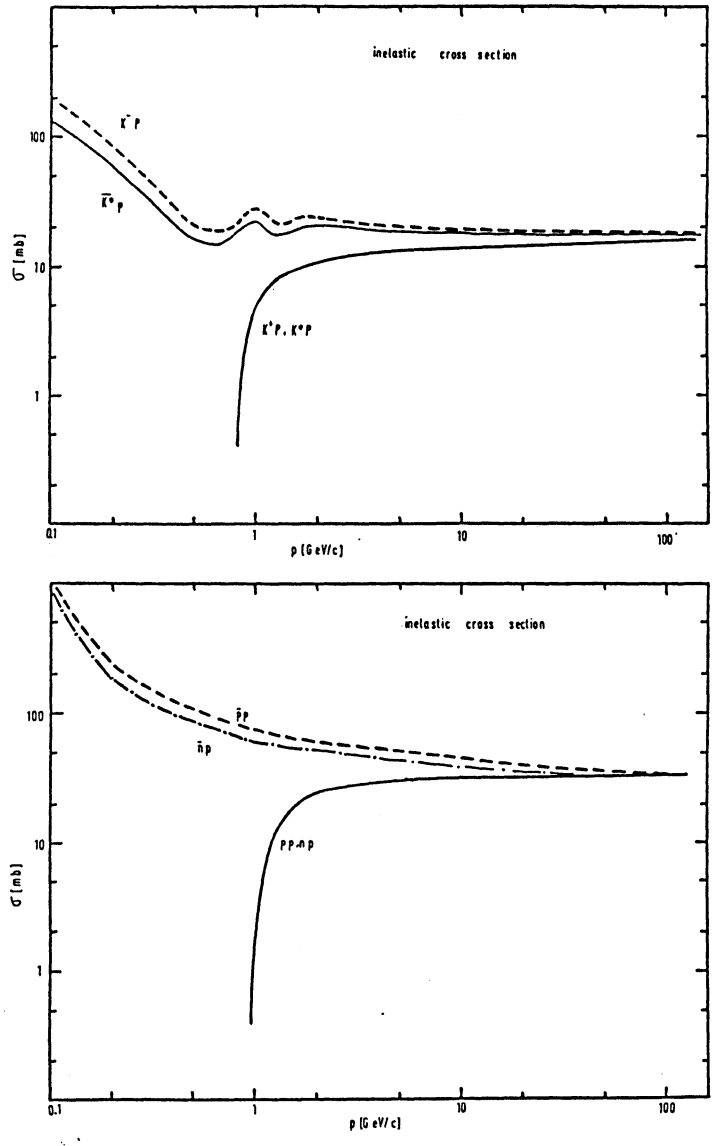

Figure 23. Elastic and inelastic cross sections on free protons for all stable particles as function of momentum p.

The physics of shower simulation 54

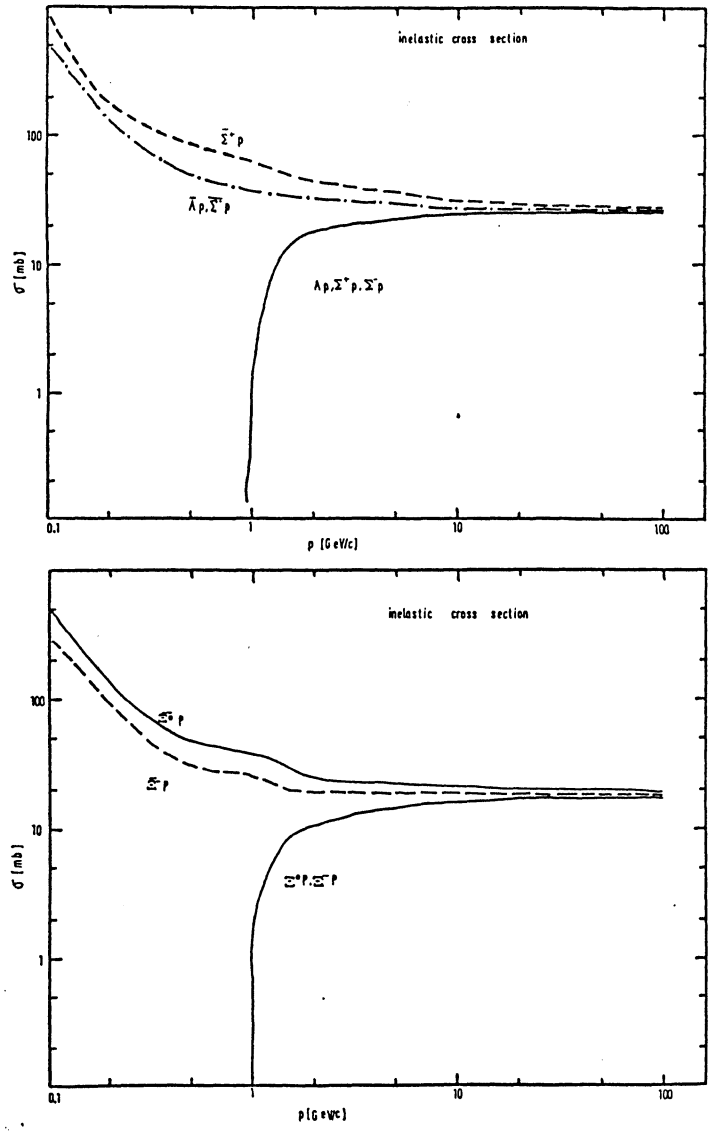

Figure 23. Elastic and inelastic cross sections on free protons for all stable particles as function of momentum p.

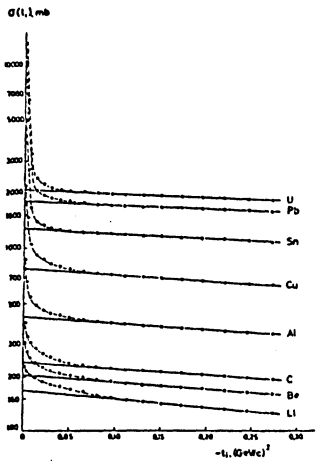

Figure 24. Single particle spectra as function of four momentum transfer for various nuclei as targets.

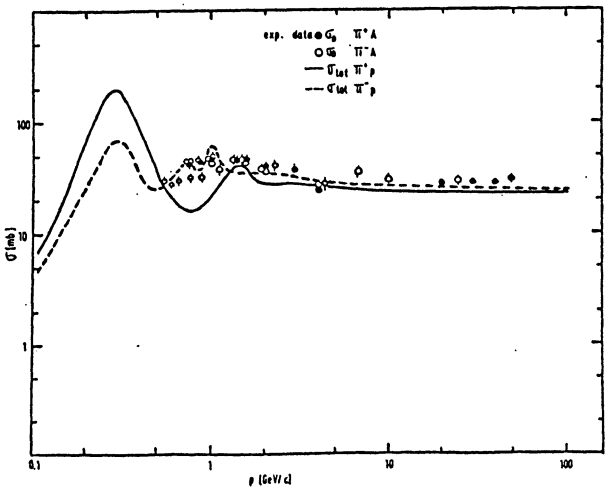

Figure 25. Parameter σ_{a0} of the parametrization (2.109) compared with total cross sections of the scattering on free protons.

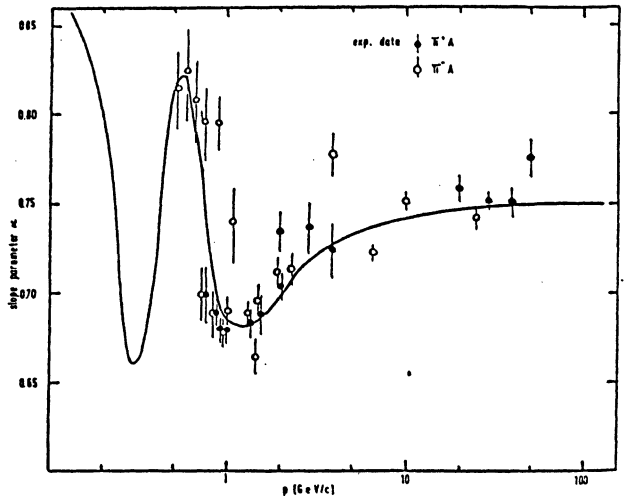

Figure 26. Parameter α_{el} of the parametrization (2.109). The curve is only to guide the eyes.

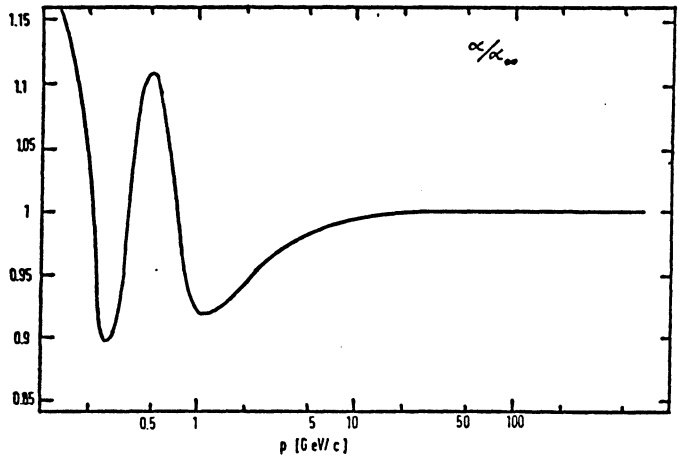

Figure 27. Curve from fig.26, but normalized to one for $p \to \infty$.

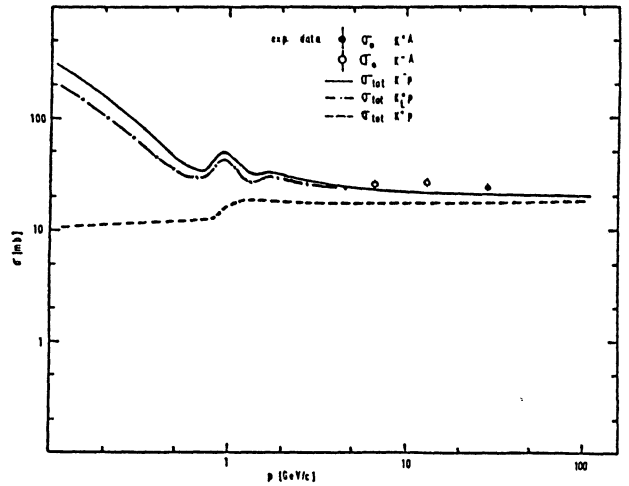

Figure 28. Same as fig.25, but for kaons.

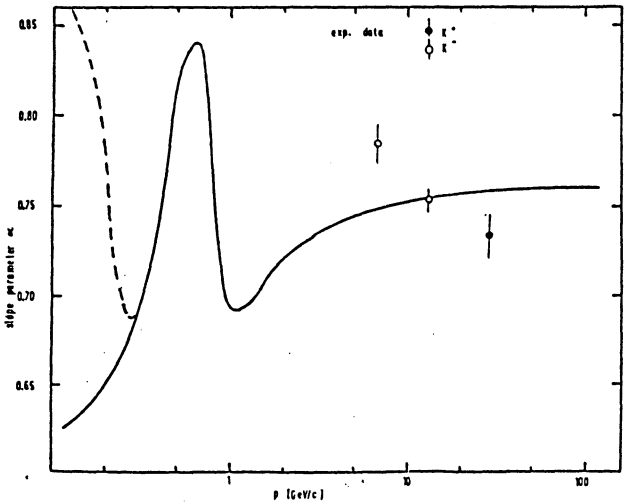

Figure 29. Same as fig.26, but for kaons.

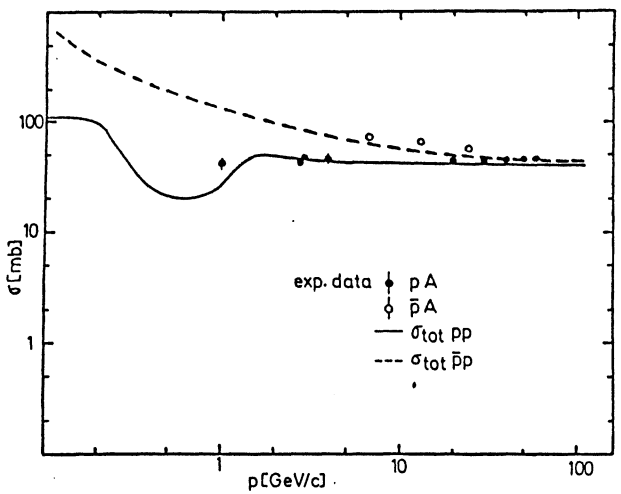

Figure 30. Same as fig.25, but for protons and antiprotons.

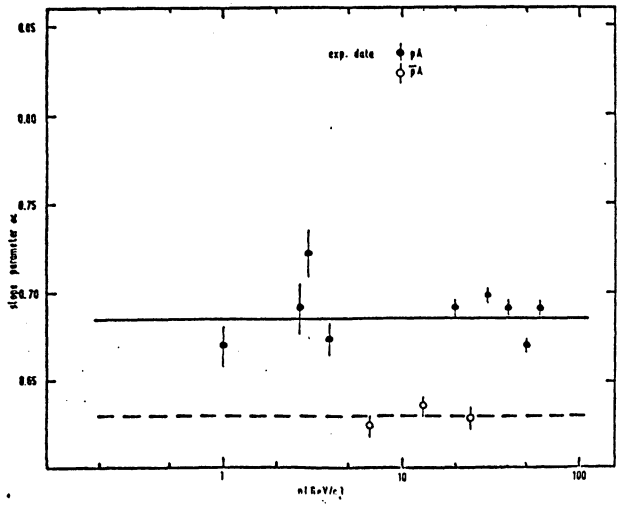

Figure 31. Same as fig.26, but for protons and anitprotons.

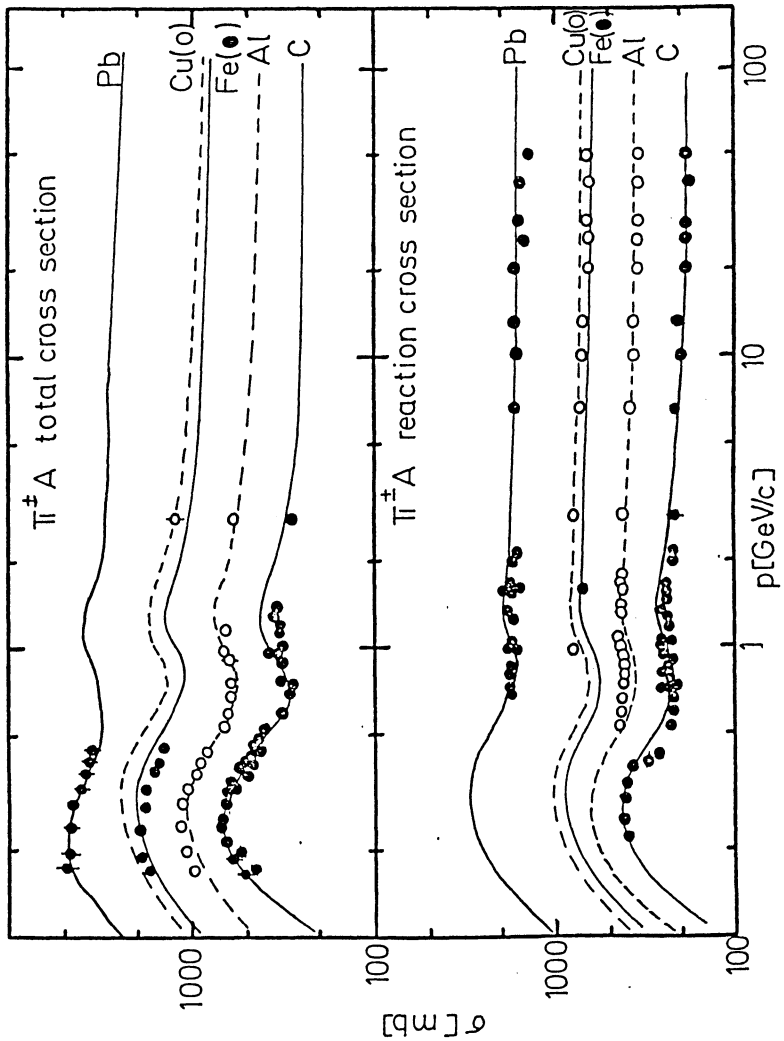

Figure 32. Nuclear cross sections as function of momentum p for various targets. The curves are from the parametrization described in the text.

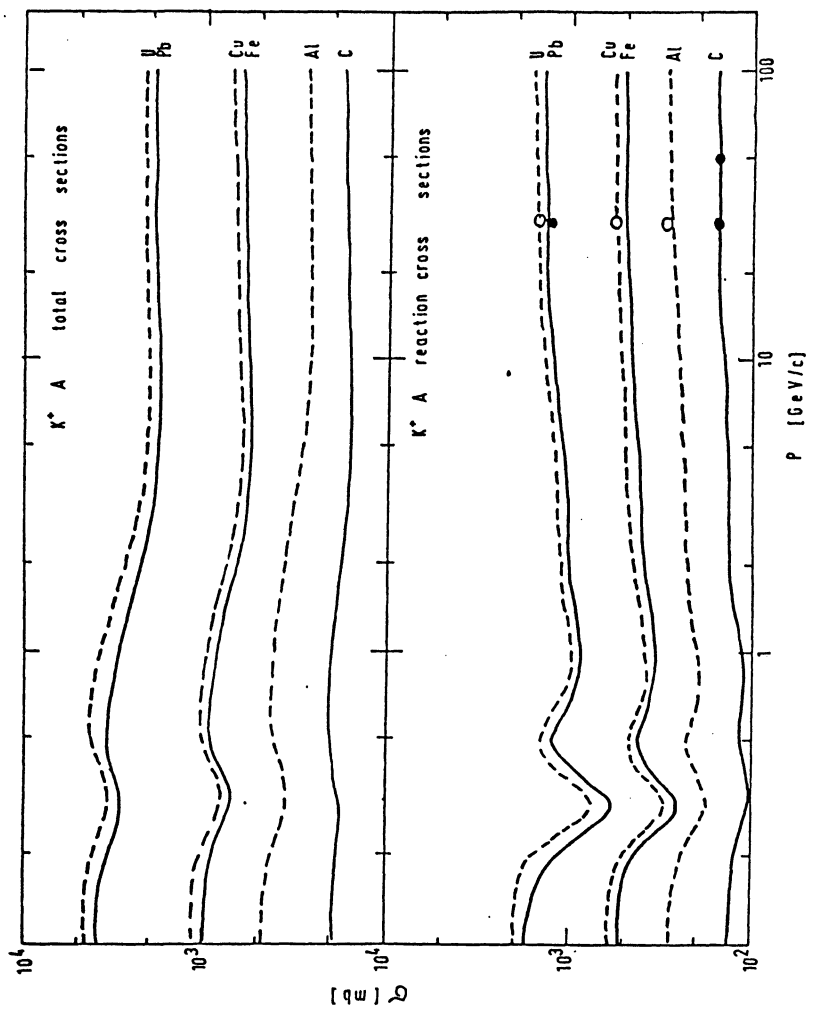

Figure 32. Nuclear cross sections as function of momentum p for various targets. The curves are from the parametrization described in the text.

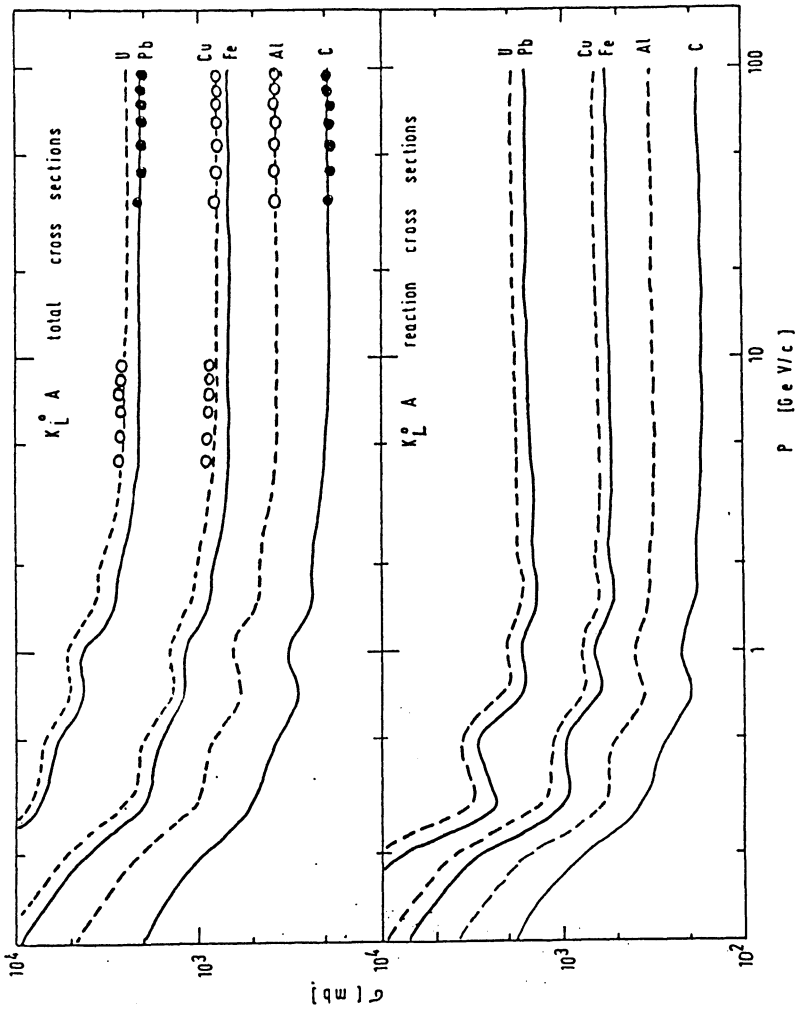

Figure 32. Nuclear cross sections as function of momentum p for various targets. The curves are from the parametrization described in the text.

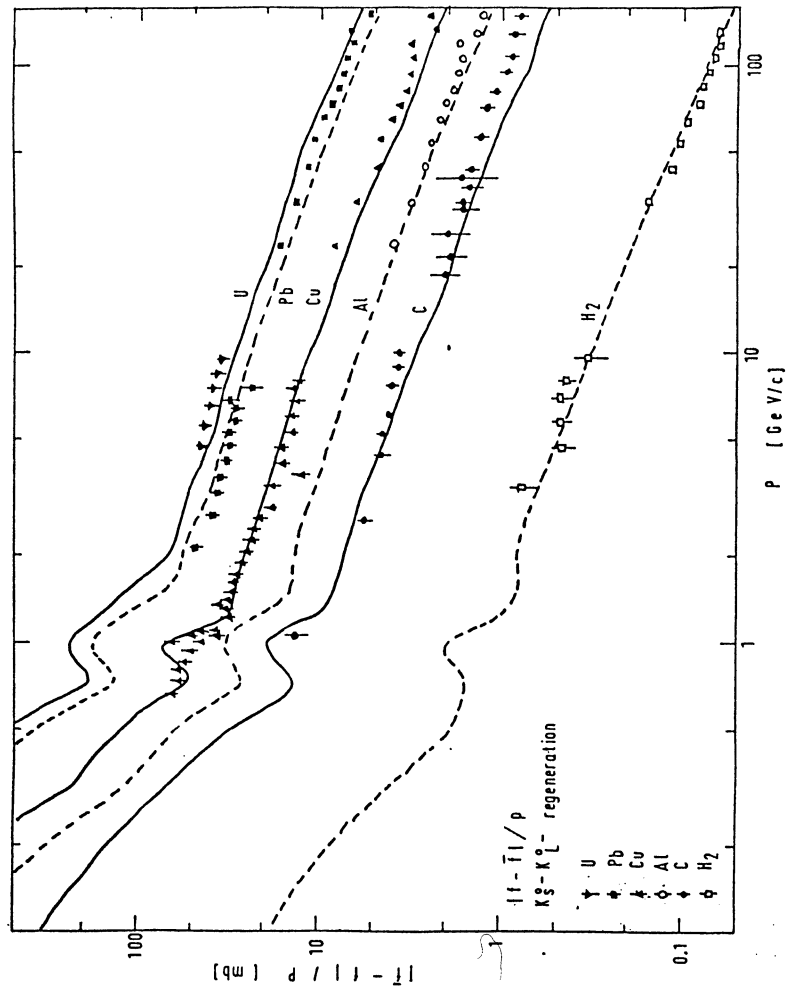

Figure 33. K^0_S-K^0_L regeneration amplitides as function of momentum p. The curves represent the Monte Carlo simulation. The points are experimental results. For details see text.

2.6.3 Optical model calculations

The slowing down process for charged particles is mainly determined by the very large cross sections for atomic processes, given in integrated form by the dE/dx formula. Thus a bad description of nuclear processes at very low energy does not play an important role. This does not hold anymore for neutrons. In this case the absorbtion is initiated only by low energy nuclear reactions, nuclear fission and neutron capture. By nuclear reactions we understand processes where the nucleus as a whole gets into an exited state and emits heavy particles like p, n, d, t and α-particles. The description of the reaction mechanisms of nuclear scattering, neutron capture and nuclear fission will be presented in later chapters.

In the low energy region the scattering cross sections can no more be described by the form (2.108) and (2.109). This is shown in fig.34 for nA interactions at p=280 Mev/c [53]. Also for compounds one does not get a simple law as function of the constituent nuclei. In fig.34 we have plotted the cross sections as function of the effective A value, which may be approximated by

$$A_{eff} = (\rho\lambda/49.14)^4 \quad , \tag{2.117}$$

where the absorbtion length λ is given by formula (2.125) in the next chapter. In order to overcome these problems, optical model calculations have been used for the neutron cross sections at very low energy. It is impracticable to summarize here all the optical model analyses that have been made, so attention has been concentrated on some analyses of extensive sets of experimental data that have yielded overall potentials that can be relied on to fit the elastic scattering cross sections to good accuracy over substantial energy ranges for all except the lightest nuclei. In the case of neutron scattering, the most extensive analysis is that of Perey and Buck [159] using a non local potential of the form

$$V(\vec{r},\vec{r}') = V(p)\ H(|\vec{r}-\vec{r}'|) \quad , \tag{2.118}$$

where

$$H(|\vec{r}-\vec{r}'|) = \pi^{-3/2}\ \beta^{-3}\ \exp\left[-((\vec{r}-\vec{r}')/\beta)^2\right] \quad , \tag{2.119}$$

and $\vec{p} = (\vec{r}-\vec{r})/2$, β beeing the the range of the non-locality. The non local potential operates on a wave function in the following form:

$$V\ \Psi(\vec{r}) = \int V(\vec{r},\vec{r}')\ \Psi(\vec{r}')\ d\vec{r}' \quad . \tag{2.120}$$

We followed the numerical analysis of Bechetti and Greenlees [160] and obtained the cross sections shown in fig.35.

Neutron capture cross sections have been parametrized at a fixed energy of 65 keV, as shown in fig.36. The energy dependence is given by

$$\sigma_c[\text{mb}] = 11.12 \cdot \sigma_c(65\ \text{keV}) \cdot E^{-0.577} \quad , \qquad (2.121)$$

where E in units of keV.

For nuclear charges Z ≧ 92 neutrons may also initiate nuclear fission reactions. Cross sections for some elements are shown in fig.37. Neutron capture and nuclear fission will be further discussed in detail in chapter 2.6.20.

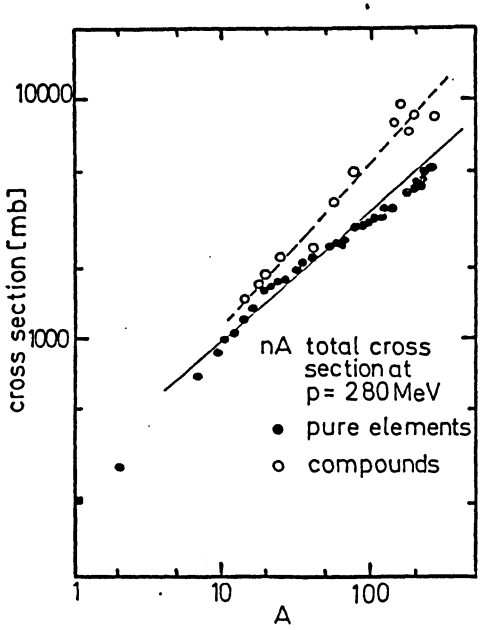

Figure 34. n A cross sections for pure elements and compounds at 280 MeV/c momentum. The solid curve is the result of our parametrization. The dashed curve is only to guide the eyes through the results for compounds.

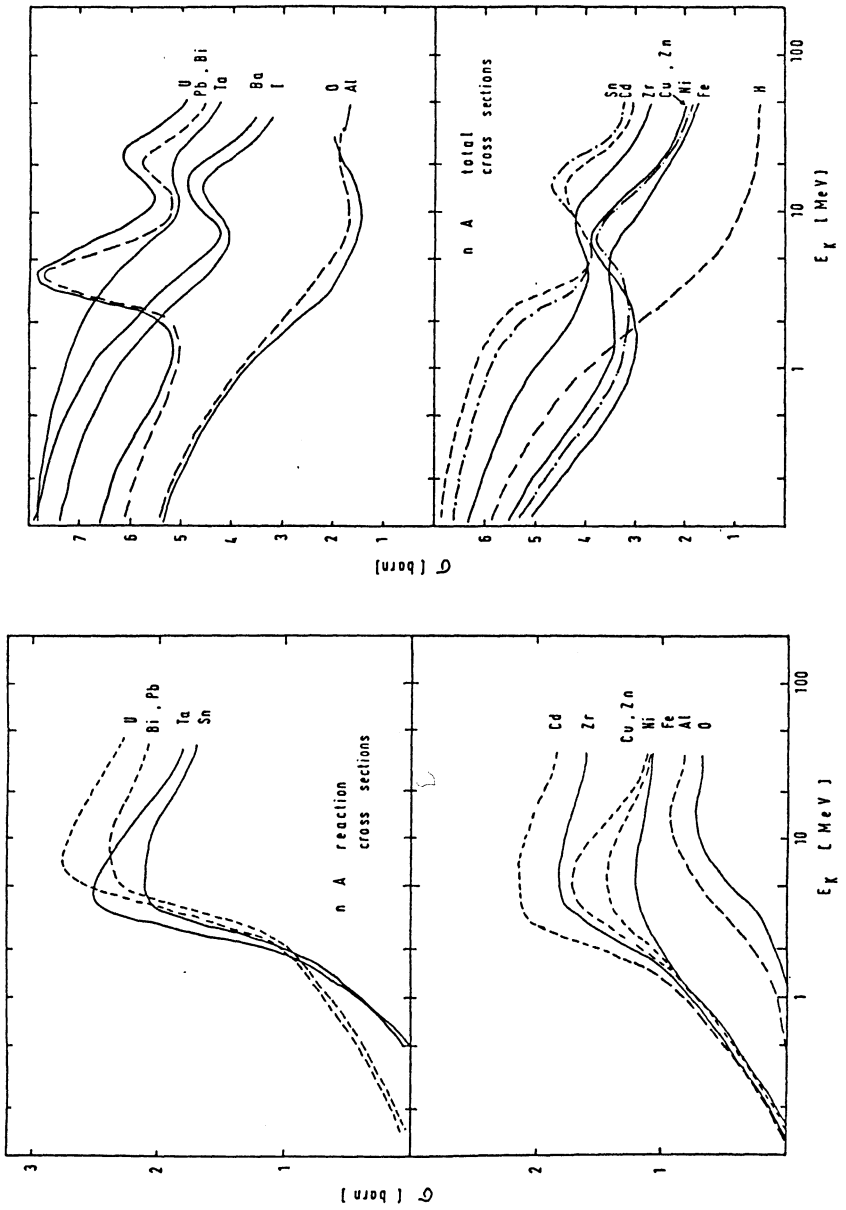

Figure 35. Reaction cross sections and total cross sections for neutron scattering in the MeV region. Shown are optical model calculations for various materials.

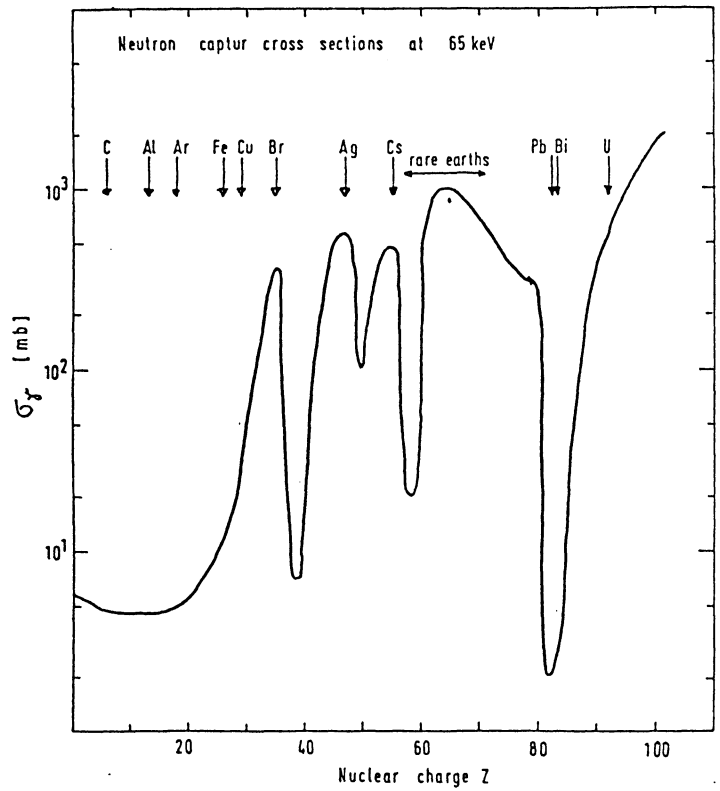

Figure 36. Neutron capture cross sections at 65 keV as function of atomic number A of the target nucleus.

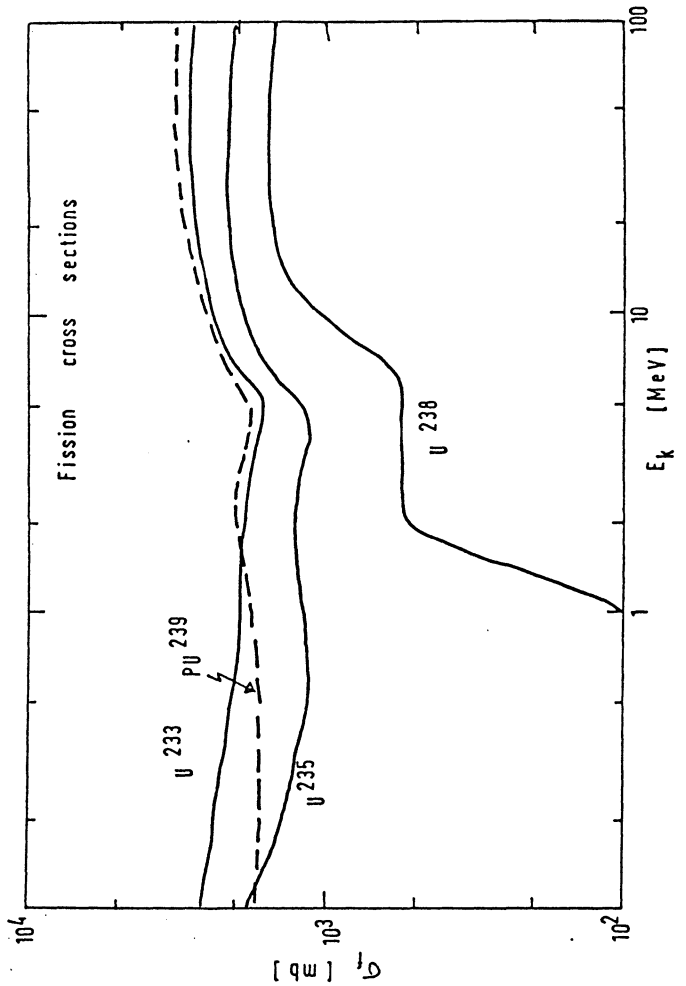

Figure 37. Fission cross sections for some elements as function of kinetic energy of the incoming neutron.

2.6.4 The cross section determination of compounds

As has been discussed in the last two chapters, the elastic and inelastic cross sections can be parametrized in terms of the atomic number A. For mixtures and compounds one has to use a suitable averaging procedure, which will be discussed in the following.

For pure elements as well as for constituents of compounds the radiation lengths and the high energy absorbtion lengths may be calculated according to

$$X_0 = 716.405 \cdot A/(\rho \cdot G(Z)) \quad , \tag{2.122}$$

$$G(Z) = Z^2\Big(\ln(184.15/Z^{1/3}) + \ln(1194/Z^{2/3})/Z - 1.202\cdot(Z/137)^2 + 1.0369\cdot(Z/137)^4 - 1.008\cdot(Z/137)^6/(1+(Z/137)^2)\Big)$$

and

$$\lambda = 49.14 \cdot A^{1/4}/\rho \quad . \tag{2.123}$$

For compounds these values are used to calculate

$$\frac{1}{X_{0,eff}} = \sum_{i=1}^{N} \frac{1}{X_i} \tag{2.124}$$

and

$$\frac{1}{\lambda_{eff}} = \sum_{i=1}^{N} \frac{1}{\lambda_i} \quad . \tag{2.125}$$

From (2.125) we determine the effective atomic number A_{eff} and charge number Z_{eff} as

$$A_{eff} = (\rho \cdot \lambda_{eff}/49.14)^4 \tag{2.126}$$

$$Z_{eff} = (-1+\sqrt{1+0.00417\cdot A_{eff}})/0.00417 \quad . \tag{2.127}$$

These numbers are used only for energy loss calculations and inside the simplified GHEISHA electromagnetic shower routines. Note especially that we do not use the precise dE/dx formula for compounds ,which would read

$$dE/dx = \sum_{i=1}^{N} (dE/dx)_i \quad , \tag{2.128}$$

with $(dE/dx)_i$ appropriate to the i^{th} chemical constituent. As examples we show in tables 4 and 5 the composition of BGO and the Ilford G5 emulsion. Both materials will be used later in the discussion of nuclear interactions and calorimetry.

Table 4 : Calculation of radiation length, high energy absorbtion length and average atomic number for BGO ($Bi_3Ge_4O_{12}$)

element	ρ_i[g/cm³]	A_i	Z_i	X_i[cm]	λ_i[cm]
Bi	4.76	209	83	1.31	39.05
Ge	1.24	72.6	32	9.82	115.07
O	1.09	16.0	8	31.15	89.43
BGO	7.13	103.6	47.2	1.12	22.0

Table 5 : Calculation of radiation length, high energy absorbtion length and average atomic number for Ilford G5 emulsion

element	ρ_i[g/cm³]	A_i	Z_i	X_i[cm]	λ_i[cm]
I	0.012	126.9	53	706.9	13747.9
Ag	1.809	107.9	47	5.0	87.6
Br	1.332	79.9	35	8.6	110.3
S	0.007	32.1	16	2785.7	16709.2
O	0.252	16.0	8	135.9	390.1
N	0.074	14.0	7	513.5	1285.0
C	0.276	12.0	6	154.7	331.5
H	0.054	1.0	1	1087.5	912.1
G5	3.82	58.5	27.7	2.97	35.6

We turn now to the cross section determinations. The partial nuclear cross sections σ_i for each of the constituents may be calculated by means of the partial densities according to (see also (2.104)) :

$$\lambda_i = \frac{A_i}{N_{av}\ \rho_i\ \sigma_i(aA_i)} = \frac{A_i\ 10^4}{6.022045\ \rho_i\ \sigma_i(aA_i)} \quad [cm] \tag{2.129}$$

Use of formula (2.125) leads after some manipulations to an approximation of the cross sections for compounds in terms of the cross sections for the constituents as

$$\sigma(aA_{eff}) = \frac{A_{eff}}{\rho} \sum_{i=1}^{N} \frac{\rho_i \, \sigma_i(aA_i)}{A_i} \quad . \tag{2.130}$$

As was discussed in the previous chapter and illustrated by fig.34, further corrections must be applied for the scattering at very low energies. A phenomenological expression

$$\sigma_0 = \sigma \cdot A^{\varepsilon} \quad , \tag{2.131}$$

is used. ε has been parametrized as function of the kinetic energy of the scattering particle, σ is the value obtained by formula (2.130). As example we show in fig.38 the total and reaction cross sections on BGO as function of momentum p.

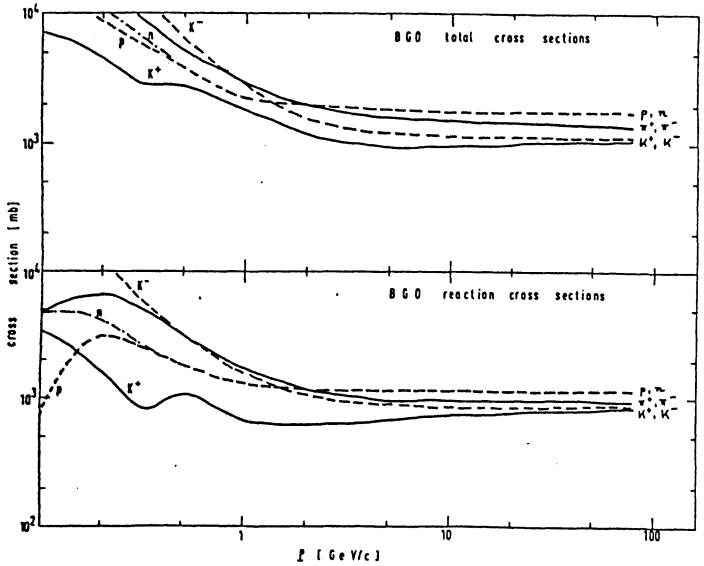

Figure 38. Nuclear cross sections as function of momentum p for BGO as target. The curves are from the parametrization described in the text.

2.6.5 Generation of secondary particles

The method of the generation of secondary particles in inelastic reactions follows very closely to that first discussed in ref.[57] and further develloped and compared in detail with experimental data in ref. [58]. We start with the description for pp-interactions and will then mention only the main differences in the treatment for other incoming particles.

Let us denote the probability for producing n_p protons, n_n neutrons, n_+ positive pions, n_0 neutral pions and n_- negative pions by the multiplicity distribution

$$w(n_p, n_n, n_+, n_0, n_-) \tag{2.132}$$

Assuming that there is no production of other particles, the numbers of particles in the final state in pp-interactions have to fullfil the following requirements

$$n_p + n_n = 2 \tag{2.133}$$

$$n_p + n_+ - n_- = 2 \tag{2.134}$$

(introduction of strange particles will be described later). Therefore as long as the production of strange particles and antibaryons is small in the average, compared to the production of protons, neutrons and pions, the multiplicity distribution can be assumed to depend on the numbers of pions only. Froyland and Skontorp [57] reported first on an attempt to describe the cross sections for the production of n pions using measured topological cross sections for pp-interactions in an energy range from 4 to 300 GeV/c. They found that the Koba-Nielsen-Olesen (KNO) scaling hypothesis [59] holds at least to the same accuracy for the total number of pions as for the number of charged particles. Therefore the multiplicity distribution can be expressed by the special KNO-formula

$$P(n) = \frac{1}{\langle n \rangle} \frac{n}{\langle n \rangle} \exp\left[-\frac{\pi}{4} \left(\frac{n}{\langle n \rangle} \right)^2 \right] \quad , \tag{2.135}$$

multiplied by a suitable chosen conditional probability $p(n_+, n_0, n_- | n)$ for the production of n_+ positive, n_0 neutral and n_- negative pions for a fixed number of total produced pions. The partitioning of the n pions with regard to their charges is strongly influenced by the charges of the two leading baryons and the numbers of the various pions tend to be equal

since the overall isospin of the system is limited. These effects can be described by a parametrization

$$p(n_+,n_0,n_-|n) = \frac{a_n \exp\left[-(n_+-n_0-n_-+b)^2/2c^2n^2\right]}{n_p!\ n_n!\ n_+!\ n_0!\ n_-!} \quad , \tag{2.136}$$

where the normalization constants a_n follow from the condition

$$\sum_{n_+-n_-+n_0=n} p(n_+,n_0,n_-|n) = 1 \tag{2.137}$$

for each n. The total multiplicity distribution reads then

$$w(n_+,n_0,n_-) = P(n)\ p(n_+,n_0,n_-|n) \tag{2.138}$$

The parameters b and c have been found to be energy independent for pp-interactions (b = 0.7, c = 1.25). For $\langle n\rangle$ a fit to the experimental data yielded ($E_{av} = \sqrt{s} - 2m_p$ for pp-interactions) :

$$\langle n\rangle = 3.62567 + 0.665843\ \ln E_{av} + 0.336514\ (\ln E_{av})^2 + 0.117712\ (\ln E_{av})^3 + \text{some higher terms} \tag{2.139}$$

It has been shown in ref. [58] that the topological cross sections, all higher moments of the multiplicity distribution and all channel cross sections for reactions without strange particles calculated from this multiplicity distribution agree to a high accuracy with experimental data for pp-interactions from 6 to 400 GeV/c. Examples are shown in figs. 39 to 44.

In fig.39a the topological cross sections for pp-interactions at 12 and 24 GeV/c lab. momentum are compared with the predictions of the just described model. In fig.39b and 39c we compare the average neutral and positive pion rates as function of the number of negative pions, whereas in fig.39d and 39e second order binomial moments are shown. These moments are generally defined as

$$\varphi_k^{k_+,k_-,k_0} = \langle n_+(n_+-1)\ldots(n_+-k_++1) \cdot n_-(n_--1)\ldots(n_--k_-+1) \cdot n_0(n_0-1)\ldots(n_0-k_0+1)\rangle \tag{2.140}$$

The index k stands for the sum of k_+, k_- and k_0. The parameters in fig.39c and 39e are correlated by charge and baryon number conservation,

$$n_- \leq \langle n_+\rangle_{n_-} \leq n_-+2 \tag{2.141}$$

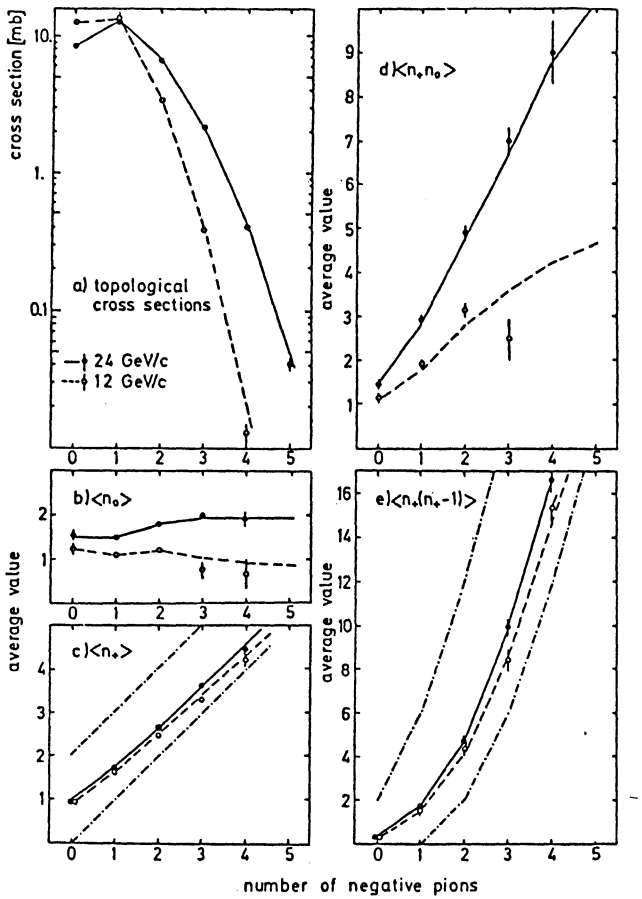

Figure 39. Topological cross sections and multiplicities for pp interactions at 12 and 24 GeV/c beam momentum. Further details are given in the text. The curves represent the prediction of the Monte Carlo simulation.

$$n_-(n_--1) \leq \langle n_+(n_+-1)\rangle_{n_-} \leq (n_-+2)(n_-+1) \quad . \tag{2.142}$$

These limits are shown as point-dashed curves. As can be seen the values of both moments seem to approach the lower limits as n_- increases. The corresponding restriction for the mixed moment

$$\langle n_0\rangle_{n_-} n_- \leq \langle n_+ n_0\rangle_{n_-} \leq \langle n_0\rangle_{n_-}(n_-+2) \tag{2.143}$$

implies a correlation between the behaviour of $\langle n_+ n_0\rangle_{n_-}$ and $\langle n_0\rangle_{n_-}$.

The model works rather well for beam momenta from 6 to 500 GeV/c. This is shown in fig.40 where we compare the average number of neutral pions as function of the number of negative pions for some arbitrary selected experiments. In fig.41 and 42 we compare data and model for the momentum dependence of the inclusive correlation intagrals

$$f_k^{k\ k\ k}_{+,\ -,\ 0} \quad ,$$

considered by many models to be the most efficient way of description. They are related to the binomial moments just in the same way as the inclusive correlation functions to the Lorentz-invariant differential cross sections (for details see [60]). In the following formulae we use instead of the previous notation the more familiar notation

$$\varphi_k{}^{pqrs} \quad .$$

where each upper index stands for the signs (+,- or 0) of only one pion, i.e.

$$\varphi_4{}^{++-0} = \varphi_4{}^{2,1,1} \quad .$$

In this notation the relations between the correlation moments and the binomial moments of first, second and third order read

$$\begin{aligned} f_1{}^p &= \varphi_1{}^p \\ f_2{}^{pq} &= \varphi_2{}^{pq} - \varphi_1{}^p\,\varphi_1{}^q \\ f_3{}^{pqr} &= \varphi_3{}^{pqr} - \varphi_2{}^{pq}\varphi_1{}^r - \varphi_2{}^{qr}\varphi_1{}^p - \varphi_2{}^{rp}\varphi_1{}^q + 2\varphi_1{}^p\varphi_1{}^q\varphi_1{}^r \quad . \end{aligned} \tag{2.144}$$

In fig.43 the topological cross sections are shown for beam momenta from 4 to 500 GeV/c, and finally in fig.44 the cross sections of some exclusive reactions. Here it is evident, that our model fails for beam momenta less than about 6 GeV/c.

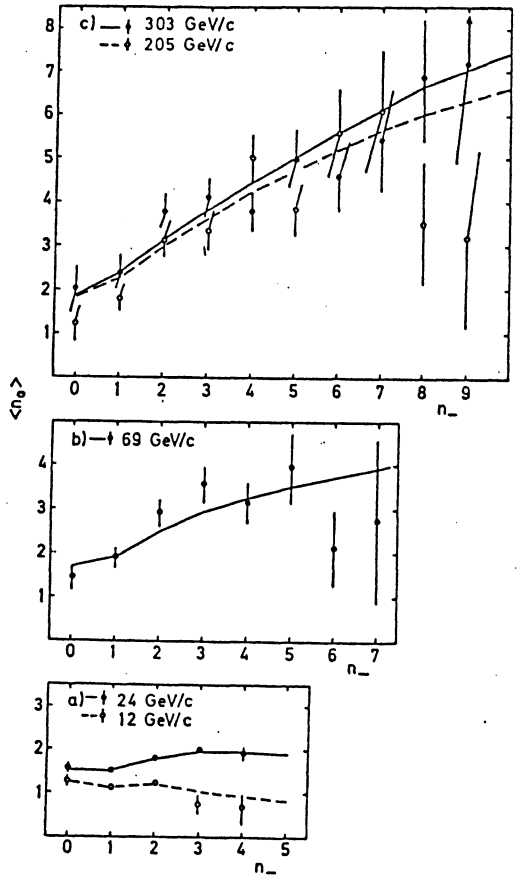

Figure 40. Average number of neutral pions as function of number of negative pions for pp interactions. The curves represent the prediction of the Monte Carlo simulation.

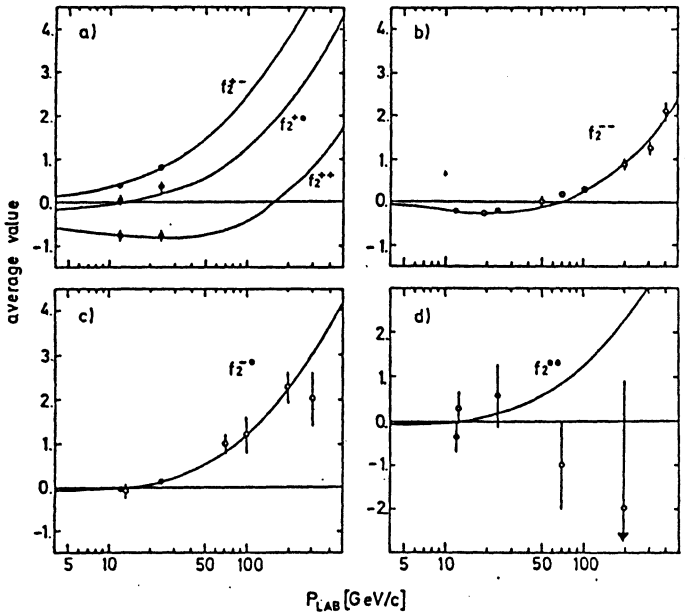

Figure 41. Inclusive correlation integrals as function of beam momentum. The curves represent the prediction of the Monte Carlo simulation. For further details see text.

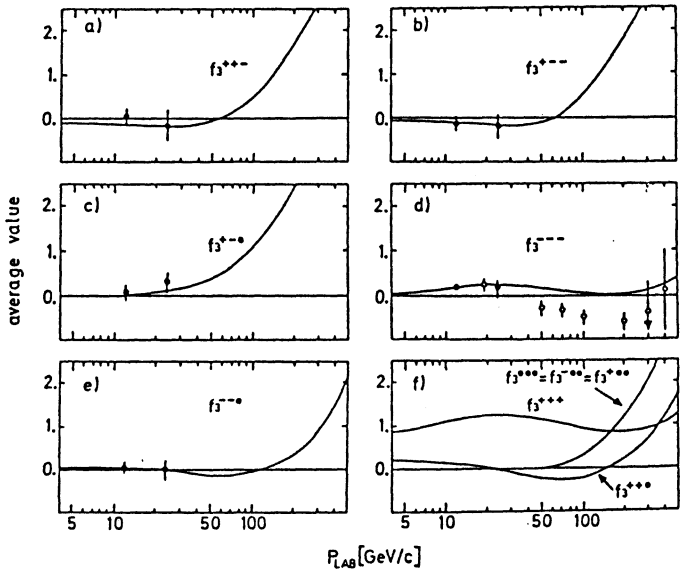

Figure 42. Inclusive correlation integrals as function of beam momentum. The curves represent the prediction of the Monte Carlo simulation. For further details see text.

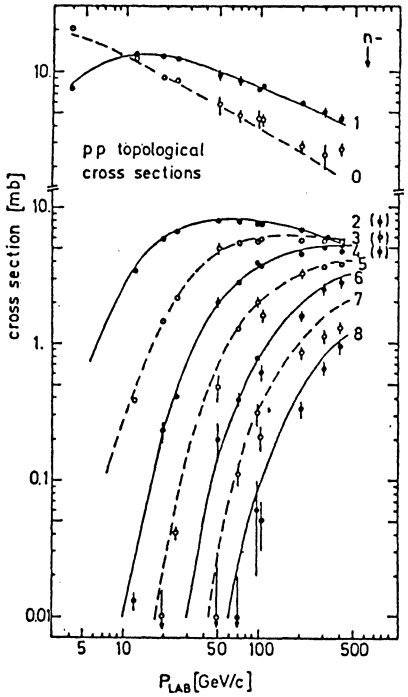

Figure 43. Topological cross sections for pp interactions. The curves represent the prediction of the Monte Carlo simulation. For further details see text.

Therefore at very low momenta the multiplicity distribution has been changed by tables in such a way, that the calculated cross sections for the final states $pp\pi^0$, $pn\pi^+$, $pp\pi^+\pi^-$, $pp\pi^+\pi^-\pi^0$, and $pn\pi^+\pi^+\pi^-$ agree with the experimental data. A comparison of cross sections at low momenta is shown in fig. 45. The Monte-Carlo results are given by crosses and the lines represent eye-ball fits through the experimental data, taken from ref. [25]. In plots 45 there is one but the same arbitrary normalization constant.

We come now to the inclusion of strange particle production. Strange particles are always produced in pairs in pp-interactions (and also in other nonstrange hadron reactions on nucleons and nucleus). The average production rates and cross sections for 12 and 24 GeV/c pp interactions are given in fig.46 [61] and table 6

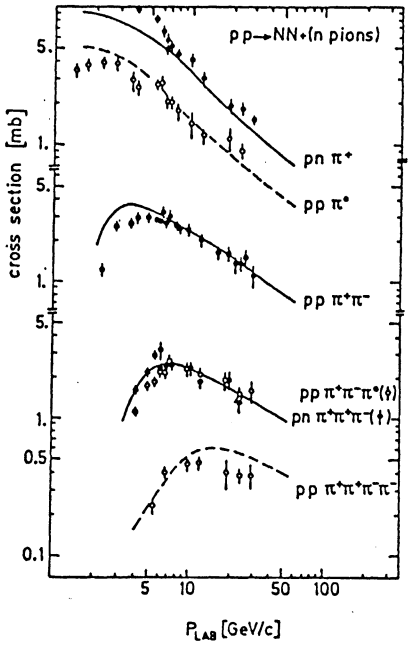

Figure 44. Cross sections of some exclusive reactions for pp interactions. The curves represent the prediction of the Monte Carlo simulation. For further details see text.

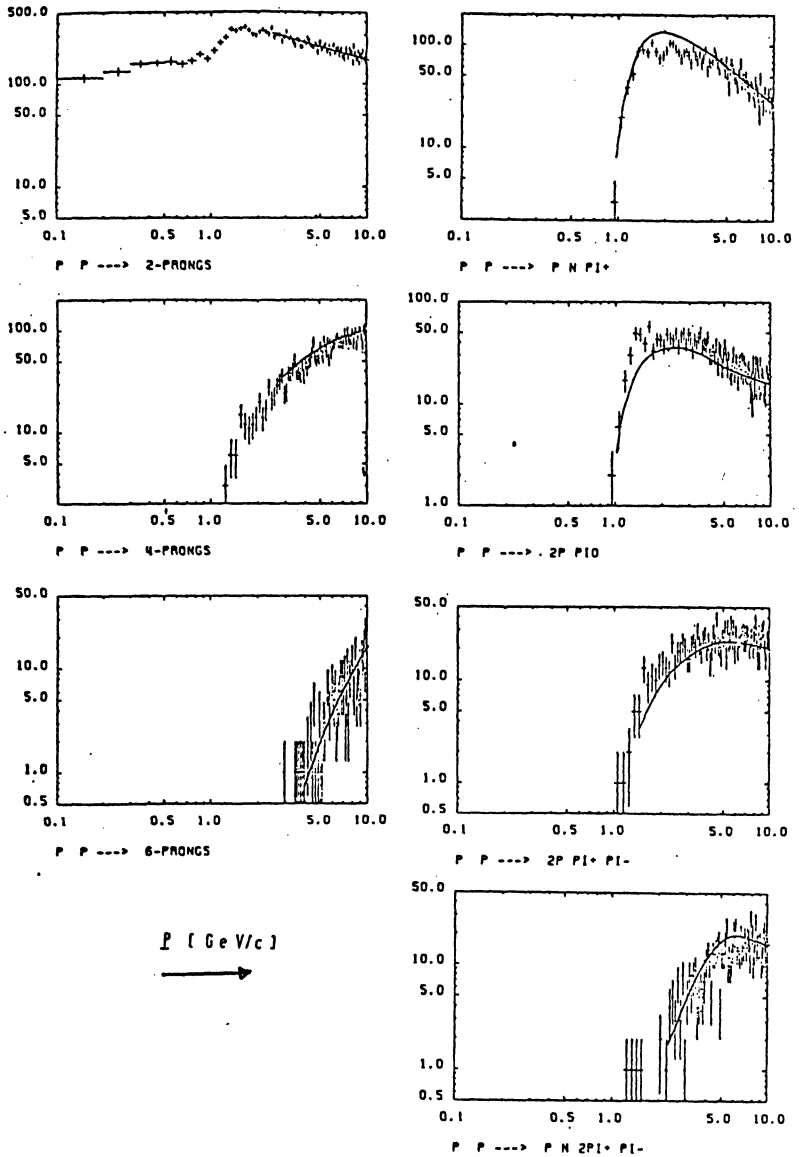

Figure 45. Production rate of some exclusive reactions for pp interactions. The crosses represent the prediction of the Monte Carlo simulation. The lines are eye ball fits through experimental data. There is one but the same arbitrary normalization constant in all plots.

Table 6 cross sections in μb for strange particle production in pp interactions.

	12 GeV/c	24 GeV/c
$K^0\bar{K}^0$	144 ± 20	500 ± 28
$K^+\bar{K}^0$	210 ± 20	600 ± 24
K^0K^-	82 ± 12	514 ± 26
K^+K^-		
$K^+\Lambda/\Sigma^0$	632 ± 28	1274 ± 40
$K^0\Lambda/\Sigma^0$	446 ± 24	820 ± 28
$K^+\Sigma^+$	372 ± 28	543 ± 40
$K^0\Sigma^+$	236 ± 34	308 ± 34
$K^+\Sigma^-$	72 ± 8	149 ± 10
$K^0\Sigma^-$	58 ± 8	124 ± 10

Below 200 GeV/c momentum the total $K\bar{K}$ and KY-production rates can be parametrized as [62] :

$$\langle K\bar{K}\rangle = -0.033 + 0.085 \ln(E_{av}) \quad (2.145)$$

$$\langle KY\rangle = -0.069 + 0.085 \ln(E_{av}) \quad (2.146)$$

where $E_{av} = \sqrt{s} - 2m_p$.

The branching ratios into the various charge states are kept momentum independent. From table 6 and other high energy data [62] we deduced the following ratios, as given in table 7. The first particle has strangeness 1 and the second strangeness -1. For K^0 and $\bar{K}_0$ we took 50% K_S^0 and K_L^0 each.

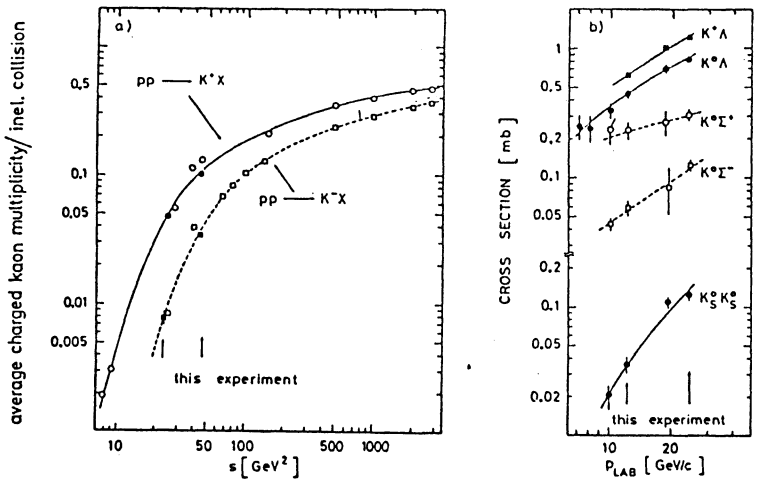

Figure 46. Inclusive cross sections of kaons (a) and pairs of strange particles (b) in pp interactions. The lines represent the prediction of the Monte Carlo simulation.

Table 7 Branching ratios into the various charge and mass states for $K\bar{K}$ and KY-production.

$K^+ K^-$	0.25	$K^+ \Lambda$	0.34
$K^+ K_S^0$	0.125	$K_S^0\Lambda$	0.17
$K^+ K_L^0$	0.125	$K_L^0\Lambda$	0.17
$K_S^0 K_S^0$	0.0625	$K^+ \Sigma^+$	0.055
$K_S^0 K_L^0$	0.0625	$K_S^0\Sigma^+$	0.0275
$K_L^0 K_S^0$	0.0625	$K_L^0\Sigma^+$	0.0275
$K_L^0 K_L^0$	0.0625	$K^+ \Sigma^0$	0.055
$K_S^0 K^-$	0.125	$K_S^0\Sigma^0$	0.0275
$K_L^0 K^-$	0.125	$K_L^0\Sigma^0$	0.0275
		$K^+ \Sigma^-$	0.055
		$K_S^0\Sigma^-$	0.0275
		$K_L^0\Sigma^-$	0.0275

These values are of course valid only very approximately and have to be improved for use of the program at higher energies, let say above 200 GeV/c. In ref. [61] it has been shown, that $K\bar{K}$- and KY- pairs are produced

in clusters or resonance-like states, $K\bar{K}$ predominantly in the central region of phase space and KY in the fragmentation region of either the beam or target proton. Therefore we proceeded as follows. If a $K\bar{K}$ or KY is produced, they replace two pions or a nucleon and a pion produced in the normal way as described above. If the sum of all masses exceeds the total c.m. energy further pions are deleted. The formula for $\langle K\bar{K}\rangle$ and $\langle KY\rangle$ given above guarantees, that no strange particle pairs are produced below the threshhold energies of $\sqrt{s} - 2m_p - 2m_K$ or $\sqrt{s} - m_p - m_Y - m_K$ respectively.

This procedure predicts the exclusive cross sections for the reactions $pp \rightarrow pK^+(\Lambda/\Sigma^0)$ and $pp \rightarrow p\pi^+(\Lambda/\Sigma^0)K^0$ as shown in fig.47. The data are taken from ref. [63].

We finish this discussion with some remarks about all other reactions treated, listed in table 8. Included in this table are all two particle final states which can not be described by the parametrization discussed above. The momentum dependence of their cross sections has been introduced into the program by tables (ref. [26] - [36]).

Table 8 Summary of all two particle final states not included in the general parametrization

reaction	final state
π^+n	π^0p
π^-p	π^0n
K^+n	K^0p
K^0p	K^+n
$\bar{K}^0p$	$\pi^+\Lambda$, $\pi^+\Sigma^0$
$\bar{K}^0n$	$\pi^0\Lambda$, $\pi^-\Sigma^+$, $\pi^0\Sigma^0$, $\pi^+\Sigma^-$
K^-p	$\pi^0\Lambda$, $\pi^-\Sigma^+$, $\pi^-\Sigma^+$, $\pi^+\Sigma^-$
K^-n	$\pi^-\Lambda$, $\pi^-\Sigma^0$, $\pi^0\Sigma^-$
pn	np
np	pn
Λp	Σ^+n, Σ^0p, $p\Lambda$, $p\Sigma^0$, $n\Sigma^+$
Λn	Σ^0n, Σ^-p, $n\Lambda$, $n\Sigma^0$, $p\Sigma^-$

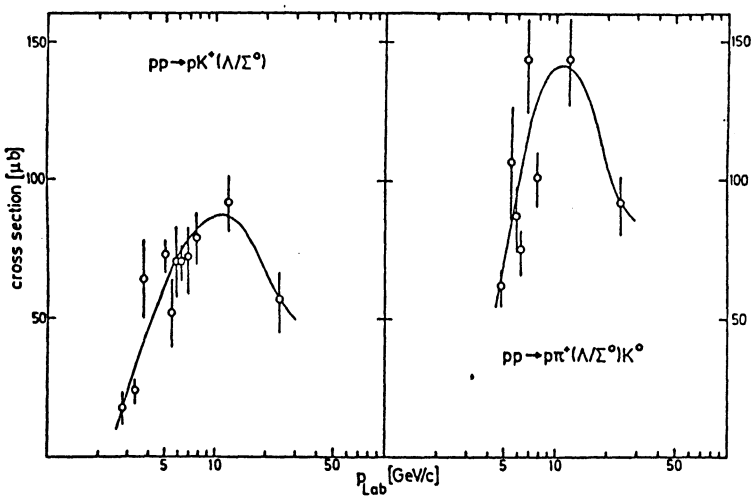

Figure 47. Cross sections of exclusive reactions with strange particles in the final state. The lines represent the prediction of the Monte Carlo simulation.

Σ^+p	$p\Sigma^+$
Σ^+n	Σ^0p, Λp, $n\Sigma^+$, $p\Sigma^0$, $p\Lambda$
Σ^-p	Σ^0n, Λn, $p\Sigma^-$, $n\Sigma^0$, $n\Lambda$
Σ^-n	$n\Sigma^-$
$\bar{p}p$	$p\bar{p}$
$\bar{p}n$	$n\bar{p}$
$\bar{n}p$	$p\bar{n}$
$\bar{n}n$	$n\bar{n}$
$\bar{\Lambda}p$	$\bar{\Sigma}^0p$, $\bar{\Sigma}^-n$, $p\bar{\Lambda}$, $p\bar{\Sigma}^0$, $n\bar{\Sigma}^-$
$\bar{\Lambda}n$	$\bar{\Sigma}^+p$, $\bar{\Sigma}^0n$, $n\bar{\Lambda}$, $n\bar{\Sigma}^0$, $p\bar{\Sigma}^+$
$\bar{\Sigma}^+p$	$\bar{\Lambda}n$, $\bar{\Sigma}^0n$, $n\bar{\Lambda}$, $n\bar{\Sigma}^0$, $p\bar{\Sigma}^+$
$\bar{\Sigma}^+n$	$n\bar{\Sigma}^+$
$\bar{\Sigma}^-p$	$p\bar{\Sigma}^-$
$\bar{\Sigma}^-n$	$\bar{\Lambda}p$, $\bar{\Sigma}^0p$, $p\bar{\Lambda}$, $n\bar{\Sigma}^-$, $p\bar{\Sigma}^0$

In case of K-nucleon reactions leading kaons and strange baryons are generated in the final state as prescripted by experimental data. For antibaryon-baryon reactions precise treatment of annihilation reactions (see e.g. [64]) are introduced. Charge-, baryon- and strangeness- number are conserved exactly. As in case of pp-interactions all measured multiplicities and cross sections of exclusive reactions have been compared with our Monte-Carlo generation. If they did not fit, changes by correction factors have been applied. In the following picture book (figs 48 to 52) comparisons are shown. We do not give these figures here to fill paper only. It has happened very often in the past, that some problems were closely connected with certain exclusive reactions, mainly at low energies where reactions with low final state multiplicities dominate. So these comparisons may give hints which reactions are poor simulated and may be further improved. For more details we have to refer to the computer code.

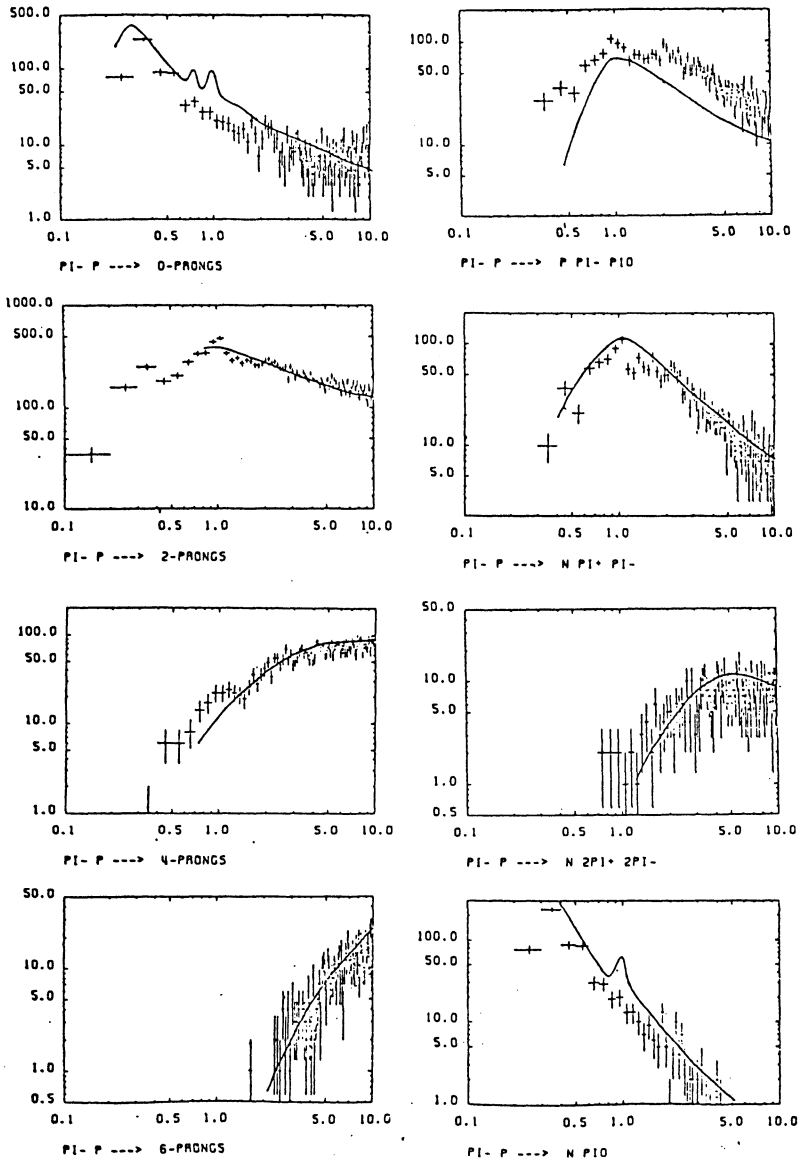

Figure 48. Production rates of some exclusive reactions for π^-p and π^-n interactions. The crosses represent the prediction of the Monte Carlo simulation. The lines are eye ball fits through experimental data. There is one but the same arbitrary normalization constant in all plots.

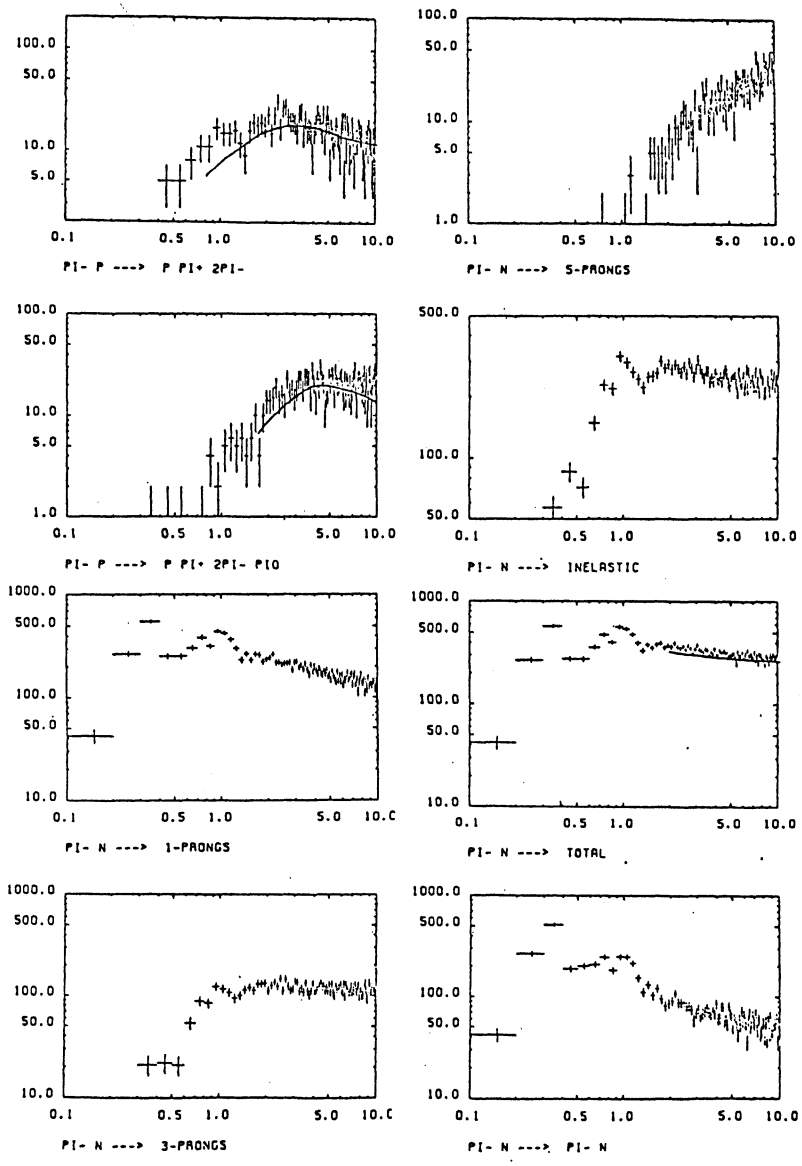

Figure 48. Production rates of some exclusive reactions for π^-p and π^-n interactions. The crosses represent the prediction of the Monte Carlo simulation. The lines are eye ball fits through experimental data. There is one but the same arbitrary normalization constant in all plots.

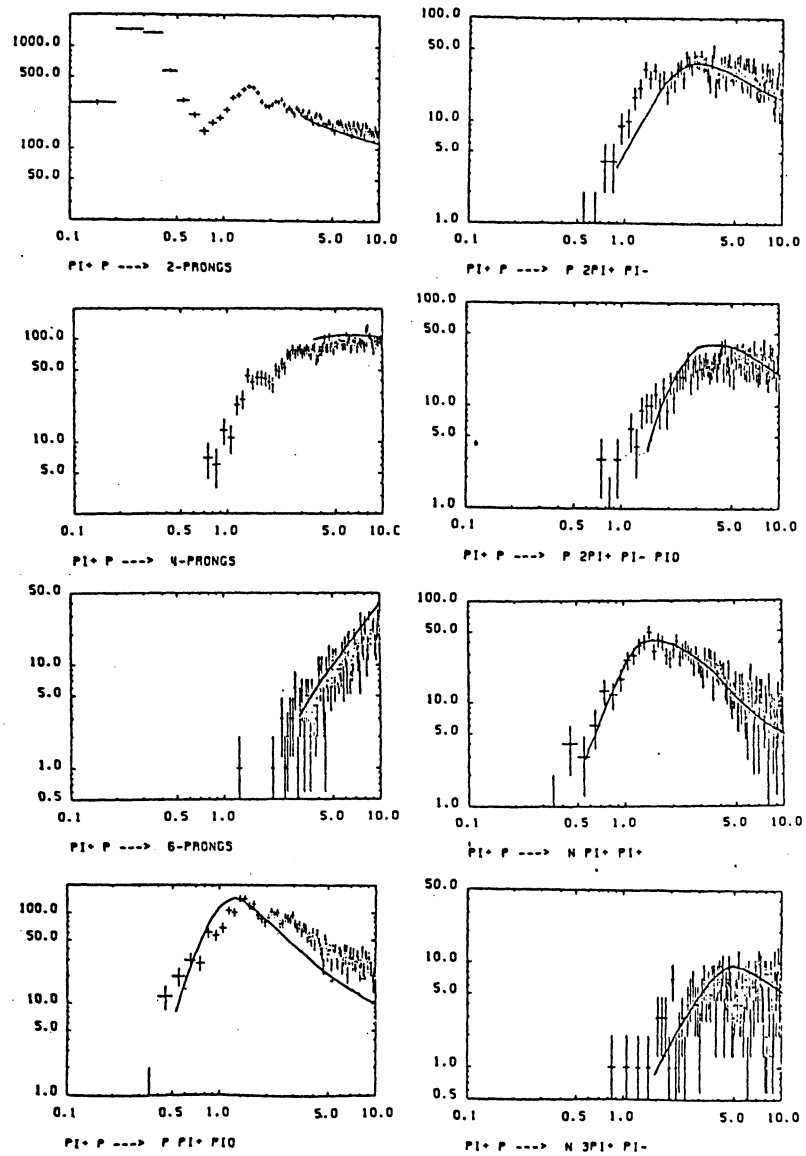

Figure 49. Production rates of some exclusive reactions for π^+p and π^+n interactions. The crosses represent the prediction of the Monte Carlo simulation. The lines are eye ball fits through experimental data. There is one but the same arbitrary normalization constant in all plots.

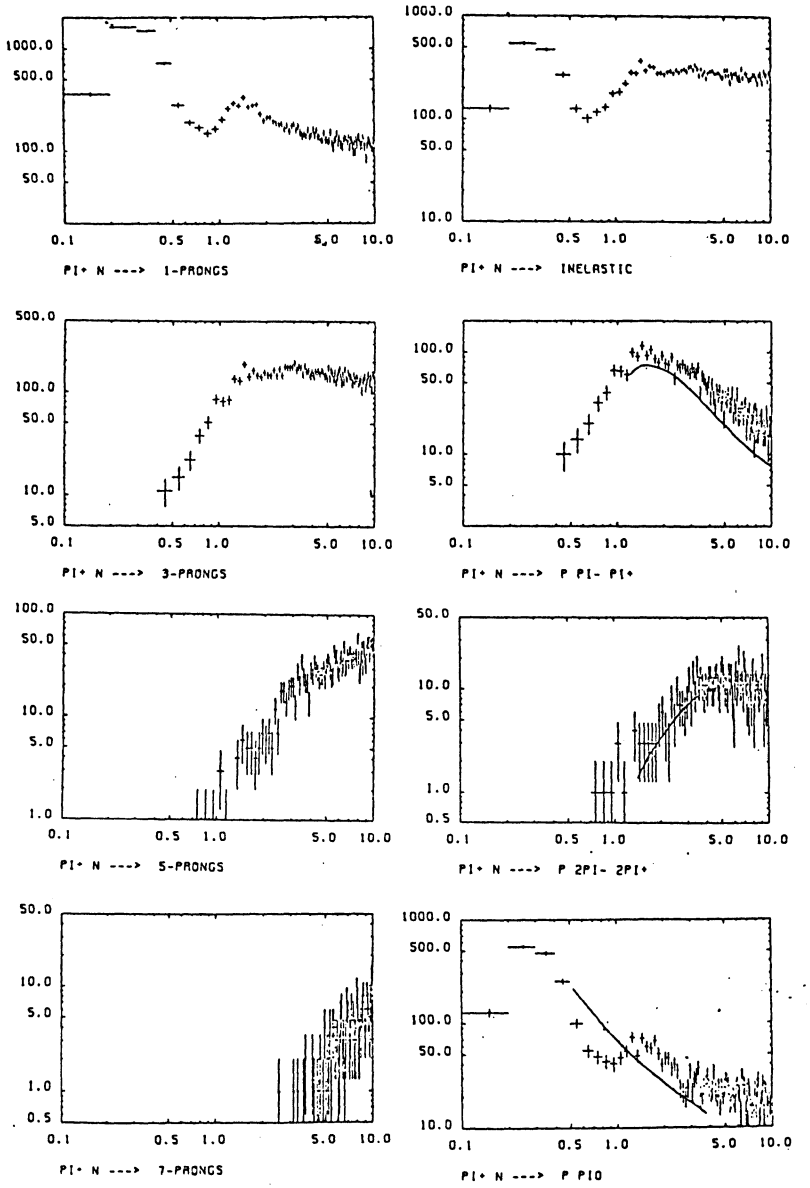

Figure 49. Production rates of some exclusive reactions for π^+p and π^+n interactions. The crosses represent the prediction of the Monte Carlo simulation. The lines are eye ball fits through experimental data. There is one but the same arbitrary normalization constant in all plots.

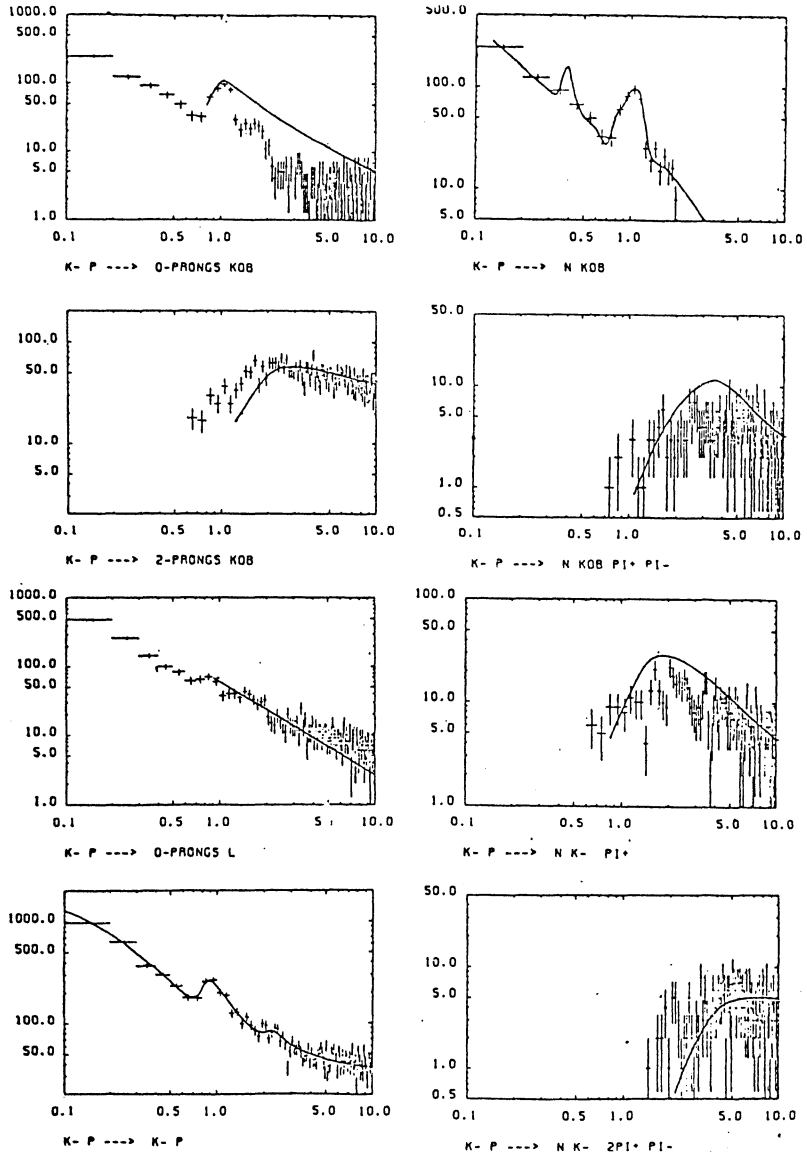

Figure 50. Production rates of some exclusive reactions for K^-p and K^-n interactions. The crosses represent the prediction of the Monte Carlo simulation. The lines are eye ball fits through experimental data. There is one but the same arbitrary normalization constant in all plots.

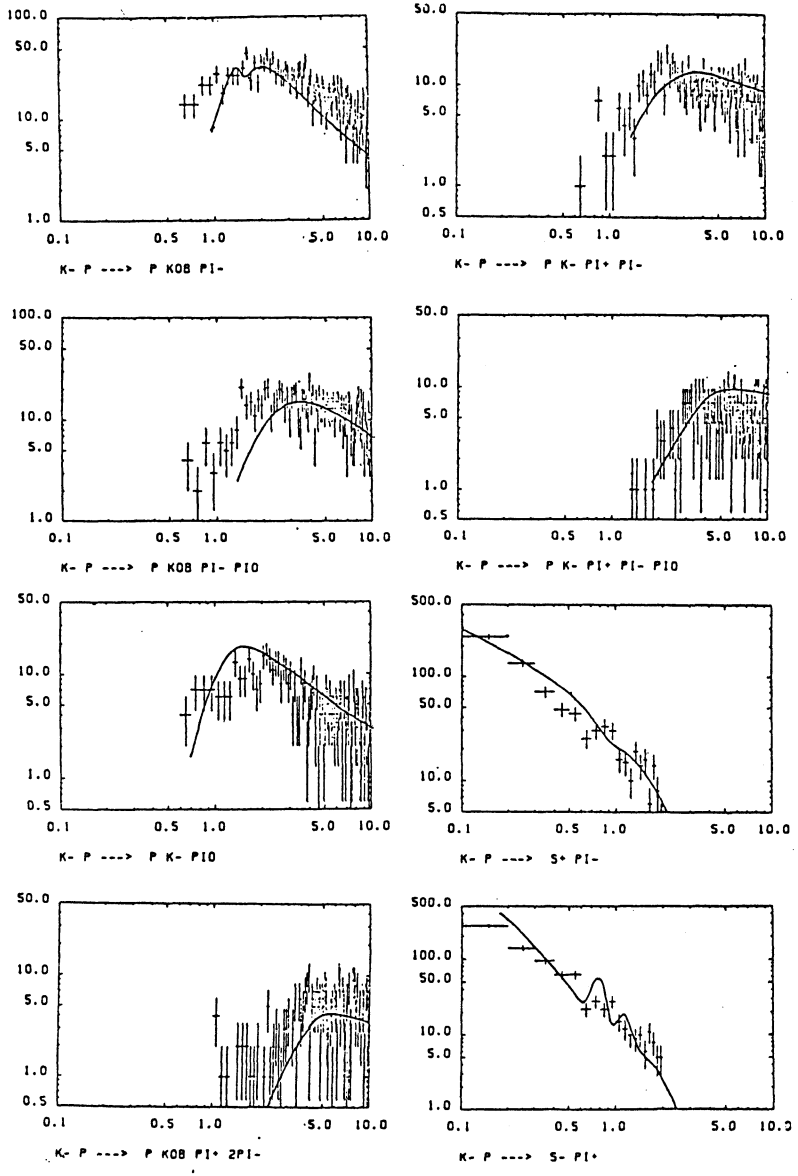

Figure 50. Production rates of some exclusive reactions for K^-p and K^-n interactions. The crosses represent the prediction of the Monte Carlo simulation. The lines are eye ball fits through experimental data. There is one but the same arbitrary normalization constant in all plots.

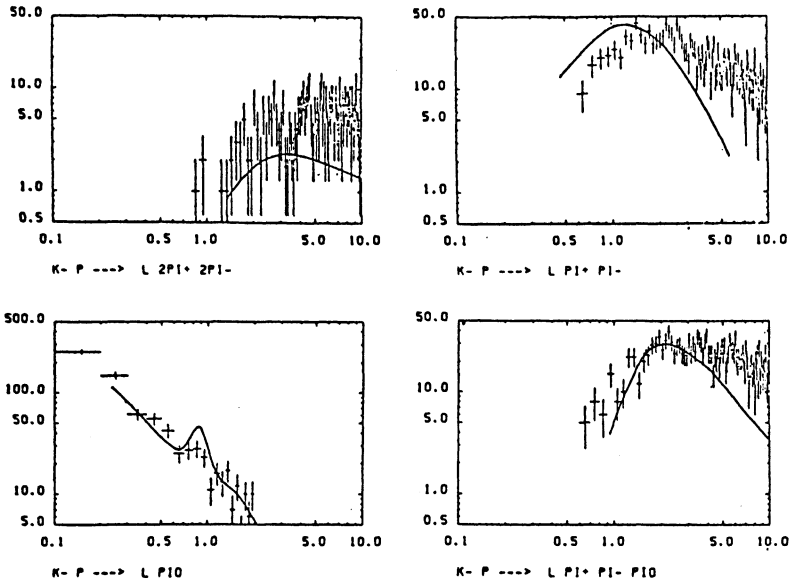

Figure 50. Production rates of some exclusive reactions for K^-p and K^-n interactions. The crosses represent the prediction of the Monte Carlo simulation. The lines are eye ball fits through experimental data. There is one but the same arbitrary normalization constant in all plots.

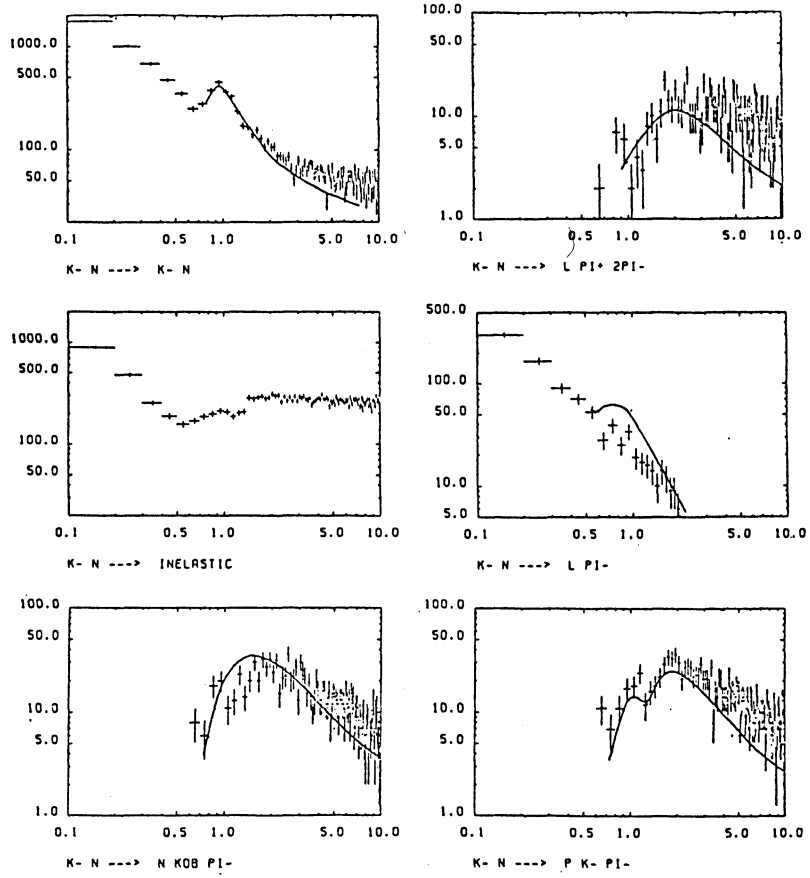

Figure 50. Production rates of some exclusive reactions for K^-p and K^-n interactions. The crosses represent the prediction of the Monte Carlo simulation. The lines are eye ball fits through experimental data. There is one but the same arbitrary normalization constant in all plots.

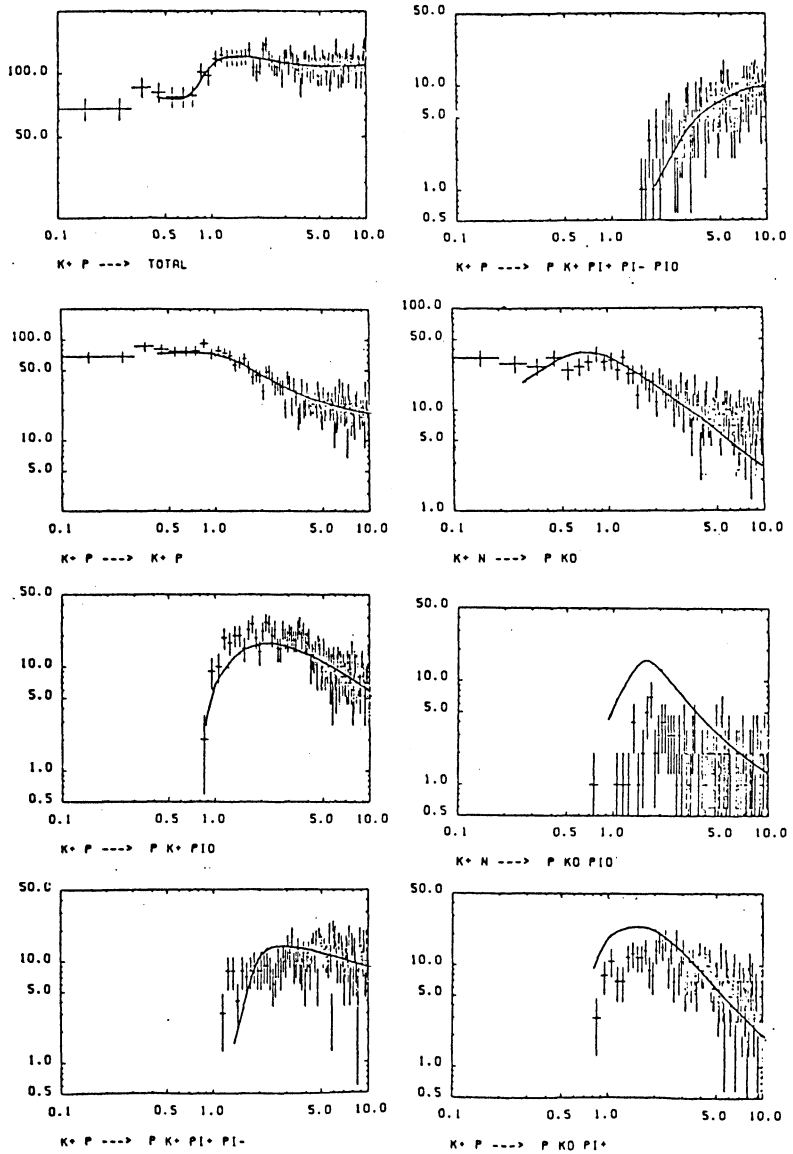

Figure 51. Production rates of some exclusive reactions for K^+p and K^+n interactions. The crosses represent the prediction of the Monte Carlo simulation. The lines are eye ball fits through experimental data. There is one but the same arbitrary normalization constant in all plots.

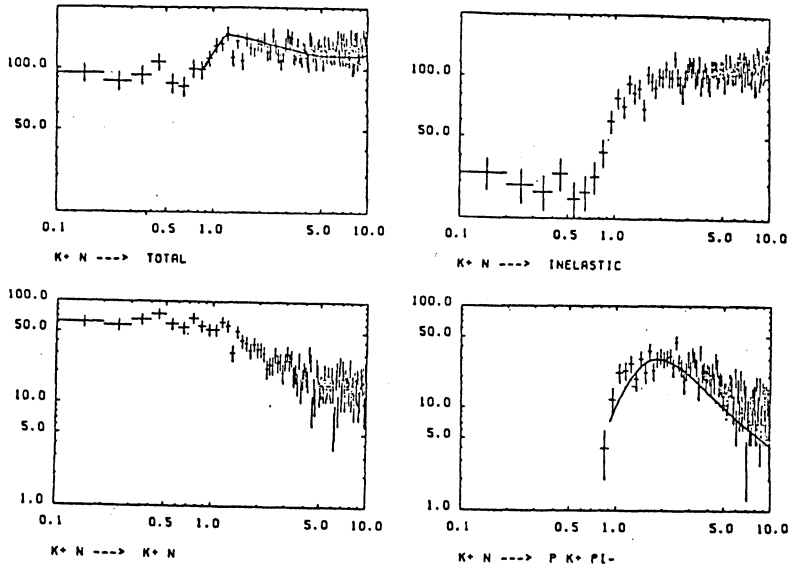

Figure 51. Production rates of some exclusive reactions for K^+p and K^+n interactions. The crosses represent the prediction of the Monte Carlo simulation. The lines are eye ball fits through experimental data. There is one but the same arbitrary normalization constant in all plots.

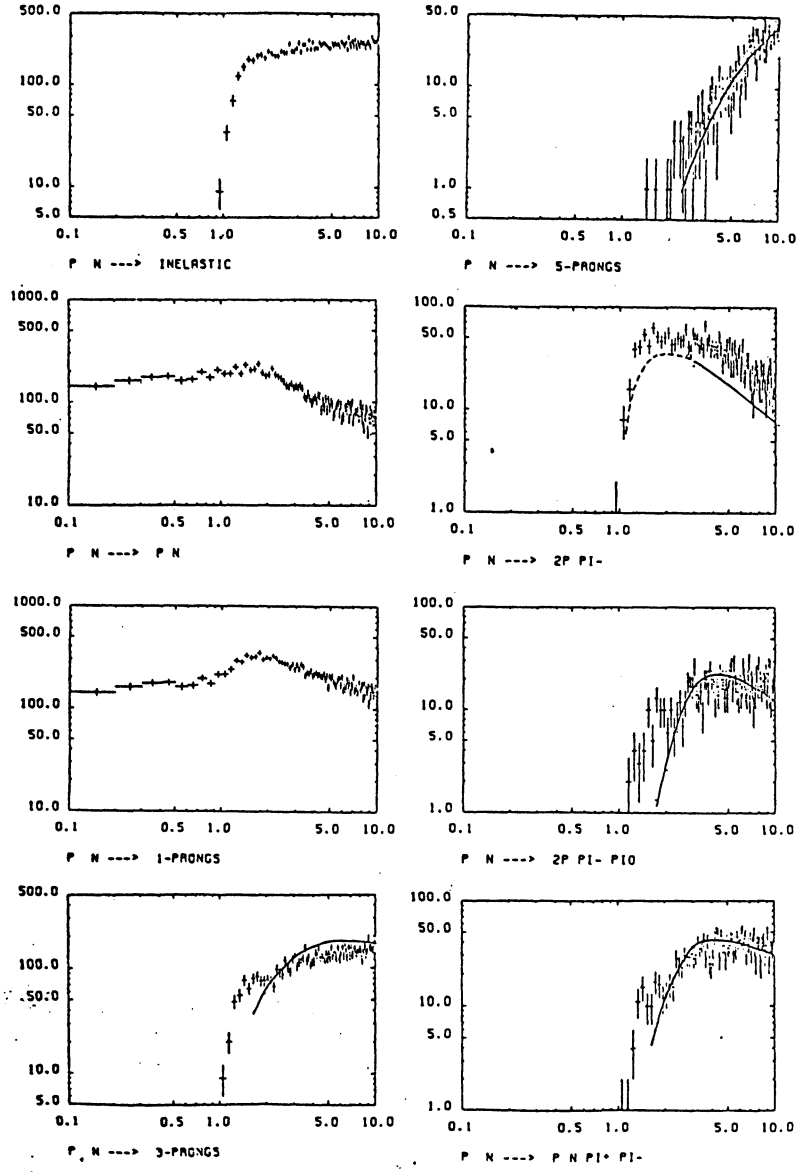

Figure 52. Production rates of some exclusive reactions for pn and $\bar{p}p$ interactions. The crosses represent the prediction of the Monte Carlo simulation. The lines are eye ball fits through experimental data. There is one but the same arbitrary normalization constant in all plots.

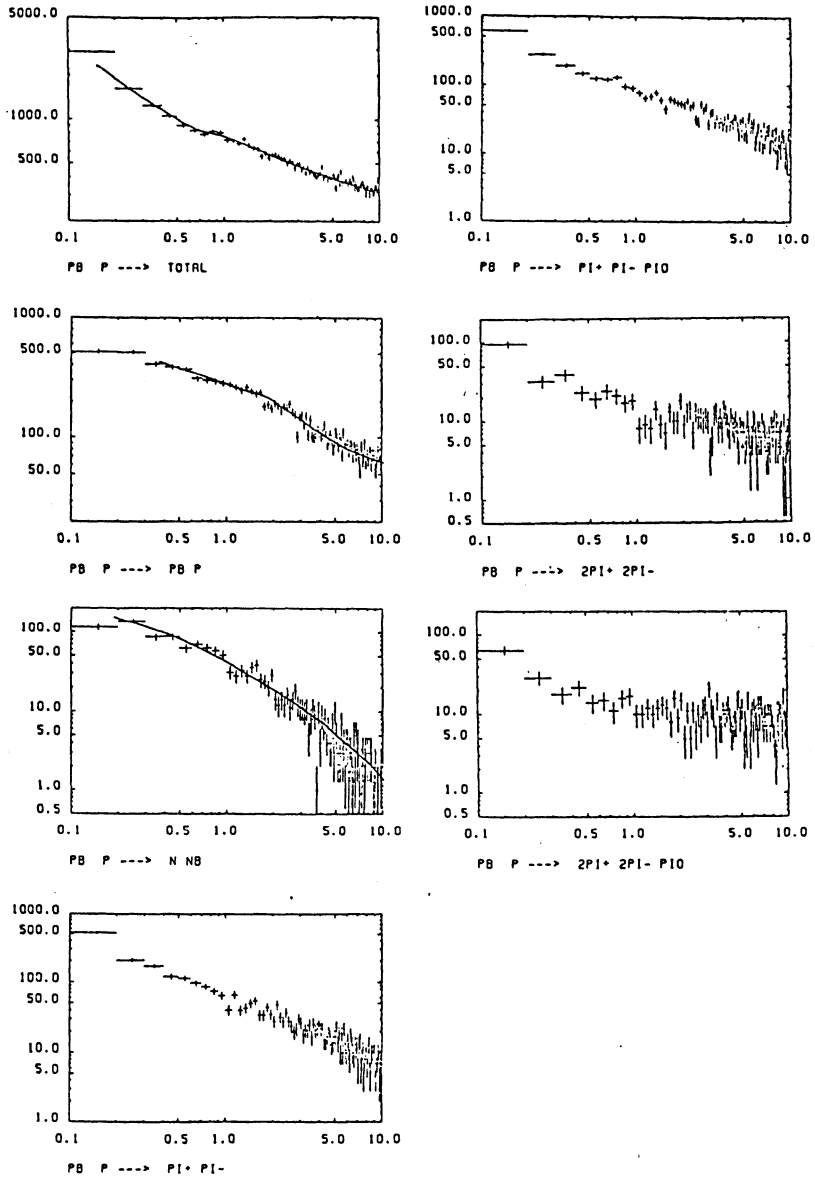

Figure 52. Production rates of some exclusive reactions for pn and $\bar{p}p$ interactions. The crosses represent the prediction of the Monte Carlo simulation. The lines are eye ball fits through experimental data. There is one but the same arbitrary normalization constant in all plots.

2.6.6 Generation of four-momenta

The method used to generate the four-momenta of the final state particles is very similar to that discussed in ref. [65], [66] and [67]. It is based on quark- or hadron- jets in soft hadron nucleon collisions. Hadron- jets means in this context the simultaneous fragmentation of more than one quark- jet within the hadron. In chapter 2.6.7 we discuss the general concept of cluster-invariant quantities, chapter 2.6.8 is devoted to the confirmation of a scaling law for low energy reactions. In chapter 2.6.9 we will see, that the model is closely connected to recursive cascade models and finally in chapter 2.6.10 di-quark fragmentation is discussed. From the results of these discussions we are then able in chapters 2.6.11 and 2.6.12 to present the method used in the present version of the program and modifications which are foreseen and also tested, but are not necessary at low energies.

2.6.7 Clustering invariant quantities

There are different ways to describe a multiparticle final state of hadrons with its complicated structure. Usually one studies the invariant cross sections $Ed^3\sigma_k/dp^3$ for producing individual particles of type k (like π, K, Λ, ...). However it has become clear that very often one should consider these particles as decay products of resonances (like ρ, K*, Y*, ...) which in turn are distributed in some other way. Even inclusive distributions of higher mass resonances have been measured. Selecting only stable particles appears quite artificial from a theoretical standpoint. If one includes resonances this description by inclusive single particle cross sections becomes quickly complicated and ambigous.

A simplification may be obtained by introduction of partons. One considers a primary distribution of partons of only a few types which later fragment or recombine into the various secondary hadrons. Especially if a parton has large transverse momentum one may hope to determine the inclusive single parton distribution by identifying the corresponding jet of particles with $Ed\sigma^{jet}/dp^3$.

The fact that not the stable hadrons but resonances, clusters or partons appear to be the more fundamental objects in hadron physics makes it desirable to focus on more properties of the multiparticle final state which do not refer to any particular particle or parton type but are defined (at least approximately) independent on whether a particle comes from a resonance or not or whether the partons inside the hadrons are primary objects or not. This is achieved by using clustering invariant quantities.

One example is the energy flow ΔE into a certain angular region $\Delta\Omega$: the energy of a resonance with momentum vector in $\Delta\Omega$ is the same as the energy of the decay products or the energy of the constituent partons. This is only exactly true within the approximation that the decay particles are contained in $\Delta\Omega$. The same is true for the quantum number flow $\Delta Q/\Delta\Omega$. Measurements of this type can be realized for example by large opening calorimeters. With such a calorimeter one can measure quantities like $d\sigma/dx_c$, the cross section to find the energy fraction $x_c = E_c/\sqrt{s}$ (in the c.m.s.) in the calorimeter, or $d\sigma/d\tau_c$ where $\tau_c = M_c^2/s$ and M_c is the total invariant mass of particles in the calorimeter. Similarly $d\sigma/dx_{tr}$, $x_{tr} = |\Sigma\vec{p}_{tr}^{\,k}|/\sqrt{s}$ or more differential distributions like $d\sigma/dx_c d\tau_c$. A further example is $\bar{Q}(x_c)$, the average charge in the calorimeter or conditional distributions $d\sigma/dx_c$ for fixed total charge Q_c in the calorimeter and so on.

Among variables which are not clustering invariant are $\Sigma|\vec{p}_T^{\,k}|$. This quantity may be useful for triggering purposes but in our sense it is a bad variable. Similarly $Q_E = \Sigma q_k E_k$ where the energies E_k of particles are weighted by their charge q_k. To see the problem with such bad variables consider as example a $p\pi^-$ system in the N^{*0} resonant state. Then $Q_E(N^{*0}) = 0$, whereas $Q_E(p\pi^-) = E_p - E_\pi \geq 0$ in general. So, the value of Q_E depends on whether particles are in a resonant state or not. Such quantities are first of all difficult and not without ambiguity to determine experimentally, and will then depend on the masses of the individual particles involved as in the above example. This is of course not what we want to have in a Monte Carlo simulation.

If clustering invariant quantities can be calculated within a theory at the parton level, say at the level of quarks and gluons one can take the result over immediately to the experimental quantities under the assumption that our quantities are the same for a collection of hadrons or partons. An example of this is the jet analysis by Sternman and Weinberg [68].

2.6.8 Quantum number flow in soft collisions

First we consider the energy flow in normal soft pp collisions where most particles emerge at small p_T. For the single particle spectra we have Feynman scaling, i.e. $\omega d^3\sigma_k/dp^3$. In order to derive a corresponding scaling law for the total energy flux into a given interval of the polar angle Θ with respect to the beam axis we define the normalized quantities $d\varepsilon = dE/E_0$ and $\lambda = \cot g\Theta/E_0$. We stay in the CMS, then $E_0 = \sqrt{s}/2$. Assuming Feynman scaling we can calculate the energy flux by integrating the single particle spectra :

$$\frac{d\varepsilon}{d\lambda} = \int \frac{\omega}{E_0} \frac{d^2n}{dx dp_T} dx\, dp_T\, \delta\left(\lambda - \frac{x}{p_T}\right) \quad , \tag{2.147}$$

where $d^2n/dxdp_T$ is the particles density in the Feynman variable x and transverse momentum p_T. We calculate

$$\frac{d^2n}{dxdp_T} = \frac{1}{\sigma_{in}} \sum_k \int \frac{d^3\sigma_k}{dp^3} d\Phi = \frac{E_0}{\omega} \frac{2\pi p_T}{\sigma_{in}} \sum f_k(x, p_T) \tag{2.148}$$

$$\frac{d\varepsilon}{d\lambda} = \sum_k \frac{2\pi}{\sigma_{in}} \int_0^{1/\lambda} dp_T\, p_T^2\, f_k(p_T\lambda, p_T) \quad . \tag{2.149}$$

The r.h.s. now depends only on λ and we obtain the scaling law for the energy flux

$$\frac{d\varepsilon}{d\lambda} = \rho(\lambda) \quad . \tag{2.150}$$

Note that the radiation profile function $\rho(\lambda)$ is normalized to

$$\int_0^\infty \rho(\lambda)\, d\lambda = 1 \quad . \tag{2.151}$$

We may compare λ with the more familiar pseudorapidity $\eta = -\ln \mathrm{tg}(\Theta/2)$. We find with $\omega = m_T \cosh y \approx m_T \cosh \eta$

$$\frac{d\varepsilon}{d\lambda} \approx \frac{dm_T}{d\eta} = \sum_k m_T^k(\eta) \frac{dn^k}{d\eta} \quad , \tag{2.152}$$

so $d\varepsilon/d\lambda$ corresponds to the rapidity density of particles weighted by their transverse mass $m_T = \sqrt{m^2+p_T^2}$. From the behaviour of the f_k one expects the limiting values

$$\frac{d\varepsilon}{d\lambda} \xrightarrow[\lambda\to\infty]{} 1/\lambda^3 \tag{2.153}$$

$$\frac{d\varepsilon}{d\lambda} \xrightarrow[\lambda\to 0]{} M \quad . \tag{2.154}$$

The mass parameter M for $\lambda = 0$ can be interpreted as the average total transverse mass in the rapidity plateau. Wheras the relevant rapidity range expands like ln E, the shape of $d\varepsilon/d\lambda$ is energy independent. Energy scaling of this type has been first discussed by Ochs and Stodolsky [65].

In fig.53 we compare data from 12 and 24 GeV/c pp collisions [66] and remarkably, there is not any indication of scale breaking . In contrast, the single particle spectra change considerably near rapidity $y = 0$ (i.e. $\lambda = 0$), namely $\pi^+(\pi^-)$ spectra rise by 20% (40%) whereas proton spectra drop by 40% with increasing energy ([69], [70]). Obviously looking at just the total energy results in a complete cancellation of scale breaking effects between the different types of particles.

Next we study charge distributions. Assuming again Feynman scaling one expects the quantity $dQ_E/d\lambda = \Sigma q_k d\varepsilon^k/d\lambda$ to be a function of λ only. Experimentally this quantity does not scale at all (see fig.54 [66]). We relate this to the fact that the above quantity is not clustering invariant and therefore mass effects may spoil an underlaying scaling law. If on the other hand we consider simply the clustering invariant definition $d(\Sigma q_k)/d\lambda$ of charge flow we find again perfect scaling (fig.55). We also note the interesting phenomenological observation that the charge flow dQ into an angular interval almost exactly equals the energy flow $d\varepsilon$ (see fig.53 for comparison). This will be discussed later in terms of iterative cascade models. Denoting the charge of the fragmenting proton as Q_p we write for later applications

$$\frac{d\varepsilon}{d\lambda} = \frac{1}{Q_p} \frac{dQ}{d\lambda} \quad . \tag{2.155}$$

Other energy inclusive measurements in soft hadronic collisions and an interpretation in terms of quark parton models are given in ref. [71].

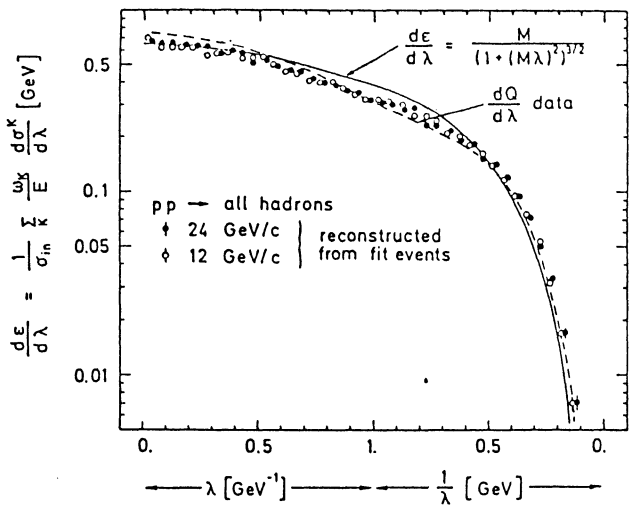

Figure 53. Energy flow distribution in pp interactions at 12 and 24 GeV/c. For details see text.

We are led to a simple parametrization of $d\varepsilon/d\lambda$ by considering the Q-variable used in the description of inclusive spectra [72]. A generalized Weizsaecker-Williams approach suggested that

$$\omega \frac{d^3\sigma}{dp^3} = f(Q) \qquad (2.156)$$

$$Q^2 = (Mx)^2 + p_T^2 \quad , \qquad (2.157)$$

where M is a mass parameter. Experimental confirmation for this scaling behaviour is shown in fig.56 ([73], [74]). Assuming an exponential shape for f(Q) we have

$$\omega \frac{d^3\sigma}{dp^3} \sim e^{-bQ} \qquad (2.158)$$

Then

$$\frac{d\varepsilon}{d\lambda} = \rho(\lambda) \sim \int_0^{1/\lambda} dp_T \; p_T^2 \; e^{-bQ} \qquad (2.159)$$

By substituting of variables we get

$$\frac{d\varepsilon}{d\lambda} = \rho(\lambda) \sim \frac{1}{(1+M^2\lambda^2)^{3/2}} \int_0^{1/\lambda} dQ \; Q^2 \; e^{-bQ} \qquad (2.160)$$

Normalization of the profile function gives then

$$\frac{d\varepsilon}{d\lambda} = \rho(\lambda) = \frac{M}{(1+M^2\lambda^2)^{3/2}} \qquad (2.161)$$

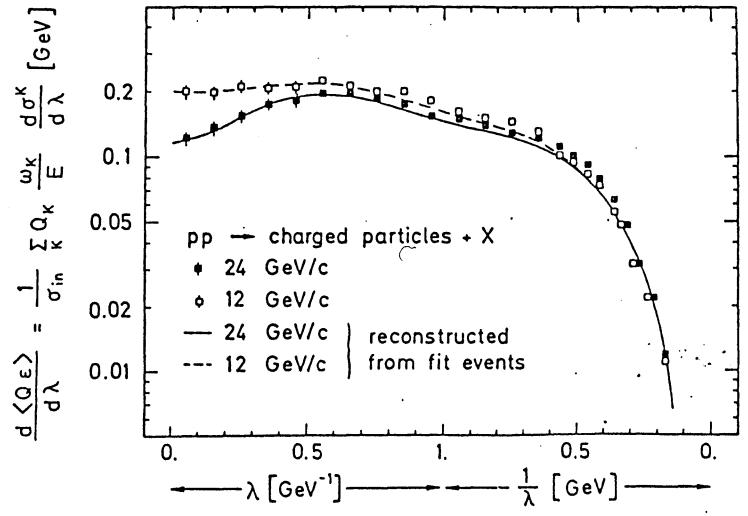

Figure 54. Charge flow distribution in pp interactions at 12 and 24 GeV/c. For details see text.

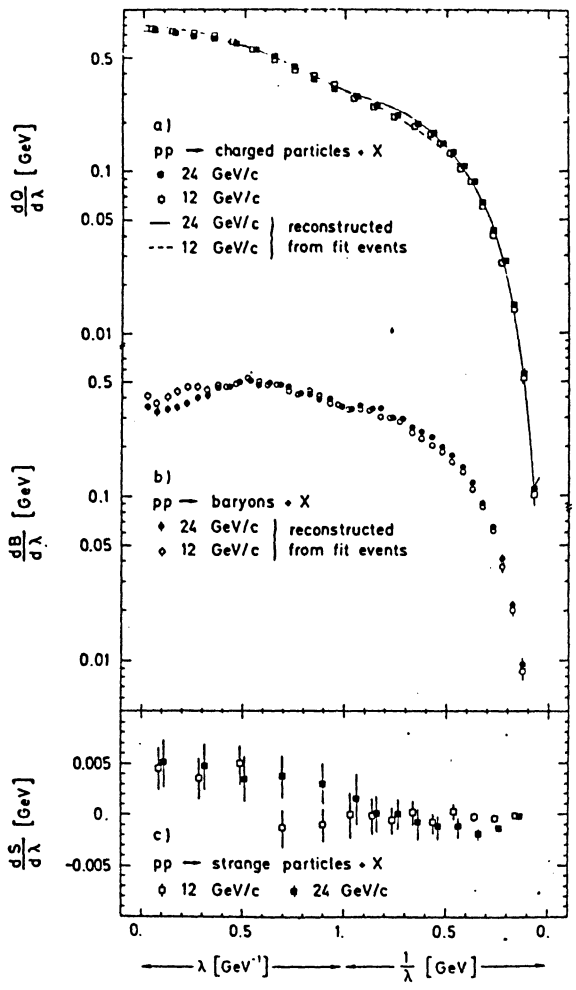

Figure 55. Charge-, baryon number- and strangeness flow in pp interactions at 12 and 24 GeV/c. For details see text.

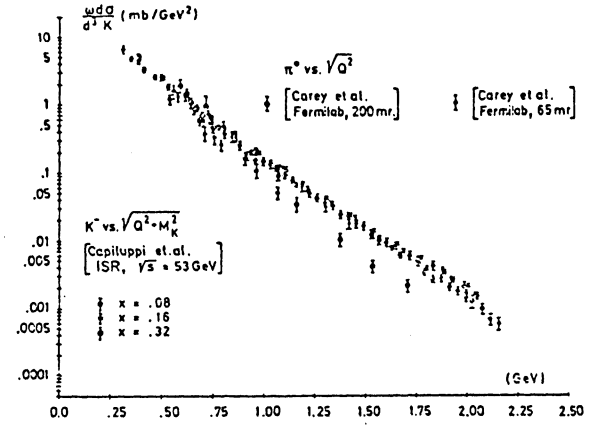

Figure 56. Distribution of the Q-variable in high energy pp interactions. For details see text.

The physical picture involved is that the fields are spherically symmetric in the fragmenting particles rest frame. The parameter M is presumably to be taken to be the mass of the fragmenting particle. In the case of soft hadronic collisions this is equivalent with the mass of the beam particle. This would mean that if we switch from proton to pion beams, at the same energy, we would expect a substantial shift in the secondary distributions, something which is in contrary to the general trend of the data and to the idea that at very high energy rest masses do not play a significant role. Even worse in case of virtual photons, as in electroproduction, the procedure degenerates into an absurdity: the photon has no rest frame in which to begin the argument. Therefore this approach does not give a satisfactory answer to the meaning of the mass parameter M. Nevertheless, as is shown in fig.53, the parametrization given above gives a good description of the data with a mass value of M = 650 MeV for pp and πp interactions and M = 900 Mev for Kp interactions. It may be accident that these values lie very near to 1.8 times the generally assumed masses for bound quarks of 350 MeV and 500 Mev for u,d and s quarks respectively.

2.6.9 Comparison with recursive cascade models

The energy and charge profile distributions $d\varepsilon/d\lambda$ and dQ/λ (and also the corresponding distributions for other additive quantum numbers) have a simple and natural interpretation in a general class of iterative quark cascade models (see e.g. ref [75], [76]). The natural dynamical variable in cascade models for quark fragmentation is the Lorentz-invariant light cone variable

$$z = \frac{p_L + \omega}{P_{L,jet}+E_{jet}} \approx \frac{1}{2}\left(x + \frac{\omega}{E_{jet}}\right) \quad , \tag{2.162}$$

where the z-axis is defined to be the jet axis and $P_{L,jet} \approx E_{jet}$. We will assume that the particle distributions factorize in z and p_T :

$$\frac{d^2n}{dzdp_T} = D(z)\ g(p_T) \quad , \tag{2.163}$$

where D(z) is in general a sum of functions $D_a^{(b\bar{c})}$ which describe the distributions of mesons with flavour $(b\bar{c})$ in a quark jet with flavour a. Then we have

$$\frac{d^2n}{dxdp_T} = \frac{E_{jet}}{\omega}\ z\ D(z)\ g(p_T) \tag{2.164}$$

and by integration over x

$$\frac{d\varepsilon}{d\lambda} = \int dp_T\ p_T\ z\ D(z)\ g(p_T) \quad . \tag{2.165}$$

The r.h.s. is now only approximately independent of the jet energy, because in z there is a term left, which depends on E_{jet} :

$$z = (1/2)\ (\lambda p_T + \sqrt{\lambda^2 p_T^2 + m_T^2 E_{jet}^2}) \quad , \tag{2.166}$$

where $m_T^2 = p_T^2+m^2$ is the transverse mass squared. In the approximation $z \approx x$, i.e. $m_T^2/E_{jet}^2 \approx 0$ the energy scaling is exact.

The charge flow is defined by

$$\frac{dQ}{d\lambda} = \int \left(\frac{d^2n_+}{dxdp_T} - \frac{d^2n_-}{dxdp_T} \right) dx\ dp_T\ \delta\left(\lambda - \frac{x}{p_T}\right) \quad , \tag{2.167}$$

where $d^2n_+/dxdp_T$ and $d^2n_-/dxdp_T$ are the distributions for particles with positive and negative charges respectively:

$$\frac{d^2n_+}{dxdp_T} = \frac{E_{jet}}{\omega}\ z\ D_+(z)\ g(p_T) \tag{2.168}$$

$$\frac{d^2n_-}{dxdp_T} = \frac{E_{jet}}{\omega}\ z\ D_-(z)\ g(p_T) \quad . \tag{2.169}$$

Here $D_+(z)$ is the sum of fragmentation functions $D_a^{(b\bar{c})}$ for positive mesons and $D_-(z)$ for negative mesons. If one introduces the approximation

$$\frac{E_{jet}}{\omega}\ z \approx 1 \quad , \tag{2.170}$$

one gets in the usual way by integration

$$\frac{dQ}{d\lambda} = \int dp_T\ p_T \left(D_+(z) - D_-(z)\right)\ g(p_T) \quad . \tag{2.171}$$

The $D_a^{(b\bar{c})}$ obey a set of coupled integral equations

$$D_a^{(b\bar{c})}(z) = \delta_{ab} f_{ac}(z) + \int_z^1 \frac{d\eta}{\eta} \sum_d f_{ad}(1-\eta) D_d^{(b\bar{c})}\left(\frac{z}{\eta}\right) \quad . \tag{2.172}$$

f_{ac} is the probability that the leading quark with flavour a combines with an antiquark of flavour $\bar{c}$ to a meson $(a\bar{c})$. As has been discussed in ref. [77], the distributions of the quantum numbers related to flavour, such as electric charge or strangeness, will be determined by the first term only, so that in $d^2n_+/dxdp_T$ and $d^2n_-/dxdp_T$ the replacement

$$D_a^{(b\varepsilon)} \to \sum_c f_{ac} \qquad (2.173)$$

is in general valid. We take the probability f_{ac} independent of the leading flavour a

$$f_{ac}(z) = \alpha_c\, f(z) \quad . \qquad (2.174)$$

This leads to

$$D_a^{(b\varepsilon)} \to f(z) \sum_c \alpha_c \quad . \qquad (2.175)$$

Let us consider as an example the u-quark fragmentation.

$$D_+(z)-D_-(z) = D_u^{(u\bar{d})}+D_u^{(us)}-D_u^{(d\bar{u})}-D_u^{(s\bar{u})} \to (\alpha_d+\alpha_s)\, f(z) \qquad (2.176)$$

so that

$$\frac{dQ}{d\lambda} = \int dp_T\, p_T\, (\alpha_d+\alpha_s)\, f(z)\, g(p_T) \qquad (2.177)$$

whereas

$$\frac{d\varepsilon}{d\lambda} = \int dp_T\, p_T\, zD(z)\, g(p_T) \quad . \qquad (2.178)$$

For

$$f(z) = \gamma\, (1-z)^{\gamma-1} \qquad (2.179)$$

the integral equations can be solved exactly

$$zD(z) = f(z) \quad . \qquad (2.180)$$

For other f(z) functions this is approximately valid. Then we arrive at the relation

$$\frac{dQ}{d\lambda} = (\alpha_d+\alpha_s)\, \frac{d\varepsilon}{d\lambda} \quad . \qquad (2.181)$$

For exact SU(3) symmetry we have

$$\alpha_u = \alpha_d = \alpha_s = 1/3 \quad , \qquad (2.182)$$

so that

$$\alpha_d+\alpha_s = 2/3 = Q_u \quad . \qquad (2.183)$$

If the strange quark production is assumed to be suppressed,

$$\alpha_u = \alpha_d = 3/7, \qquad \alpha_s = 1/7 \qquad (2.184)$$

in this case then

$$\alpha_d+\alpha_s = 4/7 \quad . \qquad (2.185)$$

This proves the proportionality between the charge and energy flow. A similar relationship holds for the strangeness flow and energy flow. In the following table we summarize the proportionality factors for different suppressions of s-quark productions.

Table 9 $(dQ/d\lambda)_q = \alpha_q\, (d\varepsilon/d\lambda)_q$

quark flavour	1:1:1	2:2:1	3:3:1
u	2/3	3/5	4/7
d	-1/3	-2/5	-3/7
s	-1/3	-2/5	-3/7
c	2/3	3/5	4/7
b	-1/3	-2/5	-3/7
$\bar{u}$	-2/3	-3/5	-4/7
$\bar{d}$	1/3	2/5	3/7
$\bar{s}$	1/3	2/5	3/7
$\bar{c}$	-2/3	-3/5	-4/7
$\bar{b}$	1/3	2/5	3/7

Our basic formulae for the fragmentation of a quark with flavour q are now written as follows

$$\left(\frac{d\varepsilon}{d\lambda}\right)_q = \int dp_T\, p_T\, f_q(z)\, g(p_T) \qquad (2.186)$$

$$\left(\frac{dQ}{d\lambda}\right)_q = \alpha_q \int dp_T \; p_T \; f_q(z) \; g(p_T) \qquad (2.187)$$

where the factors α_q can be read off from the table.

We close this chapter with a comparison of our predictions with results of a Monte Carlo generator implemented by Ali et al. [78] at DESY, which provides a detailed model of hadron production by e^+e^- annihilation in the framework of QCD. In this section we use events of the reaction

$$e^+ e^- \rightarrow q \bar{q} \rightarrow \text{hadrons} \qquad (2.188)$$

The quark pairs are produced in fractions proportional to the square of the quark charges for five flavours. The fragmentation procedure used to transform quarks into hadrons is similar to that used by Feynman and Field [75], as discussed above . The fragmentation functions used are

$$f(z) = zD(z) = 3(1-z)^2 \qquad (2.189)$$

for u,d and s quarks, i.e. $\gamma = 3$, and

$$f(z) = zD(z) = 1 \qquad (2.190)$$

for c and b quarks, i.e. $\gamma = 1$.

Heavy quarks are allowed to decay weakly according to the six quark model [79]. This might of course produce some scaling violations, especially near the threshhold for new quark flavour production. For details see ref. [80].

In fig.57 we show the results of this Monte Carlo generator for c.m. energies of 12 and 30 GeV, i.e. for jet energies of 6 and 15 GeV. There is apparently not any scaling violation. The curve is the prediction of the parametrization discussed in 2.6.8 with a mass value of M = 1.35 GeV. For quarks of different flavours we get the mass values of M = 1.1, 1.25 and 3.0 GeV for u, c and b quarks respectively (see fig.57b). We conclude, that this simple parametrization of the fragmentation process is in general valid for all flavours and energies.

In fig.58 we show the proportionality between $d\varepsilon/d\lambda$ and $dQ/d\lambda$ for u quarks of 15 GeV energy. The same has been plotted in fig.58b for $\bar{u}$ quarks. In the following table we compare

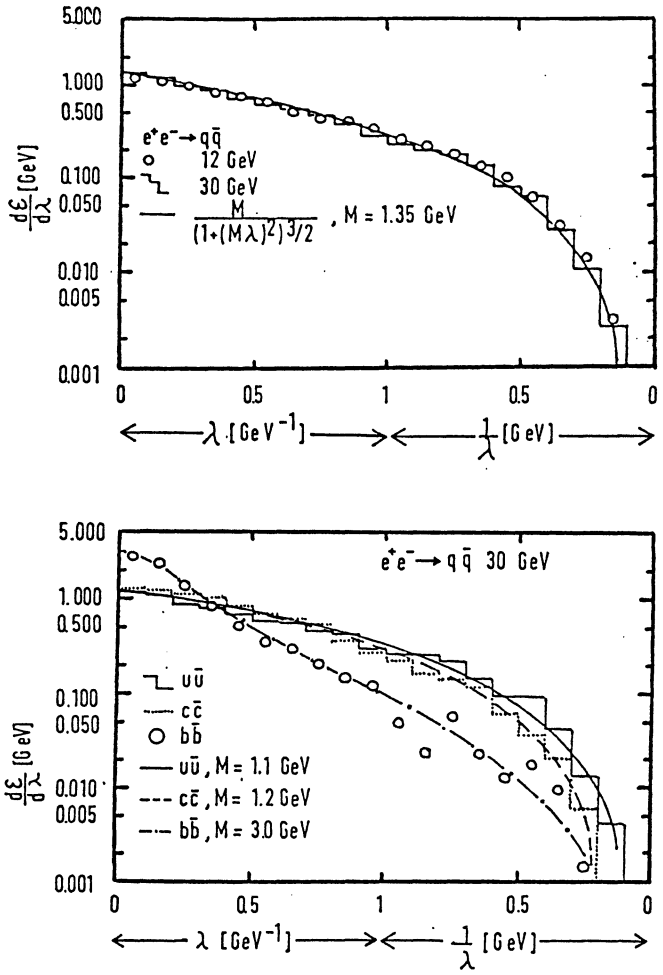

Figure 57. Energy flow distribution for QCD jets including u,d,s,c and b quarks at 12 and 30 GeV cms energies. In the lower part of the figure the energy flow is shown separately for u, c and b quarks. The curves are predictions of the Monte Carlo. For further details see text.

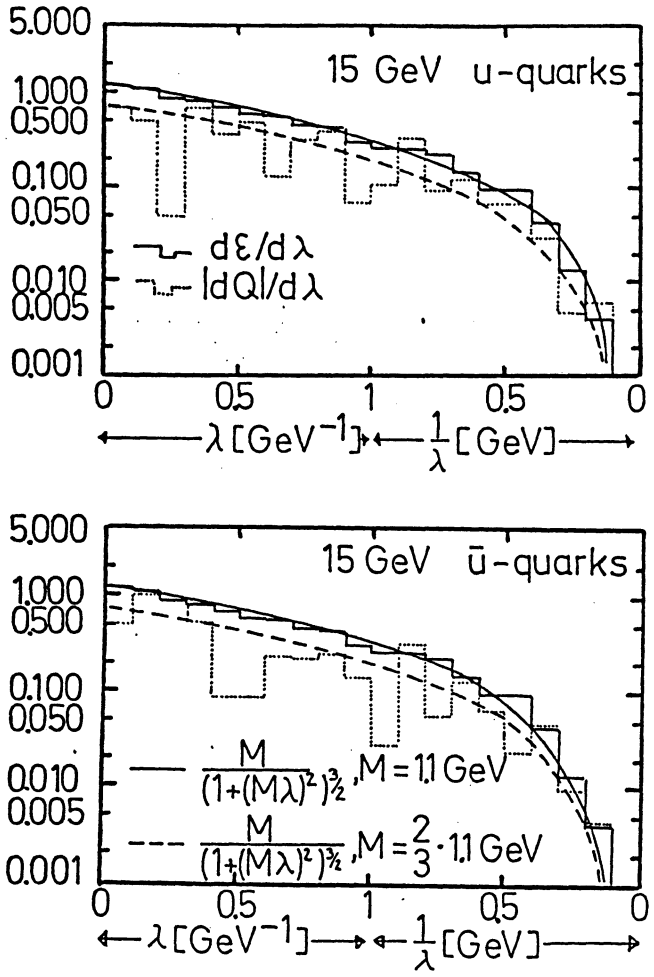

Figure 58. Comparison of energy flow and charge flow for jets from u quarks of 15 GeV energy. The curves are predictions of the Monte Carlo. For further details see text.

$$\int_0^\infty (dQ/d\lambda)_q \, d\lambda = \alpha_q \qquad (2.191)$$

for the different flavours. Note that

$$\int_0^\infty (d\varepsilon/d\lambda)_q \, d\lambda = 1 \qquad (2.192)$$

by definition. These numbers have to be compared with the parameters given in table 9 for different suppressions of s quark production

Table 10

	$\int (dQ/d\lambda)_q \, d\lambda$	α_q for s-quark suppression u:d:s=2:2:1	u:d:s=3:3:1
u	0.59	0.60	0.57
d	-0.56	-0.40	-0.43
s	-0.34	-0.40	-0.43
c	0.52	0.60	0.57
b	-0.32	-0.40	-0.43
$\bar{u}$	-0.56	-0.60	-0.57
$\bar{d}$	0.53	0.40	0.43
$\bar{s}$	0.49	0.40	0.43
$\bar{b}$	-0.52	-0.60	-0.57
$\bar{c}$	0.28	0.40	0.43

From this we see that the measurement of the charge flow gives a direct test of non integer values of the quark charges and may be used to determine the sign of the quark charges.

2.6.10 Models based on overlapping quark jets

Let us now consider the possibility that each incident hadron initiates two independent jets, an incident pion a q- and $\bar{q}$-jet, a proton a q- and a (qq)-jet. One can define models by choosing a function $g(\xi)$ which represents the probability for the quark jet to carry the momentum fraction ξ of the initial hadron. The normalization is $\int g(\xi) \, d\xi = 1$ and we have required the momentum sum rules

$$\int \xi\, g(\xi)\, d\xi = \begin{cases} 1/2 \text{ for pions} \\ 1/3 \text{ for protons} \end{cases} \qquad (2.193)$$

In the following formulae we present 4 cases :

a)

$$g(\xi) = \begin{cases} (1/2)\ (\delta(\xi)+\delta(1-\xi)) & \text{for pion} \\ \delta(\xi) & \text{for proton} \end{cases} \qquad (2.194)$$

b)

$$g(\xi) = \begin{cases} 1 & \text{for pion} \\ (105/16)\ \xi^{1/2}\ (1-\xi)^2 & \text{for proton} \end{cases} \qquad (2.195)$$

c)

$$g(\xi) = \begin{cases} 6\ \xi\ (1-\xi) & \text{for pion} \\ 20\xi\ (1-\xi)^3 & \text{for proton} \end{cases} \qquad (2.196)$$

d)

$$g(\xi) = \begin{cases} \delta(\xi-1/2) & \text{for pion} \\ \delta(\xi-1/3) & \text{for proton} \end{cases} \qquad (2.197)$$

The case (a) corresponds to the stripping quark model by Andersson et al. [81] or approximately to the model by Capella et al. [82]. Here one quark is held back with small momentum and the other quark (or diquark) carries almost the full momentum of the initial hadron. The case (d) is the other extreme limit with an equal partition of momenta. The cases (b) and (c) are in between these extremes, motivated by the two sheet models as studied by de Deus and Jadach [83]. For the angular flow and charge flow in the final state built up by two overlapping jets of charge Q_1 and Q_2 we find

$$\frac{d\varepsilon}{d\lambda} = \int_0^1 d\xi\ g(\xi)\ \left[\rho\left(\frac{\lambda}{\xi}\right)+\rho\left(\frac{\lambda}{1-\xi}\right)\right] \qquad (2.198)$$

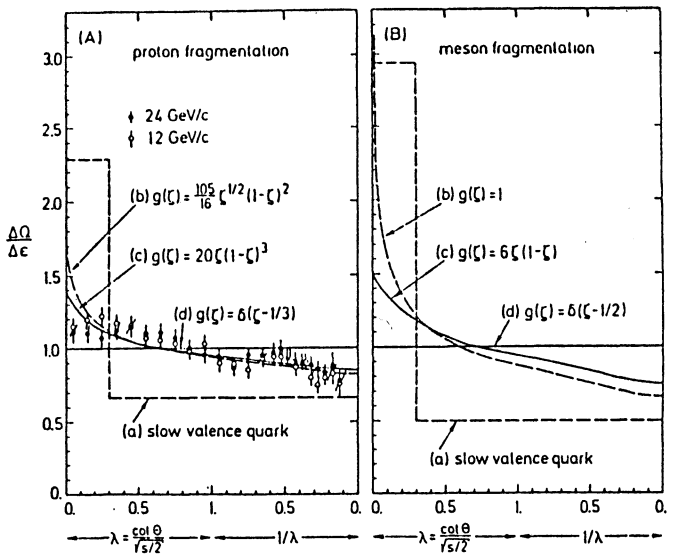

Figure 59. $\Delta Q/\Delta\varepsilon$ for pion- and proton fragmentation predicted by various models with overlapping quark jets. The experimental data are from pp interactions at 12 and 24 GeV/c.

$$\frac{dQ}{d\lambda} = \int_0^1 d\xi\ g(\xi)\ \left[\frac{Q_1}{\xi}\,\rho\left(\frac{\lambda}{\xi}\right)+\frac{Q_2}{1-\xi}\,\rho\left(\frac{\lambda}{1-\xi}\right)\right] \qquad (2.199)$$

where the profile function $\rho(\lambda)$ is the same as given above,

$$\rho(\lambda) = \frac{M}{(1+(M\lambda)^2)^{3/2}} \qquad (2.200)$$

It is important to note here that the angular variable λ must be normalized to the energies of the individual jets. In case of a π^+ the charge of the quark jet Q_1 is given by the average $Q_1 = (Q_u + Q_{\bar{d}}) = \frac{1}{2}$, in case of a proton $Q_1 = \frac{1}{3}\,(Q_u + Q_u + Q_d) = \frac{1}{3}$. The other jet has then apparently $Q_2 = 1 -$

Q_1. We show the results for $\Delta Q/\Delta\varepsilon$ in fig.59. Cases (a) or (b) seem to be a good approximation to reality.

2.6.11 Comparison of quark- and hadron- fragmentation

In the preceeding section we have outlined the physical background for the method which we have applied in this study. We have found a set of scaling laws for the distributions of energy and additive quantum numbers, from which we particularly use

$$\frac{d\varepsilon}{d\lambda} = \rho(\lambda) = \frac{M}{(1+(M\lambda)^2)^{3/2}} \qquad (2.201)$$

$$\frac{dQ}{d\lambda} = Q\,\rho(\lambda) \qquad (2.202)$$

$$\frac{dS}{d\lambda} = S\,\rho(\lambda)\ . \qquad (2.203)$$

On the level of the quark parton picture these equations have been calculated for the fragmentation of free quarks, where the variables are defined as follows :

$$\lambda = \mathrm{cotg}\ \theta/E_{jet} \qquad (2.204)$$

$$\Delta\varepsilon = E(\theta)/E_{jet} \qquad (2.205)$$

$$\Delta Q = \langle Q(\theta)\rangle \qquad (2.206)$$

$$\Delta S = \langle S(\theta)\rangle\ . \qquad (2.207)$$

θ is the polar angle with respect to the jet axis, $\Delta\varepsilon$, ΔQ and ΔS are the energy fraction, average charge and average strangeness emitted into an angular intervall between θ and $\theta + \Delta\theta$. Q and S are the charge and strangeness of the fragmenting quark.

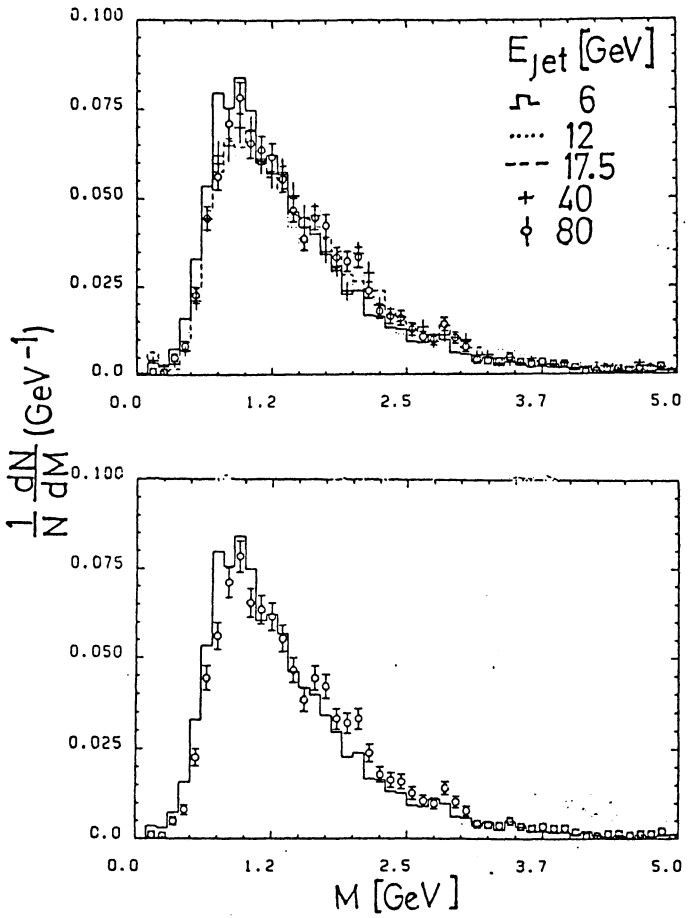

Figure 60. Distribution of the mass parameter M as obtained by fits of expression (2.201) to the energy flow distribution of QCD jets without gluon radiation.

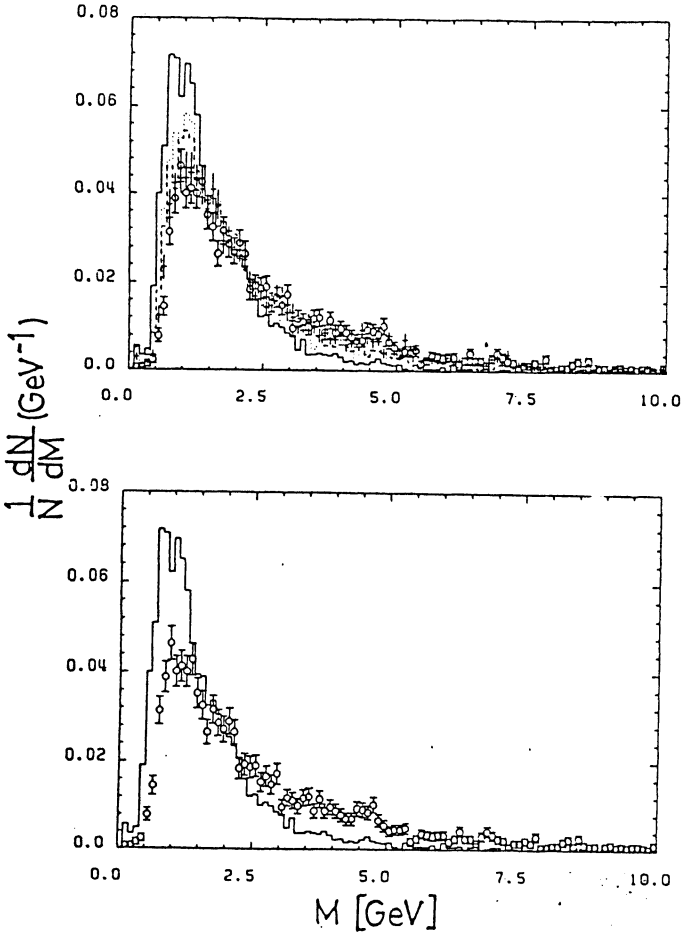

Figure 61. Distribution of the mass parameter M as obtained by fits of expression (2.201) to the energy flow distribution of QCD jets including gluon radiation. The symbols are defined as in fig.60.

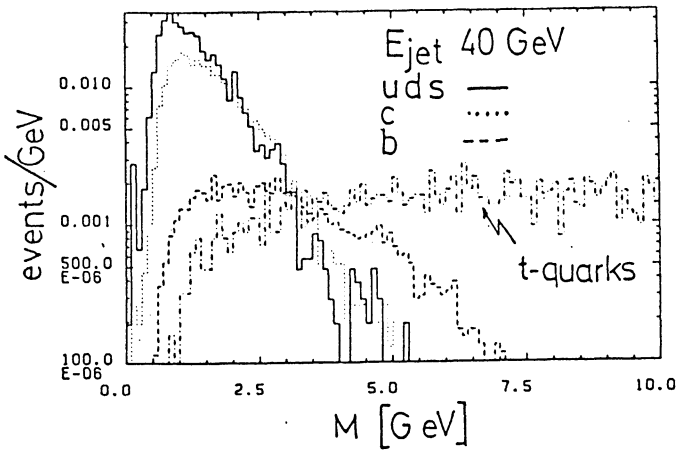

Figure 62. Distribution of the mass parameter M as obtained by fits of expression (2.201) to the energy flow distribution of quark jets at 40 GeV energy.

Some remarks have to be added to the mass parameter M. To this end we have generated hadrons as fragmentation products of u,d,s,c and b jets according to the model of Ali et al. [78]. The $d\varepsilon/d\lambda$-distribution has been fitted for each quark with the energy profile $\rho(\lambda)$ as given above. As output we got the mass parameter M for each fragmenting quark. The distribution of M is shown in fig.60. As can be seen, not only the average value of M is independent of the jet energy, but also the distribution itself scales perfectly. This scaling is of course violated, if one allows the quarks to radiate gluons (see fig.61). The mass parameter M has been interpreted as the average transverse mass (see section 2.6.7). Thus the M-distributions should reflect the same flavour dependence as the distribution of the average p_T of hadrons coming out of the fragmentation. This is shown in fig.62. For u,d and s quarks we observe a very sharply peaked distribution around $M \approx 1$ GeV. Soft hadron collisions are assumed to be produced through the fragmentation of u,d and s quarks only. As has been discussed in chapter 2.6.8, choosing a momentum distribution of the quarks inside the hadron, one can calculate the corresponding energy- and quantum number flow distributions for pion- and proton- fragmentation. In the present version of the program we use a simpler method. We did not go to the quark parton level, but instead we immidiately started at the hadron

level as discussed in chapter 2.6.6. Then Q and S have to be interpreted as the charge and strangeness of the fragmenting hadron and the angle Θ is the polar angle with respect to the beam axis in the c.m.s. The mass parameter M has been adjusted to M = 0.8 GeV, which fits best the data. A program version with overlapping quark jets is also available. The difference in the final state distributions of the hadrons is small at least for beam momenta < 50 GeV/c. For higher momenta it may become necessary to include also di-quark fragmentation.

Another point which has to be discussed here is why we did not use the fragmentation scheme as originally proposed by Feynman and Field. The answer is simply, that it does not fit at that low energies which we are interested in. We instead took the multiplicity of all final state particles as measured by experiments and generated the 4-momenta only by a fragmentation scheme. For much higher energies (>50 GeV) other authors have reported good results using the original Feynman- Field model (or other iterative cascade models like the Lund- model , colour string models e.t.c.).

2.6.12 Summary of inelastic hadron nucleon collisions

We finish the discussion of inelastic hadron-nucleon collisions with a schematic description of the method used in the present version of the program. We stay in the c.m.s. of the two colliding hadrons. Then

1. calculate number of secondary particles and assign mass, baryon-number, charge and strangeness according to the parametrization discribed in 2.6.5 ;

2. generate p_T-values and φ-values (azimuth angle) for all particles, so that the transverse momenta balance exactly in the plane perpendicular to the beam axis. The p_T-distributions are generated according to
$$\frac{d\sigma}{dp_T^2} \sim \exp(-b\ p_T^2) \qquad (2.208)$$
b is tabulated from experimental data.

3. assign λ-values between $\lambda = 0$ and $\lambda = 1/p_T$ according to the three fragmentation equations (2.201) to (2.203), where Q and S are the charge and strangeness of the fragmenting beam or target particle. The mass M is chosen slightly different for pions, kaons and baryons.

4. calculate x-values according to $x = \lambda \cdot p_T$ and $p_L = p_0 \cdot x$.

5. choose a scale factor for the longitudinal momentum conservation. This factor is normally very near to one, because of some sophisticated tricks in the simulation of the λ-values.

2.6.13 Elastic scattering and quasi-two-body reactions

Elastic scattering and quasi two body reactions are generated both in a similar way. The two kinds of reactions can be displayed in the c.m.s. as shown in fig.63. For elastic scattering $m_a = M_1$ and $m_b = M_2$. In case of quasi two body reactions M_1 and/or M_2 can be a stable particle too. The production of the secondaries with masses M_1 and M_2 obeys in both cases

$$\frac{d\sigma}{dt} \sim \exp(-b|t|) \quad , \qquad (2.209)$$

where t is the four momentum transfer in the limits between t_{min} and t_{max}. The slope parameter has been parametrized as

$$b = \begin{cases} 4.225+1.795\ \ln p & \text{for elastic scattering} \\ 4.000+1.600\ \ln p & \text{for quasi-two-body reactions} \end{cases} \quad , \qquad (2.210)$$

where p is the beam momentum in the lab. system. The masses M_1 and M_2 are distributed like

$$P(M) = gc\ [g(M-M_0)]^{c-1}\ \exp\left[-[g(M-M_0)]^c\right] \quad , \qquad (2.211)$$

where M_0 is the threshhold mass

$$M_0 = \sum_{i=1}^{N} m_i \qquad (2.212)$$

and g, c are two parameters which determine the shape of the distribution. They vary for different number of particles and the values in table 11 give a quite good approximation to the experimental observed distributions.

Table 11 Parameter used for simulation of quasi-two-body reactions

N	c	g
2	1.60	2.60
3	1.35	1.80
4	1.15	1.30
5	1.10	1.20

We want to note again that we do not produce real resonances, but instead we use an interpolation through the Breit-Wigner shapes of resonances like ρ, f and g in the 2-pion system or the K*(890) and K*(1420) in the kaon-pion system. The detailed shape of resonances have been observed experimentally in hadron nucleon collisions only. In hadron-nucleus collisions these shapes are totally smeared out (see chapter 2.6.16). In fig.64 we show some mass-distributions for pion, kaon-pion and baryon-pion states. The resonances decay phase space like into 2,3,4 and 5 particles according to experimental data. This method of the quasi two body reactions is used for all 2-particle final states and for a certain fraction of 3- to 7- particle final states, as given in the following table.

Table 12 fraction of quasi-two-body reactions for various numbers of final state particles

$N=N_1+N_2$	fraction [%]
2	100
3	70
4	50
5	30
6	20
7	10
>7	0

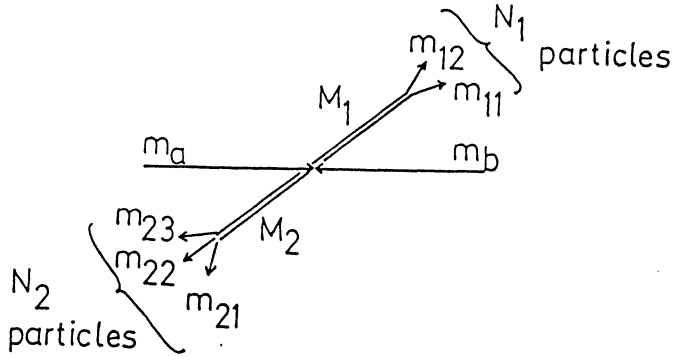

Figure 63. Schematic definition of elastic and quasi-two-body reactions.

We have not referenced all the data we used for this study, because we think that our description has to be improved in any case in future time especially at low energy. On the other hand, as we will see in the next chapter, resonance structures are not seen in hadron nucleus reactions. Thus resonance structures in the effective mass distributions have to be smeared out when going from the free proton to a heavy nucleus. For calorimetric applications this relatively rough description will be shown to be quite adequate also at low energies. We have to express only some warnings when using the program for simulation of hadron scattering on light materials, especially for hydrogen.

2.6.14 Comparison with experimental data

In this chapter we show some comparisons between the Monte-Carlo prediction and experimental data of inclusive particle production for the scattering on free protons. All data come from hydrogen bubble chamber experiments ([63], [69], [84] - [91]). Two main comments can be done already by inspection to figs. 65 and 66. π^+ and π^- spectra in π^+ and π^- induced reactions respectively are expected not to be different in our

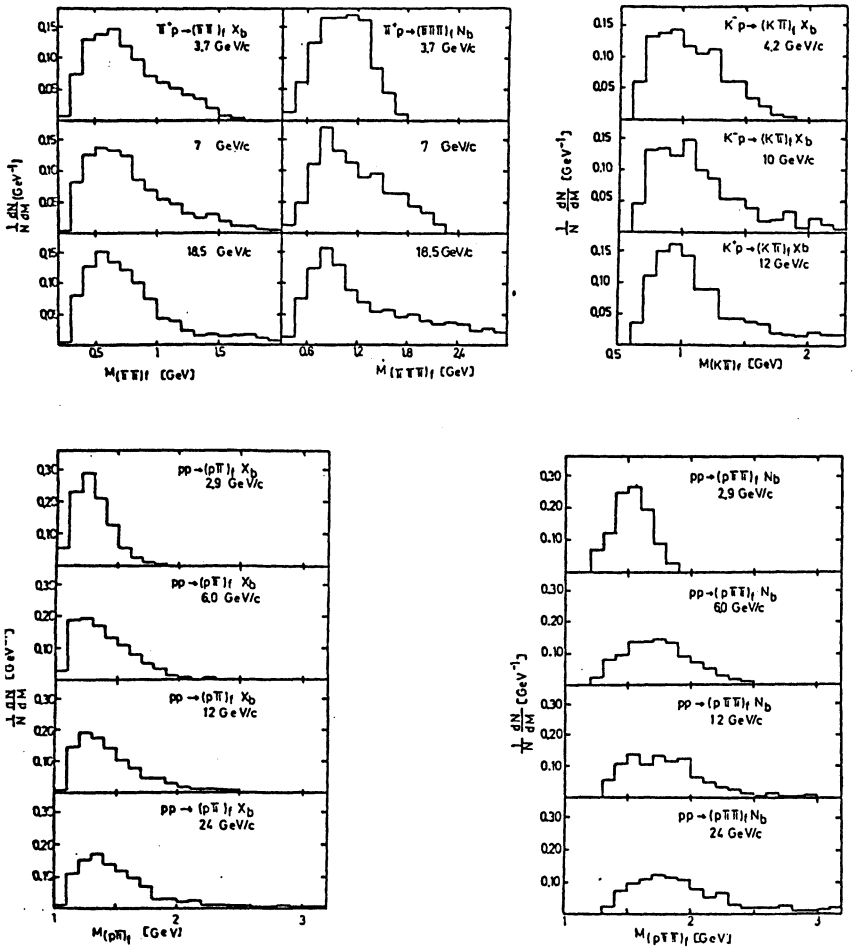

Figure 64. Two- and three- particle effective mass distributions as predicted by the Monte Carlo simulation. The indices b and f refer to the backward and forward hemisphere in the c.m.s.

Monte-Carlo calculation for a fixed beam momentum, whereas the experimental results in fig.65 show significant differences especially in the backward hemisphere, certainly due to the different rate of heavy isobars in both reactions. This indicates already one of the main limitations of our Monte Carlo prediction, which we call the invariance under inclusive charge conjugation. The other comment concerns the forward hemisphere. All parameters used in the generation of secondary particles are finally tuned (see next sections) to describe best the particle spectra in nuclear reactions. Leading particle effects are therefore much more smeared out as it is expected for the scattering on free protons. The Fermi-motion of the target nucleons in the nucleus does not describe alone the nearly total vanishing of leading particle effects for very dense materials. The same comment is valid for π^- spectra in π^+ induced reactions, as shown by an example in fig.67.

The correlation between longitudinal and transverse momentum is generated automatically by use of the λ variable in the simulation discussed in section 2.6.7 to 2.6.12. In fig.68 we have plotted the average transverse momentum squared as function of the x-values. The comparison with experimental data shows a quite good agreement. The transverse momentum distributions have been tuned to fit exp. data at low p_T values (see fig.69 as example), on the other hand they have the tendency to be too much enhanced at very high transverse momenta, as can be seen in fig.70. This is a kinematical reflection of the smearing of leading particles in the longitudinal direction as discussed above. As a further example we show in fig.71 rapidity distributions for pions, kaons, protons and lambdas in pp interactions at 12 GeV/c.

It has been suggested [92] that the cross sections may be a universal exponential function of the transverse mass $m_T = \sqrt{m^2+p_T^2}$. In fig.72 we plot logarithmically the Lorentz- invariant cross section for the Monte Carlo results of fig.69 with a superposed eye ball fit line.

From these and a lot of other comparisons we concluded, that within the two limitations discussed above the description of the scattering on free protons is quite satisfactory. Of course it is possible to tune some parameters in order to fit these interactions much better. But we do not expect that somebody will use the program for the simulation of hydrogen bubble chamber experiments.

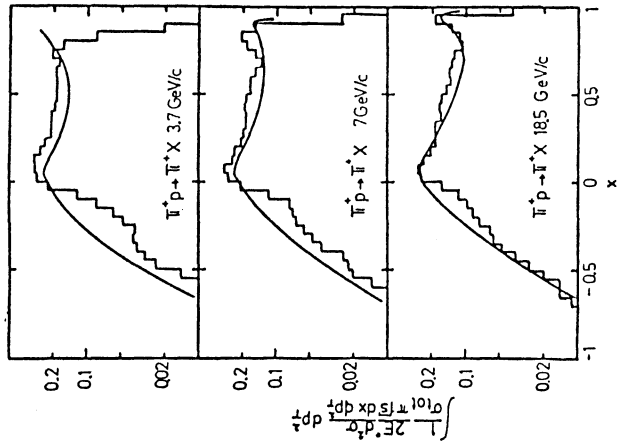

Figure 65. Distribution of the Feynman variable x for positive pions produced in π^+p interactions. The histograms are the results of the Monte Carlo. The curves represent eye ball fits through experimental data.

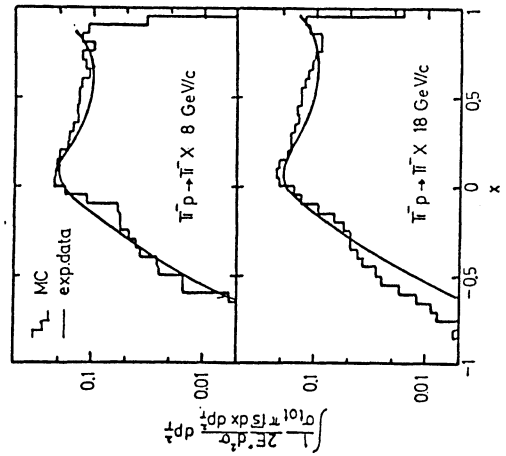

Figure 66. Distribution of the Feynman variable x for negative pions produced in π^-p interactions. The histograms are the results of the Monte Carlo. The curves represent eye ball fits through experimental data.

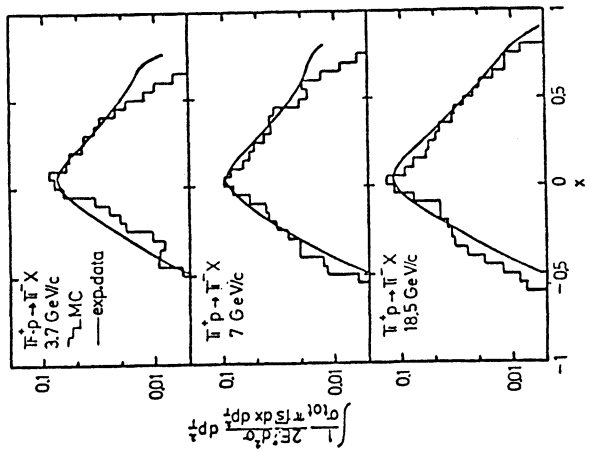

Figure 67. Distribution of the Feynman variable x for negative pions produced in π^+p interactions. The histograms are the results of the Monte Carlo. The curves represent eye ball fits through experimental data.

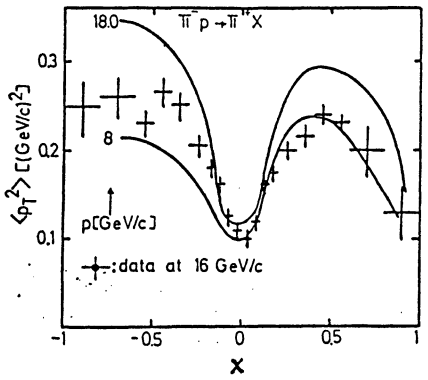

Figure 68. Average transverse momentum squared as function of the Feynman variable x. The curves are the results of the Monte Carlo. The crosses represent experimental data at 16 GeV/c beam momentum.

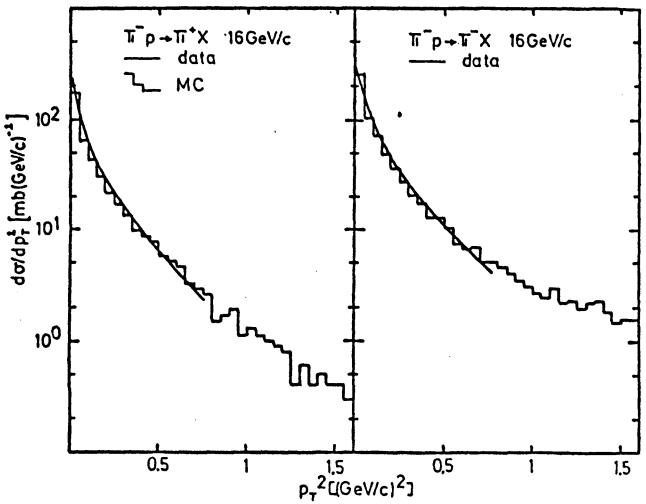

Figure 69. Distribution of the transverse momentum squared for pions produced in π^-p interactions. The histograms are the results of the Monte Carlo. The curves represent eye ball fits through experimental data.

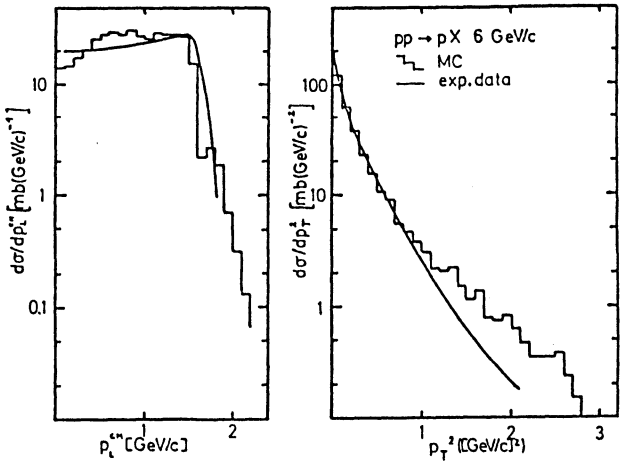

Figure 70. Distribution of the longitudinal momentum and the transverse momentum squared for protons produced in pp interactions The curves represent eye ball fits through experimental data. The histograms are the results of the Monte Carlo.

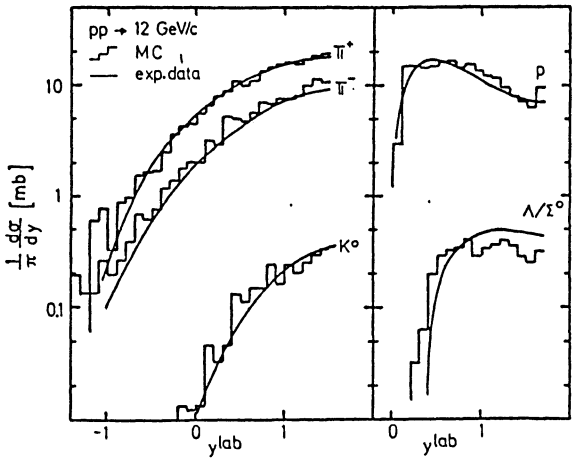

Figure 71. Rapidity distributions for pions, kaons and lambdas in pp interactions at 12 GeV/c momentum. The histograms are the results of the Monte Carlo. The curves represent eye ball fits through experimental data.

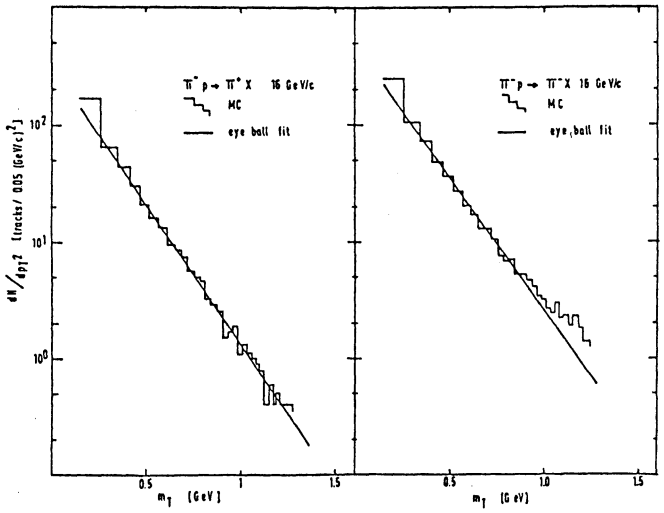

Figure 72. Distribution of the transverse mass for positive pions produced in π^-p interactions. The curves represent eye ball fits through experimental data. The histograms are the results of the Monte Carlo.

2.6.15 The intra-nuclear cascade

In high energy hadron nucleus collisions, to a good approximation the nucleus can be considered as a dense collection of nucleons. The nuclear structure, correlations between nucleons e.t.c. can be ignored. This follows from the fact that the wavelength of the incident particle is much smaller than the nuclear radii and the characteristic times of hadronic interactions are much shorter than nuclear periods. In nuclear matter pions have an absorption length of ~ 2.7 fm and protons ~ 2 fm, small compared to, say, the uranium nucleus (diameter ~ 14 fm). But it is of course not clear, that the particles do already exist as real particles inside the nucleus. For the space time development of the interaction two extreme cases can be considered. The first model is based on the assumption that the asymptotic final state in a hadron nucleon collision is created in a distance ≦ nucleon size. After approximately one mean free path the

incident hadron will interact with one of the nucleons inside the nucleus and produce $\langle n\rangle_p$ hadrons, each of them will, after another mean free path, interact with a downstream nucleon in the nucleus and, as a result, an intranuclear cascade will develop. The final number of particles leaving the nucleus is then given by

$$\langle n\rangle_A \approx \langle n\rangle_p \, A^{1/3} \quad . \tag{2.213}$$

Suppose, on the other hand, that in the initial hadron nucleon interaction the asymptotic hadrons are not created until distances » nuclear radius. After the first collision an exited hadronic state will be produced with properties most likely similar to that of the incident particle. Here we get

$$\langle n\rangle_A \approx \langle n\rangle_p \quad . \tag{2.214}$$

Experimental data show that the truth lies somewhere between these extreme cases. Very losely speaking, one can say, that particles backward produced in the c.m.s. of the first collision, do make an intranuclear cascade, whereas the forward produced particles do not. This fact can be explained quite naturally in more sophisticated models like multiperipheral chain models [93] or the energy flux cascade model [94]. Our description is closely connected to the second model, but only as a guide, because the most important quantities are given to the program in form of parametrizations. According to chapter 2.6.1 the reactions are divided into coherent elastic and inelastic. The coherent elastic reaction will be discussed in a later section. The inelastic reactions can be further divided into quasi-elastic and incoherent inelastic, depending on whether the first (primary) interaction of the incoming hadron with a nucleon of the nucleus is an elastic or inelastic one. The first interaction is exactly generated as it was discussed in previous sections. The forward produced particles are not further affected. This made it necessary to smear out the leading particle spectra (see the comments at the end of the previous section). The backward produced particles undergo a further intranuclear cascade. The average number of additionally produced particles is parametrized by the formula

$$\langle n_{add}\rangle = \alpha(s)\ (A^{1/3}-1)\ 2n_b \quad , \tag{2.215}$$

where n_b is the number of backward produced particles in the primary interaction, α given by the very slow varying function

$$\alpha(s) = 0.312 + 0.200\ \ln(\ln s) + 0.00017\ s^{1.5} \quad . \tag{2.216}$$

These formulae should not reflect any theoretical ideas, they are just parametrizations. The actual number n_{add} is Poisson distributed around

$\langle n_{add} \rangle$. Pion and nucleon masses are assigned to each of the additionally particles. At very low energy of the incoming hadron the production of further pions is strongly suppressed, whereas in the limit of high energies 30% nucleons and 70% pions seems to be a good approach to experimental data. The charges of the pions are generated randomly, whereas neutrons and protons are produced with a rate according to the neutron/proton ratio of the nucleus. Some further corrections have been applied in order to fit best experimental data.

A very similar method as that discussed in chapter 2.6.5 to 2.6.12 is used to generate the four momenta of final state particles of the intranuclear cascade. The basic formulae (2.201), (2.202) and (2.203) are applied to distribute energy, charge and strangeness in the angular intervall λ. The summarizing chapter 2.6.12 can be copied without changes.

The production of quasi two body final states in the first interaction is strongly suppressed. This can be seen by inspection to fig.73, where the inclusive lab. momentum distributions of neutrons and lambdas for proton scattering on protons and on copper are compared with each other [70]. The very clear signal at $p \approx 24$ GeV/c of the reaction $pp \rightarrow n\,\Delta^{++}$ is not seen in the scattering on copper. This justifies our very approximative description of these reactions as it was discussed in chapter 2.6.13.

As we have seen, a natural extension to that used for hadron nucleon interactions has been used for the description of secondary particles in inelastic nuclear interactions. And actually the same routines do the job for both reactions.

2.6.16 Nuclear evaporation

The particles produced by the method discussed in the previous chapter corresspond to those, which are interpreted as shower particles (mainly mesons and leading baryons) and grey track particles (nucleons from cascading process) in the phenomenology of nuclear interaction physics. The characterizing production time for these particles is in the order of the strong interaction time of 10^{-24} sec. After the interaction the nucleus remains in a high exited state and emits further nucleons, low mass fragments like d,t, and α particles and also high mass fragments. These particles are called black track particles. The kinetic energy is very low ($\leq$ 20 MeV) and the angular distribution is isotropic in the laboratory system, which shows, that the kinematic is not correlated to the nuclear cascading process. On the other hand the number of produced black track particles is nearly proportional to the number of emitted grey track particles

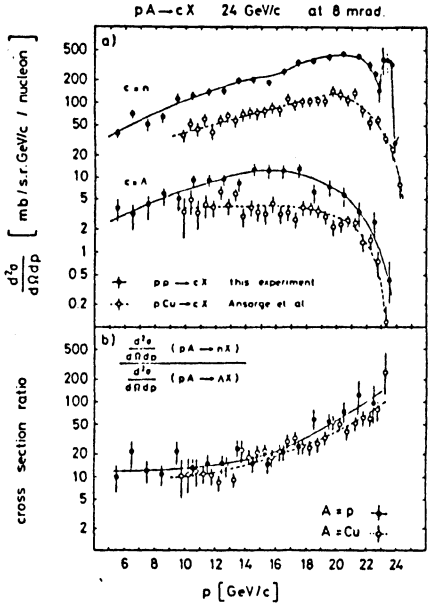

Figure 73. Comparison of lab. momentum distributions for neutrons and lambdas produced in pp and pCu interactions.

$$\langle n_b \rangle = 1.50 + 1.35\, n_g \quad , \tag{2.217}$$

which may reflect the fact that the more unordered the nucleus is left after the interaction, the more particles are emitted in the following evaporation process. The production of the black track particles is under control of a cut-off parameter, which may be chosen to 1 MeV as lower limit for the kinetic energy. In normal applications with layers of dense material of the order of a few centimeter thickness the black track particles will be absorbed in the first step from the creation point before entering a sensitive counter device. In that case a cut-off parameter of E_C = 20 - 50 MeV will be adequate. For certain other applications like very fine sampling calorimeter or background studies in high precision chambers a very small cut-off parameter may be necessary. The total amount of kinetic energy spent to all particles of the nuclear evaporation is in first approximation

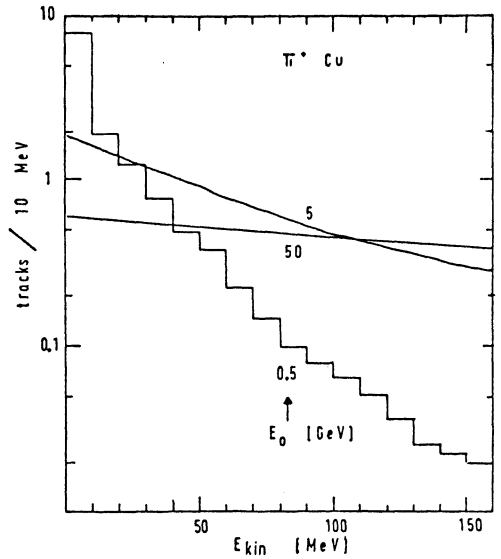

Figure 74. Distribution of kinetic energy in pion copper scattering as predicted by the Monte Carlo.

$$E_{eva} = F(A)\ G(E_k)$$

$$F(A) = \begin{cases} (A/120)\ e^{-A/120} & \text{for } A \leq 120 \\ 0.368 & \text{for } A > 120 \end{cases} \qquad (2.218)$$

$$G(E_k) = 7.716\ a(E_k)\ \exp[-a(E_k)]$$
$$a(E_k) = 0.35 + 0.13 \cdot \ln(E_k)$$

with a fluctuation depending also on the atomic number A and the kinetic energy E_0 of the primary particle. These formulae should not be taken too serious. They are used only as a starting value in the simulation of the nuclear evaporation. Phase space limitations and the energy momentum balance (see next chapter) may lower these values, especially at low energies. As an example we show in fig.74 the kinetic energy distribution of black track-, grey track- and shower- particles combined for π^+ Cu interactions at 0.5, 5 and 50 GeV. For energies E_0 of the primary particle $\geq$ 2 GeV the distribution is nearly energy independent. For much lower primary energies phase space effects shift the distributions to the lower edge. In

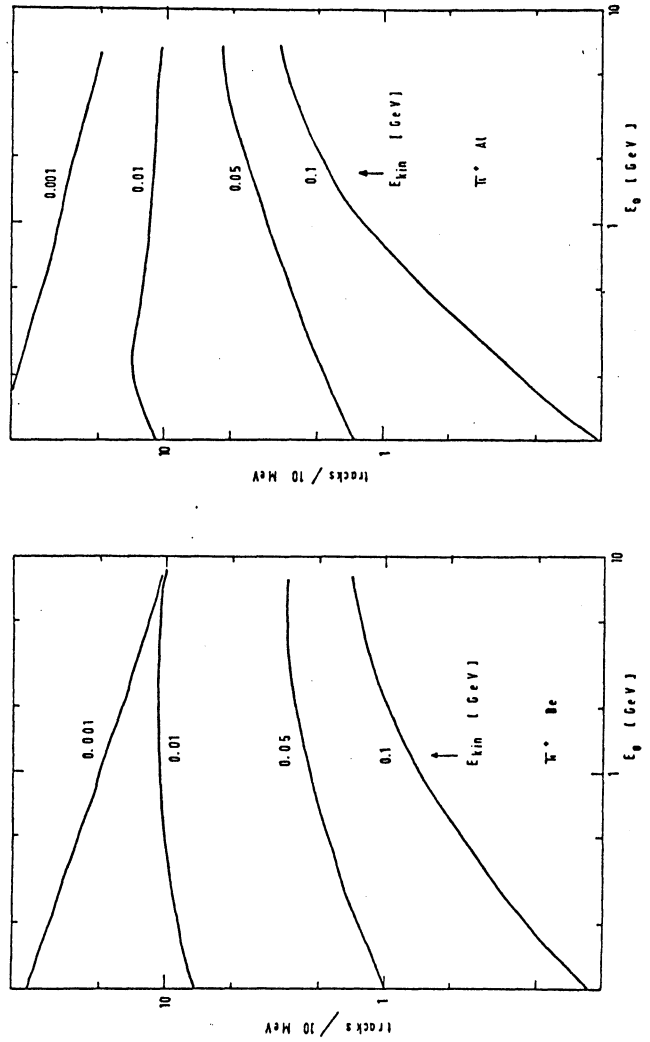

Figure 75. Production rates of particles with 0.001, 0.01, 0.05 and 0.1 GeV kinetic energy as function of the energy of the primary pion scattered on Be, Al, Cu and Pb. The curves are only to guide the eyes.

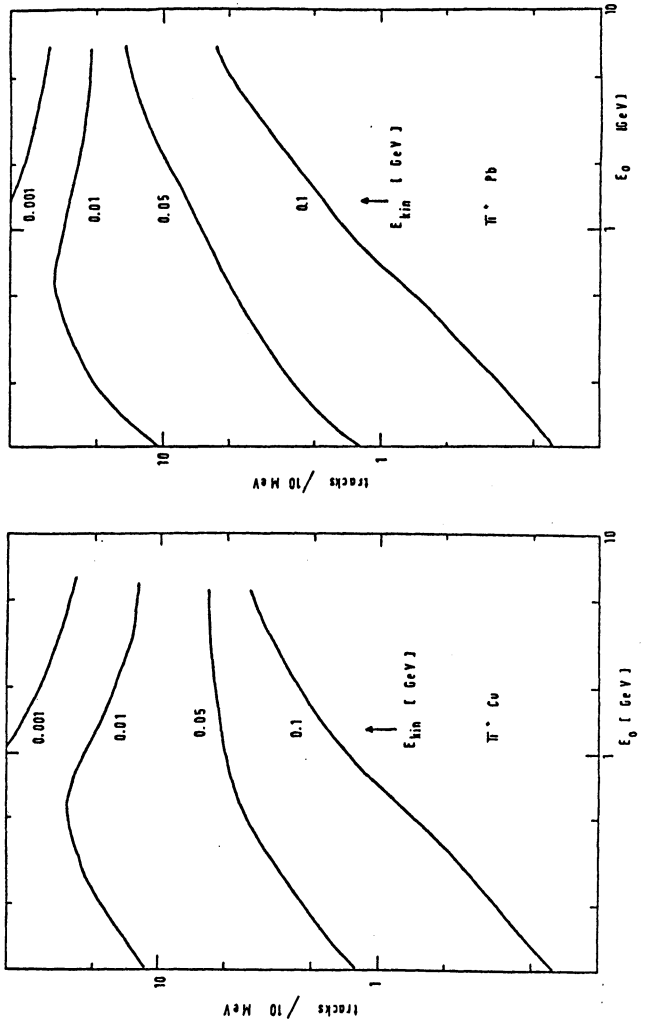

Figure 75. Production rates of particles with 0.001, 0.01, 0.05 and 0.1 GeV kinetic energy as function of the energy of the primary pion scattered on Be, Al, Cu and Pb. The curves are only to guide the eyes.

fig. 75 we observe that this energy independence holds for secondary kinetic energies ≧ 20 MeV, whereas for very low energies (E_{kin}=0-5 MeV) a strong energy dependence is observed. The kinetic energy distributions do also not vary significantly with the atomic number. For Al (and of course for even lower A-values) the rate of grey track- and black track- particles goes down and approach the limit of zero for hydrogen.

2.6.17 Energy-momentum-balance

In each inelastic interaction the total energy and momentum of the initial hadron and of the total final state system are different. Various effects like Fermi motion of the nucleons inside the nucleus, binding energies and cut-off energies due to the potential of the nucleus, instability of the nucleus after the cascading process e.t.c. are responsible for that nonconservation of total energy and momentum.

We repeat first the main steps for the production of final state particles in case of a nuclear interaction:

1.) Take some energy ΔE_{eva} of the kinetic energy E_0 of the primary particle, which is spent later to exitation and nuclear evaporation; reduce the kinetic energy of the incoming particle ($E_0 \rightarrow E_0'$);

2.) apply smearing of the kinetic energy E_0' of the incoming particle due to Fermi motion of the target nucleon;

3.) simulate primary interaction conserving momentum and total energy;

4.) simulate nuclear cascade; smear out kinetic energies E_f of final state particles due to Fermi motion; subtract the binding energies according to the nuclear potential;

5.) generate particles from nuclear evaporation; take the energy ΔE_{eva} from step 1.) as first approximation and emit eventually some further energy depending on the instability of the exited nucleus.

As can be imagined from these steps, there are a lot of tunable parameters in this simulation procedure. Nuclear scattering data are not sensitive enough to fit all these parameters. The cut-off energies due to experimental limitations are normally in the order of 20 MeV, so that a certain amount of kinetic energies is not measured at all. Neutrals can be measured only in very specific detectors. Particle separation is only possible in the very low momentum range. Therefore all the parameters belonging to the simulation of the energy momentum balance had to be fitted using

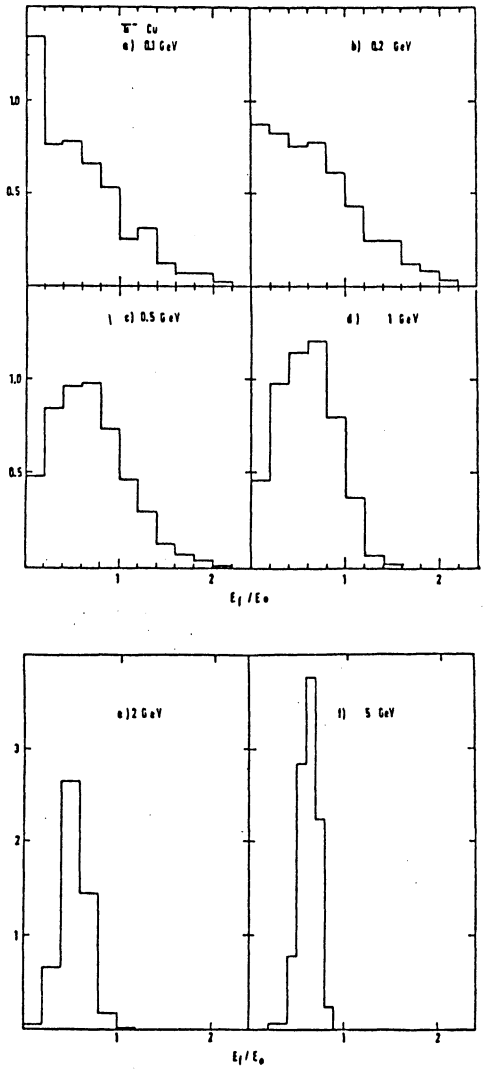

Figure 76. Sum E_f of kinetic energies of all final state particles for π^-Cu interactions at primary energies E_0 from 0.1 to 5 GeV.

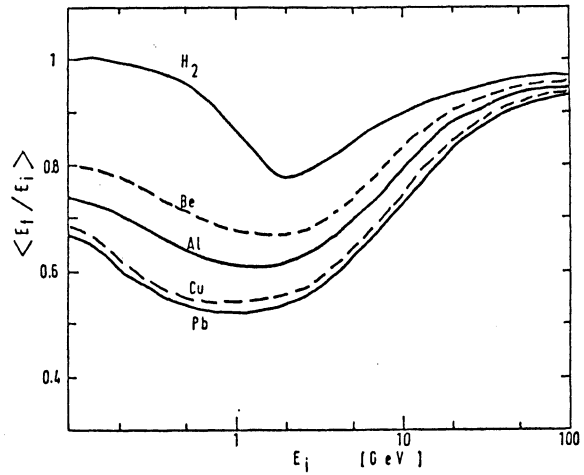

Figure 77. Mean value for the total kinetic energy E_f as function of the primary energy E_i for pion scattering on H_2, Be, Al, Cu and Pb. The curves are only to guide the eyes.

data from calorimetry. This means that the total pulse height and the energy resolution for calorimeter is not at all a prediction of the program, but an overal fit to all existing calorimeter data. This will be discussed further in chapter 5.3. The results of this tuning procedure are shown in figs. 76, 77 and 78.

In the first of these figures we show as example the sum E_f of kinetic energies of all final state particles for π^- Cu interactions at primary energies from 0.1 to 5 GeV. Note that for $E_i \leq 1$ GeV the total energy of all final state particles may be bigger than the kinetic energy $E_i$of the incoming particle. This has important consequences in calorimetry, as we will see in chapter 5. The mean values and the r.m.s. of these distributions are shown in figs. 77 and 78. The same plots are shown also for H_2, Be, Al and Pb as target nuclei. The left part of the distribution for $E_i \leq 0.5$ GeV is dominated by low energy nuclear reactions and quasi-elastic scatterings followed by evaporation. Kinetic energy is lossed by binding effects and self-absorbtion of particles inside the nucleus. These reactions alone would lead to an energy independent loss of kinetic energy and the ratio

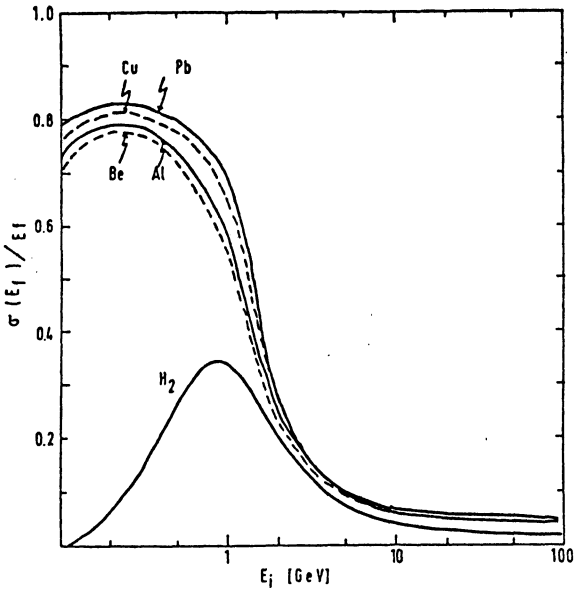

Figure 78. R.m.s. for the total kinetic energy E_f as function of the primary energy E_i for pion scattering on H_2, Be, Al, Cu and Pb. The curves are only to guide the eyes.

E_i/E_f would approach 1 at approximately $E_i = 1$ GeV. For $E_i \geq 0.5$ GeV the opening of further high energy reaction channels is observed. Here a lot of kinetic energy is converted to rest-masses. In the high energy limit the production of further particles has a logarithmic dependence. So the ratio E_i/E_f should approach 1 for $E_i \to \infty$. The results of fig.77 will be later directly connected with the total pulse height measured in calorimeter and the results of fig. 78 with the corresponding energy resolutions.

We want to note again at the end of this chapter, that the details of the simulation of energy momentum balance is much more complicated as has been discussed here. But we have no physical arguments for all our doings. The parameters have been tuned to fit calorimeter data. Especially we do not know exactly, what is really physics in the data of the previous figures. There may be also some reflections of systematic errors of the calorimeter data.

2.6.18 Coherent elastic scattering

The rate of the coherent elastic scattering is taken from the difference of the total and inelastic cross sections, as parametrized in chapter 2.6.2. The differential cross sections may be expressed by the well known formulas

$$\frac{d\sigma}{d\Omega} = \left(\frac{d\sigma}{d\Omega}\right)_0 F^2(\theta) \qquad (2.219)$$

$$\left(\frac{d\sigma}{d\Omega}\right)_0 = (KR_0^2)^2 \left[\frac{J_1(2KR_0\sin\theta/2)}{2KR_0\sin\theta/2}\right]^2 , \qquad (2.220)$$

where K is the wave vector of the incident particle, R_0 the nuclear radius and Θ the scattering angle. A diffuse nuclear surface is accounted for by e.g.

$$F(\theta) = \exp(-K^2\Delta^2\sin^2\theta/2) \quad . \qquad (2.221)$$

These formulae are certainly too inconvenient for simulation purposes. An approximation for low scattering angles has been given by ref. [95] :

for $A \leq 62$:

$$\frac{d\sigma}{d\Omega} = A^{1.63} \exp(-14.5\, A^{0.66}\, t\,) + 1.4\, A^{0.33} \exp(-10|t|) \qquad (2.222)$$

for $A \geq 63$:

$$\frac{d\sigma}{d\Omega} = A^{1.33} \exp(-60.0\, A^{0.33}\, t\,) + 0.4\, A^{0.40} \exp(-10|t|) \quad . \qquad (2.223)$$

This formula has been checked to give quite satisfactory results, so we have used it.

2.6.19 Hadron nucleus interactions

There are mainly three types of experiments which have measured data on hadron nucleus interactions: bubble chamber experiments, nuclear emulsion experiments and counter hodoscope experiments. We discuss first the problems of each of these different experiments in order to see the limitations and acceptances.

In bubble chamber exposures one normally places a target plate inside the chamber. One can measure the momenta of all charged particles leaving the target plate. Separation of pions from protons is possible below ≈ 1

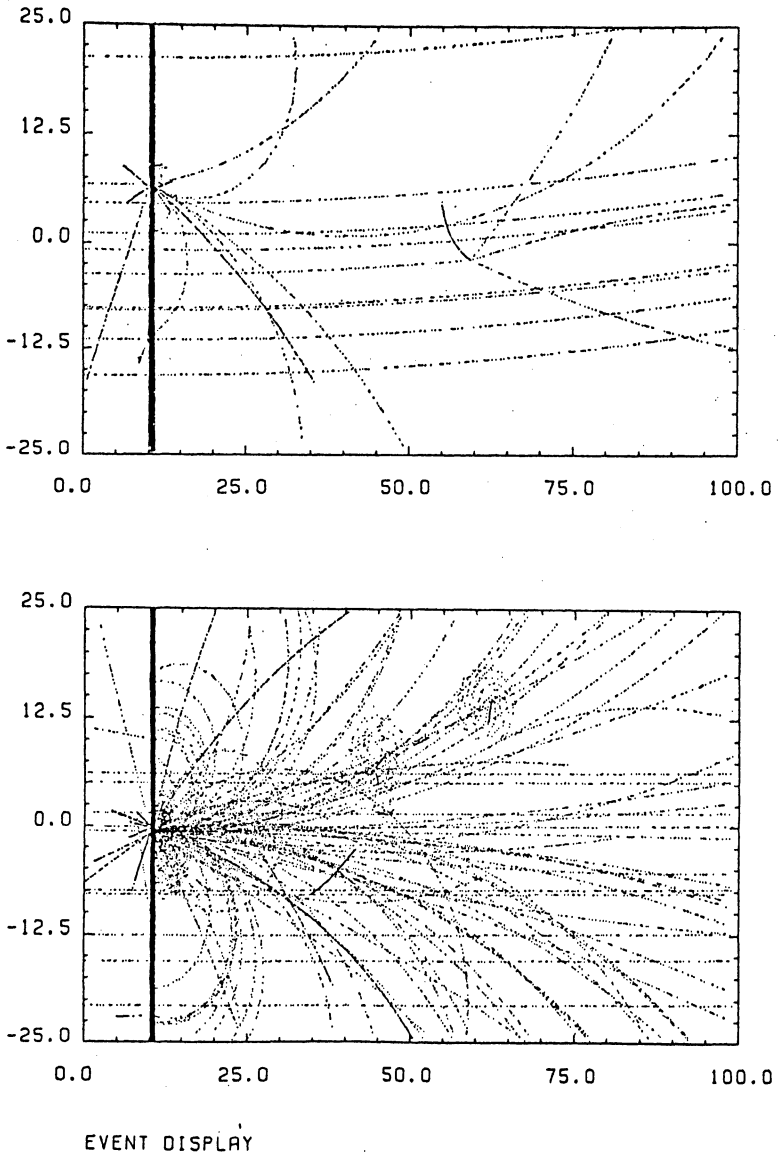

Figure 79. Graphic display of Monte Carlo generated bubble chamber events for π^-Ta interactions at 4 (upper part) and 100 (lower part) GeV/c momentum.

GeV/c momentum by ionization mesurements. Pion/kaon separation has also been reported [61], but that needs a very precise ionisation measurement , which is only possible by use of automatic measuring machines. Neutral pions can not be detected directly, but they are in principle measurable by recontruction of the two electrons from pair production by the photons. Normally the acceptance is very small, so this is limited to the measurement of the π^0-multiplicities. The bubble chamber is a perfect device to measure neutral and charged strange particles by their decay. The measurement of inclusive distributions for neutron production has also been reported [70]. The disadvantage is clearly the lack of statistics and the problems connected with the measurement of very low energy particles ($p \leq 300$ MeV/c) due to the absorption in the target plate and/or the very small path length in the bubble chamber. The target plate must not be too thin, otherwise the number of photographic pictures without any interaction is unreasonable large. The momentum cut-off is not sharp because of the varying thickness which the particles have to pass through the target, due to the point of interaction and the emission angle of the outgoing particle. In fig.79 we show two pictures for π^- Ta simulations at 4 and 100 GeV/c beam momentum respectively in a 1 m hydrogen bubble chamber with a magnetic field of 17 kG perpendicular to the picture plane. The numbers of bubbles per cm have been scaled down by a factor 10, otherwise the bubbles can no more be resolved in such a graphic representation. A look on these pictures shows immediately that this kind of experiment is very powerfull for low energy interactions. Readers which have already experiences in bubble chamber analysis can imagine the problems to measure such pictures at high energies.

The largest fraction of present data is from nuclear emulsion experiments. The observable properties of a track are its range, its ionisation density and its direction. Range measurements are of course only possible for low energy particles, but there is nearly no lower bound. Ranges of a few microns, which corresponds to protons of $\approx$ 1 MeV energy, can be measured. The ionisation density is directly related to the velocity β and is independent of the mass M of the particle (see section 2.2). The measurement of ionisation is not without problems, we refer to ref. [13] for a detailed discussion. From the direction of particles one usually calculates the pseudorapidity, given by

$$\eta = -\ln \mathrm{tg}(\Theta/2) \quad , \tag{2.224}$$

where Θ is the angle with respect to the incoming beam particle. The disadvantage of nuclear emulsion is first of all the lack of information about any A-dependence of particle production. For our simulation purposes we have used always the so called standard emulsion, the Ilford G5 emulsion, the atomic composition was given in table 5. The second disadvantage is as

in bubble chamber experiments, that the complications in data processing do not allow high statistic expermiments.

Counter experiments with suitable chosen Cerenkov counters and TOF-measurements do not have any problems in statistics, they can measure momenta by deflection in magnets and emission angles as good as bubble chambers and emulsions, particle separation is of the same order of accuracy as in the other types of experiments. The main problem is here, that any correlation measurement makes an unresonable effort in the experimental apparatus necessary. Normally one uses a single arm detector, so that only single particle distributions and multiplicities can be measured.

For our comparisons of the Monte-Carlo simulations with experiment we have used the data from ref. [96] to [102]. We will present the comparisons in the following order. First we discuss the multiplicities of the so called shower particles, which are mainly mesons and also leading baryons in baryon-induced reactions and are defined by having a velocity β greater than a value β_s = 0.7 - 0.85 depending on the choice of the authors of the specific experiment. Then we will come to the production of non-leading protons and other heavy particles, experimentally defined as not beeing shower particles. We discuss also the correlation between shower particle and heavy particle production. At the end we present comparisons for some kinematic quantities of shower particles like kinetic energies, momenta and rapidities. In the following figures we present data as points with error bars and the Monte-Carlo simulation as lines. But the reader should remind that the MC results have statistical errors which are normally only slightly smaller than the errors of the experimental results.

The average multiplicities of π^+ and π^- for bubble chamber data at 2 and 4 GeV/c beam momentum are shown in fig.80 as a function of atomic number A. The decrease of the pion multiplicity with increasing A is fairly well reproduced by the MC-simulation and can be explained by self-absorbtion of low momentum pions in the nucleus. At high energy the MC predicts nearly the same shower particle multiplicity for all incoming particles (see fig.81), whereas in the experimental data they are slightly different. In this plots the shower particles are defined to have velocities greater than β_s = 0.85. The multiplicity distribution in hadron nucleus interactions seems to scale in the same way as in hadron nucleon interactions.. If one excludes the diffractive part and plots $\langle n\rangle\sigma_n/\sigma_{inel}$ vs $n/\langle n\rangle$, data from hadron nucleon and hadron nucleus interactions fall on the same universal curve (KNO-scaling). We do not show that here, because it was one of the main input to the MC program and therefore it must fit by definition. The validity of the KNO-scaling can also be inferred from the linear dependence of the dispersion $D_s = \sqrt{\langle n_s^2\rangle - \langle n_s\rangle^2}$ on $\langle n_s\rangle$ shown in fig.82 for

π^- induced reactions. It should be remembered that for a Poisson distribution $D_s \sim \sqrt{\langle n_s\rangle}$. The distribution of the total number of shower particles per event fits extremely well the experimental data from emulsion experiments at 67 and 200 GeV/c shown in fig.83. We conclude that there seems to be no problem to describe the multiplicities of high energy particles in the intranuclear cascade simulation.

On the other hand it is much more difficult to compare the results for low energy particles, mainly low energy protons from the intranuclear cascade and higher mass particles from the nuclear evaporation, called grey track and black track particles in the language of experimentalists. We start the discussion with proton multiplicities in π^+ and π^- induced reactions at 4 GeV/c beam momentum, measured by a bubble chamber experiment. In fig.84 we compare the momentum distributions of the protons for Be, Cu and Ta as targets. It is seen that there is a experimental momentum cut-off around p ~ 300 MeV/c, due to the absorbtion of particles in the target plate and due to problems in measuring very low momentum particles which have just enough energy to leave the target plate. From a detailed simulation of a bubble chamber exposure, taking into account the thickness of the target plates, the range of particles in the hydrogen necessary for momentum measurement and other minor effects, the proton multiplicities shown in fig.85 have been obtained for π^+ and π^- induced reactions. The shaded area indicates the systematic error in this procedure. It is clear that this systematic error can only be reduced if one subjects the Monte-Carlo data the same off-line analysis chain as the experimental data.

In emulsion experiments all particles with velocities below β_s = 0.7 are defined as heavy particles. In fig.86 we show the distribution of velocity at 7 GeV/c beam momentum for pions, protons and neutrons and heavy particles. It is seen that the cut defined above includes a not negligible amount of pions in the sample for heavy particles. For a cut-off energy of E_c = 2 MeV we got the results shown in fig.87 and 88. In fig.87 the shower particle multiplicity vs the beam momentum is shown for the simultaneous production of less or equal one heavy particle ($N_h \leq 1$), of more than 8 heavy particles ($N_h > 8$) and without any restriction for the production of heavy particles. In the upper part of the figure the dispersion D_s for shower particles and the average number $\langle N_h\rangle$ of heavy particles is shown. The last quantity seems to be nearly independent on the momentum of the incoming particle. Fig.88 shows in more detail the linear dependence of shower particles on heavy particle production at beam momenta from 7 to 200 GeV/c. The increase for N_h = 0 at 7 and 23 GeV/c is significant in both the Monte Carlo and the experimental results. We conclude that the multiplicities of both the shower and heavy particles are described quite

adequate in the MC simulation over a range of beam momenta from 2 to 1000 GeV/c.

We turn now to the distributions of kinematic quantities. Fig.89 shows the average kinetic energy of pions in π^+, π^- and p induced reactions at 4 GeV/c as function of the atomic number A. The apparent discrepancy between MC and exp.data for π^- induced reactions can not be understood. In fig.90 we show for the same exp. data the momentum distributions. Here the simulations fit extremely well the exp. data. The production of particles in the very forward hemisphere is independent of the atomic number, the multiplication of particles takes place in the central and the backward region. This is shown for 50 and 100 GeV/c beam momentum in fig.91 for π^+ and p induced reactions. The exp. data for hydrogen has been aquired by subtraction of data for polyethylene and carbon. This causes of course a big systematic error.

The distribution of the transverse mass m_T was perfectly exponential distributed in hadron- nucleon reactions (see fig.72). This does not hold any more for interactions on higher nuclei, as is shown in fig.92. The grey-track and black- track particles have a different slope as that for the shower particles, so as result we get a pronounced enhancement at very low m_T - values.

The MC simulation has a small bias in the angular distribution for high energy reactions. We demonstrate that with rapidity distributions for p Em reactions at 7, 23 and 67 GeV/c in fig.93. Whereas at 7 GeV/c the distributions looks quite reasonable, from 23 GeV/c onwards a peak at $\eta \approx 2$ develops. This is a reflection from energy momentum conservation in the primary interaction of the nuclear cascade. One has the choice to simulate correctly either the energy momentum conservation or a reasonable smooth angular- and momentum- distribution. Experiences showed that good description of the energy momentum balance is much more important for calorimetric applications (see also chapter 5). We remind the reader in this context that we have used an extremely simple and computer-time saving method for the simulation of the final state phase space distribution. This is by far not a trivial problem for the production of up to 200 particles. The just described bias can also be observed in fig.94, where we compare shower particle multiplicities for various regions of the opening angle in the laboratory system. For the extreme forward region ($\Theta_L <$ 3.5 °) and the backward region (26° < Θ_L < 110°) the simulation fits well the exp. data. Problems seem to come up if one includes also the central region (Θ_L < 26°). From various other checks we have been convinced that there is no other bias in the Monte Carlo calculations.

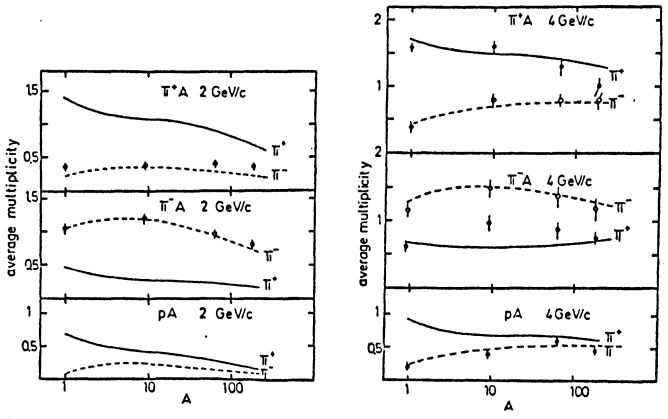

Figure 80. Average multiplicities of pions produced in pion and proton scattering on heavy targets as function of atomic number A.

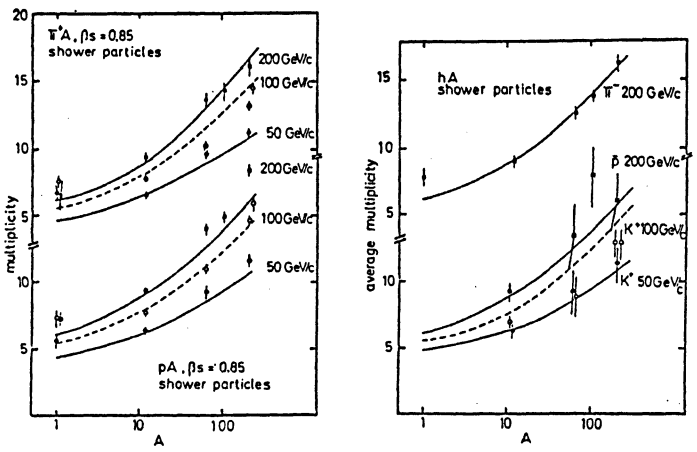

Figure 81. Average multiplicities of 'shower particles' produced in the scattering on heavy targets as function of atomic number A.

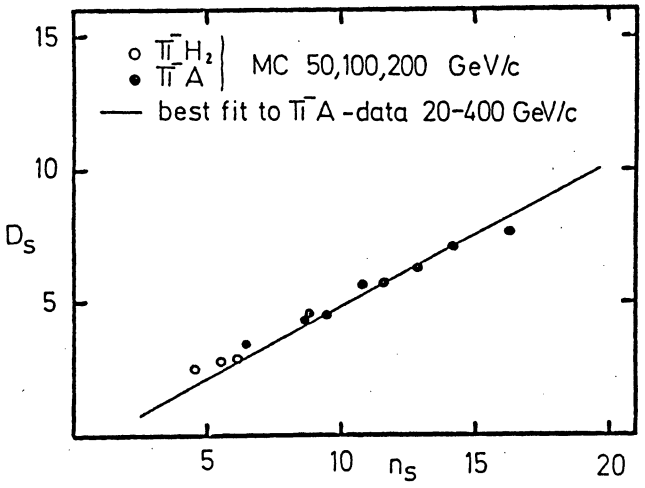

Figure 82. Dispersion as function of the number of produced 'shower particles'. For details see text.

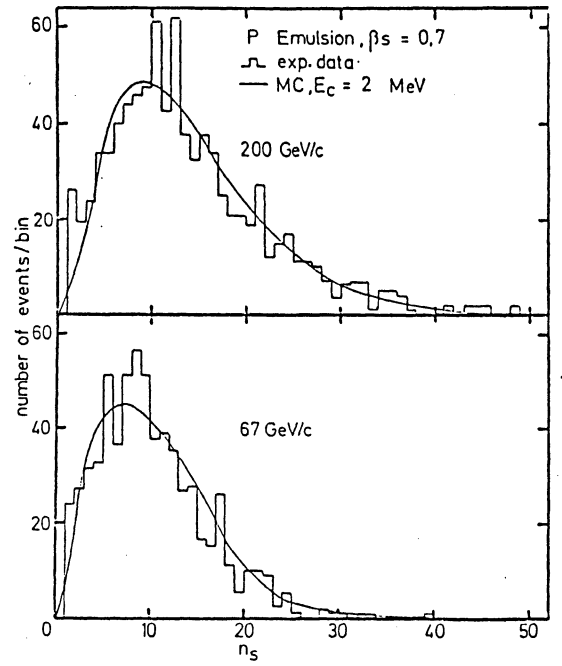

Figure 83. Distribution of number of 'shower particles' produced in proton scattering on emulsion.

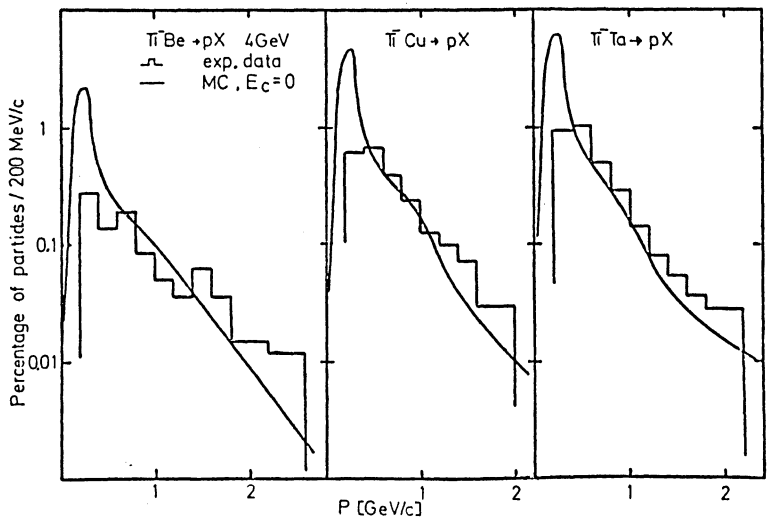

Figure 84. Lab. momentum distribution for protons produced in bubble chamber exposures for π^- scattering on Be, Cu and Ta. For details see text.

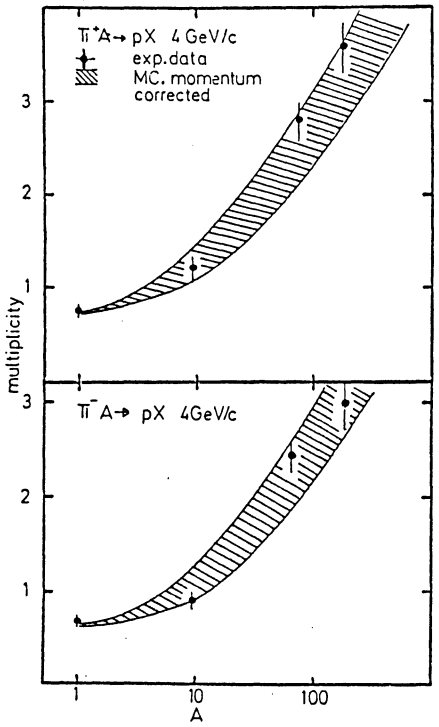

Figure 85. Average multiplicities of protons produced in pion scattering on heavy targets as function of atomic number A. For details see text.

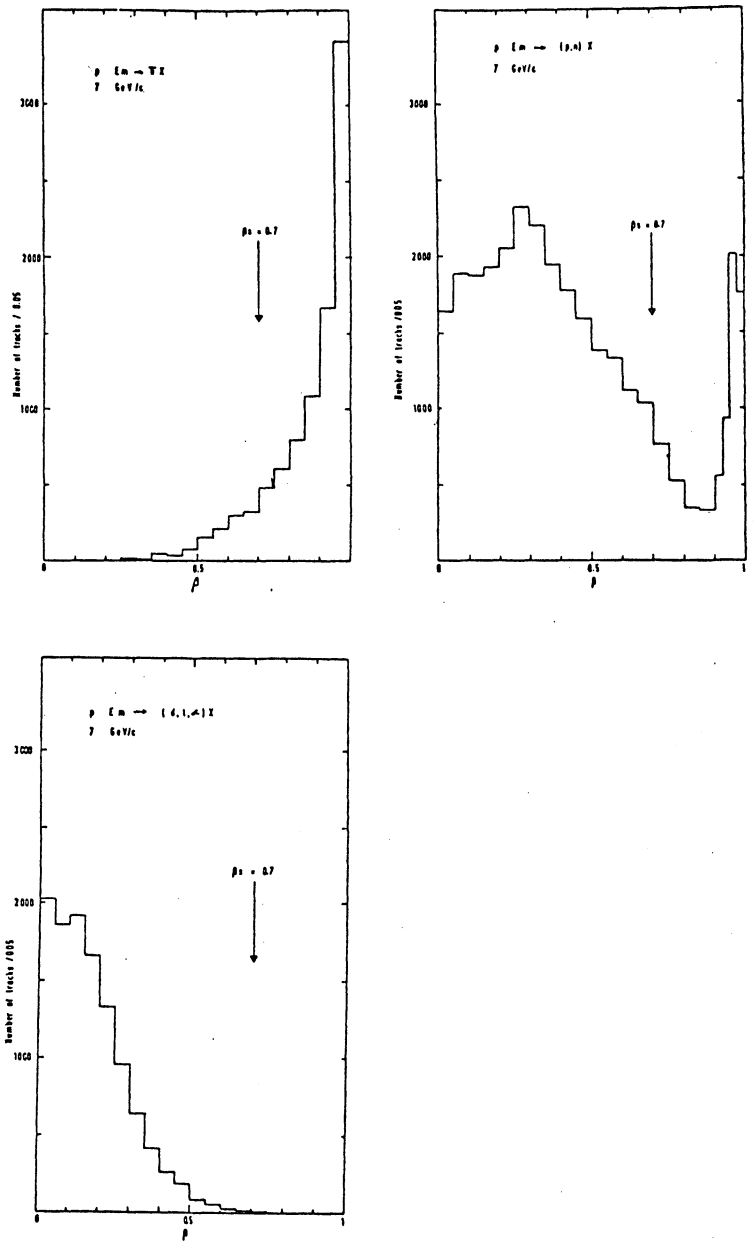

Figure 86. Distribution of velocity for pions, protons, neutrons and heavier particles in p Em interactions at 7 GeV/c beam momentum.

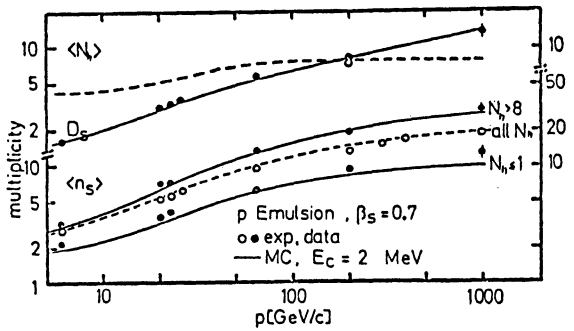

Figure 87. Summary on average multiplicities and dispersions for 'shower particles' in p Em scattering. N_h denotes the number of heavy particles. For details see text.

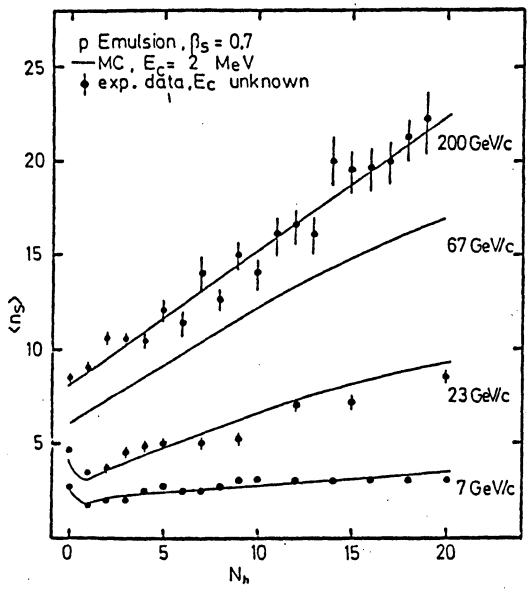

Figure 88. 'Shower particle' multiplicity as function of the number of heavy particles in p Em interactions at various energies.

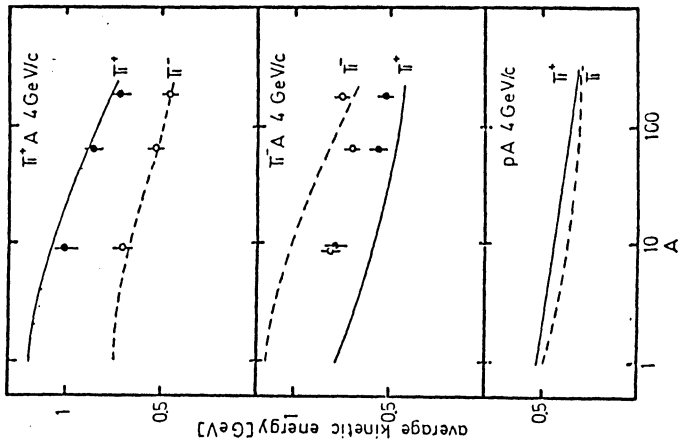

Figure 89. Average kinetic energy of pions in pion and proton induced reactions at 4 GeV/c as function of atomic number A. The curves are the results of the Monte Carlo.

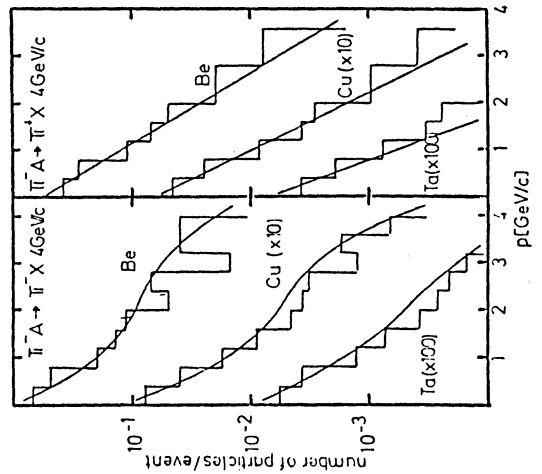

Figure 90. Lab momentum distribution of pions in pion induced reactions at 4 GeV/c. The curves are the results of the Monte Carlo.

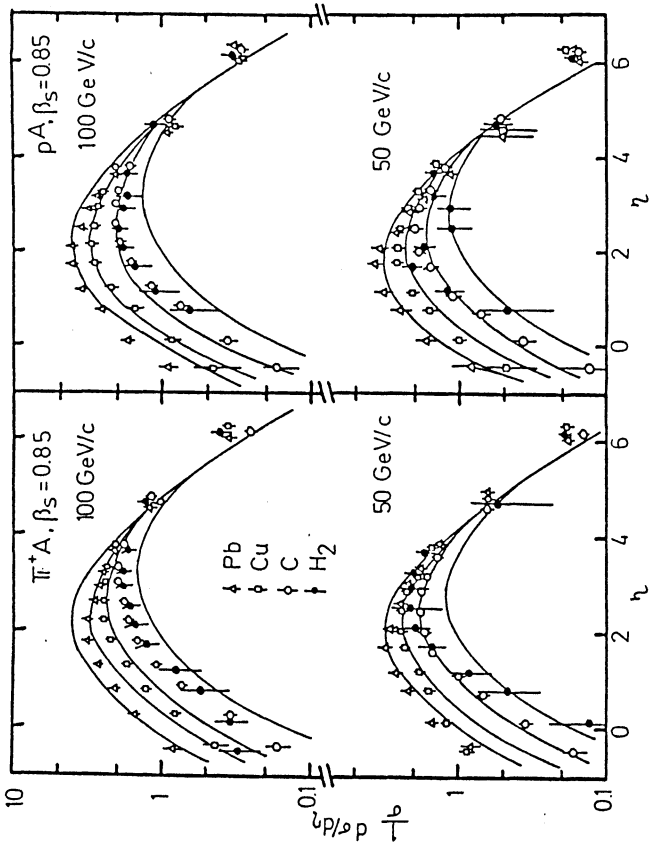

Figure 91. Rapidity distributions for 'shower particles' in pion and proton induced reactions on heavy targets. The curves are the results of the Monte Carlo.

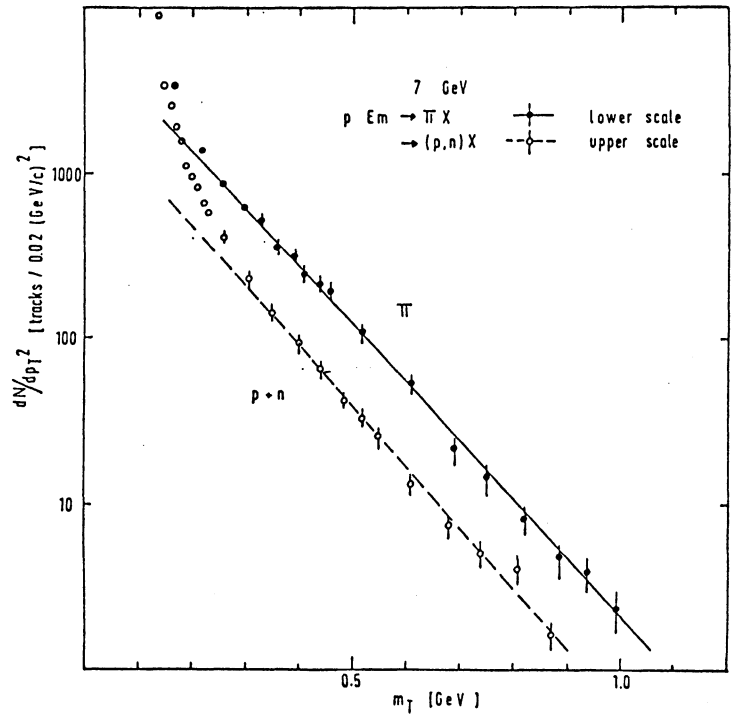

Figure 92. Distributions of the transverse mass for pions and nucleons produced in p Em scattering at 7 GeV/c. The points are the Monte Carlo results, the curves are eye ball fits through the results for $m_T > 0.3$ GeV.

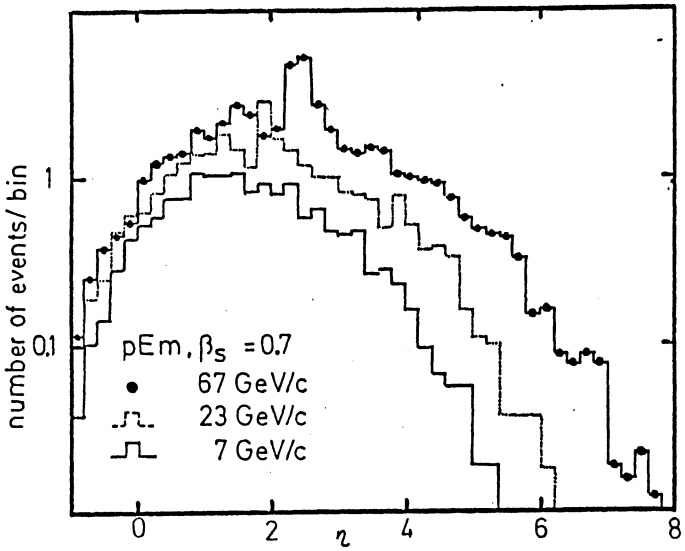

Figure 93. Rapidity distributions for 'shower particles' in proton induced reactions on emulsion. Shown are Monte Carlo results.

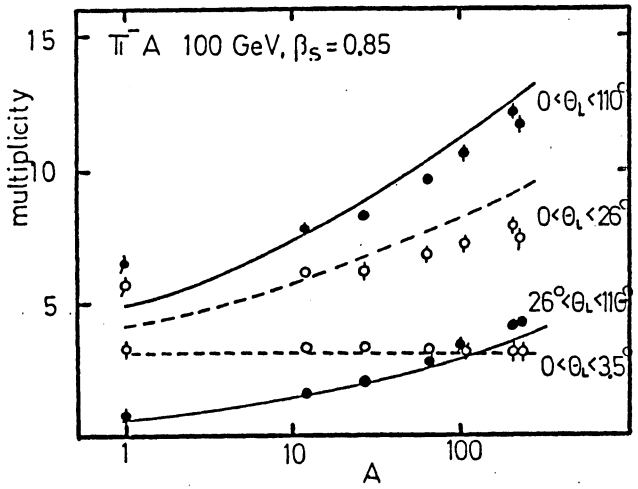

Figure 94. 'Shower particle' multiplicities as function of atomic number A for various regions of the opening angle in the lab. system.

2.6.20 Neutron capture and nuclear fission

The slowing down process for charged particles is mainly determined by the very large cross sections for atomic processes, given in integrated form by the dE/dx formula. Thus a bad description of nuclear processes at very low energies does not play an important role. This does not hold any more for neutrons. In this case the absorbtion is given only by low energy nuclear reactions, nuclear fission and neutron capture. We do not simulate nuclear processes in detail. The elastic and inelastic cross sections are parametrized as discussed in chapters 2.6.2 and 2.6.3, for inelastic reactions below the pion threshhold we use a crude approximation for the production of the final states

$$\begin{array}{l} A\,(\,n,\ \ n'\,)\,A' \\ A\,(\,n,\,2n'\,)\,A' \\ A\,(\,n,\ \ p\ \ \,)\,A' \\ A\,(\,n,\,2p\ \ )\,A' \\ A\,(\,n,\,n'p\,)\,A' \\ A\,(\,n,\,\alpha\ \ \,)\,A' \\ \ldots\ . \\ \ldots\ . \end{array} \qquad (2.225)$$

β activities of the exited nucleus A' have been totally neglected, because the decay is not in time with normal triggers of high energy experiments. Neutrons are slewed down by reactions (2.225) until they are captured by a nucleus. One or two photons with a total of 8 MeV energy are emitted. The first photon is Gaussian distributed around 6.5 MeV with a r.m.s. of 1 MeV and the second photon gets the remaining energy. This procedure fits quite well experimental data (see e.g. ref. [103]).

In fissionable elements the inelastic reaction of neutrons (and of all other particles) may be accompanied by nuclear fission. The fission cross sections for the various uranium isotopes and for plutonium have been tabulated as function of the kinetic energy of the neutron. The exp. data have been taken from ref. [103]. The same cross section depencence holds also for protons [104] and has been assumed to hold for all other strong interacting particles. For elements other than uranium and plutonium we use the parametrization of the A dependence at 3 MeV neutron energy,

$$\sigma_f(3\ \mathrm{MeV}) = -67.0 + 38.7\ Z^{4/3}/A \quad [\mathrm{barn}]\ , \qquad (2.226)$$

which implies that fission occurs only for elements with $Z \geq 90$. Formula (2.226) is adequate for energies $\gtrsim$ 1 MeV, which correspond to a neutron momentum of roughly 50 MeV/c.

In the fission process mainly four steps can be distinguished by their characteristic times :

1.) nuclear interaction with production of 2 heavy fragments ($\tau \approx 10^{-24}$ sec) ;
2.) deexitation of the fragments by neutron emission ($\tau \approx 10^{-14}$ sec) ;
3.) deexitation by photon emission ($\tau \approx 10^{-8}$ sec) ;
4.) deexitation by α-,β- and γ-decay ($\tau > 10^{-6}$ sec).

The ranges of the two heavy fragments are too small to be observed in any experimental device. So we can treat them at rest. The energy spectra of the emitted neutrons have been parametrized as

$$p(E) = e^{-E/0.965} \sinh\sqrt{2.29\,E} \quad , \; E \text{ in [MeV]} \; , \tag{2.227}$$

and the number of emitted neutrons is normal distributed around

$$\langle \bar{\nu}(E_0) \rangle = 2.569 + 0.559 \ln E_0 \tag{2.228}$$

with a r.m.s. of 1.23. E_0 is the energy of the incoming neutron in MeV. This formula is exact for U^{238} and fits approximately the results for other atomic numbers too (see [104]).

The energies of the emitted photons in the third step are given approximately by the distribution

$$p(E_\gamma) = 10 \exp(-1.15\, E_\gamma) \tag{2.229}$$

and the number of produced photons lies somewhere between $\langle n_\gamma \rangle \approx 7$-10 with a r.m.s. of 3. We have assumed the same energy dependence as for neutrons, see formula (2.228) above, so that

$$\langle \nu_\gamma(E_0) \rangle = 9.5 + 0.6 \ln E_0 \quad , \; E_0 \text{ in MeV} \quad . \tag{2.230}$$

These values correspond roughly to a total amount of 7-12 MeV released γ-energy, the average energy for each photon beeing around or even less than 1 MeV. This makes it absolutely necessary to use the EGS-code with a cut-off parameter of $\approx$ 100 keV for photons. Whereas the neutron emission is treated without any time delay, we assume a characteristic time of $\tau = 2.5 \cdot 10^{-8}$ sec for photon emission. This is roughly the same value as that which has been assumed for neutron capture.

As one could think from the previous discussion, the simulation of nuclear fission seems to be a straightforward procedure. This is by far not true.

First of all it requires a very precise simulation of photon showers at extremely low energies. This we think is solved by use of the EGS-code for electromagnetic showers. The main problem lies in the fact, that the number of produced particles in low energy nuclear interactions can not be simulated very exactly in a throughout parametrization for all elements. These numbers may be wrong by 50% for some elements. This failure has no influence in normal applications without nuclear fission, because these particles are absorbed within a few microns and can not transport their energy to other regions of the detector. But they are all able to initiate nuclear fission. This uncertainty may be accounted for by adjusting the fission cross sections for the really generated particles. In other words, the fission cross sections may be increased to get rid of not produced low energy particles. The third problem comes from the moderation of the neutrons. A small bias in the absorbtion of the neutrons may cause a big effect in the total absorbed energy, especially in calorimeters with small radial dimensions, where neutrons can leave easily the detector. For all these problems note that nuclear fission is an endotherme process, so a small bias may cause a big effect by the multiplicative nature of this process. We come back to these problems in chapter 5, where we are going to discuss the application of nuclear fission in uranium calorimeter.

2.6.21 Nuclear interactions for muons

The cross section for inelastic reactions of muons with nuclear matter is very small compared to that for hadrons [105]:

$$\sigma_{\mu N} = \begin{cases} 0.3 \;\; [\mu b] & \text{for } E \leq 30 \text{ GeV} \\ 0.3 \; (E/30)^{0.25} \;\; [\mu b] & \text{for } E > 30 \text{ GeV} \end{cases} \tag{2.231}$$

and is roughly proportional to A :

$$\sigma_{\mu A} = A \; \sigma_{\mu N} \quad . \tag{2.232}$$

The final state particles are generated according to the graph shown in fig.95. All quantities are given in the laboratory system. The differential cross section in terms of the energies E and E' of the incoming and scattered muon and in terms of the emission angles Θ and Φ can be expressed as (see e.g. [106])

$$\frac{d\sigma}{d\Omega dE'} = \Gamma \; (\sigma_T + \varepsilon \sigma_S) \tag{2.233}$$

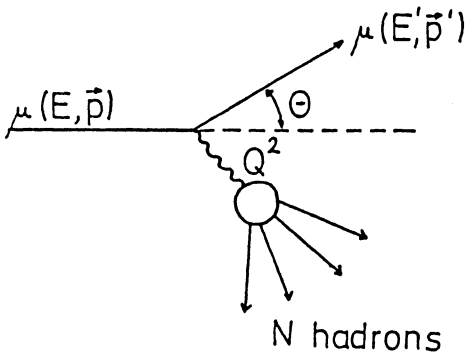

Figure 95. Feynman diagram for μ scattering.

$$\Gamma = \frac{K\alpha}{2\pi^2 Q^2} \frac{E'}{E} \frac{1}{1-\varepsilon} \tag{2.234}$$

$$\varepsilon = \left[1 + 2\frac{Q^2+\nu^2}{Q^2} tg^2\frac{\theta}{2}\right]^{-1} . \tag{2.235}$$

Q^2 and ν are the normal scaling variables, expressed by

$$Q^2 = -q^2 = 2\,(EE' - |\vec{p}|\,|\vec{p}'|\cos\theta - m_\mu^2) \tag{2.236}$$

$$\nu = E - E' \quad . \tag{2.237}$$

σ_T and σ_S are the photoabsorbtion cross sections for transverse and longitudinal photons respectively, for which we use the experimentally verified relation [106]:

$$\sigma_L = 0.3\left(1 - \frac{1}{1.868}\frac{Q^2}{\nu}\right)\sigma_T \tag{2.238}$$

σ_T is assumed to be constant, namely σ_T = 0.12 mb. For the incident flux K of the photons we use Gilman's convention

$$K = \nu + \frac{Q^2}{2\nu} \quad . \tag{2.239}$$

A three-dimensional important sampling table in the variables E, E' and Θ is generated in the set-up phase for each run of the program.

The hadrons are generated in an approximate way. The virtual photon is replaced by a real pion of random charge with the same kinetic energy as the photon, and the already existing routines for π^+ A and π^- A scattering are called. This treatment of deep inelastic muon sacttering is acceptable for problems like acceptance calculations for prompt muons (see chapter 4) or punch-trough simulations e.t.c. There is no question on the other hand, that for μ-nucleus scattering experiments, where the final state hadrons themselves are the particles to be investigated, the presently used treatment is not adequate. A more sophisticated simulation for inelastic scattering of muons and also for other leptons will be included in the next version of the program.

2.6.22 The absorbtion of particles at rest

All particles are followed through the detector, until they reach the outer limits of the detector, interact, decay or stop by the continous slowing down process as discussed in chapter 2.2.1. The stopping process is controlled by cut-off values E_C for the kinetic energies with the default values of 100 MeV for photons, electrons and positrons (in EGS: 100 keV for photons, 1.5 MeV for electrons and positrons), 1 MeV for charged and neutral hadrons other than neutrons. For neutrons we use a cut-off energy of 0.1 keV. They are tracked until they leave the detector, run out of the trigger or disappear by neutron capture or by an inelastic interaction. The remaining kinetic energy $E_{kin} \leq E_C$ is converted into ionization energy, which is emitted in a final step. The steplength R for charged hadrons is calculated according to the energy range formula

$$R = 1260. \left(\frac{m}{m_p z^2}\right) \left(\frac{m_p p}{m}\right)^{3.6} F(A)e^{-F(A)} \quad [cm] \qquad (2.240)$$

with

$F(A) = (\ln A)/6.9$.

For neutral hadrons the final steplength is zero. For photons, electrons and positrons a further one-dimensional shower parametrization is done in the GHEISHA-treatment. In case of EGS we refer to ref [4].

The rest masses are then partially converted into measurable energy by the following processes :

1.) μ^{+-}, π^+, π^0, K^+, K_S^0, K_L^0 and all strange baryons decay as will be discussed in the chapter about weak interactions.

2.) Neutrons are captured by a nucleus, followed by the emission of one or two photons (see chapter 2.6.20).

3.) $\bar{p}$ and $\bar{n}$ are captured by a nucleus and emit pions or photons (η) due to annihilation. Since the annihilation at rest is somewhat different from the annihilation at finite energies, special routines have been supplied.

4.) π^- and K^- are captured via a π-mesonic or K-mesonic atom by a nucleus. The absorption for π^- by free protons (hydrogen) obeys the Panofsky ratio

$$(\pi^- p \to n \pi^0)/(\pi^- p \to n \gamma) = 3/2 \qquad (2.241)$$

whereas for the absorption by heavier nuclei star production similar to nuclear evaporation (see chapter 2.6.16) has been assumed. Nearly the total rest mass is converted into kinetic energy of the evaporation particles. The treatment of the absorption of negative kaons is similar to that for negative pions. Again we assume for the absorption in hydrogen the production of π^0 and photons with the relative rate

$$(K^- p \to \Lambda \pi^0)/(K^- p \to \Lambda \gamma) = 3/2 \qquad (2.242)$$

The star production in heavier elements has to fulfill strangeness conservation, so there is emitted always one Λ.

The characteristic times of most of the absorption processes are in the order or somewhat lower than the trigger in modern high energy experiments : 2.5 nsec, 10 nsec and 25 nsec for π^--, K^-- absorption and neutron

capture respectively. Out of any trigger is normally the muon-decay, as will be discussed in a later chapter. The decay time of all other decays at rest is also near to the electronic time trigger.

2.6.23 Final remark

From all our investigations we concluded that the just described Monte-Carlo simulation for hadron scattering on free nucleons and on nuclear matter should be sufficient for the description of showers in calorimetric experiments. This part of the program may be also quite useful for the prediction of general properties of particle production in hadron nucleon and hadron nucleus reactions. The restrictions in the predictive power have been discussed in detail in the last 22 subchapters. The reader should not confuse this program with a simulation of a model or even a theory. Of course we have been guided by theoretical ideas to establish parametrizations. But the parameters entering in the corresponding formulae have been always finally adjusted by comparison with experimental data. Sometimes the so determined values for the parameters were in total disagreement with those of the original model. From this we may conclude that we are far away from a real understanding of the physics of soft hadron nucleus collisions.

2.7 DECAYS OF STABLE PARTICLES

In table 13 we summarize the decay channels, branching ratios and $c\tau$-values for all particles, which may decay in the present version of the program. This is first of all the level of produced particles in our generation of final state particles in nuclear interactions, and secondly defines the level of particles for the model generator input.

Table 13 decays of stable particles

particle	decay channel	branching ratio [%]	$c\tau$ [cm]
μ^+	$e^+\nu\nu$	100.	65868.
μ^-	$e^-\nu\nu$	100.	65868.

particle	decay channel	branching ratio [%]	cτ [cm]
π^+	$\mu^+\nu$	100.	780.4
π^0	$\gamma\gamma$	100.	0.
π^-	$\mu^-\nu$	100.	780.4

particle	decay channel	branching ratio [%]	cτ [cm]
K^+	$\mu^+\nu$	63.5	370.9
	$\pi^+\pi^0$	21.2	370.9
	$\pi^+\pi^+\pi^-$	5.6	370.9
	$\pi^+\pi^0\pi^0$	1.7	370.9
	$\mu^+\pi^0\nu$	3.2	370.9
	$e^+\pi^0\nu$	4.8	370.9
K_S^0	$\pi^+\pi^-$	69.0	2.675
	$\pi^0\pi^0$	31.0	2.675
K_L^0	$\pi^0\pi^0\pi^0$	21.6	1554.0
	$\pi^+\pi^-\pi^0$	12.4	1554.0
	$\pi^+\mu^-\nu$	13.6	1554.0
	$\pi^-\mu^+\nu$	13.6	1554.0
	$\pi^+e^-\nu$	19.4	1554.0
	$\pi^-e^+\nu$	19.4	1554.0
	$\pi^0\pi^0$	0.094	1554.0
	$\pi^+\pi^-$	0.203	1554.0
K^-	$\mu^-\nu$	63.5	370.9
	$\pi^-\pi^0$	21.2	370.9
	$\pi^-\pi^+\pi^-$	5.6	370.9
	$\pi^-\pi^0\pi^0$	1.7	370.9
	$\mu^-\pi^0\nu$	3.2	370.9
	$e^-\pi^0\nu$	4.8	370.9

particle	decay channel	branching ratio [%]	cτ [cm]
Λ	$p\pi^-$	64.2	7.73
	$n\pi^0$	35.8	7.73
$\bar{\Lambda}$	$\bar{p}\pi^+$	64.2	7.73
	$\bar{n}\pi^0$	35.8	7.73

particle	decay channel	branching ratio [%]	cτ [cm]
Σ^+	$p\pi^0$	51.6	2.4
	$n\pi^+$	48.4	2.4
Σ^0	$\Lambda\gamma$	100.	0.
Σ^-	$n\pi^-$	100.	4.44
$\bar{\Sigma}^+$	$\bar{p}\pi^0$	51.6	2.4
	$\bar{n}\pi^-$	48.4	2.4
$\bar{\Sigma}^0$	$\bar{\Lambda}\gamma$	100.	0.
$\bar{\Sigma}^-$	$\bar{n}\pi^+$	100.	4.44

particle	decay channel	branching ratio [%]	cτ [cm]
Ξ^0	$\Lambda\pi^0$	100.	8.87
Ξ^-	$\Lambda\pi^-$	100.	4.95
$\bar{\Xi}^0$	$\bar{\Lambda}\pi^0$	100.	8.87
$\bar{\Xi}^-$	$\bar{\Lambda}\pi^-$	100.	4.95

If t denotes the eigentime in the rest-system of the particle and τ the average lifetime, then the probability for a decay at time t is given by

$$P(t) = (1/\tau)\, e^{-t/\tau} \quad . \tag{2.243}$$

The eigentime t can be expressed by the decay length L in the lab.-system:

$$t/\tau = \frac{m_0}{c\tau} \int_0^L ds/p(s) \quad . \tag{2.244}$$

For neutral particles the momentum p does not depend on the pathlength s, for charged particles we assume the steplength L small enough, so that

$$p(s) = p = \text{constant} \quad . \tag{2.245}$$

Then the integral can be calculated :

$$P(L,p) = (1/\tau)\, \exp\left[-\left(\frac{m_0}{c\tau}\right)\left(\frac{L}{p}\right)\right] \quad . \tag{2.246}$$

The conditional probability for a decay with decaylength L for a given momentum p is then

$$P(L|p) = \frac{m_0}{c\tau p} \exp\left[-\left(\frac{m_0}{c\tau}\right)\left(\frac{L}{p}\right)\right] \qquad (2.247)$$

and the probability for a decay inside a step Δ :

$$P(L\leq\Delta|p) = 1 - \exp\left[-\left(\frac{m_0}{c\tau}\right)\left(\frac{L}{p}\right)\right] \qquad (2.248)$$

Besides for muons all particles are assumed to decay isotropically in their rest-system. Neglecting small polarisation effects, this is also justified for the strange baryons. We have taken into consideration only decay channels, which have branching ratios greater than 1%. The branching ratios of the other channels have been increased to add up to 100%. The K_s^0 and all strange baryons have normally a big chance to decay, compared to that the interaction probability is small. But for heavy elements like uranium the absorption length of $\approx$ 12 cm reaches the same order of magnitude as the $c\tau$-values. Unfortunately we can't proof our nuclear scattering treatment for strange baryons, because no experimental data are available. Therefore some uncertainty especially for high A-values can not be excluded for these particles.

The electron spectrum in μ-decay is given by (see e.g. [107]) :

$$\frac{d\lambda}{dE_e d\Omega} = \frac{G^2}{4\pi^4} E_0 E_e^2 \left[E_0 - (2/3)\ E_e \pm \frac{\vec{\sigma}_\mu \vec{p}_e}{|\vec{p}_e|}(2E - E_0)\right] \qquad (2.249)$$

where $\vec{\sigma}_\mu$ represents the direction of the muon spin, the signs + or - are associated with μ^+ and μ^- respectively, and $E_0 = m_\mu/2$ represents the maximum energy of the electron. It is convenient to rewrite (2.249) in a simpler form by introducing the substitutions

$$x = \frac{E}{E_0} \quad , \quad \cos\theta = \frac{\vec{\sigma}_\mu\ \vec{p}_e}{|\vec{p}_e|} \qquad (2.250)$$

hence

$$\frac{d\lambda}{dx d\Omega} = \frac{1}{4\pi\tau_\mu} 2x^2(3-2x)\left[1 \pm \cos\theta \frac{(2x-1)}{(3-2x)}\right] \qquad (2.251)$$

with

$$\frac{1}{\tau_\mu} = \frac{G^2 m_\mu^5}{192\pi^3} \qquad (2.252)$$

In an approximate way we use the integrated expressions for the energy spectrum and angular distributions

$$\frac{d\lambda}{dx} = \frac{2x^2}{\tau_\mu}(3-2x) \qquad (2.253)$$

$$\frac{d\lambda}{d\Omega} = \frac{1}{4\pi\tau_\mu}(1 \pm (1/3)\cos\theta) \qquad (2.254)$$

This factorization is of course not valid in general.

3.0 SHORT WRITE-UP OF THE GHEISHA-PROGRAM

3.1 THE CURRENT VERSION

3.1.1 General remarks

The general data flow from the user side of routines is shown in fig.96. In the BLOCK DATA most of the particle-, material- and stepping- constants are defined. Beside that the dimension of the shower-track stack has to be given. The routine INIT has been introduced to define the geometry of the detector set-up. As will be explained later in detail, the geometry definition is totally under control of the user and is not limited by any special restriction like orthogonal or cylindrical geometries. The only information necessary for the program is the material index, which refers to the array index of the material constants as has been previously stored in BLOCK DATA.

Certain cuts have been defined in BLOCK DATA. Run-specific changes may be done in the routine CUTS. Also some of the materials may be redefined in routine CHMAT. The last two routines have been supplied only for convenience of the user. In the development phase of a Monte-Carlo program for a new detector one normally plays around with cuts and materials. In the final version then the changes in CUTS and CHMAT will be copied to the BLOCK DATA and will be frozen in. The initialization of a Monte-Carlo run is finished by a first call to the routine ANALYS(0). ANALYS is the main output-interface routine. Initialization of histogramms as well as initialization of user-dependent output quantities to be summed over the total run are foreseen at this first call.

The loop over all events to be processed starts with a call to one of the INPUT-routines. All tracks of the primary interaction have to be defined by the four-momenta, masses, charges, the cartesian coordinates and the time zero of the starting point. Up to 10 different INPUT-routines (INPUT0, INPUT1, INPUT2, ..., INPUT9) may be used in the same run. The calling sequence is determined by a user-controlled flag. The second call to the analysis routine (ANALYS(1)) may be used to initialize all event specific output quantities.

The second loop over all tracks of one event starts with a third call to the analysis routine (ANALYS(2)). This is for initialization of single track specific quantities.

After the initialization all tracks from the generator input are followed one after the other through the detector, until they reach the outer geomet-

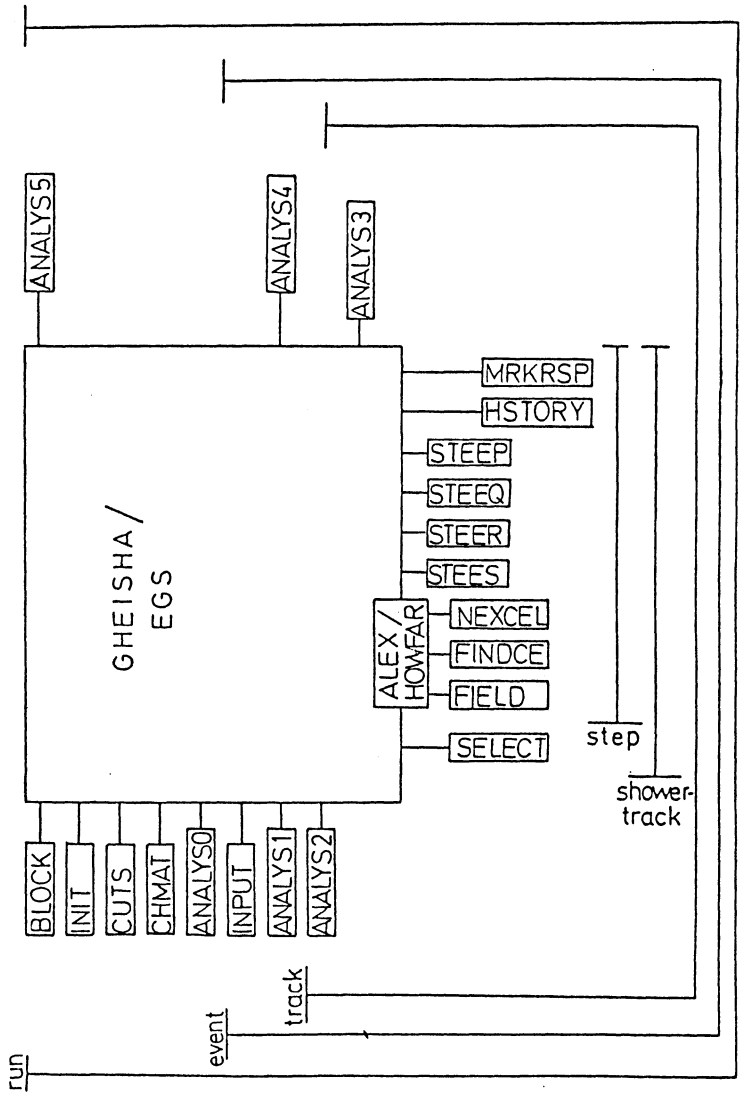

Figure 96. General data flow from the user side of routines.

rical limits, stop by ionization energy loss, decay or interact. In the latter two cases one of the final state particles are followed further instead of the original particle, the remaining ones are written on the track stack. If a particle stops without further production of particles or leaves the detector, one of the particles from the stack are copied to the working buffer. For each new track in the working buffer the SELECT routine is called, which allows the user to skip this track for further tracking. In the default version all produced neutrinos only are thrown away. Other applications will be discussed in later chapters.

The steering routines for the tracking are ALEX in GHEISHA and HOWFAR in EGS. They both work in a similar way and use a general tracking algorithm which may be not very efficient for exotic geometry definitions. They may be used as starting versions, but have certainly to be improved for the final version of the Monte Carlo program for a specific detector. The use of the cell finding routines FINDCE and NEXCEL will be explained in chapter 3.1.6.

If the track interacts within a step, the tuning routines STEES, STEER, STEEQ and STEEP are called. These routines allow the user to tune some parameters of the simulation of nuclear interactions by himself. The HSTORY routine is called in case of production of new particles. The four-momenta, masses and charges of the initial interacting and of all final state particles are written on a two dimensional array and may be used to set up a shower history. Note that the shower history is not done by the GHEISHA program (see chapter 3.1.8).

The main response routine is named MRKRSP (=mark response). It is called once for each step of each shower track and delivers the absorbed energy by ionization to the digitization routines. In this routine all informations necassary for the digitization have to be sampled. The step is finished by carrying out the transformations of the coordinates and directions as were previously prepared in the ALEX/HOWFAR- routines. Output quantities may be plotted or written out in the analysis routine at calls ANALYS(3), ANALYS(4) and ANALYS(5) at the end of the simulation of one generator track, at the end of one event and at the end of the run respectively.

In the next chapters we will describe in more detail the program flow of GHEISHA. In chapter 3.1.8 we will come back to the user routines.

3.1.2 The initialization

The flow diagram of the initialization is shown in more detail in fig.97.

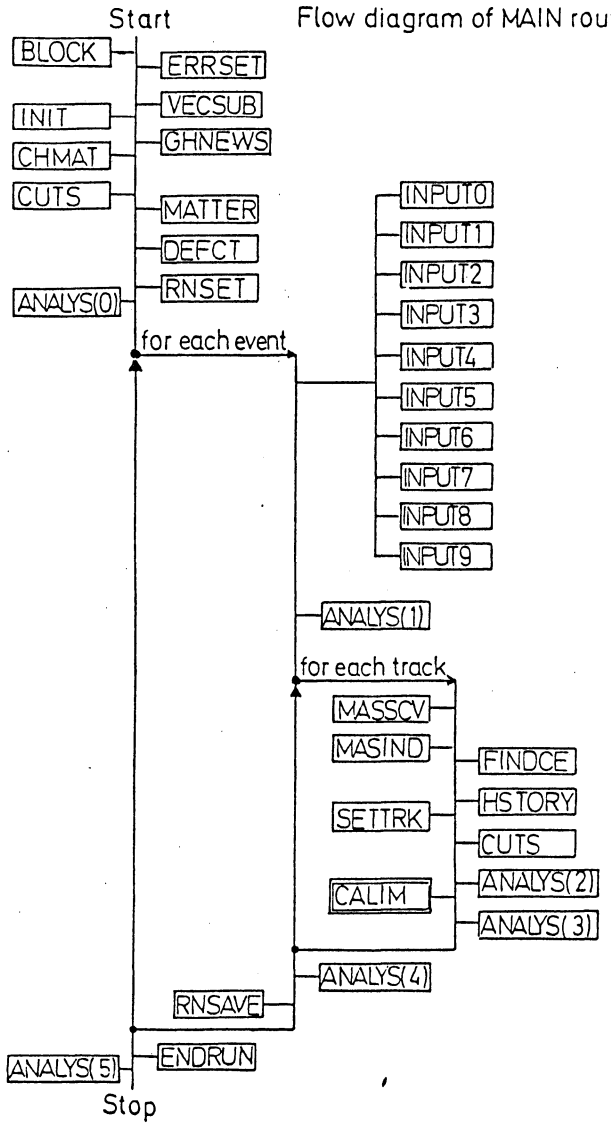

Figure 97. Flow diagram of the initialization.

The BLOCK-DATA is used to define the following quantities :

1.) particle constants, stored on the common

```
COMMON/CONSTS/ PI,TWPI,PIBTW,MP,MPI,MMU,MEL,MKCH,MK0,SMP,SMPI,
               SMU,CT,CTKCH,CTK0,
               ML0,MSP,MS0,MSM,MX0,MXM,CTL0,CTSP,CTSM,CTX0,CTXM
               REAL MP,MPI,MMU,MEL,MKCH,MK0,
                    ML0,MSP,MS0,MSM,MX0,MXM
```

with

PI	3.1415927
TWPI	2*PI
PIBTW	PI/2
MP	mass of proton
MPI	pion
MMU	muon
MEL	electron
MKCH	charged kaon
MK0	neutral kaon
SMP	SQRT(MP)
SMPI	SQRT(MPI)
SMU	SQRT(MMU)
CT	$c\tau$ of pions
CTKCH	charged kaons
CTK0	neutral kaons
ML0	mass of Λ
MSP	Σ^+
MS0	Σ^0
MSM	Σ^-
MX0	Ξ^0
MXM	Ξ^-
CTL0	$c\tau$ of Λ
CTSP	Σ^+
CTS0	Σ^0
CTSM	Σ^-
CTX0	Ξ^0
CTXM	Ξ^-

2.) run constants, stored on common

```
COMMON/CURPAR/WEIGHT(10),DDELTN,IFILE,IRUN,NEVT,NEVENT,SHFLAG,
              ITHST,ITTOT,ITLST,IFRND,TOFCUT,CMOM(5),CENG(5),
              RS,S,ENP(10),NP,NM,NN,NR,NO,NZ,IPA(200),
              ATNO2,ZNO2
```

with

SHFLAG	Flag for electromagnetic showers : = 0 EGS (default value). > 0 GHEISHA electromagnetic shower routines with one-dimensional parametrizations below the cut-off energy CENG(1).
ITHST	The run should stop ITHST seconds before end of GO-step (default=0).
TOFCUT	Timing cut (in 1/20 nsec), default value = 2000.
CENG(1)	Energy cut-off for electromagnetic particles, below this energy parametrizations are used. Default value = 100 MeV.
CENG(2)	Energy cut-off for muon bremsstrahlung. Default value = 10 MeV.
CENG(3)	Energy cut-off for charged hadrons. Default value = 1 MeV.
CENG(4)	Energy cut-off for neutral hadrons. Default value = 1.5 MeV.
CENG(5)	Energy cut-off for δ-rays, below this energy δ-electrons are tracked only, above this energy they are stored on the stack and treated with the respective shower routines (GHEISHA or EGS).

3.) material constants, stored on the common

```
COMMON/MAT   / DEN(11),RADLTH(11),ATNO(11),ZNO(11),ABSL(11),
               CDEN(11),MDEN(11),XODEN(11),X1DEN(11),RION(11),
               IMAT(3),IFRAC(3),IFRAT,FRAC1(3,10),DEN1(3,10),
               ATNO1(3,10),ZNO1(3,10)
```

with

DEN (IND+1)	Density (gr/cm^3).
RADLTH(IND+1)	Radiation length (cm).
ATNO (IND+1)	Atomic number (average value, see later).
ZNO (IND+1)	Charge number of nucleus (average value, see later).
ABSL (IND+1)	Absorption length (only used for step size calculations).
CDEN (IND+1)	C - parameter in Sternheimers theory.

The density, atomic number and charge number , defined above, are average values for compound materials like BGO or emulsion. These values are used for dE/dx- calculations and total cross section determinations. Three of the so defined materials may be further specified by

```
IMAT(J)        Material index = IND+1.
IFRAC(J)       Number of constituents in this material.
FRAC1(J,I)     Fraction        of the i.th constituent.
DEN1 (J,I)     Partial density of the i.th constituent.
ATNO1(J,I)     Atomic number   of the i.th constituent.
ZNO1 (J,I)     Charge number   of the i.th constituent.
```

4.) Define the dimension of the shower track stack
COMMON/EVENT / NSIZE,NCUR,NEXT,NTOT,EVE(24000)
with

NSIZE Total length of the stack, default value = 24000, must be a multiple of 12, we propose to use $1200 \leq NSIZE \leq 24000$.

NCUR Pointer to the track which should be copied next from the stack to the working buffer, initial value = 0.

NEXT Pointer to the location where the next produced track should be stored, initial value = 0.

NTOT Total number of tracks currently stored, initial value = 0.

5.) Include BLOCK DATA for EGS (see ref. [4]).

6.) Zeroing of some working buffers (/RESULT, /PRNTFL, /CALSTR, /ERRCOM , see later).

By the call of the IBM-ERRSET routines arithmetic- and I/O- errors are handled and the error messages are suppressed. The following calls are introduced in the MAIN routine :

```
ERRSET(207,....)    exponent overflow
ERRSET(208,....)    exponent underflow
ERRSET(209,....)    divide check
ERRSET(213,....)    I/O error
ERRSET(251,....)    square root argument negative
ERRSET(265,....)    arctg arguments both zero
```

Users should make shure that the appearence of these errors are exeptionally. Only the exponent underflow is uncritical. The ERRSET- routines are not included in the main library and must thus be replaced by other routines running the program not on an IBM.

By the call to VECSUB we initialize the DESY vector operation package [108]. The various entries work all on the blank common

```
COMMON/      /PV(10,200)
```
with
PV(1,*) = p_x
PV(2,*) = p_y
PV(3,*) = p_z
PV(4,*) = E
PV(5,*) = M

and are used throughout the program for kinematic calculations. The following quantities, if not yet defined in the BLOCK DATA, have to be specified in the routine INIT :

```
COMMON/PRNTFL/INBCD,NEWBCD,INBIN,NEWBIN,NPEVT,NEVTP,LPRT,NPRT(10)
              LOGICAL LPRT,NPRT
INBCD     Card-reader ( =5).
NEWBCD    Printer     ( =6).
INBIN     Input-tape  ( =1),   not used.
NEWBIN    Output-tape ( =2),   not used.
NPEVT     Number of events for debug-printing.
NEVTP     First event for debug-printing.
```

The following logicals are flags for various debug- printing options. If they are on (.TRUE.), the following printout will be done (for NPEVT events) :

```
NPRT(1)   One header for each track in the shower.
NPRT(2)   All cell search and boundary search informations.
NPRT(3)   Kinematic of decays.
NPRT(4)   Kinematic of nuclear interactions.
NPRT(5)   Kinematic of electromagnetic interactions.
NPRT(6)   Material constants, dE/dx and absorbed energies.
NPRT(7)   Event summary.
NPRT(8)   History of all interactions/decays.
NPRT(9)   Not used.
NPRT(10)  Tables of the geometry, cross sections e.t.c..
```

NPRT(1),NPRT(2) and NPRT(6) should be used only in case of errors and bugs. NPRT(8) produces the most illustrative output.

```
COMMON/CURPAR/WEIGHT(10),DDELTN,IFILE,IRUN,NEVT,NEVENT,SHFLAG,
              ITHST,ITTOT,ITLST,IFRND,TOFCUT,CMOM(5),CENG(5),
              RS,S,ENP(10),NP,NM,NN,NR,NO,NZ,IPA(200),
              ATNO2,ZNO2
```

with

IFILE Number of INPUT-routine to be called (=0,1,...9), may be changed during the run.

IRUN Run-number , not used in program.

NEVENT Total number of events to be processed.

IFRND First random number for random number generator RN.

```
COMMON/CALSTR/ NCALO,MATCL(20,100),XLO(20,100),XHI(20,100),
               YLO(20,100),YHI(20,100),ZLO(20,100),ZHI(20,100),
               MCELL(20)
```

In this buffer the geometry of the detector has to be stored :

NCALO Number of modules (also called 'calorimeter')

MCELL(I) Number of cells in the I.th module.

MATCL(I,J) Material index of cell J in the I.th module.

XLO(I,J), XHI(I,J), YLO(I,J) 6 variables, which define the geometry of the J.th cell in the I.th module in a unique, but arbitrary, way. These quantities are only used in the user-routine FINDCE. Thus the program must not have any kwnoledge of their meaning.

YHI(I,J), ZLO(I,J), ZHI(I,J) 6 variables, which define the geometry of the J.th cell in the I.th module in a unique, but arbitrary, way. These quantities are only used in the user-routine FINDCE. Thus the program must not have any kwnoledge of their meaning.

GHNEWS has been introduced to document the changes in the program, done by the author. In routines CHMAT and CUTS all constants already defined in BLOCK DATA and INIT may be changed. Note that the routine CUTS is also called just before the program enters the steering routine for the shower devellopment. Thus in CUTS one can specify the cuts as function of the type of the particle/track. The routine MATTER calculates the parameters needed for the relativistic density formula as discussed in chapter 2.2.1. Beside that the reaction probabilities for interaction on the various constituents of compounds/mixtures are determined. The following quantities are written on the /MAT- common :

MDEN (IND+1) m - parameter in Sternheimers theory.

XODEN (IND+1) x_0- parameter in Sternheimers theory.

X1DEN (IND+1) x_1- parameter in Sternheimers theory.

RION (IND+1) Ionisation potential.

FRAC1(J,I) Reaction probability for the I.th constituent.

In EGS we do not use the simple dE/dx-formula as discussed in chapter 2.2.1. The ionization energy loss, cross sections and related quantities for

electrons, positrons and photons for the different materials in use have to be supplied by tables, which must be produced by the preprocessor PEGS3. All routines needed are included in the library. #JELEM, #JMIXT and #JCOMP contain the job-control language for producing an EGS data file for pure elements, mixtures and compounds respectively. For the long write-up see member #PEGS3. The tables for our default materials are already included in the library as

member name	material	material index
#PEGSBGO	BGO	1
#PEGSFE	iron	2
#PEGSCU	copper	3
#PEGSAL	alluminum	4
#PEGSU	uranium	5
#PEGSPB	lead	6
#PEGSSCI	plastic scintilator	7
#PEGSAIR	air	8
#PEGSIS	isobuthan	9
#PEGSLA	liquid argon	10

The data sets for EGS are not read in during the initialization phase of the program, but at the first call to the EGS routine. That means, if the GHEISHA electromagnetic shower routines are used, all these tables have not to be supplied.

DEFCT makes some printout on the dE/dx as function of E for muons. As random number generator we use the DESY routine RN with the additional entries RNSET and RNSAVE. The first random number, defined in BLOCK DATA or INIT, is delivered to the random number generator RN by the RNSET call.

According to the value on the variable IFILE one of the input- routines INPUT0, INPUT1,....., INPUT9 is called for each event. IFILE was initialized in BLOCK DATA or INIT, but may be changed during the run. At return the program expects the common

COMMON/INPEV /NTRK,TRAK(10,200)
to be filled with

NTRK	Number of tracks	
TRAK(1,*)	p_x	All in GeV. The masses should roughly agree with those given in the PDG-table. A mass-conversion routine is called to set the masses used in the program.
2,*)	p_y	
3,*)	p_z	
4,*)	E	
5,*)	m	
6,*)	Charge	In floating-point (+2.,+1.,0.,-1.).
7,*)	X_0	Starting coordinates of track (in cm).
8,*)	Y_0	
9,*)	Z_0	
10,*)	t_0	Time zero of beam particle or primary interaction at (X_0,Y_0,Z_0).

If possible, set also the calorimeter and cell number on LCALO and ICEL in the /CURPAR-common, this helps the program in the set-up phase, i.e.

LCALO	Calorimeter of the starting point.
ICEL	Cell of the starting point.

The two calls ANALYS(1) and ANALYS(2) (see chapter 3.1) enclose the loop over all tracks of the event (1,...,NTRK).The mass- convention of the program is checked in routine MASSCV and a mass-index is calculated in MASIND. These are as follows :

Particle	mass (GeV)	mass-index
γ	0.	1
ν	0.00001	2
e^+	0.00051	3
e^-	0.00051	4
μ^+	0.106	5
μ^-	0.106	6
π^+	0.140	7
π^0	0.140	8
π^-	0.140	9
K^+	0.494	10
K_S^0	0.498	11
K_L^0	-0.498	12
K^-	0.494	13

p	0.938	14
$\bar{p}$	-0.938	15
n	0.938	16
$\bar{n}$	-0.938	17
Λ	1.1156	18
$\bar{\Lambda}$	-1.1156	19
Σ^+	1.1894	20
Σ^0	1.1925	21
Σ^-	1.1974	22
$\bar{\Sigma}^+$	-1.1894	23
$\bar{\Sigma}^0$	-1.1925	24
$\bar{\Sigma}^-$	-1.1974	25
Ξ^0	1.3149	26
Ξ^-	1.3213	27
$\bar{\Xi}^0$	-1.3149	28
$\bar{\Xi}^-$	-1.3213	29
d	unchanged	30
t	unchanged	31
α+heavier fragments	unchanged	32
new particles	unchanged	33

Note that all antibaryons and the K_L^0 have negative masses. This sign-convention must also be used in the input- routines.

The FINDCE-routine (see later) is used to check or to find the calorimeter number LCALO and cell number ICEL of the starting point (X_0,Y_0,Z_0). If LCALO and ICEL were already given by the user in routine INPUTi, it is only checked, if not, LCALO and ICEL are determined by a loop over all calorimeter and cells. The call to routine CUTS enables the user to fit the cuts for the kinetic energy and time trigger to the specific particles. The two calls ANALYS(2) and ANALYS(3) enclose the call to the steering routine CALIM for the tracking and/or shower expansion of the track.

3.1.3 The shower routine CALIM

CALIM is the steering routine for the tracking and/or shower expansion of one primary track. A flow diagram is shown in fig. 98. CALIM calls first SETRES, which fills the working buffer /RESULT from the track parameters on the stack. The primary track is initially written as first track on the stack, shower particles will be written in the decay- and cascading- routines somewhere on this stack, the location of the particle to be copied next to the working buffer is indicated by a pointer.

The parameters on the stack and the working buffer are as follows:

1.) Track on the stack:

```
COMMON/EVENT / NSIZE,NCUR,NEXT,NTOT,EVE(1200)
```

NSIZE Total length of the stack (from BLOCK-DATA).
NCUR Pointer to the track which should be copied next from the stack to the RESULT-common.
NEXT Pointer to the location where the next produced track should be stored.
NTOT Total number of tracks currently stored.

The track next to be copied from the stack then looks like

EVE(NCUR)	X
EVE(NCUR+ 1)	Y
EVE(NCUR+ 2)	Z
EVE(NCUR+ 3)	RCA
EVE(NCUR+ 4)	RCE
EVE(NCUR+ 5)	Mass
EVE(NCUR+ 6)	Charge
EVE(NCUR+ 7)	TOF
EVE(NCUR+ 8)	P_X
EVE(NCUR+ 9)	P_Y
EVE(NCUR+10)	P_Z
EVE(NCUR+11)	USERW

2.) Track on the working buffer:

```
COMMON/RESULT/XEND,YEND,ZEND,RCA,RCE,AMAS,NCH,TOF,PX,PY,PZ,
              USERW,INTCT,P,EN,EK,AMASQ,DELTN,ITK,NTK,IPART,IND,
              LCALO,ICEL,SINL,COSL,SINP,COSP
              REAL NCH,INTCT
```

with

XEND, YEND, ZEND Start- or end- coordinates of the current step.

RCA CALO1*1000.+CALO2*1.
RCE CELL1*1000.+CELL2*1.
CALO1 and CALO2 (CELL1 AND CELL2) are the calorimeter (cells), where this step comes from and points to.

AMAS Mass
NCH Charge
TOF Time of flight (in 1/20 nsec)
PX p_X/p = COSL*COSP
PY p_Y/p = COSL*SINP
PZ p_Z/p = SINL
USERW Userword (see HSTORY)

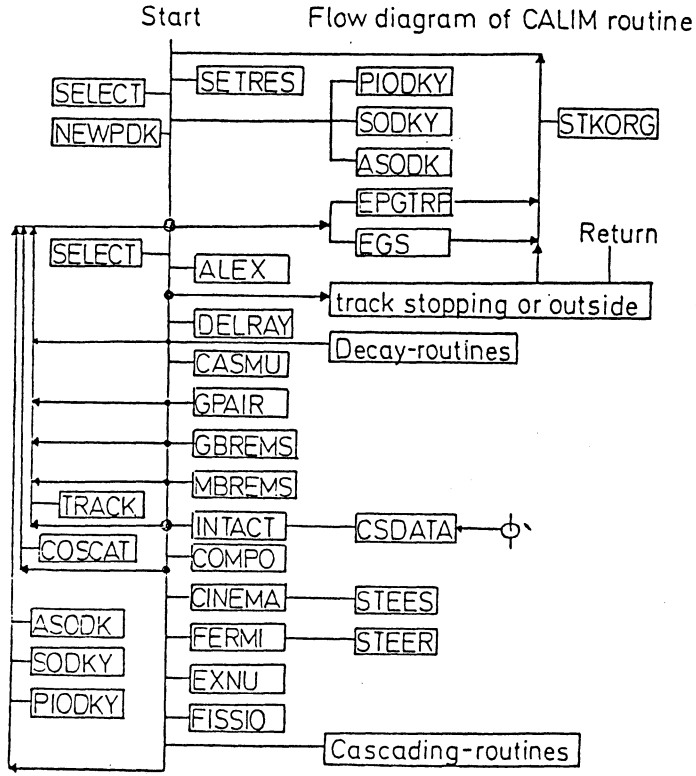

Figure 98. Flow diagram of the CALIM routine.

INTCT	Interaction/decay-counter
P	Momentum
EN	Total energy
EK	Kinetic energy
AMASQ	AMAS**2
DELTN	Actual stepsize (see also DDELTN in /CURPAR).
ITK	Number of generator track (see INPUT-routines).
NTK	Number of the present track in the shower.
IPART	Particle index (SEE MASIND).
IND	Material index (SEE MATTER)
LCALO	Calorimeter number (= CALO1 in RCA).
ICEL	Cell number (= CELL1 in RCE).
SINL	Sinus of dip-angle.
COSL	Cosinus of dip-angle.
SINP	Sinus of normal phi-angle (with respect to x-axis).
COSP	Cosinus of normal phi-angle.

This information may be used by the user to remove this track for further treatment in SELECT. In case of a π^0, Σ^0 or $\bar{\Sigma}^0$ the particles undergo a decay immediately by a call to PIODKY, SODKY or ASODK respectively. The routine NEWPDK is a decay routine for new long-lived particles, which have not been introduced in our particle table in chapter 3.1.2. It has been used in the past mainly to check the performance of high precision vertex chambers. All particles, which do not fit to a mass given in MASIND, are tracked only and the routine NEWPDK is called, no interaction will be done. As default we have included the decay of the τ in NEWPDK.

Next we come to the main branch point. In case of a γ, e^+ and e^- we decide from the value on SHFLAG to handle the track by the GHEISHA electromagnetic interaction routines GPAIR and GBREMS, or by a one-dimensional parametrization (EPGTRP, for $E_{kin} < CENG(1)$), or by the EGS-package.The value on SHFLAG may be changed during the run. In the latter two cases, at return from EPGTRP or EGS, the track is finished and the next track will be copied from the stack to the working buffer. Which track on the stack should be copied next, may be decided in routine STKORG. There are two possibilities already included. But experiences show that all off-line analysis experts like to realize their own ideas on stack-organization. This can be done in STKORG together with the user-routine HSTORY. Note that no changes have been done in the stack organization of EGS. This means especially that EGS works with its own shower stack. If there are no more tracks on the stack, CALIM returns to the MAIN-routine.

For SHFLAG > 0 and $E_{kin} > CENG(1)$ for photons, electrons and positrons and for all other particles we prepare the transformations of coordinates

and directions of the next step by a call to ALEX. If the track stops within the next step or leaves the detector, we branch to a separate treatment which will be discussed later. δ-rays may be produced in routine DELRAY. In our present version only muons produce δ-rays, and only in gaseous materials (air and isobuthan). This may be changed by the user. For more details see chapter 3.1.11.

Next we ask for a decay of the particle. Note that we always ask first for a decay and afterwards for an interaction. To make this scheme working, the step-size has to be chosen appropriate small. Bremsstrahlung by muons is generated in routine MBREMS. For photons, electrons, positrons, bremsstrahlunging muons and for all other decaying particles the current step is finished. In case of an interaction or decay, we carry out the stepping to the interaction/decay- point in the respective routine (see later), otherwise we branch to the routine TRACK and prepare the next step in ALEX. Hadron production by muons is more complicated. We first generate the scattered muon in CASMU and produce the final state hadrons in one of the cascading routines (see chapter 3.1.9).

For all particles, which may interact strongly with a nucleus, the interaction probability is calculated in routine INTACT. This routine calls in turn CSDATA, which reads in all measured cross sections from a data file and calculates unmeasured cross sections, as was described in chapter 2.6.2. If the interaction fails we turn to TRACK, carry out the transformations of coordinates and directions and go back to ALEX in order to prepare the next step. Otherwise we ask in case of a mixture or compound, on which of the various constituents the interaction took place. The atomic number and charge number are written on ATNO2 and ZNO2 in the /CURPAR- common. In case of a coherent elastic scattering we branch to COSCAT and in turn back to ALEX. For inelastic reactions we call CINEMA, FERMI and EXNU to prepare some kinematic corrections, apply Fermi-motion and subtract the nuclear evaporation energy respectively. For uranium as target nucleus we call FISSIO to produce neutrons and photons as prescripted by our formulae in chapter 2.6.20. The final state particles are generated by a call to one of the cascading-routines.

In general one of the final state particles replaces the original incoming particle in the working buffer /RESULT. If that particle turns out to be a π^0, Σ^0 or $\bar{\Sigma}^0$, we generate immediately the decay in routines PIODKY, SODKY or ASODK respectively.

3.1.4 The decay-routines

The decay-routines work all in a similar way (see fig.99). We first generate the decay vertex randomly on the step prepared by ALEX. Then the routine TRACK is used to step forward to this point. The respective decay routine generates the final state particles by use of the various entries of the VECSUB routine and by use of the phase space generator PHASP. The HSTORY routine is called to enable the user to make his shower history. One of the decay tracks replaces the original one on the working buffer (SETCUR), the other ones are written on the stack (SETTRK). Note that we have included in fig.99 the electromagnetic interaction routines GPAIR, GBREMS and MBREMS. They work in a similar way.

3.1.5 The cascading-routines

The cascading routines work similar as the decay routines (see fig.100). We first generate the interaction vertex and step forward to this point. In the cascading routines we generate the final state multiplicity and the quantum numbers for all particles. The special routine STPAIR is used to include production of strange particle pairs. Routines GENXPT and TWOB are called to generate the four-momenta of all final state particles. GENXPT may branch to TWOCLU and that in turn to TWOB for interactions at low energy. TWOCLU generates a final state according to the two-body resonance model and TWOB an inelastic two-body final state as was described in chapter 2.6.13. These routines call again the VECSUB package for kinematical calculations and PHASP for phase space calculations. The calling sequence HSTORY, SETCUR and SETTRK was already described in connection with the decay routines.

3.1.6 The tracking algorithm

The transformations of the coordinates and directions are prepared in ALEX and stored in MFSTP, the routine TRACK is used to carry out the transformation if required. A schematic flow diagram is shown in fig.101. We first call FIELD to calculate the magnetic field at the start-coordinates of the step.
The first call to the magnetic field stepping routine MFSTP calculates the basic transformation matrix, as described in chapter 2.4. We first check then, whether a default step-size, given by the radiation length for γ, e^+ and e^- or by the absorption length for all other particles, leads to an end-point of the step within the same material as that of the starting point. Otherwise we use an iteration loop to find the material boundary. This loop is relatively complicated and calls in turn the user-routines

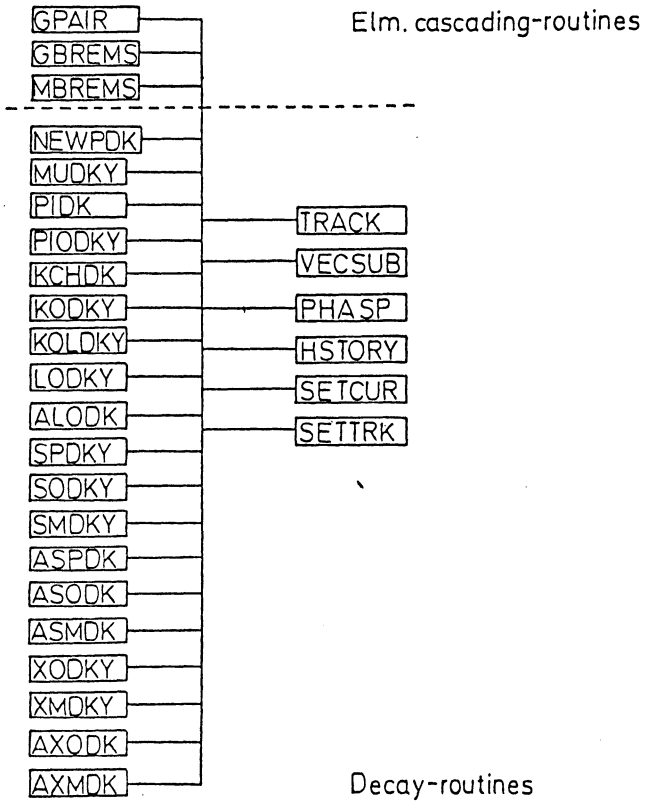

Figure 99. Flow diagram of the decay routines.

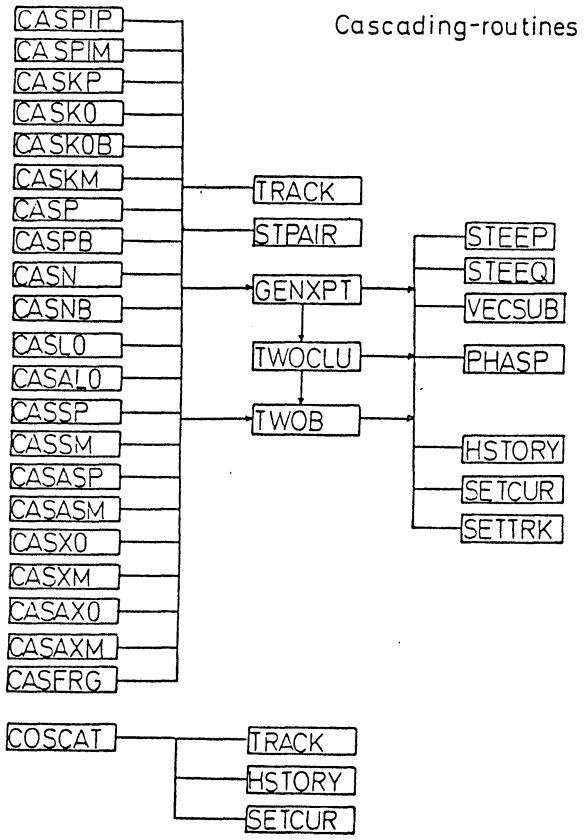

Figure 100. Flow diagram of the cascading routines.

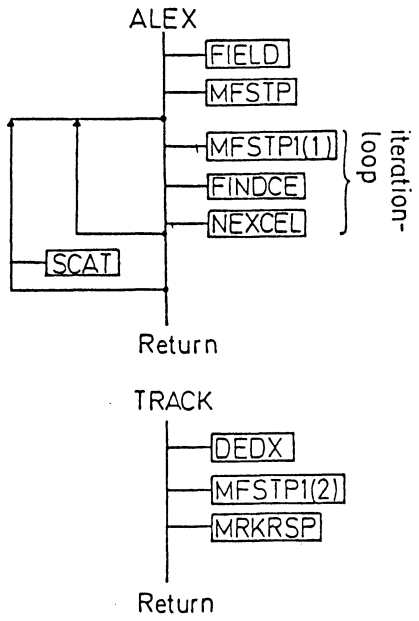

Figure 101. Schematic flow diagram of the cell search and boundary search.

FINDCE and NEXCEL. In FINDCE the user has to answer the question whether the point (X,Y,X) lies within a detector volume labeled by (LCALO,ICEL). At return from NEXCEL, the program expects as output the calorimeter number and cell number (LCALO,ICEL) for the point (X,Y,Z). As input for the latter routine the calorimeter number and cell number of the previous step is given, so one has to search only in the vicinity of this last step. These are the only routines, where the geometry definition of the /CALSTR- common is used. As can be seen by the previous explanations, the definition of the geometry and the numbering of the various calorimeters and cells should be done in such a way, that the two tasks of routines FINDCE and NEXCEL can be programmed as efficient as possible.

If the coordinates of the material boundary have been found within some accuracy, multiple scattering is applied in routine SCAT. Here we change the coordinates of the starting point and the directions of the track. Thus the iteration loop has to be called again. In the second loop we try to find

the coordintes of the material boundary with higher accuracy than it was done in the first loop.

The final output from ALEX is the stepsize DELTN, which is copied also to DDELTN in the /CURPAR- common, and the index of the material passed through in this step. In case of an interaction or decay in the present step, DELTN will be changed to the actual stepsize to the interaction/decay vertex. DDELTN is not changed from one call to ALEX to the next call. The transformations are stored in routine MFSTP and may be used by a call to the entry MFSTP1. The transformations may be performed permanently changing all stepping parameters on the /RESULT- common (MFSTP1(2)) or only temporary with the coordinates of the end-point as arguments (MFSTP1(1)).

In TRACK we first calculate the reduction of energy by ionisation (DEDX), then the transformation is carried out (MFSTP1(2)) and finally the main response routine MRKRSP is called.

3.1.7 Stopping tracks

If the kinetic energy of a particle is less than the cut-off energy or if the range of charged particles is less than the calculated step-size, the program flow branch into the separate treatment of stopping tracks (see fig.102). For charged particles the range is calculated in RANGE and replaces the step-size as was calculated in ALEX. For neutral particles the stepsize is unaltered.
We first carry out the final step (MFSTP1) and absorb all kinetic energy (MRKRSP). For the particles at rest the following routines are called :

1.) For e^-, γ, ν, p, d, t, α and all heavier fragments we do nothing, except that the HSTORY routine is called to inform the user on the vanishing of this track.

2.) For positrons we absorb the rest mass by a call to the response routine and call again the HSTORY routine.

3.) For π^- and K^- special routines for the star production by particle absorption are used (PIMABS, KMABS).

4.) $\bar{p}$ and $\bar{n}$ are assumed to annihilate into pions (PBANH, NBANH).

5.) Neutrons are captured and emit in turn one or two photons (CAPTUR).

5.) For all other particles we call the respective decay routine.

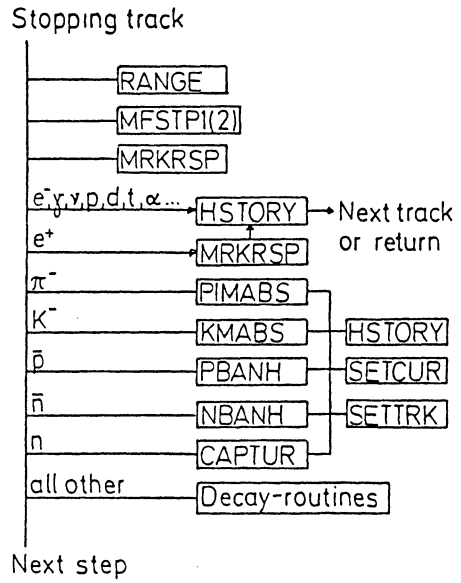

Figure 102. Flow diagram for the handling of stopping tracks.

Note that this scheme is valid for γ, e^- and e^+ only, if the GHEISHA electromagnetic shower routines are used with a very small cut-off energy (CENG(1) < 2 MeV). Otherwise the program has already branched before to the shower parametrization routine EPGTRP. For EGS we refer to chapter 3.1.12.

3.1.8 The user routines

Most of the user routines have already been described in the previous chapters. INIT, CUTS, CHMAT, ANALYS and the various INPUT- routines in chapter 3.1.2, SELECT in chapter 3.1.3, ALEX, FINDCE and NEXCEL in chapter 3.1.6. The remaining routines to be discussed are MRKRSP as interface to the digitization routines, HSTORY for introducing a shower history and STEEP, STEEQ, STEER and STEES for the tuning of nuclear interactions.

For each step, for charged particles as well as for neutral particles, the main response routine MRKRSP is called once. As arguments the absorbed energy EDEP and the cartesian coordinates X,Y,Z of the middle of the step are given. The working buffer /RESULT is filled with the parameters of the current track. Note that the stepsize DELTN may be zero for stopping tracks and EDEP is naturally zero for neutral particles.

In case of particle production by a decay or an interaction, all produced tracks are temporary written on the /BLANK- common PV(10,200) with

PV(1,*)	p_x
PV(2,*)	p_y
PV(3,*)	p_z
PV(4,*)	E
PV(5,*)	M
PV(6,*)	Charge
PV(7,*)	TOF
PV(8,*)	Mass-index
PV(9,*)	0.
PV(10,*)	(Track-label or userword)

The arguments of the call HSTORY(NFLG,NMODE,NIN,NOUT1,NOUT2) specify, in which locations the primary particle (PV(*,NIN)) and the secondary particles (PV(*,NOUT1) - PV(*,NOUT2)) are stored. NFLG and NMODE describe the type of decay/interaction as follows :

NFLG	NMODE	
		Stopping and skipped tracks :
0	0	Particle leaves (NIN=NOUT1=NOUT2=0) or enters (NIN=NOUT1=NOUT2=1)the detector.
	1	Particle stops by dE/dx.
	2	Particle out of time trigger (TOF>TOFCUT).
	3	Particle skipped by SELECT.
	4	Particle energy too low, start shower parametrization.
	5	Shower parametrization stops.

NFLG	NMODE	
1	NOPT	Decay with the decay mode NOPT.

NFLG	NMODE	
		Nuclear interactions :
2	1	Coherent elastic scattering (COSCAT).
	2	Qusai elastic scattering (TWOB).
	3	Two cluster scattering model (TWOCLU).
	4	Iterative cascade model (GENXPT).
	5	Inelastic muon scattering (CASMU).
	6	Nuclear fission (FISSIO).
	7	Photo fission (IPFISS).
	8	π^-- absorption at rest (PIMABS).
	9	K^-- absorption at rest (KMABS).
	10	Neutron capture at rest (CAPTUR).
	11	$\bar{p}$ annihilation at rest (PBANH).
	12	$\bar{n}$ annihilation at rest (NBANH).

NFLG	NMODE	
		GHEISHA electromagnetic shower routines :
3	1	Electron/positron bremsstrahlung (GBREMS).
	2	Photon pair production (GPAIR).
	3	Muon bremsstrahlung (MBREMS).
	4	δ-ray production (DELRAY).

NFLG	NMODE	
		EGS electromagnetic shower routines :
4	1	Bremsstrahlung.
	2	Moeller scattering.
	3	Bhabha scattering.
	4	Positron annihilation.
	5	Annihilation at rest.
	6	Pair production.
	7	Compton scattering.
	8	Photoelectric interaction.

At the call to HSTORY the working buffer contains the decay/interaction vertex on (XEND,YEND,ZEND). The calling sequence in the decay/interaction routine is normally :

```
CALL HSTORY(NFLG,NMODE,NIN,NOUT1,NOUT2)
CALL SETCUR(NOUT1  )
CALL SETTRK(NOUT1+1)
CALL SETTRK(NOUT1+2)
.
CALL SETTRK(NOUT2-1)
CALL SETTRK(NOUT2  )
```

One of the outgoing tracks replaces the primary track on the working buffer (SETCUR), the other ones are written on the stack (SETTRK). Normally the program will continue with the first track, as shown in the example above, only for NFLG=2 and NMODE=3 or 4 the program continues with the last track :

```
CALL HSTORY(NFLG,NMODE,NIN,NOUT1,NOUT2)
CALL SETCUR(NOUT2  )
CALL SETTRK(NOUT1  )
CALL SETTRK(NOUT1+1)
.
CALL SETTRK(NOUT2-2)
CALL SETTRK(NOUT2-1)
```

If the user wants to continue with a track of his own choice, he can simply exchange the location of the tracks stored in PV(*,K1) and PV(*,K2) by a call to routine EXCHPV(K1,K2). The SETCUR- routine, which includes the option that the program continues with one of the particles of the current interaction/decay, may be jumped over by increasing the number of final state particles by 1 and by zeroing the PV(J,*)-vector to be written in SETCUR to the working buffer.

The tuning routines STEEP, STEEQ, STEER, STEES should be changed by experts only. As can be imagined from our discussuons in chapter 2, there are a lot of parameters in nuclear interactions, which are only poor measured or not known at all. Thus an overall tuning may be done by adjusting the following quantities :

1.) The sum $E_{kin,tot}$ of the total kinetic energy of all final state particles may be changed in routine STEES(X) by :

$$E'_{kin,tot} = X \cdot E_{kin,tot} \quad .$$

This will influence mainly the total pulse height as measured in calorimetric devices.

2.) The fluctuation of this kinetic energy may be tuned by a call to STEER(Y) according to :

$$\sigma'(E'_{kin,tot}) = Y \cdot \sigma(E'_{kin,tot}) \quad .$$

This will change mainly the intrinsinc energy resolution.

3.) STEEQ(XS,XG) and STEEP(XB) affect the single particle kinetic energy for shower particles, grey track particles and black track particles respectively :

$$E'_{kin,s} = XS \cdot E_{kin,s}$$
$$E'_{kin,g} = XG \cdot E_{kin,g}$$
$$E'_{kin,b} = XB \cdot E_{kin,b}$$

As can be seen, STEES and STEER introduce an overall change of the released kinetic energy, whereas with STEEP and STEEQ a fine adjustment may be done. All four routines are enclosed on the library as dummy versions with X = Y = XS = XG = XB = 1. At the call to these routines the working common is filled with the parameters of the incoming interacting track and the atomic and charge number of the target nucleus is written on ATNO2 and ZNO2 of the /CURPAR- common.

3.1.9 Hadron production by muons

There are three physical processes in the program, which may cause some confusion. Therefore we will spend the next three subchapters to discuss the following points : a) hadron production by muons; b) neutral kaons and c) δ-ray production. In this chapter we start with the first question.

The program flow for hadron production by muons is sketched in fig.103 (compare also the general flow diagram of the CALIM routine). Muons may loose energy by ionisation (DEDX called from TRACK), by δ-ray production (DELRAY) and by bremsstrahlung (MBREMS), or may decay (MUDKY). Hadron production is initiated in CASMU. We track as usual to the interaction vertex (TRACK) and calculate the current parameters of the scattered muon. Different to the normal scheme for interactions we now write the scattered muon track on the stack (SETTRK) and a (physically virtual) charged pion on the working buffer /RESULT. After return from CASMU we immediately jump to COMPO and generate the interaction of the pion with a nucleus of the material in the normal way as was discussed in chapter 3.1.5. Note that the HSTORY routine is called twice. Once from CASMU to indicate the scattering of the muon only and secondly from CASPIM or CASPIP to show the final state hadrons.

According to this scheme the muon track is written on the stack and the program continues with tracking of one of the final state hadrons.

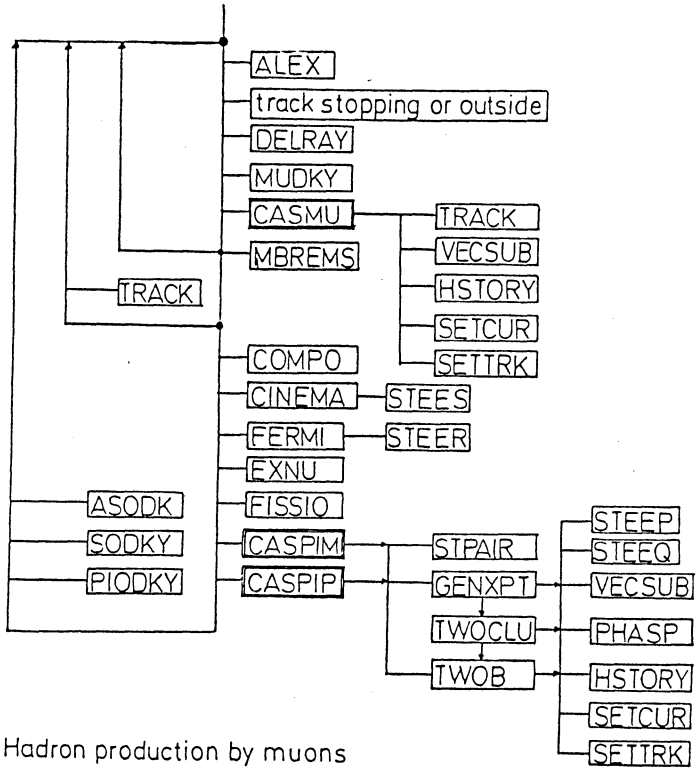

Hadron production by muons

Figure 103. Flow diagram for hadron production by muons.

3.1.10 The neutral kaon problem

Normally the program recognizes neutral kaons by a positive or negative mass as K_S^0 or K_L^0 respectively and assigns a particle index IPART=11 for K_S^0 and IPART=12 for K_L^0 (MASIND). In the decay routines they are trivially handled as K_S^0 and K_L^0(see fig.104). The elastic and inelastic cross sections have only been measured for K_L^0. These are tabulated on a disk-file . For K_S^0 we calculate the cross sections in routine CSDATA (see chapter 2.6.2). The complication arises if we enter the cascading routines. Here we have to convert the K_S^0 and K_L^0 into K^0 and $\bar{K}^0$. Thus the particle index may change from 11 to 12 or from 12 to 11. Our convention is IPART=11 for K^0 and IPART=12 for $\bar{K}^0$. The sign of the kaon mass is not changed. So the user may recognize in the HSTORY routine, called by CASK0 or CASK0B, whether the original particle was a K_S^0 or K_L^0.

3.1.11 Production of δ-rays

δ-ray production by muons in gaseous materials is treated differently from the general scheme. The number of electrons may become extremely large in dense materials. This makes it impossible to write all δ-rays on the stack. We proceed as follows, as is diagrammed in fig. 105.

The original muon track parameters on the working buffer are copied to a temporare buffer (UCOPY). Then we enter a loop for the generation of one δ-ray after the other, calculating first the emission vertex, stepping forward to this vertex by a call to MFSTP1(1) and by using the VECSUB package for kinematical calculations. If the kinetic energy of the electron exceeds CENG(2), the track parameters are written on the stack (SETTRK) and the HSTORY routine is called. These tracks are treated afterwards in the normal way, using GHEISHA or EGS for the electromagnetic shower expansion.

For E_{kin} < CENG(2) we immediately track the electron through the detector, until it reaches a non-gaseous material. In that case it will be absorbed without further action. The tracking procedure is similar to that used in the ALEX- routine, but much more simplified and less accurate. The magnetic field stepping routine MFSTQ with the entry MFSTQ1 is an exact copy from MFSTP, and is used only in connection with δ-rays. DELRAY has to use its own stepping routine, because we do not want to overwrite the transformations for the step of the muon track, which are stored in MFSTP. We do need this transformations to calculate the emission vertex of each electron. If all δ-rays are treated in one or the other way, we copy back the parameters of the muon track to the working buffer.

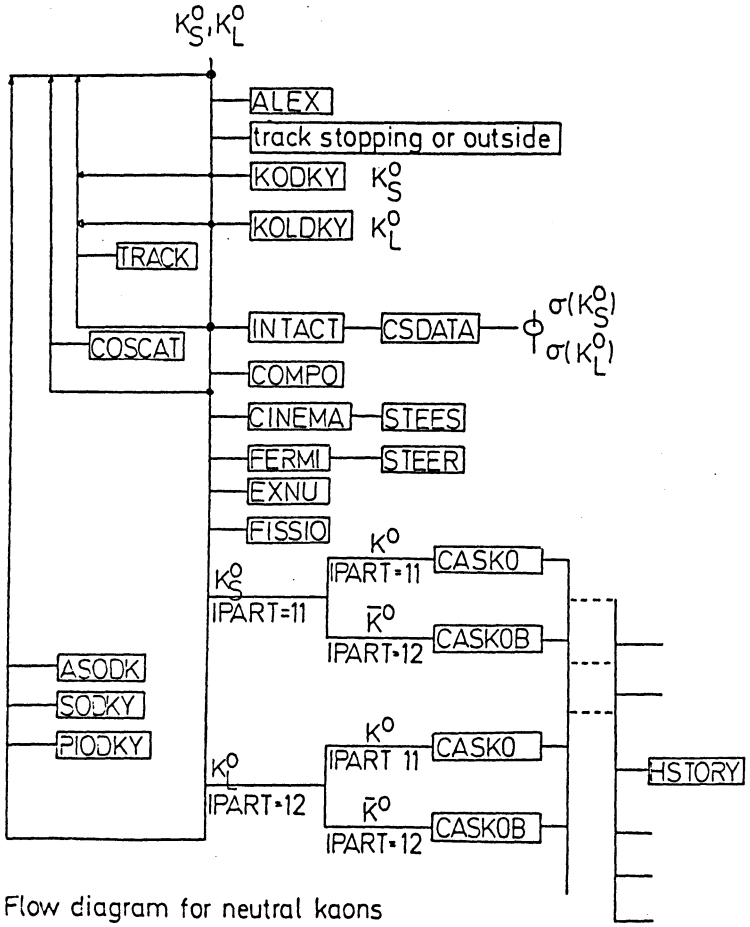

Flow diagram for neutral kaons

Figure 104. Flow diagram for K_S^0-K_L^0 regeneration.

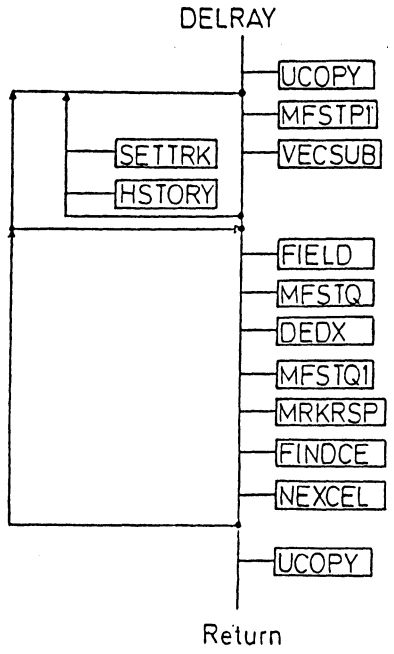

Figure 105. Flow diagram for the tracking of δ-rays.

As can be seen the HSTORY routine is called for high energetic electrons only, but here it is called for each produced electron. This is unavoidable, because the emission vertices are different . For low energetic δ-rays we neither do call the HSTORY routine nor do we change the particle index. The program does not distinguish low energy δ-rays from the original muon track. The total kinetic energy of all produced electrons are finally subtracted from the ionization energy as calculated by DEDX in routine TRACK. If the result is negative the remaining energy is subtracted from the kinetic energy of the muon. But note that the ionization energy may vanish in case of multiple δ-ray production in one step.

3.1.12 Use of the EGS package

EGS for electromagnetic showers (see ref. [4]) is used more or less as black box. The implementation into the GHEISHA- system has been done by

D.Braun [109]. The data-files for all materials used in the present version are already included in the library or may be produced using the pre-processor PEGS3 (see also chapter 3.1.2). If SHFLAG is set to zero, the interface routine EGS is called for all photons, electrons and positrons. In that case one has to include the member BLOCK as block-data definition, which combines the EGS block data and the GHEISHA block data. Otherwise the member BLDATA is sufficient. The value on SHFLAG may be changed during a run, so that EGS and the GHEISHA electromagnetic shower routines may be used alternatively.

The subroutine EGS makes some further initialization at the first call, which are all taken from the corresponding initializations done in GHEISHA before. The only exceptions are the cut-off parameter. They are defined as P_c = 1.5 MeV for electrons and positrons and by E_c = 100 keV for photons. These may only be changed in the EGS interface routine itself.

The tracking routine HOWFAR calls also FINDCE and NEXCEL for cell-finding and MRKRSP for the detector response. The history routine HSTORY has been introduced for all interactions (see also chapter 3.1.8) in subroutine SHOWER.

3.2 CHANGES FOR THE IMPROVED GHEISHA7 VERSION

3.2.1 Materials

In the last version GHEISHA7 the input and description of the material constants have been changed. In routine MATTER the EGS data files and an additional GHEISHA data file (#MATDATA) with some further informations are read in. Missing material parameters are, if possible, calculated. EGS data files are already prepared for some hundred different materials, for elements as well as for mixtures and compounds. There may be selected up to 20 materials by input cards. The order of the input stream defines the material index IND. IND = 0 is always interpreted as vacuum in the program. This material index must be given for each cell of each module in the geometry input cards too (see later). The COMMON /MAT has been reorganized in the following way:

```
COMMON/MAT    / LMAT,
              DEN(21),RADLTH(21),ATNO(21),ZNO(21),ABSL(21),
              CDEN(21),MDEN(21),XODEN(21),X1DEN(21),RION(21),
              MATID(21),MATID1(21,24),PARMAT(21,10),
              IFRAT,IFRAC(21),FRAC1(21,10),DEN1(21,10),
              ATNO1(21,10),ZNO1(21,10)
```


with meaning of the variables:

```
DEN    (IND+1) :  density;
RADLTH(IND+1) :  radiation length;
ATNO   (IND+1) :  atomic number (average value, see later);
ZNO    (IND+1) :  charge number of nucleus (average value, see later);
```

The previous numbers are taken first from the EGS files, are overwritten by the values given in #MATDATA (if different from zero), and may be finally changed by the material input cards.

```
ABSL   (IND+1) :  absorbtion length (asymptotic value, used only for
                  stepsize calculations);
```

The radiation length and absorbtion length are calculated in routine MATTER, if they are set to zero in the data files;

```
CDEN   (IND+1)     :
MDEN   (IND+1)     :
XODEN  (IND+1)     :  Sternheimer's parameter;
X1DEN  (IND+1)     :
RION   (IND+1)     :
MATID  (IND+1)     :  GHEISHA alphanuneric label (A4);
MATID1(IND+1,24)   :  EGS alphanumeric label (24*A1);
```

There follow 10 parameter used at various places in the program. These numbers have to be specified in the GHEISHA data file and may be overwritten in the material input cards.

```
PARMAT(IND+1, 1) = x    changed the width of dE/dx distribution,
                        σ(dE/dx)= x·σ(dE/dx,theor);
PARMAT(IND+1, 2) = 1.   solids;
                 = 2.   fluids;
                 = 3.   gaseous materials;
PARMAT(IND+1, 3) = 1.   δ-ray selection : all particles;
                 = 2.   δ-ray selection : muons only;
                 = 3.   δ-ray selection : muons and electrons;
                 = 4.   δ-ray selection : muons,electrons and pions;
PARMAT(IND+1, 4) = x    minimum range for δ-rays;
```

```
PARMAT(IND+1, 5) = 1.   apply cross section corrections in INTACT;
PARMAT(IND+1, 6) = x    saturation coefficient in Birk's law;
PARMAT(IND+1, 7) = 1.   induced nuclear fission;
                 = 2.   natural radioactivity;
                 = 3.   induced fission and radioactivity;
PARMAT(IND+1, 8) = u
PARMAT(IND+1, 9) = v    correction parameters in CINEMA, for experts;
PARMAT(IND+1,10) = w
```

All materials may be defined as compounds or mixtures, the following numbers are taken from the EGS data file:

```
IFRAC(J)     : number of constituents;
FRAC1(J,I)   : partial interaction lengths;
DEN1 (J,I)   : partial densities;
ATNO1(J,I)   : atomic number of the constituents;
ZNO1 (J,I)   : charge number of the constituents;
```

The material input cards are read in by routine INIT.

3.2.2 Geometry

The geometry definition used in the GHEISHA6 version was too inconvinient for some applications. A fixed array of 20 modules with a maximum of 100 cells for each module was not sufficient for very large high energy detectors. Consequently in the GHEISHA7 version a variable one-dimensional storage has been introduced. The COMMON /CALSTR now looks like:

```
COMMON/CALSTR/ NCALO,KCALO(1000)
DIMENSION RCALO(100)
EQUIVALENCE (KCALO(1),RCALO(1))
```

with

```
NCALO                 number of modules;
KCALO(1)        ┐
                ├     number of cells in each module;
KCALO(NCALO)    ┘
KCALO(NCALO+1)  ┐
                ├     number of words to be stored for each cell;
KCALO(2*NCALO)  ┘
```



```
KCALO(2*NCALO+1)  ┐
                  ├   link to the position for the beginning of
KCALO(3*NCALO)    ┘   storage of a certain module;
```

The geometry description of the j.th cell in the i.th module starts at location

```
LOCIJ=KCALO(2*NCALO+I)+(J-1)*KCALO(NCALO+I)
```

and the following words have to fulfill the following contraints:

```
NWORD=KCALO(NCALO+I)   number of words;
KCALO(LOCIJ+1)         material index as given by the sequence of
                       the material input data cards;
RCALO(LOCIJ+2)         maximum stepsize allowed in this cell.
RCALO(LOCIJ+3)  ┐
RCALO(LOCIJ+4)  │      (NWORD-2) variables which define the geometry
RCALO(LOCIJ+5)  │      of this cell in a unique, but arbitrary, way.
RCALO(LOCIJ+6)  ├      These quantities are only used in the user-
RCALO(LOCIJ+7)  │      FINDCEL, NEXCEL and OUTCEL. Other parts
RCALO(LOCIJ+8)  │      of the program use the material index and the
RCALO(LOCIJ+9)  │      maximal stepsize only.
RCALO(LOCIJ+NWORD) ┘
```

In the GHEISHA7 version each module may have up to 1000 cells, the number of modules is limited to 100. The number of words per cell may vary for different modules, but must be the same for all cells of a certain module.

3.2.3 Improved physics

Nearly all physics improvements for the GHEISHA7 version have already been discussed in chapter 2. Nevertheless we want to point out here the main differences between the GHEISHA6 and GHEISHA7 versions:

1.) The physics of the K^0_S - K^0_L interference has been reconsidered. The two pion decay of the K^0_L was missing in the previous version. For a discussion see the text to fig.33 in chapter 2.

2.) Comparisons of the prediction for uranium calorimters with experimental data can not be done without simulation of the noise from radioactivity. Thus spontaneous decays of uranium isotopes and of their

daughter elements have been included in the last version. This work is not finished.

3.) Longitudinal shower profile measurements in BGO have been used to tune the π^0 energy spectra for heavy elements. This will be described in chapter 5.6.

4.) Nuclear spallation at low and medium energies has been reconsidered. Small changes in the number of particles emitted have been carried out. A sizable effect for the response of sampling calorimeter has not been observed.

5.) The treatment of neutrons at very low energies has been totally changed. Optical model calculations have been carried out to calculate the elastic and inelastic cross sections. A separate routine NSLDOW has been introduced to simulate the moderation down to thermic energies. It includes also the capture of the neutrons by nuclei. The response of an experimental set-up to neutrons is a function of the sensitive trigger time. Thus we recommend to careful adjust the cut-off energy CENG(4) in accordance with the sensitive time, given by the TOFCUT- parameter. For a few microseconds trigger time it seems to be unavoidable to choose a cut-off energy in the order of keV. For some hundred nanoseconds a cut-off energy in the order of 100 keV or even some MeV may be sufficient.

4.0 MUONS IN TRACKING CALORIMETER

4.1 MOMENTUM SPREAD IN TRACKING CALORIMETER

In future storage ring experiments the hadron filter will be normally built up by absorber layers of thickness in the order of centimeters or even millimeters, interspaced by chambers with one-or two- dimensional read-out. Such structures will be studied in later sections in great detail. Here we want only to discuss a quite amazing application, namely the momentum measurement by multiple scattering. This technique has a long history in old emulsion experiments.

To achieve a total absorber thickness of about 1 m one has, with 2.5 cm iron layer thickness, 40 layers of iron and chambers respectively. Such a structure allows the measurement of the multiple scattering constant ($a\sigma_\vartheta^2$) and via equ.(2.39) the measurement of momentum. We discuss here the method of sagittas, which has been worked out by nuclear emulsion and bubble chamber experiments.

Consider three points with coordinates (Z_i-s,X_{i-1}), (Z_i,X_i) and (Z_i+s,X_{i+1}) (see fig.106), then the sagitta of zero order is defined as

$$S_i^{(0)} = X_{i+1}-2X_i+X_{i-1} \quad . \tag{4.1}$$

Similarly one can define higher order sagittas by

$$S_i^{(1)} = X_{i+2}-2X_i+X_{i-2} \tag{4.2}$$

$$S_i^{(2)} = X_{i+4}-2X_i+X_{i-4} \quad . \tag{4.3}$$

It is evident that in this quantities any inclination angle of the track with respect to the absorber cancels out.

The sagitta $S_i^{(0)}$ at any point Z_i can be expressed in terms of the position and angle z_k and ϑ_k of the elementary scattering process as

$$S_i^{(0)} = \sum \Delta(Z_i-z_k)\ \vartheta_k \tag{4.4}$$

$$\Delta(Z-z) = \begin{cases} 0 \text{ for } |Z-z|>s \\ s-|Z-z| \text{ for } |Z-z|<s \end{cases} \quad . \tag{4.5}$$

$S_i^{(0)}$ is defined in such a way that $\langle S_i^{(0)}\rangle = 0$, whereas (see also fig.107)

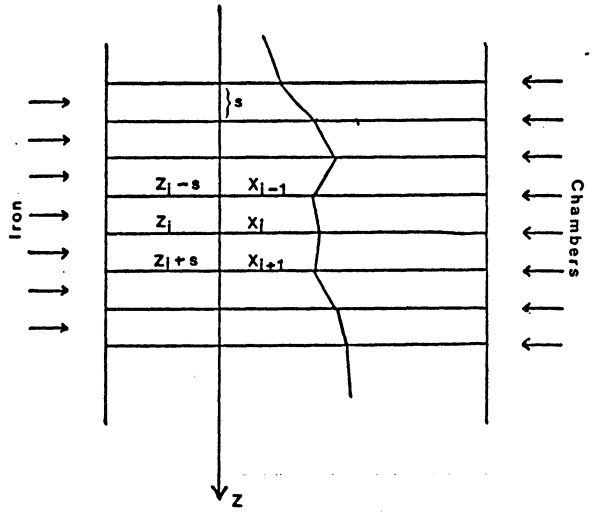

Figure 106. Definition of variables used in multiple scattering.

$$\langle (S_i^{(0)})^2 \rangle = \iint a\Phi(\vartheta)\, \Delta^2(Z_i-z)\vartheta^2\, dz\, d\vartheta \qquad (4.6)$$
$$= a\sigma_\vartheta^2\, 2\int_0^s dz\, z^2$$
$$= (2/3)\, a\sigma_\vartheta^2 s^3 \quad .$$

In practice each measured coordinate X_i is subject to setting errors of the chambers

$$X_i = X^C_i + X^E_i \quad , \qquad (4.7)$$

where index C denotes Coulomb scattering and E setting error. Trivially we have

$$\langle X^E_i \rangle = 0$$
$$\langle X^E_i X^E_k \rangle = \begin{cases} 0 & \text{for } i \neq k \\ \sigma_E^2 & \text{for } i=k \end{cases} \qquad (4.8)$$
$$\langle X^C_i X^E_k \rangle = 0 \quad .$$

Now we have N+1 points of the track with Z-coordinates

$$Z_i = i \cdot s \quad , \; i=0,1,\ldots,N \quad . \qquad (4.9)$$

We may form N-1 sagittas of zero order

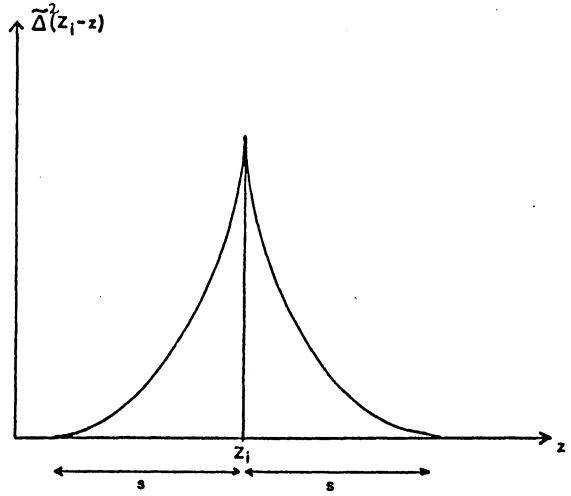

Figure 107. $\tilde{\Delta}^2$-function used in multiple scattering.

$$S_i^{(0)} = X_{i+1}-2X_i+X_{i-1} \quad . \qquad (4.10)$$

To a good approximation the sagittas due to multiple scattering and to setting errors are both Gaussian distributed and by folding we get for

$$S_i^{(0)} = S^C{}_i^{(0)} + S^E{}_i^{(0)} \qquad (4.11)$$

the distribution function

$$P(S^{(0)}) = C \exp\left[-\tfrac{1}{2} \sum_{ik} A_{ik}\, S_i^{(0)} S_k^{(0)} \right] \quad , \qquad (4.12)$$

where the elements $(A^+)_{ik}$ of the inverse matrix A^{-1} are given by

$$(A^+)_{ik} = \langle S_i^{(0)} S_k^{(0)} \rangle = \langle S^C{}_i^{(0)} S^C{}_k^{(0)} \rangle + \langle S^E{}_i^{(0)} S^E{}_k^{(0)} \rangle \quad . \qquad (4.13)$$

With a similar calculation as that leading to equ.(4.6) we get

$$A^{-1} = \varepsilon^C B^C + \varepsilon^E B^E \qquad (4.14)$$

with

$$\varepsilon^C = \frac{1}{6} a\sigma_\vartheta^2 s^3 \tag{4.15}$$

$$B^C_{ik} = \begin{cases} 4 \text{ for } i=k \\ 1 \text{ for } |i-k|=1 \\ 0 \text{ for } |i-k|>1 \end{cases} \tag{4.16}$$

$$B^E_{ik} = \begin{cases} 6 \text{ for } i=k \\ -4 \text{ for } |i-k|=1 \\ 1 \text{ for } |i-k|=2 \\ 0 \text{ for } |i-k|>2 \end{cases} \tag{4.17}$$

From statistical theory we get the maximum likelihood equation for determination of parameters ε^C and ε^E:

$$\sum_{ik} \frac{\partial A_{ik}}{\partial \varepsilon} \left((A^{-1})_{ik} - S_i^{(0)} S_k^{(0)} \right) = 0 \tag{4.18}$$

$\varepsilon = \varepsilon^C$ or ε^E

In equ. (4.18) there has a matrix to be inverted, which contains the parameters ε^C and ε^E. Therefore this inversion has to be done analytically before the derivatives can be calculated. This is far too inconvinient for our applications in this moment. Thus we apply some approximate determinations. In the next section we come back to a discussion of equ. (4.18).

For zero setting errors, i.e. $\varepsilon^E = 0$, we get:

$$(A^+)_{ik} = \langle S^C_i{}^{(0)} S^C_k{}^{(0)} \rangle = \varepsilon^C B^C_{ik} \tag{4.19}$$

$$A_{ik} = \frac{1}{\varepsilon^C} ((B^C)^{-1})_{ik} \tag{4.20}$$

Then equ. (4.18) is simply solved by

$$\langle \bar{\varepsilon}^C \rangle = \frac{1}{N} \sum_{ik}^{N} (B^{C+})_{ik} S_i^{(0)} S_k^{(0)} \tag{4.21}$$

with the scatter

$$\frac{\langle (\bar{\varepsilon}^C - \langle \bar{\varepsilon}^C \rangle)^2 \rangle}{(\bar{\varepsilon}^C)^2} = \frac{2}{N} \tag{4.22}$$

The relative error for ε^C is then

$$\frac{\delta \bar{\varepsilon}^C}{\bar{\varepsilon}^C} = \sqrt{\frac{2}{N}} \tag{4.23}$$

With

$$\bar{\varepsilon}^C = \frac{1}{6} \frac{\alpha^2}{p^2} \frac{s^3}{X_0} \tag{4.24}$$

we get for the momentum determination

$$\bar{p} = \frac{1}{\sqrt{6}} \frac{\alpha}{\sqrt{\bar{\varepsilon}^C}} \frac{s\sqrt{s}}{\sqrt{X_0}} \tag{4.25}$$

with the scatter

$$\frac{\delta \bar{p}}{\bar{p}} = \frac{1}{2} \frac{\delta \bar{\varepsilon}^C}{\bar{\varepsilon}^C} = \frac{1}{2} \sqrt{\frac{2}{N}} \tag{4.26}$$

This method has been studied for a detector set-up consisting of 40 layers of iron, each with a thickness of 2.5 cm, and 40 layers of chambers, 0.5 cm thick each. In figs. 108 and 109 we show the simulation results for $\bar{\varepsilon}^C$ and $\bar{p}$ compared to the expectation from (4.24). Fig. 110 shows the results for $\delta\bar{p}/\bar{p}$. Note that in our calculations leading to equs. (4.18) and (4.21) energy loss has not been taken into account (a(z)=a=constant). Therefore we do not expect a perfect agreement at low momenta. For $p \leq 1.8$ GeV/c the muons stop inside the filter and a much better method for momentum determination is given by energy-range formulae. Also shown are results for iron replaced by lead and alluminum. For Al we get a nearly linear response in p. The same improvement in the linearity could also be obtained by choosing thinner Fe-layers at low momenta. For a set-up of 20 Fe-layers with 1 cm thickness and 30 additional layers of 2.5 cm thickness one gets a perfect linearity (not shown).

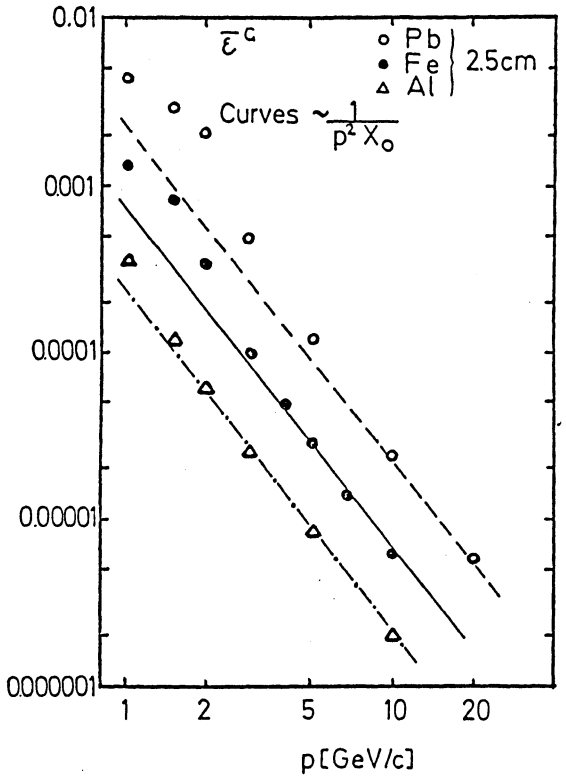

Figure 108. Multiple scattering constant $\bar{\varepsilon}^c$ as function of momentum for Al, Fe and Pb. The curves represent the expectation from (4.24).

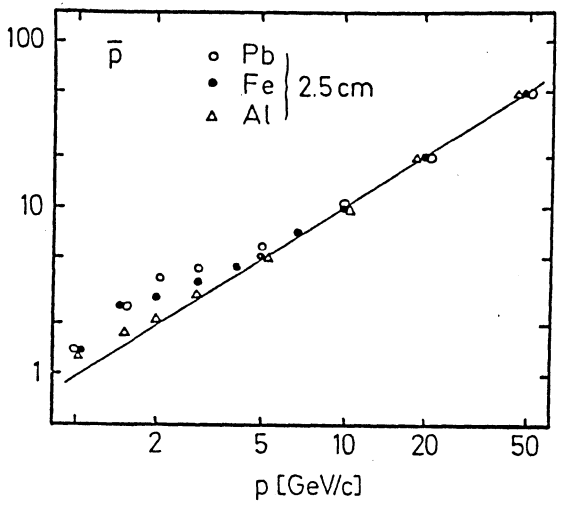

Figure 109. Momentum determined by multiple scattering as function of momentum of the primary muon. The curves represent the expectation from (4.25).

To get some feeling for the influence of the setting error to the momentum resolution, we have used a very approximate method. We calculate the average squared sagittas

$$d^{(0)} = \frac{1}{N} \sum_{i=1}^{N} (S_i^{(0)})^2 \tag{4.27}$$

$$d^{(1)} = \frac{1}{N} \sum_{i=1}^{N} (S_i^{(1)})^2 \tag{4.28}$$

$$d^{(2)} = \frac{1}{N} \sum_{i=1}^{N} (S_i^{(2)})^2 \tag{4.29}$$

and get after some cumbersone manipulations

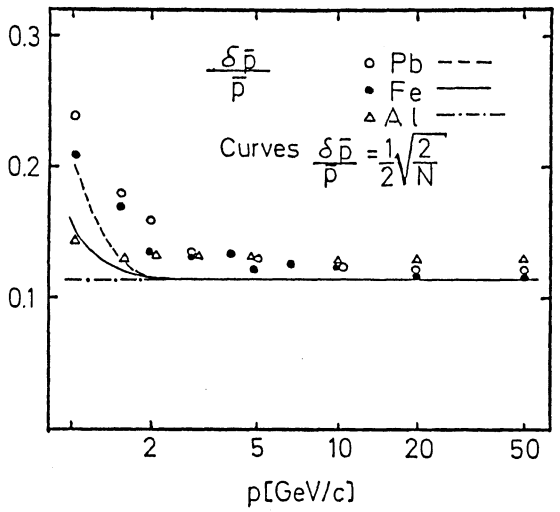

Figure 110. Momentum resolution determined by multiple scattering as function of momentum of the primary muon. The curves represent the expectation from (4.26).

$$\bar{\varepsilon}^C = \frac{1}{28}\,(-d^{(0)}+d^{(1)}) \tag{4.30}$$

$$\bar{\varepsilon}^E = \frac{1}{42}\,(8d^{(0)}-d^{(1)}) \tag{4.31}$$

with the expected scatter

$$\frac{\langle(\delta\bar{\varepsilon}^C)^2\rangle}{(\bar{\varepsilon}^C)^2} = \frac{2}{N}\left[\frac{1}{392}(42x^2+96x+941)\right] \tag{4.32}$$

and $x = \bar{\varepsilon}^E/\bar{\varepsilon}^C$. Another estimate is

$$\bar{\varepsilon}^C = \frac{1}{252}\,(-d^{(0)}+d^{(2)}) \tag{4.33}$$

$$\bar{\varepsilon}^E = \frac{1}{378}\,(64d^{(0)}-d^{(2)}) \tag{4.34}$$

with

$$\frac{\langle(\delta\bar{\varepsilon}^C)^2\rangle}{(\bar{\varepsilon}^C)^2} = \frac{2}{N}\left[\frac{1}{31752}(34x^2+992x+139895)\right] \tag{4.35}$$

From (4.32) and (4.35) one can conclude that (4.30) and (4.31) should be used for $x < 3.5$ and (4.33) and (4.44) for $x > 3.5$. We see from (4.32) and (4.35) that even for vanishing setting errors this method gives a resolution worse by a factor 1.5 and 2.1 respectively compared to the maximum likelihood method. But the dependence of the momentum resolution as function of the setting errors should be comparable. The limit of acceptable setting errors is approximately given by

$$\sigma_E^2 = \bar{\varepsilon}^E \approx \bar{\varepsilon}^C = \frac{1}{6}\left(\frac{\alpha}{p}\right)^2 \frac{s^3}{X_0} \tag{4.36}$$

Inserting the values $X_0 = 1.76$ cm , $\alpha = 0.015$ GeV/c, $s = 2.5$ cm one gets

$$\sigma_E \approx \frac{0.018}{p[\mathrm{GeV}]} \quad [\mathrm{cm}] \tag{4.37}$$

i.e. the setting error of 200 microns seems to be a reasonable choice for the momentum range of 1-10 GeV/c.

The results of the simulation are shown in fig. 111 for the measured momentum resolution and in fig. 112 for the measured setting errors. We conclude that even with a setting error of 300 - 500 mμ one can obtain a momentum resolution of better than 30 %. The method of multiple scattering for momentum measurement may be applied in end cap tracking calorimeter in toroidal magnetic fields.

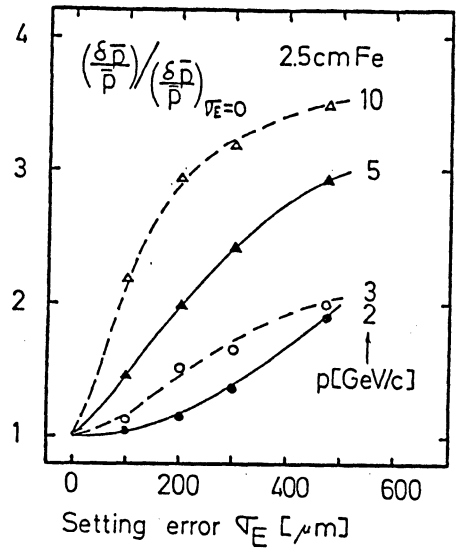

Figure 111. Momentum resolution as function of the setting error σ_E The sampling is 2.5 cm Fe. For details see text.

The momentum measurement by multiple scattering is limited by setting errors and by problems due to the survey of the chambers. On the other hand, the methods discussed in this section are very powerfull for measuring the setting errors and systematic distortions due to an uncertain survey in complex calorimeter systems like those proposed for LEP.

Then we have

$$\langle S_\nu^{(0)} \rangle = f_\nu \quad , \nu=1,\ldots,N \quad . \tag{4.38}$$

The distribution of the sagittas is in generalization of equ. (4.12)

$$P(S^{(0)}) = C \exp\left(-\tfrac{1}{2} \sum_{\nu\mu} A_{\nu\mu}(S_\nu^{(0)}-f_\nu)(S_\mu^{(0)}-f_\mu)\right) \quad . \tag{4.39}$$

As the S_ν-f_ν are independent of f_ν, the last parameters can be easily measured by equ. (4.38) and the estimation of ε^C and ε^E can be carried out according to the methods discussed above replacing the measured $S_\nu^{(0)}$ by $S_\nu^{(0)}-f_\nu$.

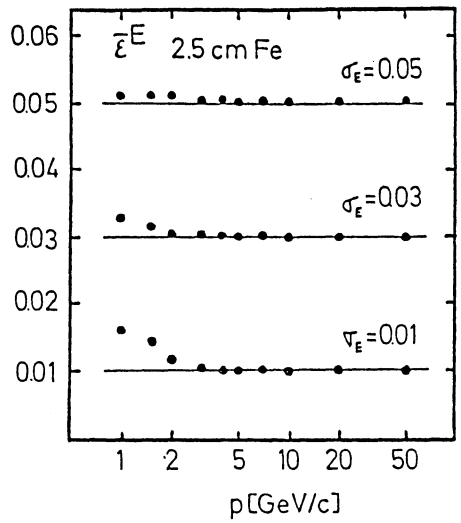

Figure 112. Measured setting errors (in cm) as function of momentum. The sampling is 2.5 cm Fe. For details see text.

4.2 MEASUREMENT OF COORDINATES

In the following we shall study an absorber structure like that shown in fig.113. N absorber layers, each of a thickness of s cm, are interspaced by N chambers, which measure the x-coordinate only.
The magnetic field B is in positive y-direction. In the approximation (2.72) and (2.73), i.e.

$$x_k = -\tfrac{1}{2} \frac{qBk^2s^2}{3336\ p} = f_k \quad , \tag{4.40}$$

energy loss is neglected. The combined probability for all coordinates can be written

$$G(X_1, X_2, \ldots, X_N) = \tag{4.41}$$
$$C \exp\left(-\tfrac{1}{2} \sum_{\nu\mu} \hat{A}_{\nu\mu}(X_\nu-f_\nu)(X_\mu-f_\mu)\right) \quad .$$

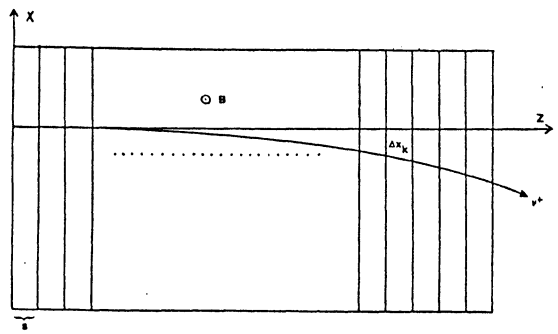

Figure 113. Definition of variables used in magnetic field tracking.

The maximum likelihood solution gives for the scatter of the momentum

$$\frac{1}{\langle(\delta p)^2\rangle} = -\left\langle \frac{\partial^2 \ln G}{\partial^2 p} \right\rangle \quad , \tag{4.42}$$

which can be solved by

$$\frac{1}{\langle(\delta p)^2\rangle} = \tfrac{1}{2}\,\mathrm{tr}\left(\hat{A}\,\frac{d\hat{A}^{-1}}{dp}\,\hat{A}\,\frac{d\hat{A}^{-1}}{dp}\right) + \sum \hat{A}_{ik}\,\frac{df_i}{dp}\,\frac{df_k}{dp} \quad . \tag{4.43}$$

The inverse $\hat{A}^{-1}$ of matrix $\hat{A}$ can be calculated (see equs (4.7) and (4.8))

$$(\hat{A}^{-1})_{\nu\mu} = \langle \hat{X}^C{}_\nu \hat{X}^C{}_\mu \rangle + \langle \hat{X}^E{}_\nu \hat{X}^E{}_\mu \rangle \quad , \tag{4.44}$$

$$\hat{X}_\nu = X_\nu - f_\nu = \hat{X}^C{}_\nu + \hat{X}^E{}_\nu \quad .$$

The indices C and E refer to Coulomb scattering and setting error respectively. Inspection to formulas (2.48)-(2.54) tells us that

$$(\hat{A}^{-1})_{\nu\mu} = -\frac{1}{6}\left(\frac{\alpha}{p}\right)^2 \frac{s^3}{X_0}\,\hat{G}_{\nu\mu} + \sigma_E{}^2 \delta_{\nu\mu} \tag{4.45}$$

with

$$\hat{G}_{\nu\mu} = \begin{cases} 3\nu^2\mu - \nu^3 & \text{for } \mu \geq \nu \\ 3\nu\mu^2 - \mu^3 & \text{for } \mu \leq \nu \end{cases} \tag{4.46}$$

and

$$\frac{d(\hat{A}^{-1})_{\nu\mu}}{dp} = -\tfrac{1}{3}\left(\frac{\alpha}{p}\right)^2 \frac{s^3}{X_0}\,\frac{1}{p} - \hat{G}_{\nu\mu} \tag{4.47}$$

$$\frac{df_\nu}{dp} = \tfrac{1}{2}\,\frac{qB\nu^2 s^2}{3336\ p^2} \quad . \tag{4.48}$$

It is no problem to solve equ.(4.43) with (4.45) to (4.48) with numerical matrix-inversion. For some extreme cases equ.(4.43) can also be solved analytically. For $X_0 \to \infty$, i.e. no multiple scattering, we get

$$(\hat{A}^{-1})_{\nu\mu} = \sigma_E{}^2 \delta_{\nu\mu}$$

$$\hat{A}_{\nu\mu} = \frac{1}{\sigma_E{}^2}\,\delta_{\nu\mu} \tag{4.49}$$

$$\frac{d(\hat{A}^{-1})_{\nu\mu}}{dp} = 0$$

and

$$\left(\frac{p^2}{\langle(\delta p)^2\rangle}\right)_{X_0 \to \infty}^{\text{Coord.}} = \frac{1}{4}\,\frac{1}{\sigma_E{}^2}\,\frac{B^2\ s^4}{(3336)^2\ p^2}\,F^E(N) \tag{4.50}$$

with

$$F^E(N) = \sum_{k=1}^{N} k^4 = \frac{N(N+1)(2N+1)(3N^2+3N-1)}{30} \tag{4.51}$$

On the other hand, for $\sigma_E = 0$, one finds

$$(\hat{A}^{-1})_{\nu\mu} = \frac{1}{6}\left(\frac{\alpha}{p}\right)^2 \frac{s^3}{X_0}\hat{G}_{\nu\mu}$$

$$\hat{A}_{\nu\mu} = 6\left(\frac{p}{\alpha}\right)^2 \frac{X_0}{s^3}(\hat{G}^{-1})_{\nu\mu} \qquad (4.52)$$

$$\frac{d(\hat{A}^{-1})_{\nu\mu}}{dp} = -\tfrac{1}{3}\left(\frac{\alpha}{p}\right)^2 \frac{s^3}{X_0}\frac{1}{p}\hat{G}_{\nu\mu}$$

and

$$\left(\frac{p^2}{\langle(\delta p)^2\rangle}\right)^{\text{Coord.}}_{\sigma_E=0} = 2N + (3/2)\frac{X_0 B^2 s}{(3336)^2\alpha^2}F^c(N) \qquad (4.53)$$

where

$$F^c(N) = \sum_{ik}^{N}(\hat{G}^{-1})_{ik}\, i^2k^2 \qquad (4.54)$$

is given in fig.114 and can be approximated by

$$F^c(N) \approx -0.20 + 0.68\ N \ . \qquad (4.55)$$

4.3 THE METHOD OF SAGITTAS

Instead of the coordinates one can also use the sagittas defined by

$$S_k = X_{k+1} - 2X_k + X_{k-1} \qquad (4.56)$$

Then

$$G(S_1,\ldots,S_M) = C\exp\left[-\tfrac{1}{2}\sum_{ik}\hat{B}_{ik}(S_i-g_i)(S_k-g_k)\right] \qquad (4.57)$$

where the

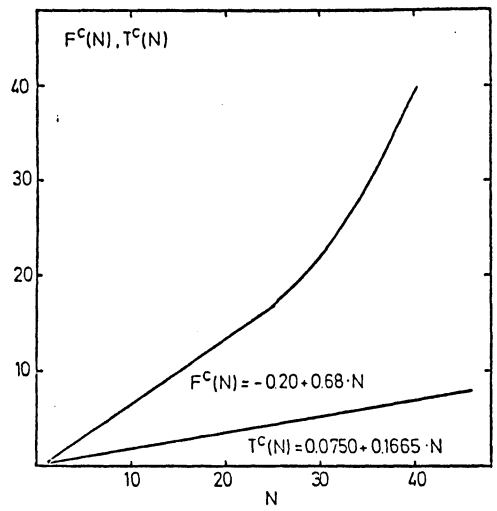

Figure 114. Function F^c and T^c as function of number of layers. For details see text.

$$g_i = \langle S_i\rangle = \frac{qBs^2}{3336\ p} \qquad (4.58)$$

do not depend on the layer number i or equivalently on the z-position of the chambers. The total number M of sagittas which can be built up is N - 2, where N is the number of chamber layers. The scatter of momentum is given by

$$\frac{1}{\langle(\delta p)^2\rangle} = \tfrac{1}{2}\,\mathrm{tr}\left(\hat{B}\frac{d\hat{B}^{-1}}{dp}\hat{B}\frac{d\hat{B}^{-1}}{dp}\right) + \sum\hat{B}_{ik}\frac{dg_i}{dp}\frac{dg_k}{dp} \qquad (4.59)$$

From the previous section we know that

$$(\hat{B}^{-1})_{\nu\mu} = \frac{1}{6}\left(\frac{\alpha}{p}\right)^2\frac{s^3}{X_0}(\hat{B}^c)_{\nu\mu} + \sigma_E^2(\hat{B}^E)_{\nu\mu} \qquad (4.60)$$

where

$$(\hat{B}^C)_{\nu\mu} = \begin{cases} 4 & \text{for } \nu=\mu \\ 1 & \text{for } |\nu-\mu|=1 \\ 0 & \text{for } |\nu-\mu|>1 \end{cases} \tag{4.61}$$

$$(\hat{B}^E)_{\nu\mu} = \begin{cases} 6 & \text{for } \nu=\mu \\ -4 & \text{for } |\nu-\mu|=1 \\ 1 & \text{for } |\nu-\mu|=2 \\ 0 & \text{for } |\nu-\mu|>2 \end{cases} \tag{4.62}$$

$$\frac{d(\hat{B}^{-1})_{\nu\mu}}{dp} = -\tfrac{1}{3}\left(\frac{\alpha}{p}\right)^2 \frac{s^3}{X_0}\frac{1}{p} (\hat{B}^C)_{\nu\mu} \tag{4.63}$$

$$\frac{dg_1}{dp} = -\frac{qBs^2}{3336\ p^2} \tag{4.64}$$

Similar to the calculation leading to equ.(4.50) and (4.53) we get in the present case

$$\left(\frac{p^2}{\langle(\delta p)^2\rangle}\right)^{\text{Sag.}}_{X_0\to\infty} = \frac{1}{\sigma_E^2}\frac{B^2s^4}{(3336)^2\ p^2} T^E(M) \tag{4.65}$$

$$\left(\frac{p^2}{\langle(\delta p)^2\rangle}\right)^{\text{Sag.}}_{\sigma_E=0} = 2M + 6\frac{X_0B^2s}{(3336)^2\ \alpha^2} T^C(M) \tag{4.66}$$

where

$$T^E(M) = \sum_{ik}^{M} ((\hat{B}^E)^{-1})_{ik} \tag{4.67}$$

and

$$T^C(M) = \sum_{ik}^{M} ((\hat{B}^C)^{-1})_{ik} \tag{4.68}$$

are given in figs.114 and 115. (4.68) can be approximated by

$$T^C(M) = 0.0750 + 0.1665\ M \quad . \tag{4.69}$$

Equ.(4.59) can also be solved generally by matrix inversion.

Comparing equs.(4.50) and (4.65) or (4.53) and (4.66) one concludes that the use of coordinates gives always a slightly better momentum resolution as the use of sagittas. But one has to keep in mind that using the coordinates one has to know the initial direction of the particle entering the absorber, whereas in the method of sagittas this direction must not be known. Therefore in practice the sagitta-method may be preferred. But on the other hand

$$\frac{1}{4} F^E(N) \gg T^E(N) \quad , \tag{4.70}$$

i.e. the momentum resolution in the sagitta-method is very sensitive to the setting errors. As we will see the sagittas are useless for $\sigma_E > 0.05$ cm.

4.4 INCLUSION OF ANGLE MEASUREMENTS

As we have already stated in the previous section, the best way to measure the momentum is the determination of one or more coordinates inside the absorber and the angle of the particle leaving the absorber. Then our distribution function is given by

$$G(X_1,\ldots,X_N,\theta_N) = C\ \exp\left(-\tfrac{1}{2}\sum_{\nu\mu}^{N+1}\hat{A}_{\nu\mu}(X_\nu-f_\nu)(X_\mu-f_\mu)\right) \quad , \tag{4.71}$$

where we have defined

$$X_{n+1} = \theta_n \tag{4.72}$$

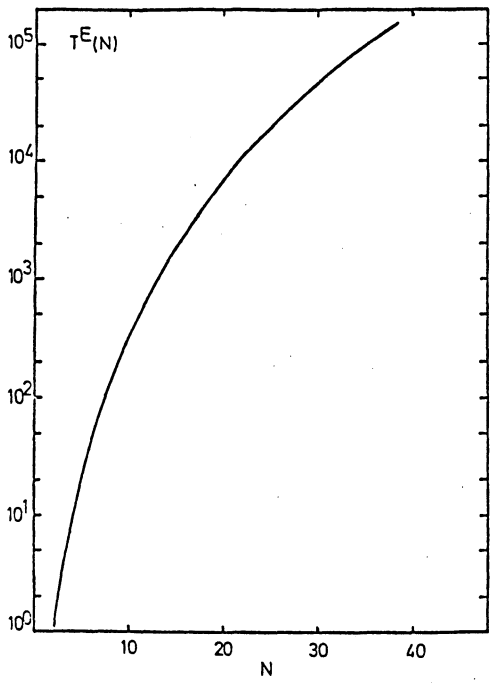

Figure 115. Function $T+^E$ as function of number of layers. For details see text.

$$f_{n+1} = \langle\theta_n\rangle = -tg(\gamma S) \approx \frac{2X_N}{N\ s} \quad . \tag{4.73}$$

The solution is again given by equ.(4.43) with equs.(4.45) to (4.48), one only has to add the following elements (see formulae (2.48) - (2.54)) :

$$(\hat{A}^{-1})_{\nu,N+1} = (\hat{A}^{-1})_{N+1,\nu} = \frac{1}{2}\left(\frac{\alpha}{p}\right)^2 \frac{\nu^2 s^2}{X_0} \qquad \text{for } \nu=1,N \tag{4.74}$$

$$(\hat{A}^{-1})_{N+1,N+1} = \left(\frac{\alpha}{p}\right)^2 \frac{Ns}{X_0} + \sigma_\theta^2 \tag{4.75}$$

$$\frac{d(\hat{A}^{-1})_{\nu,N+1}}{dp} = \frac{d(\hat{A}^{-1})_{N+1,\nu}}{dp} = -\left(\frac{\alpha}{p}\right)^2 \frac{\nu^2 s^2}{X_0}\frac{1}{p} \tag{4.76}$$

$$\frac{d(\hat{A}^{-1})_{N+1,N+1}}{dp} = -2\left(\frac{\alpha}{p}\right)^2 \frac{Ns}{X_0}\frac{1}{p} \tag{4.77}$$

$$\frac{df_{N+1}}{dp} = \frac{2}{N\ s}\frac{df_N}{dp} = \frac{qBNs}{3336\ p^2} \quad . \tag{4.78}$$

An analytic expression can only be derived for vanishing multiple scattering. Here we get

$$(\hat{A}^{-1})_{\nu\mu} = \sigma_E^2\ \delta_{\nu\mu} \qquad \text{for } \nu,\mu=1,N \tag{4.79}$$

$$(\hat{A}^{-1})_{\nu\mu} = \sigma_\Theta^2\ \delta_{\nu\mu} \qquad \text{for } \nu,\mu=N+1 \tag{4.80}$$

and

$$\left(\frac{p^2}{\langle(\delta p)^2\rangle}\right)^{\text{Coord.}+\Theta}_{X_0\to\infty} = \frac{1}{4}\frac{1}{\sigma_E^2}\frac{B^2 s^4}{(3336)^2\ p^2} F^E(N) + \frac{1}{\sigma_\Theta^2}\frac{B^2 s^2}{(3336)^2\ p^2} N^2 \tag{4.81}$$

where $F^E(N)$ is given by equ.(4.51). For all other cases the solution must be obtained by numerical matrix inversion. From equ.(4.81) one concludes that for $X_0 \to \infty$, i.e. for track chamber devices, there is no big advantage in measuring additionally the angle of the track in a magnetic free space. One wins in momentum resolution the more multiple scattering is expected. This is most easily seen mathematically in comparing the elements $(\hat{A}^{-1})_{\nu\mu}$, the inverse of which acts as weighting factors in the extended χ^2- and ML- solutions. The smaller the $(\hat{A}^{-1})_{\nu\mu}$, the bigger $\hat{A}_{\nu\mu}$. The diagonal-elements of $\hat{A}^{-1}$ go with $\frac{1}{3}\nu^3 s^3$ for the coordinate measurement,

whereas $(\hat{A}^{-1})_{N1N1}$ goes with only N·s for the measurement of the emission angle. Therefore the angle measurement is weighted by factors which may be some orders of magnetude bigger than those for the coordinate measurements. On the other hand one needs a lot of chamber layers to obtain a precise angle measurement. Therefore the main task will be to optimize the momentum resolution for a given number of chambers by distributing them inside the absorber to measure coordinates and outside the absorber to measure the emission angle. This will be done at the end of this section. It is no problem to generalize our formulae for any detector design with non equidistant distribution of measurement points, coordinate measurement and angle measurement in any order or more than one materials as absorbers. The elements of matrix $\hat{A}^{-1}$ can be read off from formulae (2.48) to (2.54), the f_ν can be calculated using (2.72) and (2.73). Multiple scattering is uncorrelated in both projections. Therefore for two-dimensional read-out the number of measurements is simply doubled. We come back to special solutions in later chapters. There we will also study a total other solution as discussed here, namely the momentum measurement outside the absorber using a magnetized experimental hall. This has of course nothing to do with tracking calorimters, but offers the best method for momentum measurement of muons. This method has been proposed for one of the future LEP-experiments.

4.5 MOMENTUM FITTING UNDER VARIOUS CONDITIONS

In order to compare our previous calculations with the results of the Monte-Carlo simulations, an experimental set-up like that shown in fig.113 has been chosen, with variable thickness s of the absorber layers and variable number N of absorber and chamber layers, demanding a total amount of absorbing material of 100 cm, a number which will be close to all today and future storage ring experiments :

$$S = s\,N = 100 \text{ cm} \quad . \tag{4.82}$$

Various materials have been chosen as absorbers like Pb, Fe, Al, liquid argon and isobutan with the radiation lengthes 0.56, 1.76, 8.90, 14.0 and ≈1000 cm respectively. The last two "absorbers" have been used to extrapolate our results to track chamber devices too. Between the absorber layers the x-coordinate is measured with various resolutions σ_E. First we shall study only the measurements of coordinates. After that we will answer the question how much one gains by measuring also the emission angle outside the absorber. Muons are produced at X = Y = Z = 0 perpendicular to the surface of the first absorber plate and are followed through the detector. In this special simulation energy losses have not been

applied. The coordinates of the muon track in the chambers have been recorded on files and analysed in a later step.

The maximum likelihood solution of equ.(4.41) is given by

$$\frac{\partial \ln G(X_1,\ldots,X_N;p)}{\partial p} = 0 \tag{4.83}$$

or

$$F(p) = \tfrac{1}{2}\sum_{\nu\mu}\left((A^{-1})_{\nu\mu}-(X_\nu-f_\nu)(X_\mu-f_\mu)\right)\frac{dA_{\nu\mu}}{dp} + \sum_{\nu\mu}A_{\nu\mu}(X_\nu-f_\nu)\frac{df_\mu}{dp} = 0 \quad , \tag{4.84}$$

where $(A^{-1})_{\nu\mu}$, f_μ and df_μ/dp are given by equ.(4.45),(4.40) and (4.48) respectively. $dA_{\nu\mu}/dp$ can be calculated by

$$\frac{dA_{\nu\mu}}{dp} = -\sum_{ik}A_{\nu i}\frac{d(A^{-1})_{ik}}{dp}A_{k\mu} \quad , \tag{4.85}$$

$d(A^{-1})_{ik}/dp$ given by equ.(4.47).

This can be solved exactly by numerical methods. But because of the tremendeous computer time consumption needed one has to look for simpler methods. If the momentum dependence of $(A^{-1})_{\nu\mu}$ is neglected, i.e.

$$\frac{dA_{\nu\mu}}{dp} \approx 0 \tag{4.86}$$

then equ.(4.84) reduces to an extended least-square fit,

$$\sum_{\nu\mu}A_{\nu\mu}(X_\nu-f_\nu)\frac{df_\mu}{dp} = 0 \quad , \tag{4.87}$$

which is solved by

$$\bar{p}_1 = -\tfrac{1}{2}\,\frac{qBs^2}{3336}\,\frac{\sum A_{\nu\mu}\nu^2\mu^2}{\sum A_{\nu\mu}X_\nu\mu^2} \qquad (4.88)$$

$$(A^{-1})_{\nu\mu} = -\frac{1}{6}\left(\frac{\alpha}{\bar{p}_{i-1}}\right)^2 \frac{s^3}{X_0}\,C_{\nu\mu} + \sigma_E^2\delta_{\nu\mu} \quad . \qquad (4.89)$$

(4.88) together with (4.89) build up an iteration method to get the measured value $\bar{p}$. The start value $\bar{p}_0$ can be obtained by the simple least-square fit with the further approximation

$$(A^{-1})_{\nu\mu} \approx \sigma_E^2\delta_{\nu\mu} \quad . \qquad (4.90)$$

Then (4.87) reduces to the normal least-square equation

$$\sum_\nu \frac{(X_\nu - f_\nu)}{\sigma_E^2}\,\frac{df_\nu}{dp} = 0 \qquad (4.91)$$

with the solution

$$\bar{p}_0 = -\tfrac{1}{2}\,\frac{qBs^2}{3336}\,\frac{\sum \nu^4}{\sum \nu^2 X_\nu} \quad . \qquad (4.92)$$

With the normal least-square (4.91) or the extended least-square solution (4.87) one can hope to get good results for absorbers with large radiation length and/or detectors with large setting errors, so that conditions (4.90) or (4.86) are at least approximately fullfilled. Very sophisticated χ^2-methods have been worked out for the bubble chamber analysis [111], nuclear emulsion analysis ([112] and further references therein) and for track chamber devices ([113] and further references therein). We do not go into the details of these computer codes. They all uses the optimization by the least-square condition. The advantages lie mainly in saving computer time by code optimization, in different treatments of the energy loss (which has been neglected totally in this study), and in the treatment of detector imperfections like field inhomogenities, non-stochastic measurement errors. Instead we discuss in the present section only "perfect" detectors. One should have in mind that these imperfections may worsen the resolutions by a factor 2 to 3 (see for example ref. [114]).

For heavy absorbers the exact maximum likelihood equation has to be solved. Therefore the problems of solving this equation within reasonable computer time should be treated first, before one starts to build a sophisticated absorber for μ-identification. We do not discuss in this report the problem how to get large magnetic fields in non-ferromagnetic materials. Naturally we will concentrate on iron as a prototype of a ferromagnetic material with good absorbing behaviour and with a saturated field of approximately 17 kG.

Comparisons of the three fitting methods and the theoretical prediction from equ.(4.43) are shown in fig.116 for arbitrary selected values of B, σ_E and s, as function of the radiation length X_0. The plots are simply ordered with increasing momentum resolution. The first one ($\sigma_E = 0$) can of course not be realized experimentally, we show it only for the demonstration of vanishing setting errors in comparison to the set-up with the same parameters except of a setting error $\sigma_E = 0.03$ cm. All practical designs have momentum resolutions between 0.15 and 0.30 for iron as absorber ($X_0 = 1.76$ cm). Only for very low magnetic fields, large setting errors or very few chamber layers the expected momentum resolution exceeds 0.3. It is also seen that the maximum-likelihood solution has to be used for iron and heavier materials as absorbers, whereas for track chambers ($X_0 > 10$ cm) both χ^2-methods are sufficient.

In fig.117 we show solutions of equ.(4.43) for some sets of parameters for iron as absorber material. The dependence of the momentum resolution on the thickness s of each layer (or equivalently on the number N of layers) and on the setting errors is given in fig.117a and 117b for two extreme magnetic fields respectively. For B = 2 kG the momentum is mainly determined by multiple scattering alone, one sees the $1/\sqrt{2N}$ -behaviour for $\sigma_E = 0$, as was discussed in detail in the previous section. If the setting error increases, the momentum dependent fluctuations in multiple scattering can no more be measured and thus one observes a drastically increase in momentum resolution. On the other hand for large magnetic fields the momentum is measured mainly by the bending of the track and the influence of the setting error will be small. This is shown in fig.117a. The same can be observed in figs.117c and 117d, where we show the results as function of B for two extreme setting errors. For vanishing errors and large number of measurements the magnetic field does not help at all for momentum determination, whereas for increasing setting errors one has to use also larger fields. To give a practical example, one obtains a momentum resolution of ≤ 0.2 either by a large number of precise chambers (say $\sigma_E \leq 0.01$ cm and (s,N) $\approx$ (5 cm,20)) with any (or vanishing) magnetic field or by use of magnetic saturated iron (B $\approx$ 17 kG)

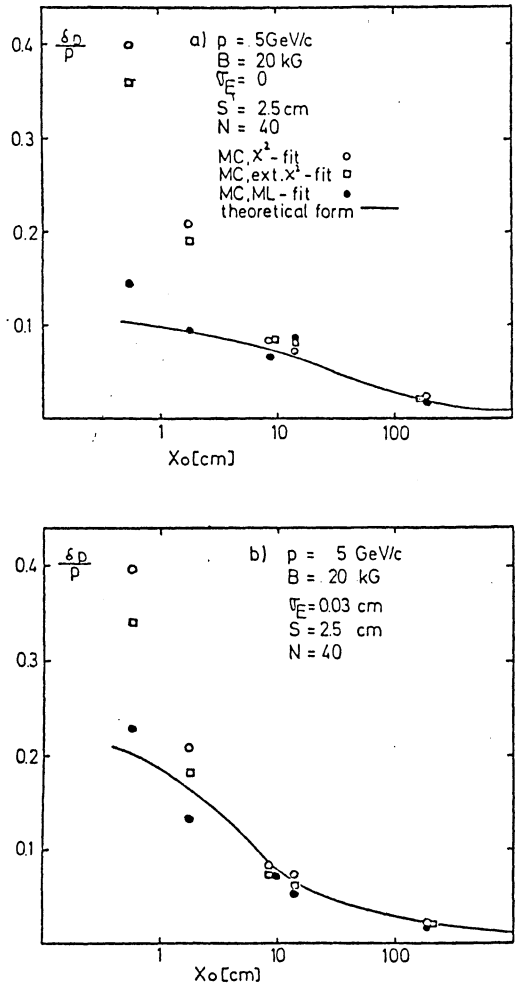

Figure 116. Momentum resolution in magnetized tracking calorimeter under various conditions. For details see text.

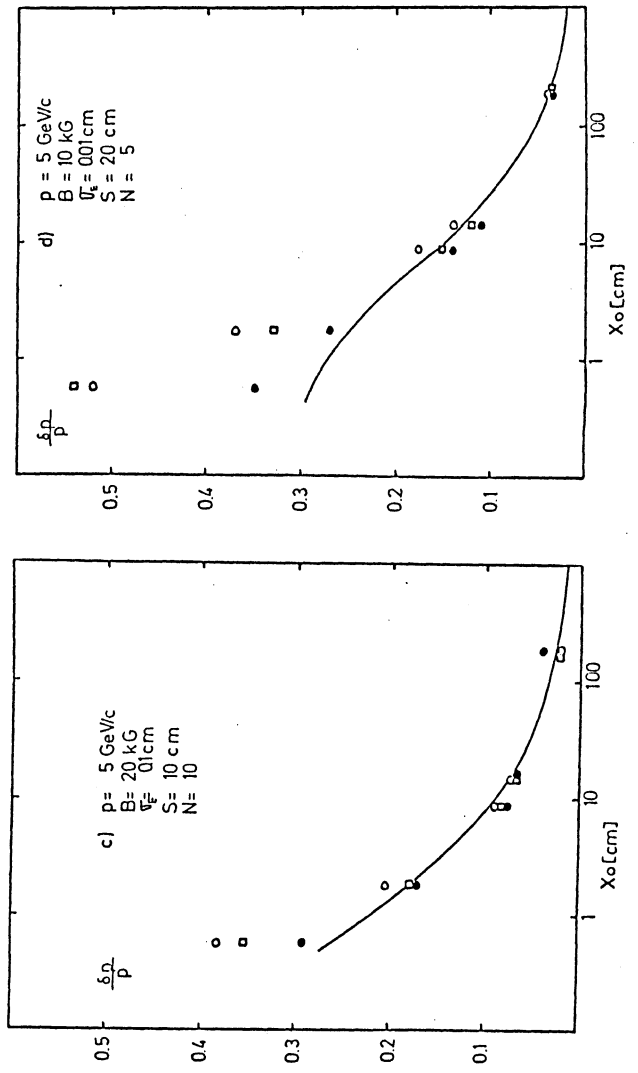

Figure 116. Momentum resolution in magnetized tracking calorimeter under various conditions. For details see text.

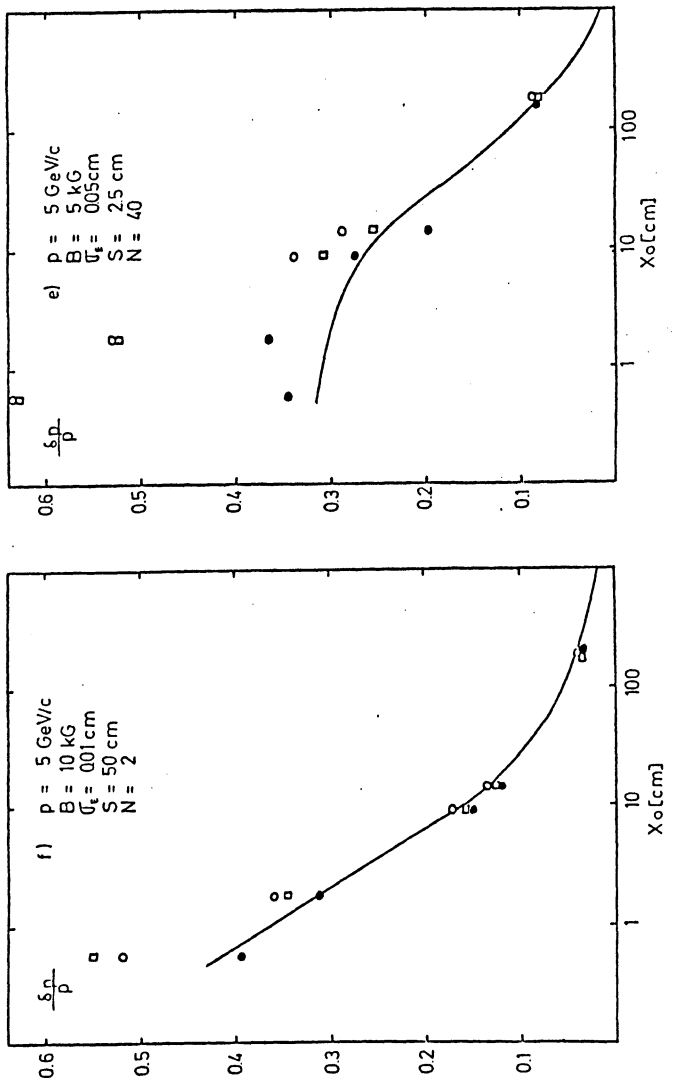

Figure 116. Momentum resolution in magnetized tracking calorimeter under various conditions. For details see text.

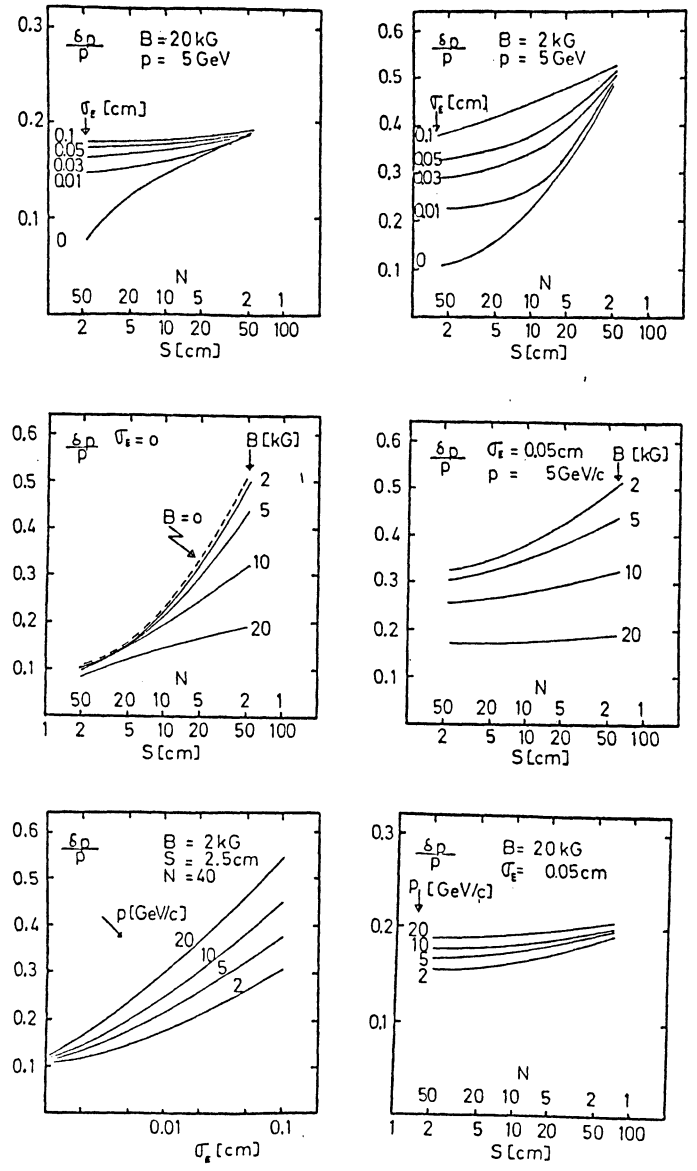

Figure 117. Momentum resolution in magnetized tracking calorimeter under various conditions. For details see text.

with $\sigma_E \approx 0.05$ cm and any number of chamber layers ($N \geq 1$). The dependence on the momentum is in general small. As can be seen in fig.117e and 117f, there is only a sizeable effect for small magnetic fields and large setting errors. But this is quite evident. The fluctuations of multiple scattering can no more be resolved at large momenta.

In fig.118 we compare for a practical example (s = 2.5 cm, N = 40, M = 38, B = 20 kG) the momentum resolutions obtained by both methods, the coordinate measurement and sagitta measurement. As has already been stated above, for small setting errors $\sigma_E \leq 0.03$ cm we observe approximately the same results for both methods. For $\sigma_E \approx 0.1$ cm the use of sagittas is no more practical. The sagitta method has a lot of advantages. First of all the direction of the incoming particle cancels out, secondly only the correlations of measurements between neighbouring layers enter into the calculations, so non-stochastic survey errors between chambers far distanced cancel out.

The influence of the setting error and the multiple scattering on the resolutions as function of the radiation length of the absorber material is shown in fig.119. One observes that for all practical devices (including high pressure track chambers) the momentum dependence is small. Only for $X_0 \geq 0.5 \cdot 10^3$ cm one enters into the region dominated by the setting error, where the resolution $\delta p/p$ is nearly proportional to p. However practical examples of low pressure track chambers have never reached these resolutions (see for example [115]). Normally one gets results a factor 2 worse. This is mainly because of field inhomogenities and survey uncertainties, both beeing the more important the smaller the multiple scattering fluctuations. On the other hand for heavier absorbers and also for dE/dx-chambers there exist practical examples [116,117], which have reached the theoretical expected resolution.

Our last investigation in this section concerns the inclusion of the angle of the track leaving the absorber. Our theoretical formula is again equ.(4.43) with inclusion of the further elements given in equs.(4.74) to (4.78). The expression for the maximum-likelihood solution (4.84) remains unaltered, one only has to extend the summation over the N coordinate measurement and the additional angle measurement. Formulae (4.88) and (4.89) for the solution of the extended least-square may be rewritten in the following form

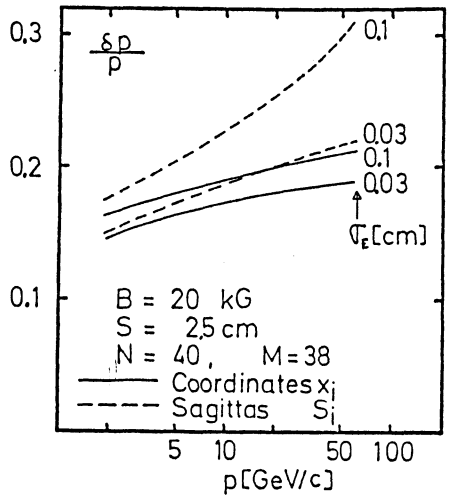

Figure 118. Momentum resolution as function of momentum for different values of the setting error. The methods of coordinates and sagittas are compared with each other.

$$\bar{p}_i = \frac{\sum_{\nu\mu}^{N+1} A_{\nu\mu} h_\nu h_\mu}{\sum_{\nu\mu}^{N+1} A_{\nu\mu} X_\nu h_\mu} \tag{4.93}$$

with

$$h_\nu = f_\nu p = \tfrac{1}{2} \frac{B\nu^2 s^2}{3336} \tag{4.94}$$

$$h_{N+1} = \frac{2h_N}{Ns} = \frac{BNs}{3336} \tag{4.95}$$

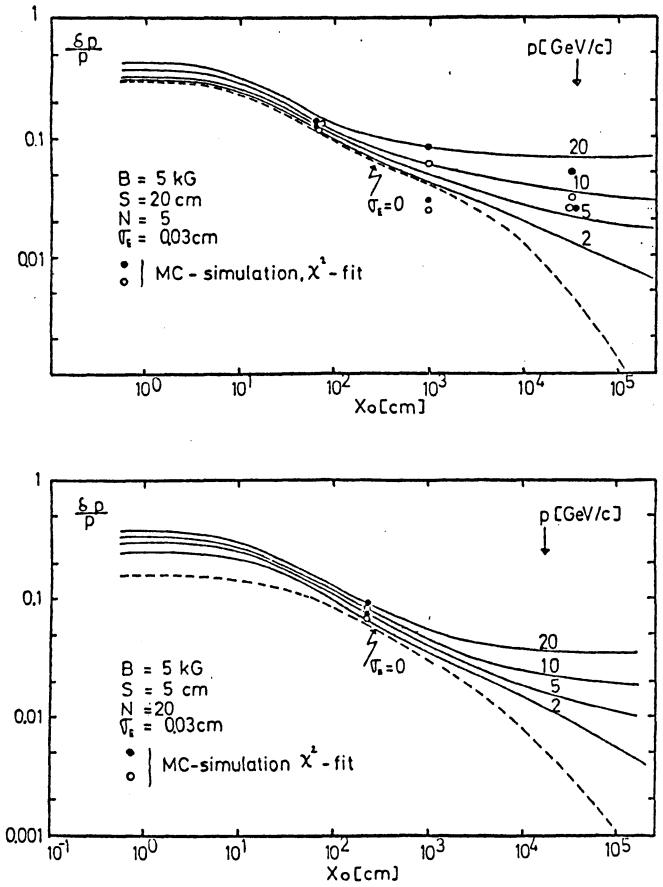

Figure 119. Momentum resolution as function of radiation length of absorber material for various momenta. A comparison is shown between the theoretical calculation and the Monte Carlo simulation.

$$X_{N+1} = \theta \quad . \tag{4.96}$$

For the iteration the matrix A^{-1} is given by equ.(4.89) for $\nu,\mu = 1,N$ and

$$(A^{-1})_{\nu,N+1} = (A^{-1})_{N+1,\nu} = \tfrac{1}{2}\left(\frac{\alpha}{\bar{p}_{i-1}}\right)^2 \frac{\nu^2 s^2}{X_0} \tag{4.97}$$

$$(A^{-1})_{N+1,N+1} = \left(\frac{\alpha}{\bar{p}_{i-1}}\right)^2 \frac{Ns}{X_0} + \sigma_\theta^2 \tag{4.98}$$

For the normal least-square fit we get

$$\bar{p}_0 = \frac{\sum_{\nu=1}^{N+1} h_\nu^2/\sigma_\nu^2}{\sum_{\nu=1}^{N+1} X_\nu h_\nu/\sigma_\nu^2} \quad , \tag{4.99}$$

where

$$\sigma_\nu = \sigma_E \quad \text{for } \nu=1,N$$
$$\sigma_\nu = \sigma_\theta \quad \text{for } \nu=N+1 \quad . \tag{4.100}$$

Given the number L of outside layers and the distance d between the layers, the angle resolution can be connected with the setting error of the drift chambers by

$$\frac{1}{\sigma_\theta^2} = \sum_{k=1}^{L} \frac{1}{\sigma_E^2} k^2 d^2 = \frac{1}{\sigma_E^2} \frac{d^2 L(L+1)(2L+1)}{6} \tag{4.101}$$

or

$$\sigma_\theta = \sigma_E \frac{\sqrt{6}}{d\sqrt{L(L+1)(2L+1)}} = \varphi(d,L)\ \sigma_E \tag{4.102}$$

Here $X_0 \to \infty$ and $\tan\Theta \approx \Theta$ has been assumed. Thus with 5 drift chamber layers, each with a position resolution of σ_E = 0.03 cm and a distance d = 10 cm between wire planes one gets a resolution of 0.3 mrad. Therefore the range of practical angle resolutions is from $\leq$ 0.1 mrad to 10 mrad. σ_Θ = 1 mrad is a good practical value for L $\approx$ 2,3 and $\sigma_E \approx$ 0.03 cm.

Our theoretical calculation are compared with the GHEISHA- simulation for two sets of absorber-parameters in figs.120a and 120b. The calculation have been done for 3 values of angle resolutions. One observes only a very small increase in the resolution for additional angle determination. This is shown more clearly in fig.121, where the momentum resolution for a very simple structure is shown, namely 2 coordinate-measurements with a medium resolution of 0.03 cm and an additional angle measurement with variable resolution. The points for σ_Θ = 0.1 rad correspond of course to the case for only coordinate measurements and σ_Θ = 0.0001 rad for mainly angle measurement. Therefore we asked a somewhat different question. Suppose one has a number of M chambers, each with a space resolution of σ_E cm. Is there an optimal way to distribute them inside the absorber to measure N coordinates and outside the absorber to measure the emission angle? The angle resolution is calculated according to formula (4.102) with L = M - N and d = 10 cm. Plots shown in fig.122 indicate that for high magnetic fields there is practically no effect.

We get the somewhat trivial results, that there are two extreme cases for momentum measurement in tracking calorimeter : 1.) For a magnetic saturated iron-absorber it is nearly not possible to make anything wrong for momentum resolution. The structure of the absorber should be built according to the requirements of background rejection The momentum resolution is limited by multiple scattering. 2.) In low magnetic fields one has to use chambers with good position resolution ($\sigma_E \leq$ 0.03 cm) and the number of coordinate read-outs must be greater than 5 at least. The momentum is measured by the fluctuations of the multiple scattering. This method may be useful in end cap tracking calorimeter in toroidal magnetic fields.

Estimates show that the costs for these extreme cases and comparable solutions between them are nearly the same. There is no single solution which may be clearly preferred.

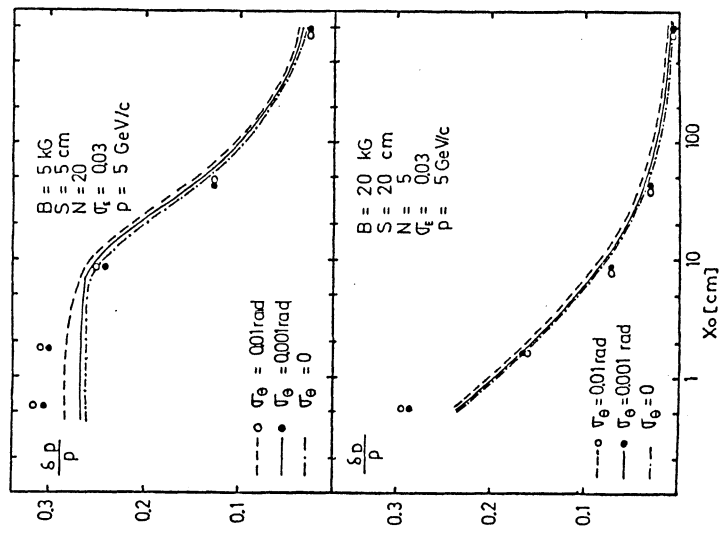

Figure 120. Comparison of theoretical calculation and Monte Carlo simulation for two sets of absorber parameters.

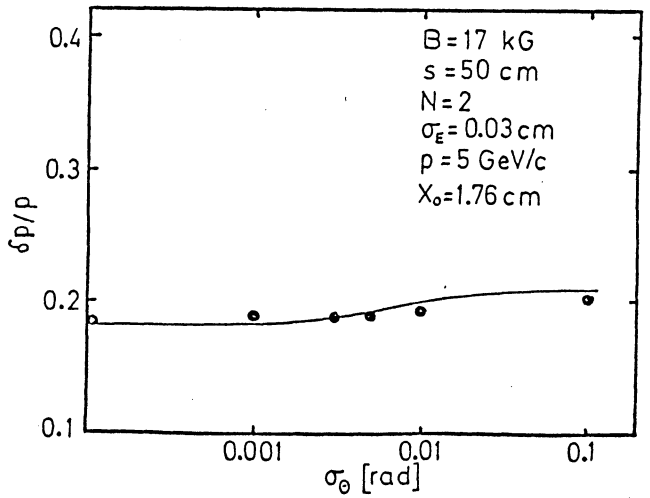

Figure 121. Momentum resolution as function of setting error for a very simple configuration.

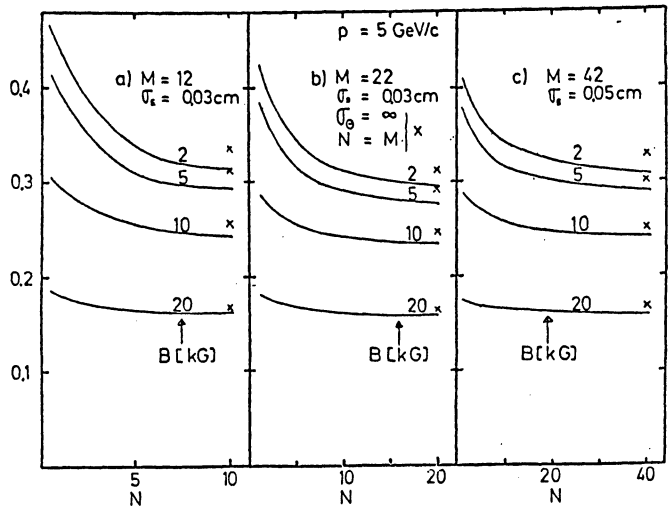

Figure 122. Momentum resolution as function of the distribution of read-out layers inside (N) and ouside (M-N) the absorber. The total number of layers used is M. Plots are shown for various configurations.

5.0 CALORIMETRY

5.1 INTRODUCTION

In the present chapter we have to discuss the final tuning of the program. We do not want to give a review about calorimetry. Excellent works can be found in the literature (see e.g. [118]and [119] and further references therein). Most of the calculations, to be presented in this report, have been done for calorimeter with scintilators as active read-out material. Thus we first spend some remarks to the conversion of absorbed energy into scintilation light, especially for very low energy particles. The attanuation of this light passing through the scintlators and light guides, the following conversion of light into photoelectrons in the photomultiplier (PM), the multiplication of these electrons into a measurable current and the final current integration, pulse shaping and read-out by analog-to-digital converter (ADC) and time-digital converter (TDC) may introduce biases, which can disturb the response as expected from the initially absorbed ionization energy.

A discussion about the performance of scintilation counter read-out is thus devoted to the next chapter. We continue with a presentation of general trends of the Monte-Carlo simulation for sampling calorimeter. These results and some further calculations are used then in chapter 5.4 to compare with experimental test-beam data. Some more special problems are discussed in the following chapters, the position reconstruction of the path of a particle by the shower shape in chapter 5.5 and in chapters 5.6 and 5.7 electron-hadron separation and muon hadron separation as it is done in present experiments and planned in future storage ring experiments.

Nearly all results of this final chapter 5 have been obtained with the GHEISHA6 version. In some very few cases we will compare these calculations with those obtained with the last version GHEISHA7.

5.2 SIMULATION OF THE SCINTILATION PROCESS

The read-out can be described in general by a system-analytical process, as sketched in fig. 123. If the answer $g(t)$ is known for a δ-function as input signal (e.g. the absorbed energy of a muon in a sufficient small step passing a scintilator, $u_1(t) = E_{abs}\,\delta(t-t_0)$), then the reaction of the read-out system is in general given by

$$u_2(t) = \int_0^t u_1(t-\tau)\, g(\tau)\, d\tau \qquad (5.1)$$

for any signal $u_1(t)$. If we denote by X(t) the corresponding random process, then we can also write

$$X_2(t) = \int_0^t X_1(t-\tau)\, g(\tau)\, d\tau \quad . \qquad (5.2)$$

Here the integral has to be understood as is explained in each text book about network analysis. The function g(t) can be calculated or measured experimentally. Then at least in principle one can calculate the response for any detector geometry and for any particle using (5.1) or (5.2). As we will see later, the integration can only be performed for a very simplified response function g(t) and very simple input signals $u_1(t)$. We start by establishing the function g(t) (see fig.124).

The fluorescence mechanism is different for different scintilator types, and the amount of light produced per unit energy ΔE absorbed in the scintilator depends generally on the particle species and the particle energy. From experimental data one may infer the nature of the quenching processes which occur for ionizing particles. The scintilation response, as calculated by [120], is

$$\Delta L_0 = \text{const.} \ln\left(1 + \alpha \frac{dE}{dx}\right) \Delta x \quad , \qquad (5.3)$$

which may be rewritten in the form

$$\frac{dL_0}{dx} = \text{const.} \frac{dE}{dx} \Big/ \left(1 + \frac{\alpha}{2} \frac{dE}{dx}\right) \qquad (5.4)$$

in agreement with the semiempirical expression proposed by [121] (Birk's law). We have fitted the parameter α to experimental data ([122] and [123]) and obtained the values given in table 14.

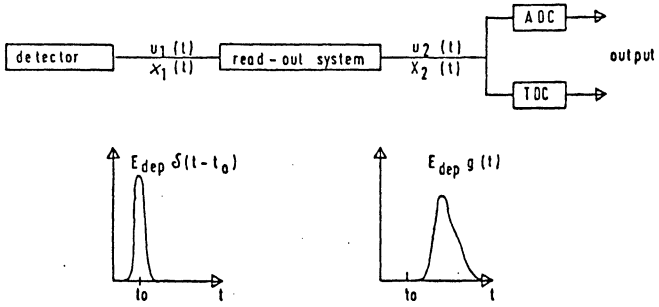

Figure 123. The detector and read-out system as system analytical process.

Table 14 α-parameters in Birks law for various materials in cm/MeV

Material	α
BGO	0.0011
plastic scintilator	0.0035
liquid argon	0.0050

Fig. 125 shows the light output in units of MeV, obtained by the absorbtion of kinetic energy of particles only. This can be measured experimentally for electrons, protons, tritons and higher mass fragments. Positrons, mesons, strange baryons and antibaryons do interact or decay if they are slewed down to rest, so some part of the rest masses will be converted to kinetic energy of the reaction products. In fig.126 we show the average pulse height for positive charged mesons measured in scintilators with a gate of 100 nsec. Here and in the following plots we have not applied any broadening of the pulse shapes due to the read-out system. As we will see later, this means we assume a fast electronic and a vanishing fluorescence decay time. The pulse height spectra for mesons at 5 MeV kinetic energy are shown in fig.127. Again we applied a gate of 100 nsec. For positive and negative charged myons one observes the energy spectrum of the decay electrons, as was given in formula (2.234). For myons not yet decayed we observe the peak at $\approx$ 4.5 MeV. A very similar spectrum is observed for

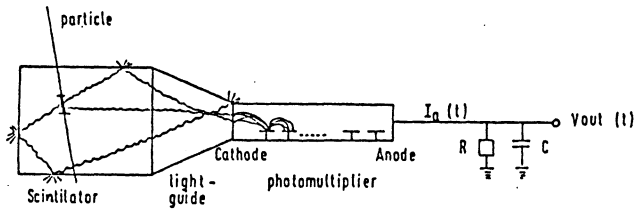

Figure 124. Scintilation counter read-out.

positive charged pions. Most of the pions have already been decayed within 100 nsec into a myon, the myon adds only ≈ 4 MeV kinetic energy to the pulse height spectrum. For negative charged mesons we observe a total different spectrum. It is dominated by π^-- absorbtion with following star production. The insert in this figure shows that only a small amount of pions has decayed in flight and that a negligible amount of pions has not interact at all. Similar spectra are obtained for positive and negative kaons respectively. The spectrum for K^+ is dominated by the various decay cascades, whereas for K^- the absorbtion process is the dominating one. The influence of the gate length on the total sampled energy is shown in fig.128 for particles of 500 MeV kinetic energy. Myon pulse heights come into saturation after a few nanoseconds, the following decay is very slow and certainly out of a reasonable trigger of most of high energy experiments. For all other particles the showers need at least 100 nsec to be totally absorbed. The value of the saturated pulse height is determined by the various interactions and decays, which the particles can undergo. Note especially the very high value obtained for antibaryons. Annihilation of $\bar{n}$ and $\bar{p}$ always contributes roughly two proton masses to the ionization energy. From the previous discussion we see that a gate of ≈ 100 nsec is the lower limit for pulse height measurements in a total absorbing calorimeter. Beside that we saw that the time dependence of the pulse height is total different for myons and electrons on one side and for the strongly interacting particles on the other side.

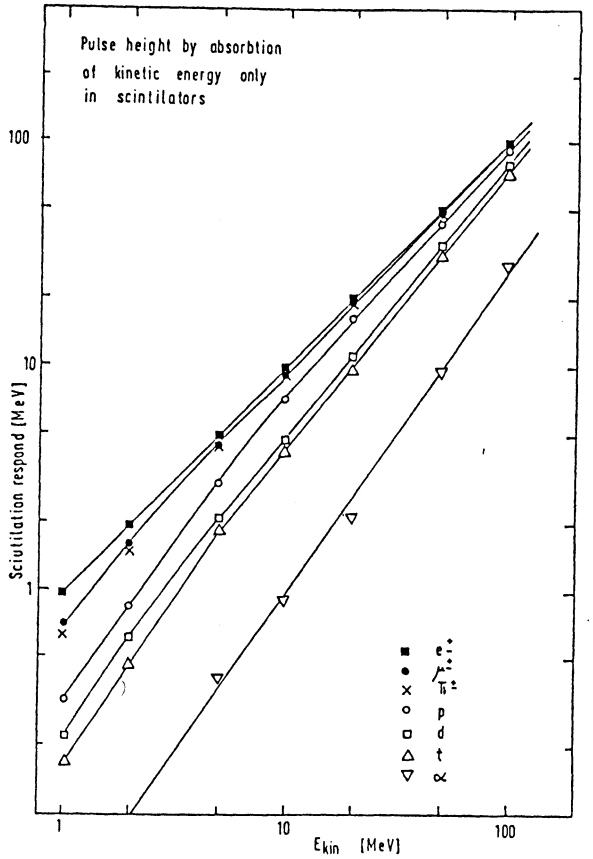

Figure 125. Light output in units of absorbed energy (MeV) for scintilators, as function of the primary kinetic energy. In this plot only the kinetic energies have been absorbed.

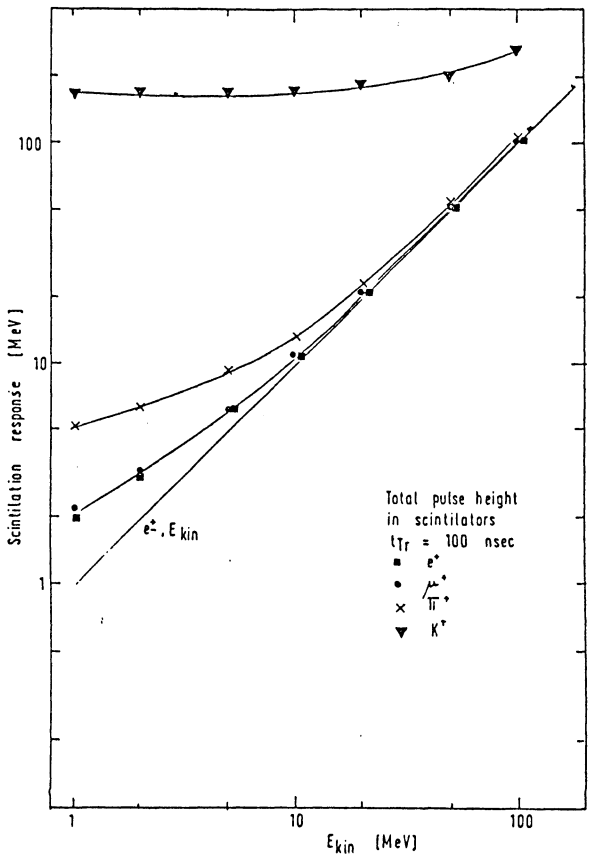

Figure 126. Light output in units of absorbed energy (MeV) for scintilators, as function of the primary kinetic energy. Conversion of the rest masses into measurable energy is taken into account.

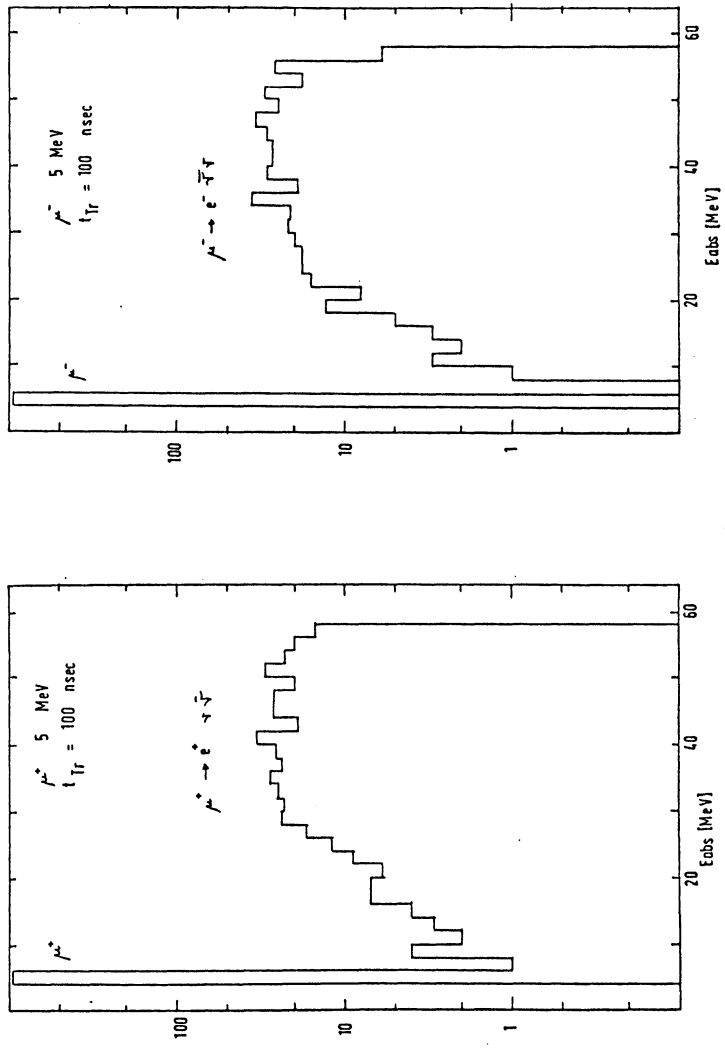

Figure 127. Pulse height spectra for muons, pions and kaons of 5 MeV kinetic energy in scintilators. For details see text.

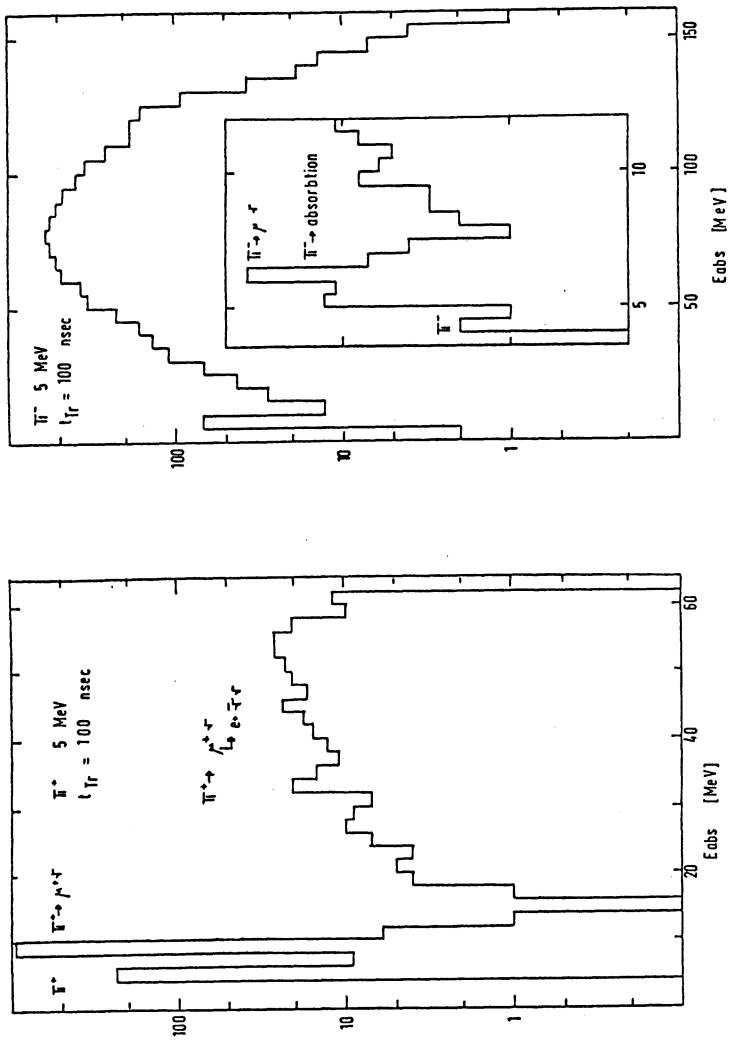

Figure 127. Pulse height spectra for muons, pions and kaons of 5 MeV kinetic energy in scintilators. For details see text.

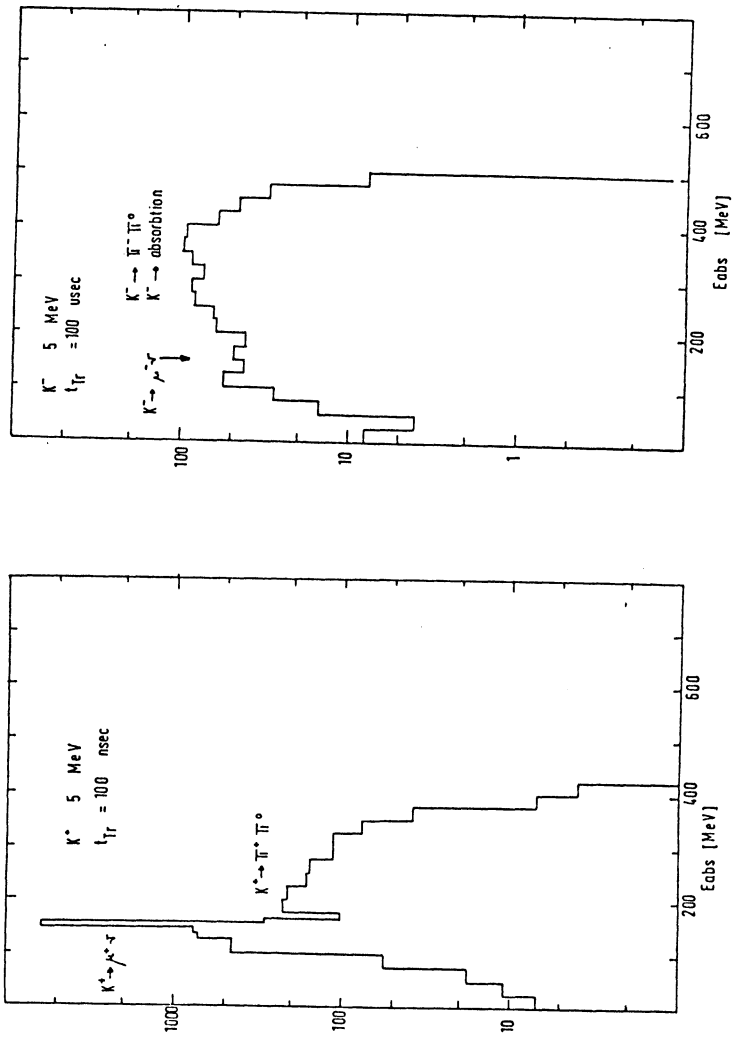

Figure 127. Pulse height spectra for muons, pions and kaons of 5 MeV kinetic energy in scintilators. For details see text.

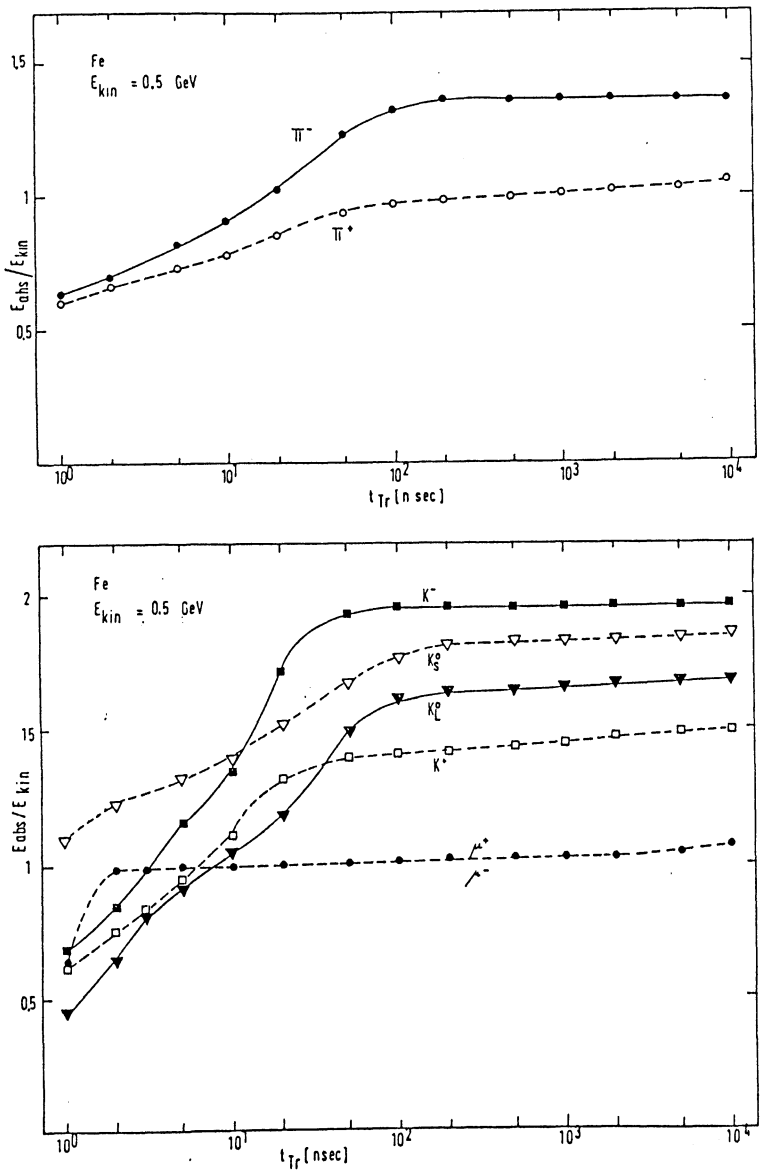

Figure 128. Total absorbed energy as function of time in an iron block for mesons and baryons at 0.5 GeV kinetic energy.

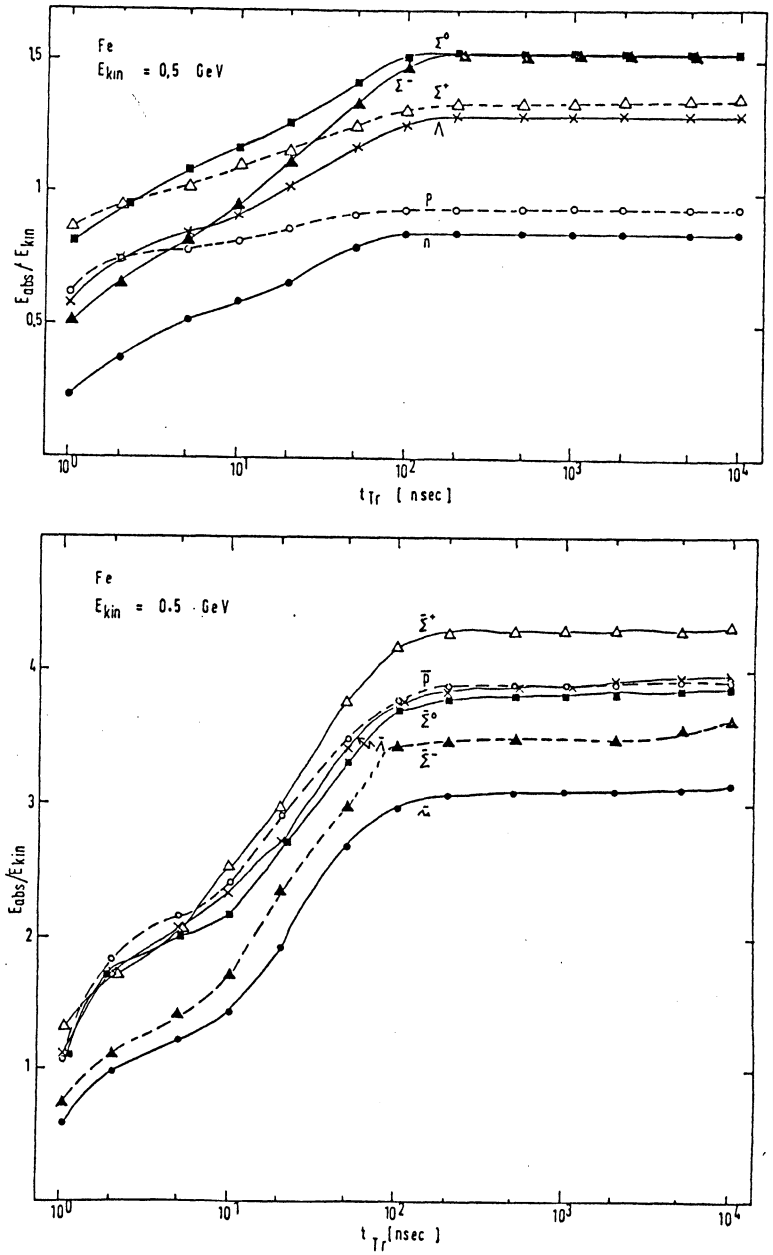

Figure 128. Total absorbed energy as function of time in an iron block for mesons and baryons at 0.5 GeV kinetic energy.

The scintilator atoms or molecules excited at the time t_0 by a primary event have a certain lifetime, so that the intensity L of the emitted light will decrease exponentially with time according to

$$L_1(t) = (L_0/\tau_{fl}) \exp[-(t-t_0)/\tau_{fl}] \, H(t-t_0) \quad , \tag{5.5}$$

where H(t) denotes the step function

$$H(t) = \begin{cases} 1 & \text{for } t > 0 \\ 0 & \text{for } t < 0 \end{cases} \tag{5.6}$$

Fluorescence decay time measurements are reported by numerous authors (see e.g. the general reviews [124]- [128]). Inorganic scintilators are commonly slower (τ_{fl}(NaI(Tl)) = 250 nsec., τ_{fl}(CsI(Tl)) = 1 μsec, $\tau_{fl}(Bi_3Ge_4O_{12})$ ≈ 320 nsec.) than organic scintilators (τ_{fl}(anthracene) = 30 nsec, τ_{fl}(liquid scintilator) ≈ 1-5 nsec). The widely used plastic scintilator on the polyvinyltoluol basis (e.g. NE114 from Nuclear Enterprise) have τ_{fl} ≈ 4 nsec. However, the simplified description of the fluorescence decay by only one decay constant proves to be insufficient for some applications, since in addition to the dominant fast fluorescence component, most of the scintilators exhibit other slower components. The relative weight of the particular components is generally a function of the particle species.

The light loss between the position of the fluorescence and the photocathode of the PM is minimized by using suitable reflectors and taking precautions to achieve an effective optical contact between the scintilator and the light guide on the one side and between the light guide and the phototube window on the other side. The attanuation of the light passing through the scintilator may be described by an effective attanuation length λ_{att}, which combines all effects like secondary excitation, light loss by diffuse reflections on the surfaces e.t.c.. The total light loss by the light guide system may be described by a constant ε, so that we have for the light at the PM

$$L_2(t) = \varepsilon \, L_1(t - x/c_{Sci} - d/c_{LG}) \exp[- x/\lambda_{att}] \quad . \tag{5.7}$$

x is the length of the light rays in the scintilator, d the length of the light guide, c_{Sci} and c_{LG} the velocities of light in the scintilator and light guide respectively. The light is emitted isotropically. This results in a spectrum of x values. In the present Monte Carlo studies, we did never follow each light ray in detail. Instead we used always a geometrical model of the scintilator, described by a distribution function F(x) of light ray lengthes. This function has to be folded then into the expression (5.7).

At the anode the initial charge pulse appears magnified by the secondary emission of n dynodes. In the approximation of an integration time constant RC beeing much greater than the pulse duration, the output voltage V_0 is

$$V_0 = \frac{\bar{A}}{C} e\alpha(\Delta L_2) \, p_{max} \int_0^\infty \sigma(\lambda) \, \pi(\lambda) \, d\lambda \tag{5.8}$$

$$= \frac{\bar{A}}{C} e \, \bar{N}$$

where e = electron charge, α = total photon yield of the scintilator, $\sigma(\lambda)$ = emission spectrum of the scintilator, $p_{max}\cdot\pi(\lambda)$ = probability of the release of one photo cathode electron reaching the multiplier system for every photon reaching the PM, $\bar{A}$ = mean amplifier gain. The integral describes the spectral response matching of the system scintilator - photomultiplier. The emission spectrum $\sigma(\lambda)$ often depends also on the particle species. If wavelength shifters are used between the scintilator and the photocathode, this can be used for discrimination of different particles (see e.g. [129]). In the right hand side the corresponding quantities are summarized in $\bar{N}$, the number of electrons reaching the multiplier system. The energy $W = \Delta E/\bar{N}$ required to form one photoelectron is relatively high because of the multistage conversion process (300 - 1000 eV in NaI(Tl), 1 - 3 keV in organic scintilators and 5 - 20 keV in glas scintilators). The multiplier gain $\bar{A}$ is given by the product of the secondary emission factors $\bar{\delta}_i$ of the particular dynodes:

$$\bar{A} = \bar{\delta}^n \tag{5.9}$$

$\bar{\delta}$ approximately equal to 3 - 4.

Due to the variations in the times of flight of the secondary electrons in the multiplier system, the emission of even one single photoelectron leads to a cloud of secondary electrons with a finite space- (and thus also time-) spread. Of course, $I_a(t)$ is delayed against the primary event by the total propagation time t_{PM}, which is constant for given operating conditions. The current is then given by the convolution of $L_2(t)$ with this process:

$$I_a(t) = \frac{\bar{A}e\bar{N}}{t_p} \frac{1}{\sqrt{\pi}} \int_0^t \exp\left[- \frac{(t-t'-t_{PM})^2}{t_p^2} \right] L_2(t') \, dt' \tag{5.10}$$

We normally assume t_p and t_{PM} to be small ($\approx$ 1 nsec), so it can be neglected against the decay fluorescence time. Then (5.10) reduces to

$$I_a(t) = \bar{A}\, e\, \bar{N}\, L_2(t) \quad . \tag{5.11}$$

The anode current may be integrated over by a RC network at the output of the PM in order to obtain a voltage pulse with amplitude proportional to ΔE. The time dependence of the output voltage is given by ($t_{RC} = RC$):

$$V_{out}(t) = -\frac{\bar{A}e\bar{N}}{C}\,\tau_{RC}\int_0^t \exp[-(t-t')/\tau_{RC}]\; I_a(t')\; dt' \quad . \tag{5.12}$$

Obviously $\tau_{RC} \gg \tau_{fl}$ must be chosen so as to avoid an early discharge of the capacitor, what would result in a pulse height loss measured by the ADC. With sufficient long time constants τ_{RC}, the voltage pulse height is given by

$$V_0 = \frac{\bar{A}\, e\, \bar{N}}{C} \quad . \tag{5.13}$$

Instead of the resistor one can also use a transistor, which discharges the capacitor after a certain time duration. The timing must then be controlled by a TDC measurement.

The deviation σ_V of the total pulse height V_0 depends, apart from the statistical deviation σ_N of the number N of photo cathode electrons, on the deviation σ_A of the multiplier gain:

$$\left(\frac{\sigma_V}{V_0}\right)^2 = \left(\frac{\sigma_N}{\bar{N}}\right)^2 + \frac{1}{\bar{N}}\left(\frac{\sigma_A}{\bar{A}}\right)^2 \tag{5.14}$$

Since $\sigma_N = \sqrt{\bar{N}}$, (5.14) simplifies to

$$\left(\frac{\sigma_V}{V_0}\right)^2 = \frac{1}{\bar{N}}\left[\,1 + \left(\frac{\sigma_A}{\bar{A}}\right)^2\,\right] \tag{5.15}$$

If $\tau_{RC} \gg \tau_{fl}$ cannot be presumed, then instaed of $\bar{N}$, only that part of the total photo cathode electron number which in fact influences the pulse height must be introduced. (5.15) may be rewritten in the form

$$\left(\frac{\sigma_V}{V_0}\right)^2 = \frac{1}{\bar{N}}\,\frac{\bar{\delta}}{\bar{\delta}-1} \quad . \tag{5.16}$$

After this review on the performance of scintilation counter and photomultiplier we are now in the position to discuss the Monte Carlo simulation as it is done in the present program. Of course the most elegant (and computer time saving) way would be to solve the integral (5.12) or (5.11), replacing $L_2(t)$ by (5.7) and $L_1(t)$ by (5.5). This results in the response function g(t). Then one has to sample the absorbed energy of the total event in all scintilators, which are connected to the photomultiplier, as function of space- and time- vector $\vec{r}$ and t, $\vec{r}$ may be converted to x, and the integral (5.1) gives immediately the output voltage as function of t. Unfortunatively this is only possible if the function F(x), which describes the geometrical model of the distribution of light ray lengthes, is sufficient simple. For $F(x) = x_0 \cdot \delta(x-x_0)$, i.e. only the direct light ray can reach the photomultiplier, the integration is simple and can be performed.

In a more general way one produces n light rays at the position of the energy absorbtion, applies a time delay for each light ray according to formula (5.5), uses formula (5.7) for the absorbtion of the light, assuming some distribution function F(x) of the light ray lengthes x. For every light ray we use (5.12) to calculate $V_i(t)$ by numerical integration. The total pulse shape is then obtained by sampling all $V_i(t)$ in a histogram. Results of this method are shown in the following figures. For these plots we used the following set-up. One scintilation counter of 0.5 cm thickness and a square area of 50 × 50 cm is viewed from all sides by light guides of 1 m length. The scintilation counter has only one fluorescence decay time constant of τ_{fl} = 4 nsec and the RC network has been dimensioned to τ_{RC} = 1 μsec. The light ray distribution has been varied according to

$$F(x) = \frac{1}{g\, x_0}\, H(x-x_0)\; H((1+g)x_0-x) \tag{5.17}$$

with g as adjustable parameter. Of course (5.17) represents a very simplified model. More realistic ones would suggest an exponential behaviour like

$$F(x) = \frac{1}{\sigma_x}\exp\left[\,-(x-x_0)/\sigma_x\right] H(x-x_0) \quad . \tag{5.18}$$

The voltage amplitude V_0 has been arbitrary calibrated. In fig.129 we show the voltage pulse, averaged over all simulated events. The geometry factor g has been varied from 0 to 0.5. For comparison we show also a simulation with two slower fluorescence decay components included: τ_{fl} = 20 nsec with a relative weight of 15% and τ_{fl} = 80 nsec with a weight of 5%. The corresponding current pulse is shown in fig.130. For most of the applications only the absolute height and the leading edge are important for the ADC- and TDC- read-out. We have always assumed that the ADC measures the pulse height between 100 and 120 nsec and the TDC measures the time for a threshold voltage of V(DISCR) = 0.5.

We will discuss first the pulse height, as measured by the ADC. In fig.131 we present the dependence of the average and the fluctuation of the total pulse height V_{out} and the total charge Q, both sampled within 100 nsec, on the geometry factor g. V_{out} is somewhat smaller as Q, due to the discharge of the capacitor C. Only for the average values one observes a small decrease for increasing g. The r.m.s. of the pulse height distributions does not depend on g and is nearly exactly equal to the r.m.s. of the distribution of the absorbed energy. Of course we expect some worsening of the response due to the PM statistic. To show this we have plotted in fig.132 the dependence of the voltage pulse height V_{out} as function of the absorbed energy. A smeared out one to one correlation is seen. As insert we give the V_{out} distribution for a fixed value of E_{abs}. From that it is seen that the PM statistic introduces a broadening of ≈ 10%. This can no more be seen in the convolution of E_{abs} into V_{out}. We conclude that the geometry model is not very sensitive to the response and will therefore no more be discussed. In the following we have fixed this value to g = 0.3. On the other hand the inclusion of slower fluorescence decay time constants changes dramatically the results (see e.g. fig.130).

The second quantity measured in normal applications is the output of the TDC, which is started from a beam trigger signal and closed by a discriminator signal with an adjustable threshold voltage. We have chosen a threshold of 0.5 in our arbitrary units shown in fig.129. In fig.133 we show the TDC measurement as function of the length x of the scintilator. A perfect linear dependence is observed for ⟨TDC⟩ with increasing x. The fluctuation, expressed by the r.m.s., increases with increasing x. If we apply a time slewing correction, as is shown in fig.134, we end up with the values given as open circles. From that we determine a position reconstruction resolution of $2\sigma_x$ ≈ 15 cm for not too large scintilators. This result agrees with experimental observations (see e.g. [130]).

If we analyse the current pulse itself, instead of the voltage pulse, we may define the average time ⟨t⟩ and the r.m.s. σ(t), both measured within the first 200 nsec. These quantities may be determined by a fast FADC or a similar device. The geometry model is not very sensitive to these quantities (see fig.135). There is only a small shift for ⟨t⟩ with increasing g, whereas σ(t) does not change at all. Inclusion of higher fluorescence decay time constants, on the other hand, disturbs totally the response compared to that with only one decay time constant. This is shown in fig.136 for a geometry parameter g = 0.3.

So far we have discussed the response of a single scintilator to the absorbed energy of a muon only. Next we come to the performance of a total absorbing calorimeter. 200 plates of scintilators, each with a dimension of 25×25×0.5 cm are connected on all sides with light guide systems and viewed by only one photomultiplier . The scintilators are interspaced by copper plates with the same dimensions as the scintilator plates. The current pulse, averaged over all events, is shown for a muon and a pion of 5 GeV energy in fig.137. These plots may be compared with fig.130. The muon pulse is similar to that measured by only one scintilator, beside a constant shift to higher t values due to the longer light guide system (d_{LG} ≈ 100 - 300 cm, depending on the longitudinal coordinate of the scintilator position). The pulse for the pion is dominated by the nuclear decay times. If we analyze the fluctuations of these pulses again by the average time ⟨t⟩ and the r.m.s. σ(t), as was discussed above for a single scintilator, we arrive at the plots shown in figs.138 and 139. In fig.138 we have used the fast decay fluorescence decay time τ_1 = 4 nsec only, in fig.139 two slower decay times of τ_2 = 20 nsec and τ_3 = 80 nsec have been included. In all cases we get a reasonable method for μ/π particle separation. Determined by the average time ⟨t⟩, the number of pions in the μ - sample is smaller than 1%, if we start from the same number of muons and pions produced. Similar good results have been obtained for π/e - separation (see also chapters 5.6 and 5.7).

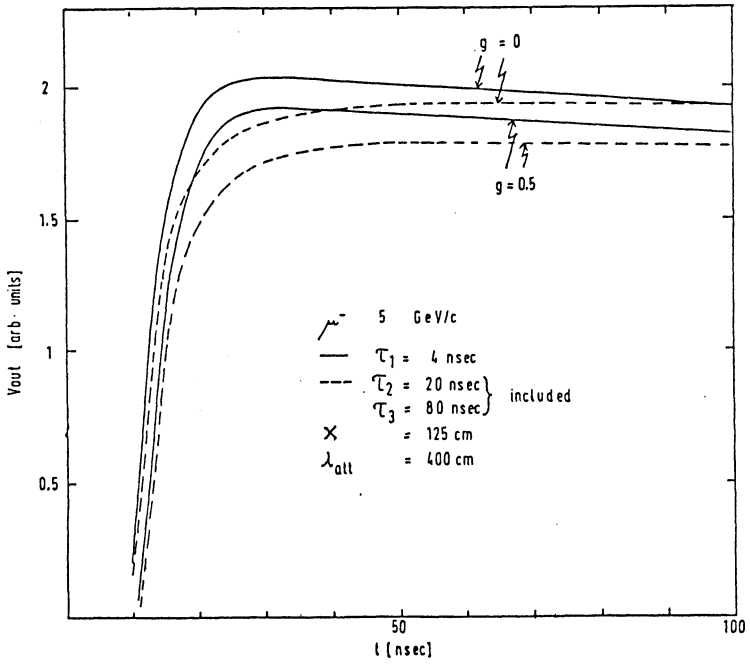

Figure 129. Average voltage pulse as function of time. For details see text.

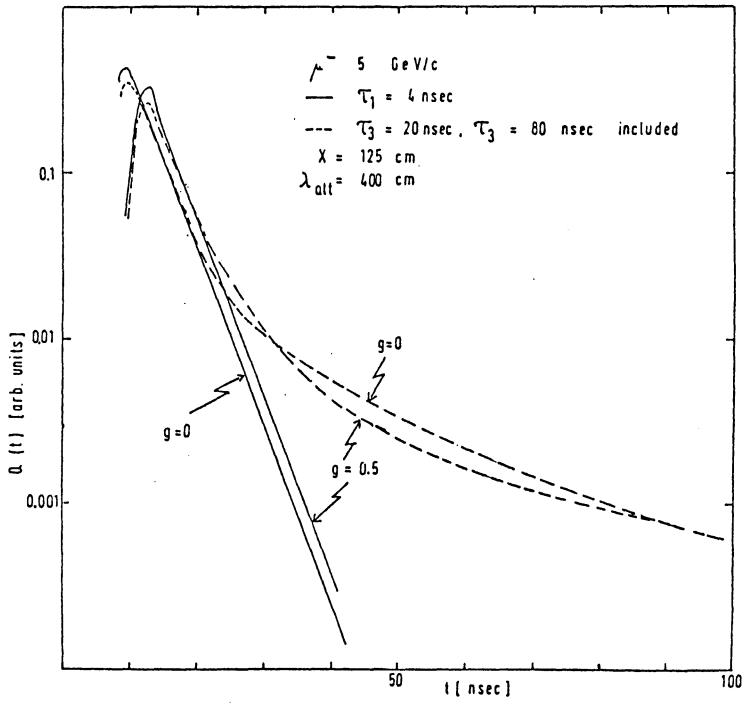

Figure 130. Average current pulse as function of time. For details see text.

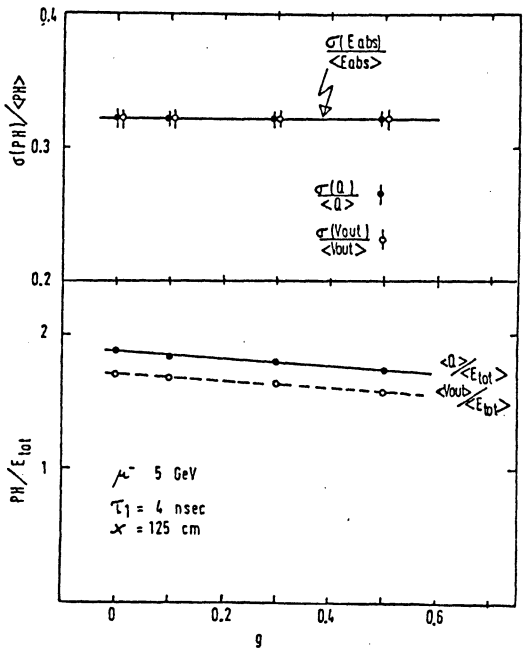

Figure 131. Average pulse height and fluctuation as function of a parameter g, which describes a geometrical model for the light collection in scintilators. For comparison we show both the average current and the average voltage pulse.

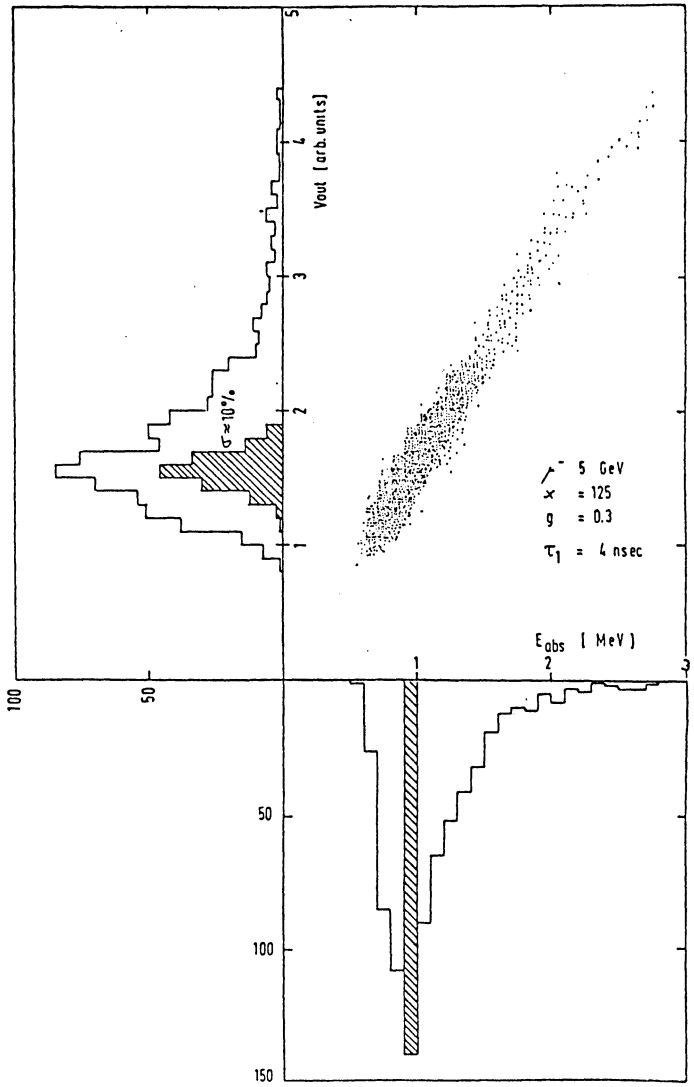

Figure 132. Correlation between the total pulse height and the total absorbed energy in a scintilator.

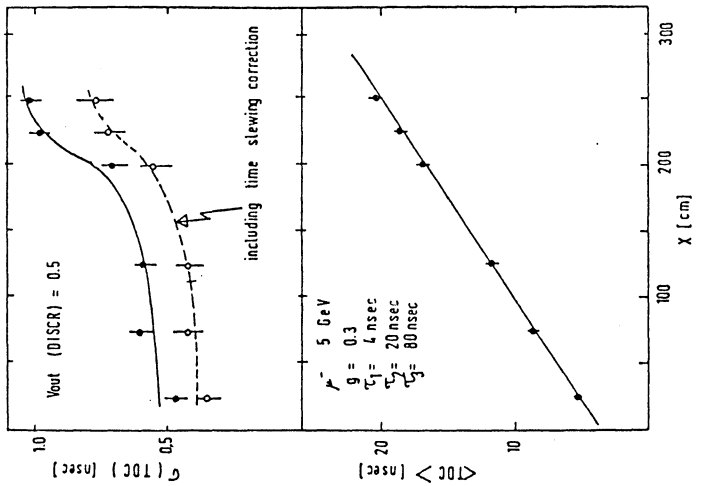

Figure 133. Average TDC measurement and fluctuation as function of the length x of the light ray in the scintilator. The dashed curve represents the results with time slewing correction included.

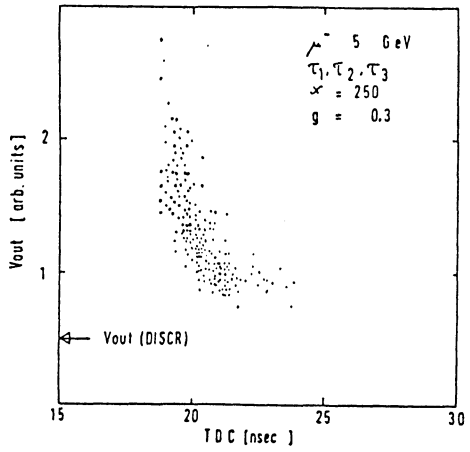

Figure 134. Illustration for the time slewing correction. Shown is the dependence of the total pulse height on the TDC measurement.

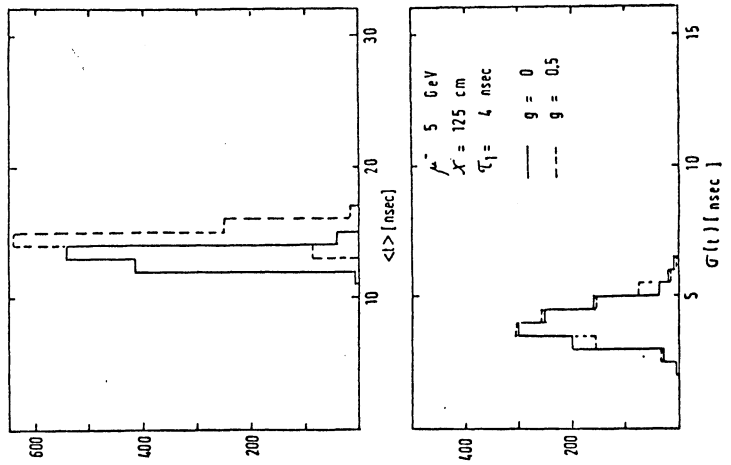

Figure 135. Distributions of the average time and fluctuation of the current pulse. Only a fast decay fluorescence decay time has been assumed. Results are shown for two geometrical models of light ray collection.

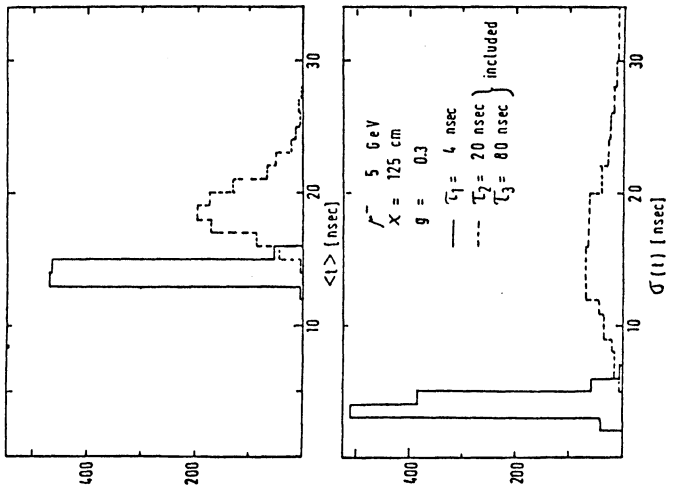

Figure 136. Distributions of the average time and fluctuation of the current pulse. Slow decay fluorescence decay time constants have been included.

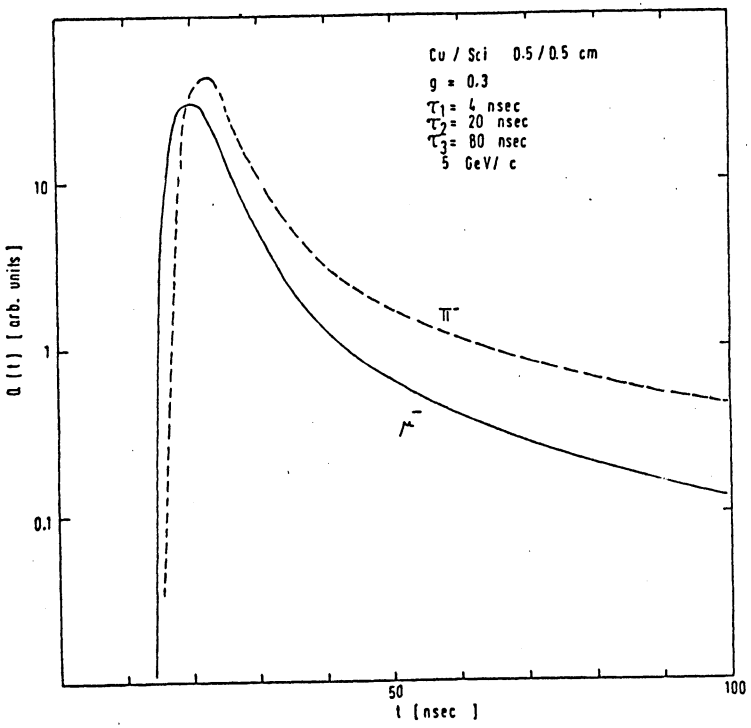

Figure 137. Current pulse in a Cu-scintilator sandwich calorimeter as function of time. Results are shown for muons and pions as incoming particles.

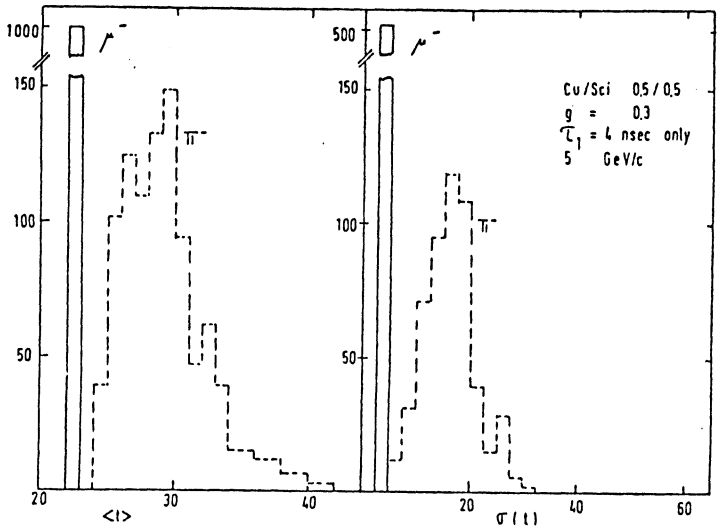

Figure 138. Distributions of the average time and fluctuation of the current pulse as measured for muons and pions in a sandwich calorimeter. Only one fast decay fluorescence decay constant has been assumed.

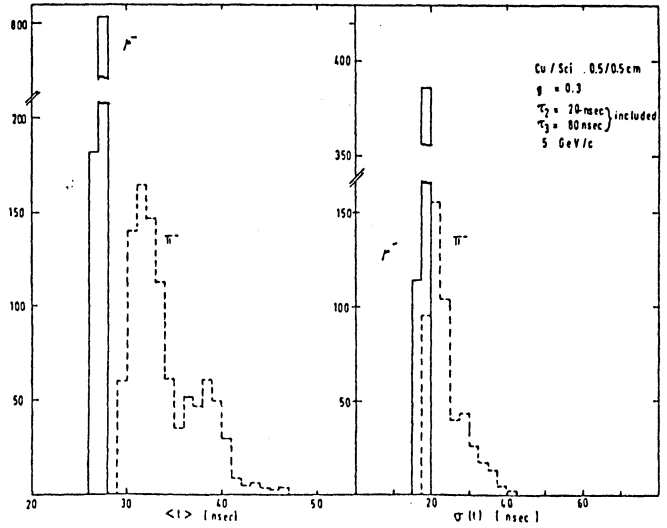

Figure 139. Distributions of the average time and fluctuation of the current pulse as measured for muons and pions in a sandwich calorimeter. Slow decay fluorescence decay constants have been included.

5.3 PULSE HEIGHTS AND ENERGY RESOLUTIONS

Experiences using the GHEISHA program during the last two years showed that two things are very sensitive to the results concerning calorimetry and particle identification. This is first the difference between the visible energy (mainly kinetic energy of charged particles) of initial and final state particles in each individual interaction, which determines directly the resolution of energy measurements in calorimeter. Secondly the final tuning of total elastic and inelastic cross sections, which determines the hadronic punch-through in μ-identification. Note that a change of 1% in the inelastic cross section causes an increase of ≈ 6% in the punch-trough by a 1 m Fe-absorber. In this chapter we will discuss only the problem of kinetic energy balance and devote chapter 5.7 to the second problem.

As an introduction we repeat the main steps of the treatment of hadron nucleus interaction. We have parametrized as careful as possible the total and inelastic cross sections, the multiplicity and quantum numbers of final state particles in each individual interaction. The longitudinal and transverse momentum spectra are simulated by an iterative cascade model, fitting some adjustable parameters to available data. The intra-nuclear cascade multiplication has been parametrized according to nuclear scattering data. Finally we end up with the kinetic energies E_{fk} of all final state particles k (note that by E we normally denote the kinetic energy). The relative difference

$$\frac{\Delta E}{E_i} = \frac{E_i - \sum_k E_{fk}}{E_i} \qquad (5.19)$$

between the initial and final state particles determines directly (at least at low initial particle energy, where only a very few interactions contribute to a shower) the intrinsinc resolution of a calorimeter. The intrinsinc resolution is defined by the r.m.s. of the distribution of the total absorbed ionization energy. The balance of kinetic energy is determined in nature by a lot of processes. We mention only the rest-mass production by high energy interactions, Fermi motion of nucleons inside a nucleus, statistic of the binding energy loss e.t.c.. Experimental data are not available, so one has to use model dependent calculations (see e.g. [131]). We have proceeded in another way, which is somewhat unphysical, but allows a simple tuning of the program without understanding of all the details. Before the particles interact (but only for nuclear interactions), the routines CINEMA and FERMI are called, which change the kinetic energy of the interacting particle according to a gaussian distribution

$$P(\hat{E}_i) = \frac{1}{\sqrt{2\pi\sigma_E^2}} \exp\left[-(\hat{E}_i - \langle\hat{E}_i\rangle)^2/2\sigma_E^2 \right] . \qquad (5.20)$$

$\langle\hat{E}_i\rangle$ is calculated in CINEMA, σ_E in FERMI. Some energy for nuclear evaporation is subtracted in routine EXNU, so that

$$\hat{E}_i' = \hat{E}_i - E_{eva} \qquad (5.21)$$

is the actual kinetic energy, which is used for the simulation of final state particles in the cascading routines. The average values $\langle\hat{E}_i\rangle$ and $\langle E_{eva}\rangle$ and the r.m.s. σ_E and σ_{eva} have been parametrized as function of the kinetic energy of the interacting particle and as function of the atomic number A of the target nucleus. For these fits we used experimental calorimeter data. This means that the intrinsinc resolutions are not at all predictions from nuclear scattering data. They simply describe the average behaviour of calorimeter data.

For the following figures we introduce the convention, that a calorimeter of the sampling thickness s_1 cm absorber of atomic number A and s_2 cm scintilator will be denoted by (A/Sci s_1/s_2 cm). The square dimensions are always assumed to be 100×100 cm and the longitudinal length is at least 7 absorbtion lengths, so that leakage on the sides and at the back of the calorimeter can be neglected. In front of each calorimeter we have placed a BGO block with a small hole of 1×1 cm in the beam line. This calorimeter serves for measuring the backscattering. All scintilators are connected on each side by a common light guide system, which brings the light to only one photomultiplier at the back of the calorimeter. The scintilation response and the performance of the photomultiplier- and electronic-read-out has been simulated as was discussed in detail in the previous chapter.

The ratio of the pulse heights for electrons and negative charged pions (see fig.140a) has a pronounced minimum at ≦500 MeV, increases to a maximum at ≈ 3 GeV and decreases very slowly above 3 GeV, approaching a constant ≧1 for $E_{kin}\to\infty$. These curves reflect directly the same behaviour as those shown already in fig.77. In fig.140a we compare the pulse heights for electrons and pions both at the same kinetic energy ($E_{aval}=E_{kin}$). Since the negative charged pions spend also some amount of their rest-masses to ionization energy, due to star production by pion absorbtion, this ratio may become smaller than one. This may be avoided by comparing the pulse heights of pions with those of electrons at a kinetic energy equal to the total energy of the pion ($E_{aval}=E_{tot}$). As can be seen in fig.140c, at the minimum of ≈ 500 MeV this ratio is then roughly ≈ 1.1 - 1.2 for non

fissionable absorbers and ≈ 0.8 for uranium (U^{238}). For lower kinetic energies the pulse height ratio increases (not shown). For uranium we observe a value ≦ 1 for all kinetic energies, only between 2 and 5 GeV the pulse heights for electrons and pions are nearly the same.

These results are compared in fig.140b and 140d with those of GHEISHA7. A drastic increase by 20% can be observed for the pion pulse heights, obtained for lead calorimeter. Good experimental data are not available up to now for lead, tungsten or other extreme heavy materials. As has been tried to explain at various places in this report, the total pulse height is, within some limits, a tunable quantity in the GHEISHA program. Consequently, if reliable data for lead will be available, a retuning may become necessary.

Our main verification for the GHEISHA7 treatment is shown in fig.141. Plotted are the pulse heights for π- induced showers as function of the sampling thickness s, expressed in units of absorbtion lengths (fig.141a), and as function of the atomic number A for a fixed sampling rate of $s = 0.1\,\lambda_0$. As can be seen, the results for all materials, except of the heaviest elements and some elements in the vicinity of A ≈ 50, lie on a universal curve, for a given energy of the showering pion. In the GHEISHA6 version the pulse heights for lead are even lower by 20%, which looks unreasonable in terms of the expected smooth behaviour as function of the sampling thickness when expressed in absorbtion lengths. The drastic decrease of the $PH(e^-)/PH(\pi^-)$ - ratio with increasing atomic number A of the absorber material can be simply related to the fact of the decreasing X_0/λ_0- ratio with increasing A- value and has thus to do with the e^-- showers.

The same quantity is compared in fig.142 for negative and positive charged pions and for protons with another choices of the sampling thickness. For π^+ and p the kinetic energy is the natural choice to compare with electrons, for π^- we again show both curves, for the kinetic energy and for the total energy respectively. Differences at low energy can be easily explained by the different processes at very low energies for pions of either charge and for protons respectively. For energies exceeding 5 GeV the values for all particles lie on the same curve.

Another way to compare the pulse heights for electrons and hadrons is given by the quantity shown in fig.143, the pulse height divided by the total or kinetic energy of the hadron. For electrons this quantity is exactly a constant, depending only on the absorber material and the sampling rate (not shown). For negative charged pions the total energy is the natural choice, for positive charged pions the definition PH/E_{kin} seems to be more adequate. This is shown in fig.144 for a Fe calorimeter with 2.5 cm thickness of the absorber layers. The results from fig.141 may be compared with

those of fig.145 to see that the general behaviour of the pulse height ratios are also observed in the more fundamental ratio of the energy of the primary hadron and the total ionization energy absorbed in both, the scintilator and the absorber plates. The total absorbed energy by ionization is always smaller than the total available energy. For a more complex calorimeter of uranium and copper plates, interspaced by scintilators, we compare the two quantities, $PH(e^-)/PH(\pi^-)$ and E_{kin}/E_{abs}, in fig.146. The resolutions, defined by the r.m.s., of the previous pulse height measurements are shown in figs.147 and 148. We have adopted the commonly used parametrization

$$\frac{\sigma(PH)}{\langle PH\rangle} = \frac{\sigma_0}{\sqrt{E_{kin}}} \qquad (5.22)$$

As can be seen in the plots formula (5.22) can only be used for energies above ≈ 1 GeV. At lower energies the resolution is a very complicated function of the particle species, the absorber material and the sampling rate. We do not have investigated the behaviour of the resolution at very low energy in the present study, because no experimental data are available for E_{kin} ≦ 1 GeV to compare with. Also for high energies the parametrization (5.22) makes no sense. This may be concluded from the figures 149 and 150, where we present the corresponding intrinsinc resolutions. One sees that for $E_{kin} \to \infty$ the latter quantity approaches a constant, so that

$$\frac{\sigma(E_{abs})}{\langle E_{abs}\rangle} = \sigma + \frac{\sigma_1 - \sigma}{\sqrt{E_{kin}}} \qquad (5.23)$$

For E_{kin} ≦ 1 GeV the same complicated structure as in $\sigma(PH)/\langle PH\rangle$ is observed.

The energy resolutions of a copper calorimeter with 0.5 cm thick scintilator plates are studied as function of the thickness s of the absorber plates in fig.151. A straight line describes quite well the simulated results,

$$\frac{\sigma(PH)}{\langle PH\rangle} = 0.19 + 0.067 \cdot s \qquad (5.24)$$

The pulse height resolution is compared with the intrinsinc resolution (total absorbed energy). For $s \to 0$ they both approach nearly the same value. As can be seen the intrinsinc resolution is slightly increasing with

decreasing thickness of the absorber plates. This is of course due to the fact that we use a constant scintilator thickness of 0.5 cm, so that the relative amount of absorber material and scintilator material changes. For s = 0 we actually would have a pure total absorbing scintilator block. The same quantities are shown in fig.152 for uranium instead of copper. For s $\geq$ 1 cm we again observe a straight line behaviour. For very fine sampling rates photon multiplication from nuclear fission is responsible for the clear improvement of the resolution. If we express the absorber thickness s in absorbtion lengths (λ_0 = 14.8 cm for Cu, λ_0 = 10.5 cm for U^{238}), then the resolutions for both materials lie on the same curve (see fig.153), at least for s $\geq$ 0.1 λ_0).

Another quantity of interest in calorimetric applications is the center of gravity. Expressed in absorbtion lengths, we got the results shown in fig.154. The values for all absorber materials, sampling rates and particle species lie nearly on the same curve. The straight lines represent fits, the results of which are summarized in table 15.

Table 15 : Center of gravity $g=g_1+g_2 \cdot \ln E_{kin}$ expressed in units of absorbtion lengths λ_0

Calorimter		particles	g_1	g_2
Fe/Sci	0.5/0.5	π^-,π^+,p	1.14±0.07	0.46±0.05
Cu/Sci	0.5/0.5	π^-	1.20±0.05	0.37±0.04
Pb/Sci	0.5/0.5	π^-	0.98±0.07	0.31±0.04
U/Sci	0.5/0.5	π^-	1.06±0.08	0.37±0.06
Fe/Sci	0.3/0.3	π^-,p	1.10±0.06	0.43±0.04
Fe/Sci	2.5/0.5	π^-,π^+	1.08±0.08	0.38±0.06
U/Cu/Sci	0.3/0.5/0.2	π^-	1.07±0.04	0.33±0.04

For detectors with 4π geometry only the leakage in the back and in the front have certain influences on the performance. The leakage in the back is closely connected to the punch through and will be discussed in detail in chapter 5.7, the backscattering in the front may appear as background in track chambers, placed in front of the calorimeter.The amount of backscattered energy is plotted in fig.155 as function of the kinetic energy of the incoming particle. The results are nearly independent on the material, the sampling rate and particle species (not shown).

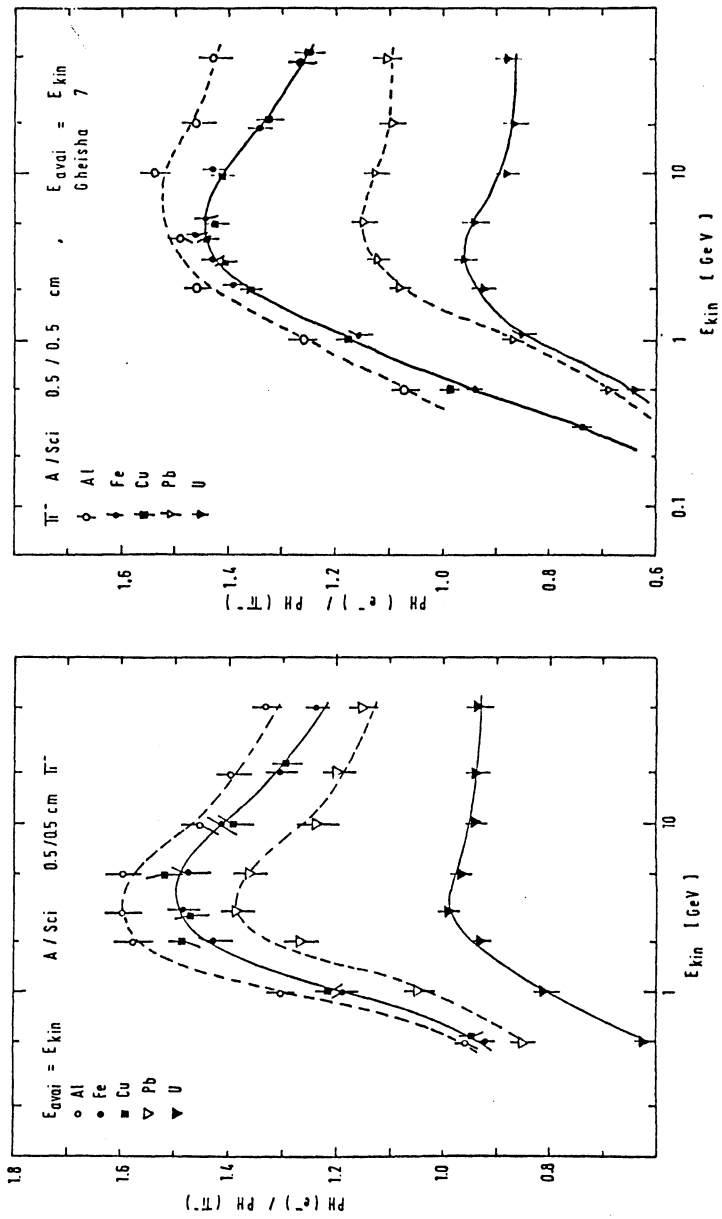

Figure 140. Pulse height ratio for electrons and negative charged pions as function of kinetic energy for various materials as absorber. As available energy the kinetic or total energy is chosen.

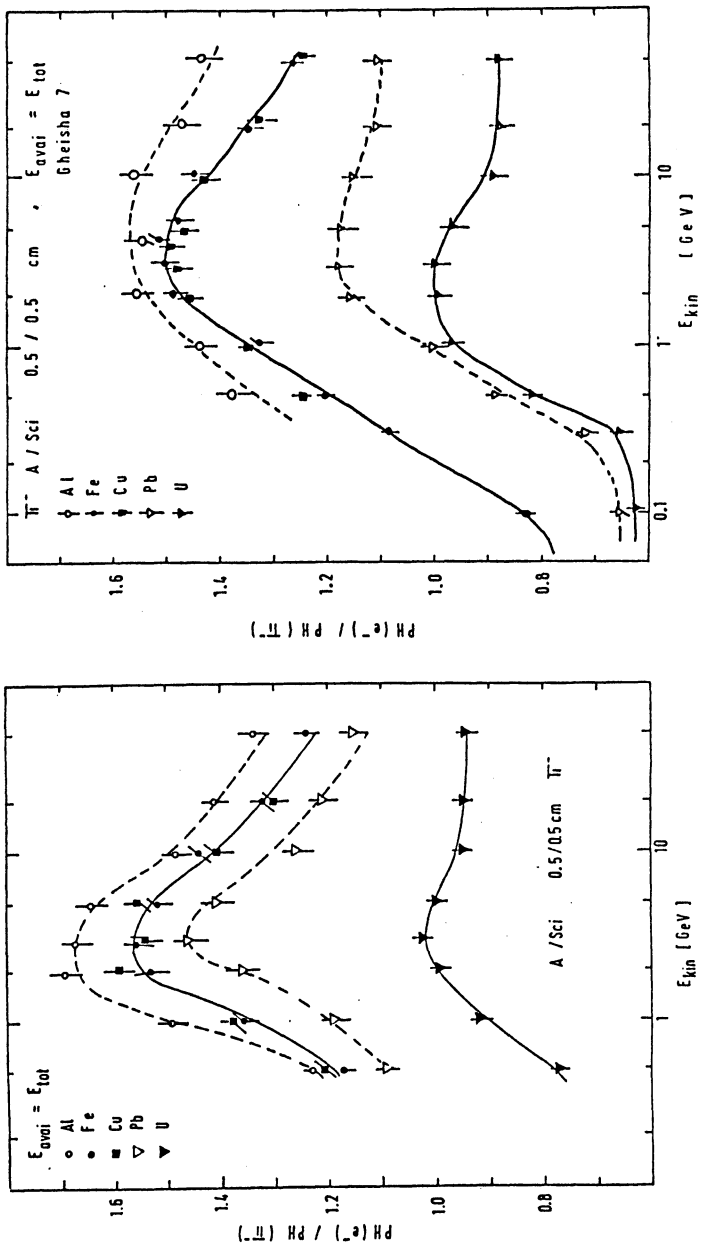

Figure 140. Pulse height ratio for electrons and negative charged pions as function of kinetic energy for various materials as absorber. As available energy the kinetic or total energy is chosen.

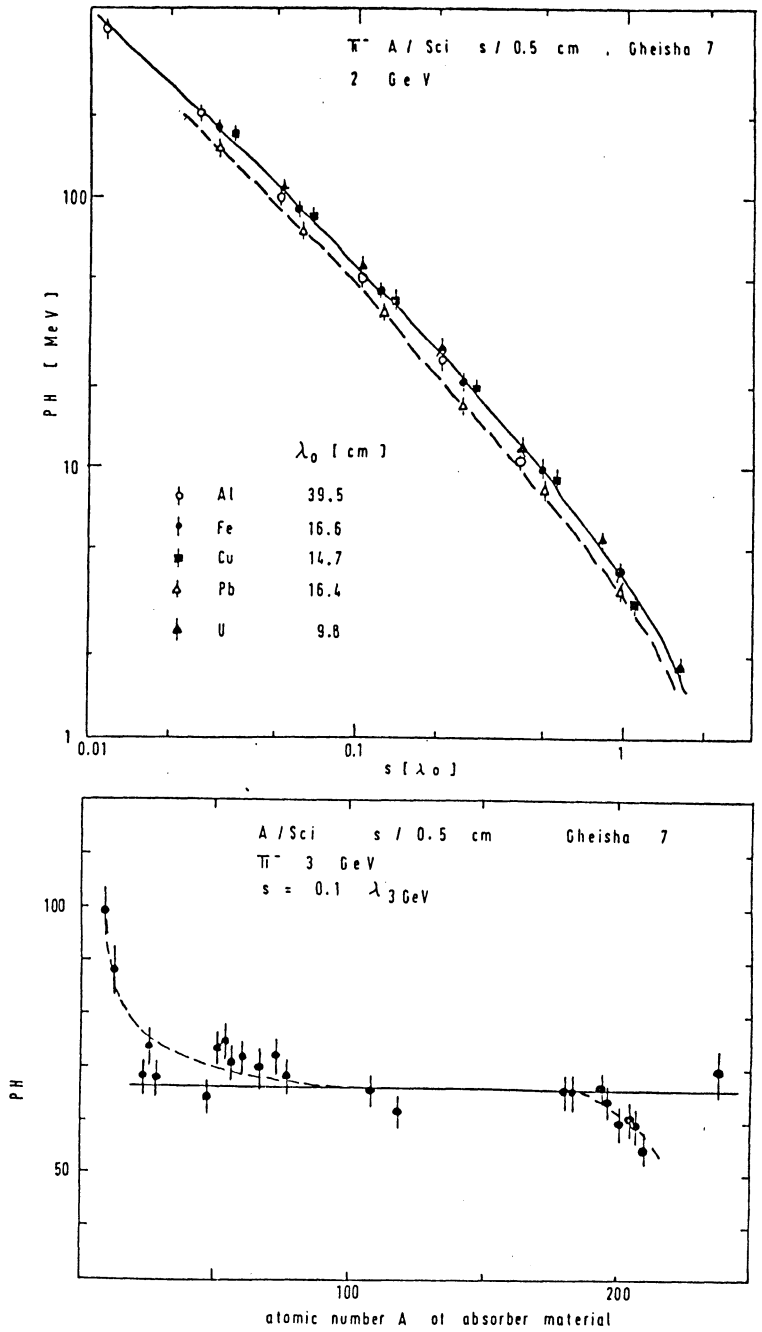

Figure 141. Pulse heights for negative charged pions as function of the sampling thickness (a) and as function of the atomic number of the absorber material (b). For details see text.

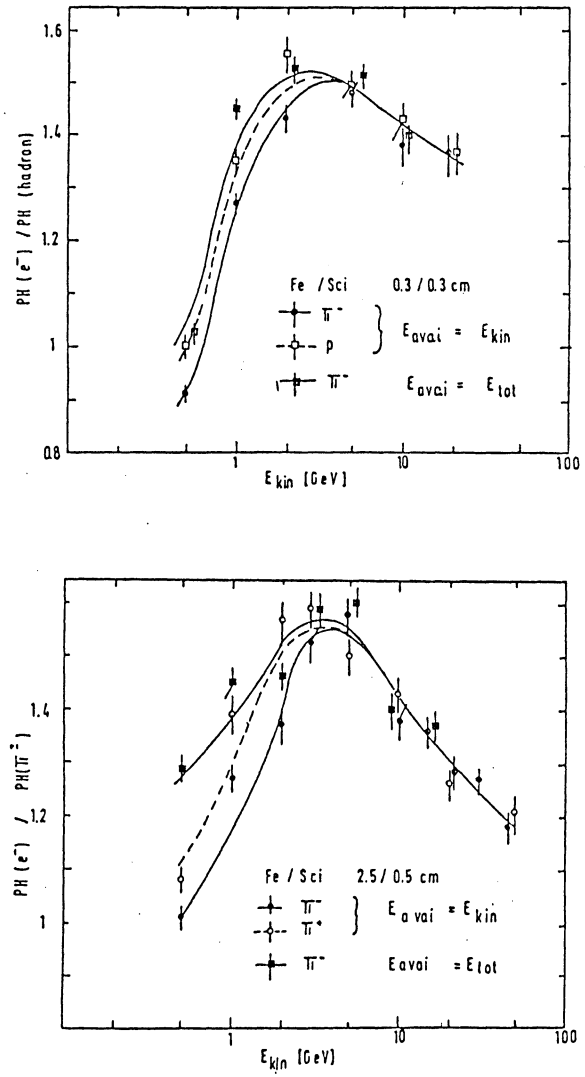

Figure 142. Pulse height ratio for electrons and various hadrons as function of kinetic energy for iron as absorber. For the available energy the kinetic energy is chosen. Only for negative pions we show also the results with the total energy as available energy for comparison.

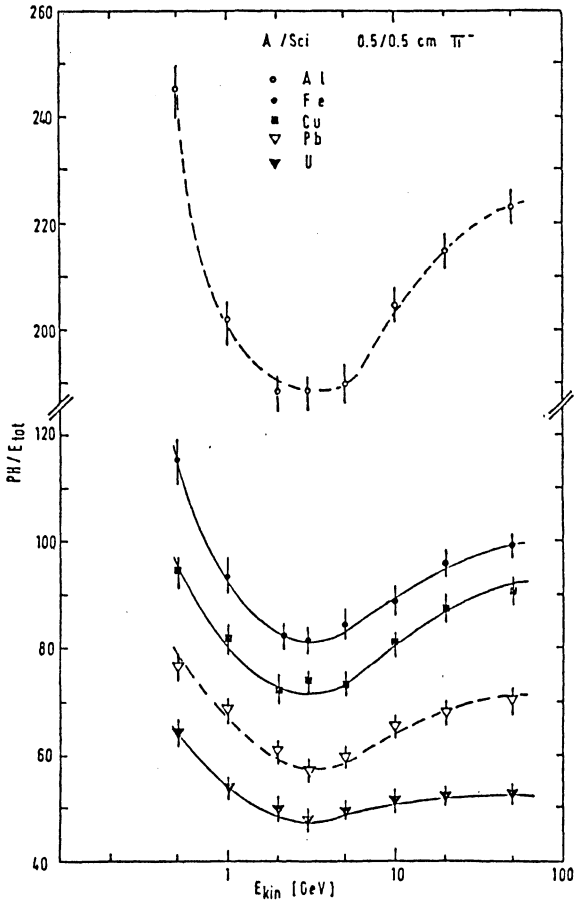

Figure 143. Pulse height divided by the total energy for negative charged pions as function of kinetic energy for various materials as absorber.

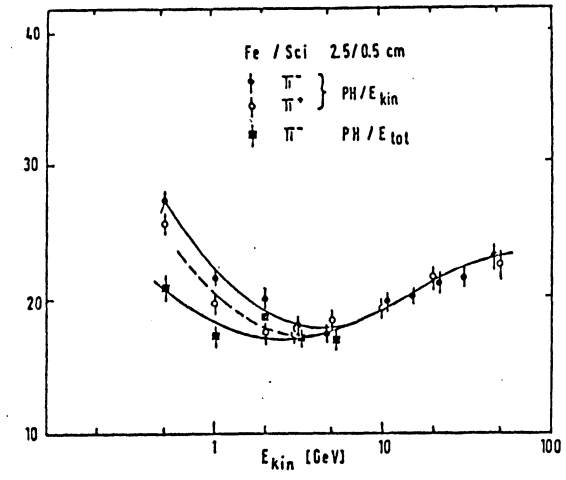

Figure 144. Ratio of pulse height and total or kinetic energy as function of kinetic energy for iron as absorber.

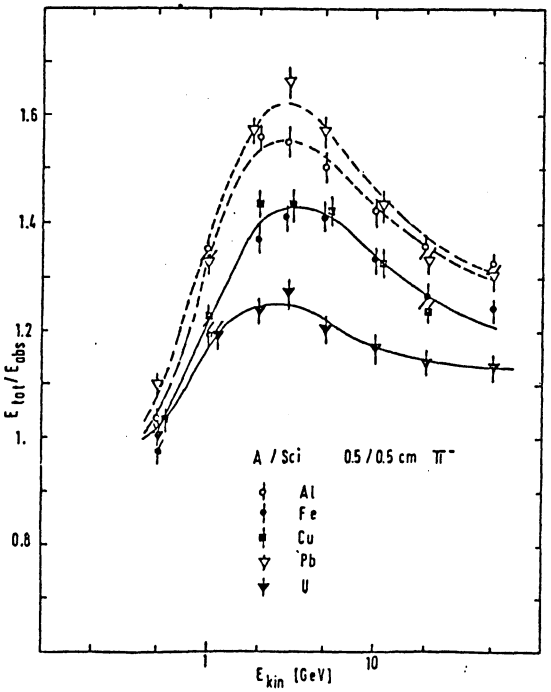

Figure 145. Ratio of total energy and total absorbed energy as function of kinetic energy for various materials as absorber.

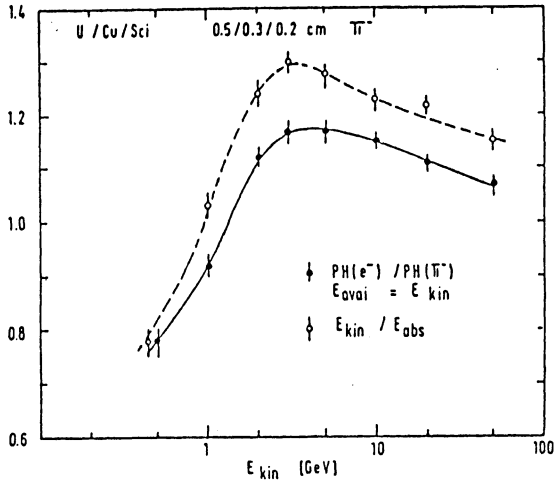

Figure 146. Pulse height ratio of electrons and negative charged pions as function of kinetic energy for a mixed uranium-copper calorimeter. For comparison we show also the ratio of the kinetic energy and the total absorbed energy.

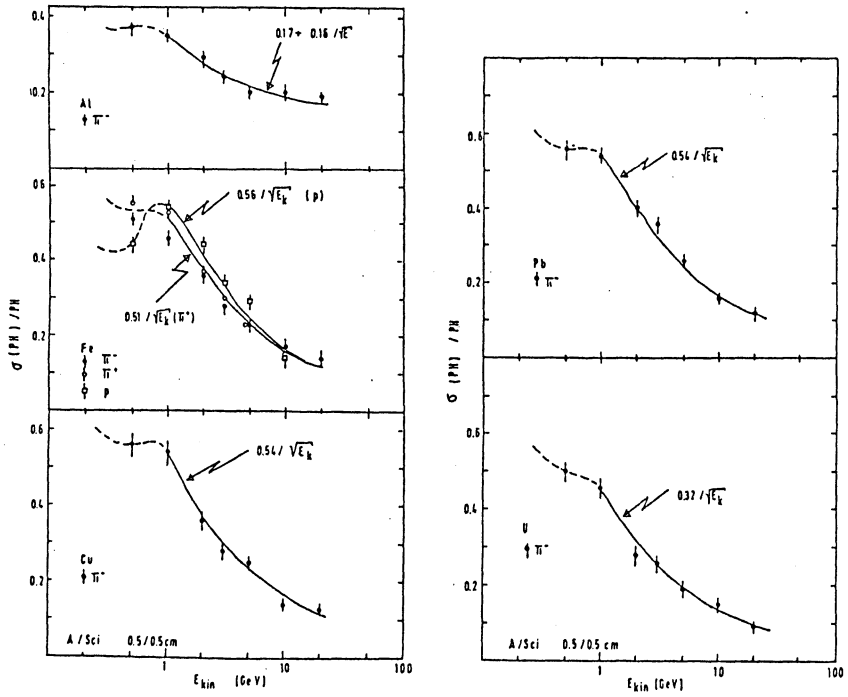

Figure 147. Pulse height resolution as function of kinetic energy for various materials as absorber.

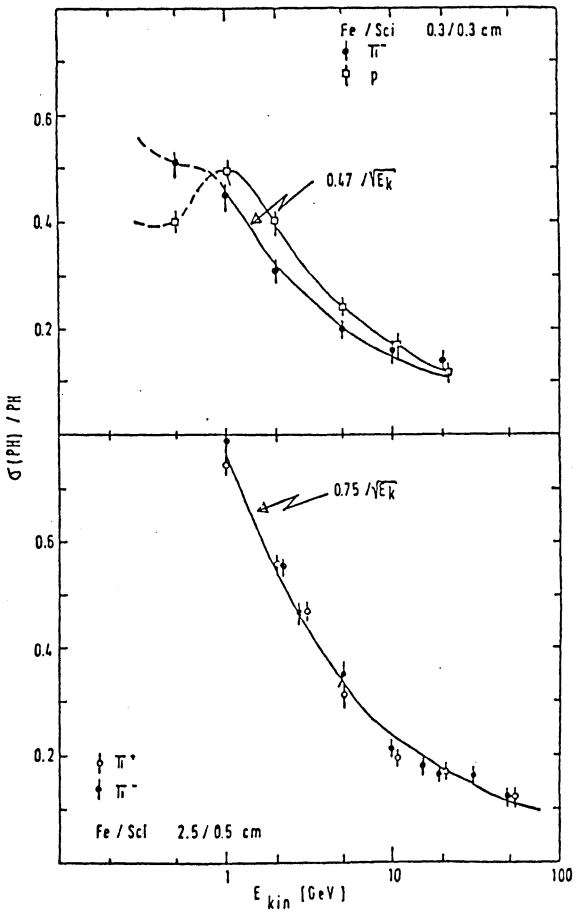

Figure 148. Pulse height resolution as function of kinetic energy for iron as absorber.

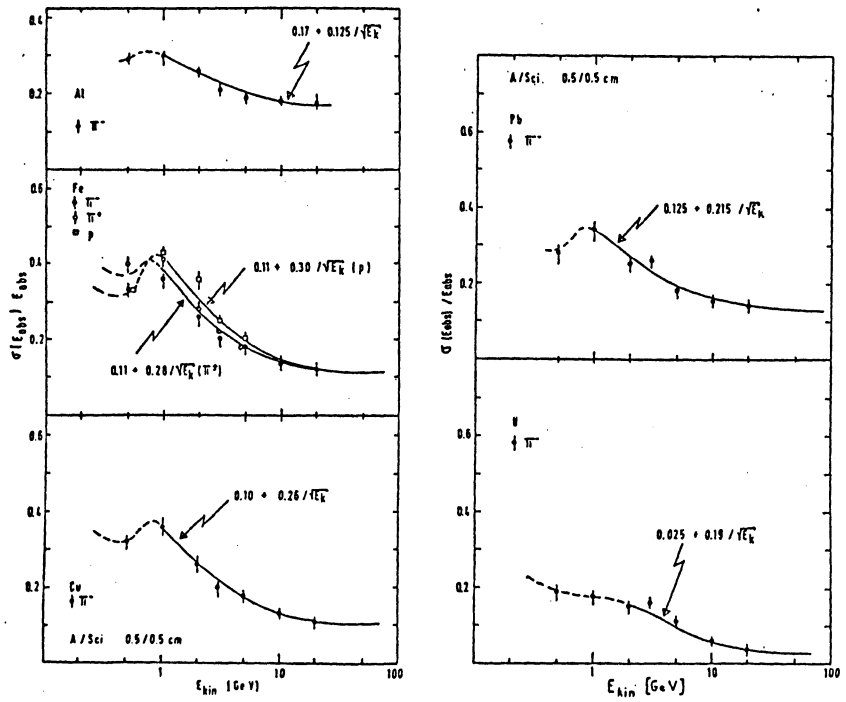

Figure 149. Resolution of the total absorbed energy as function of kinetic energy for various materials as absorber.

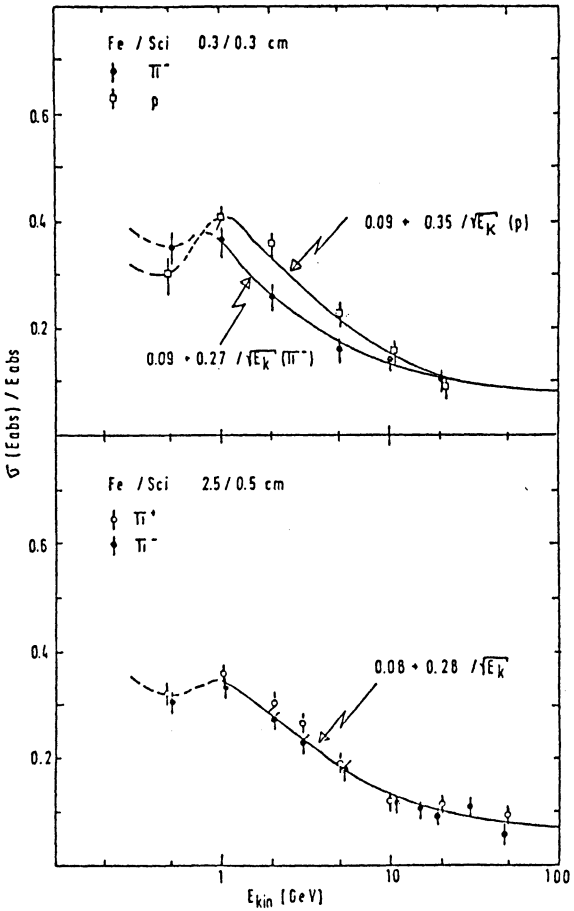

Figure 150. Resolution of the total absorbed energy as function of kinetic energy for iron as absorber.

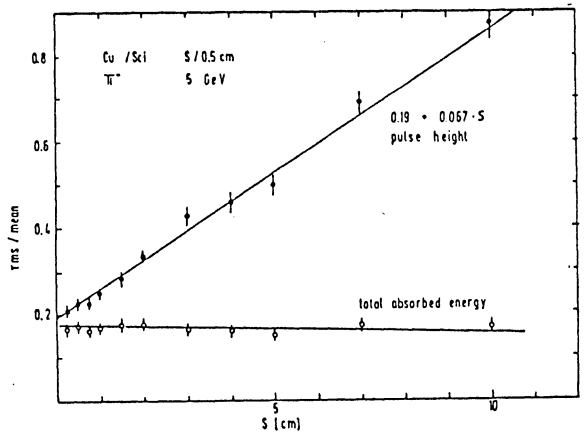

Figure 151. Pulse height resolution for pions in a copper scintilator sandwich calorimeter as function of the sampling thickness s. For comparison the resolution of the total absorbed energy is shown too. The lines represents fits to the data.

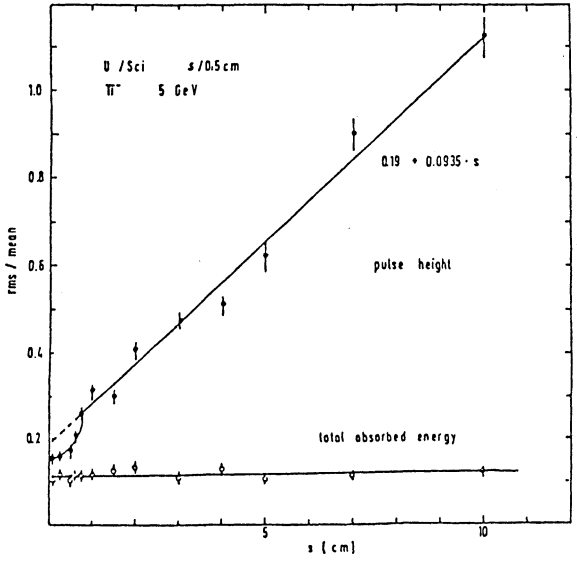

Figure 152. Pulse height resolution for pions in a uranium scintilator sandwich calorimeter as function of the sampling thickness s. For comparison the resolution of the total absorbed energy is shown too. The lines represents fits to the data.

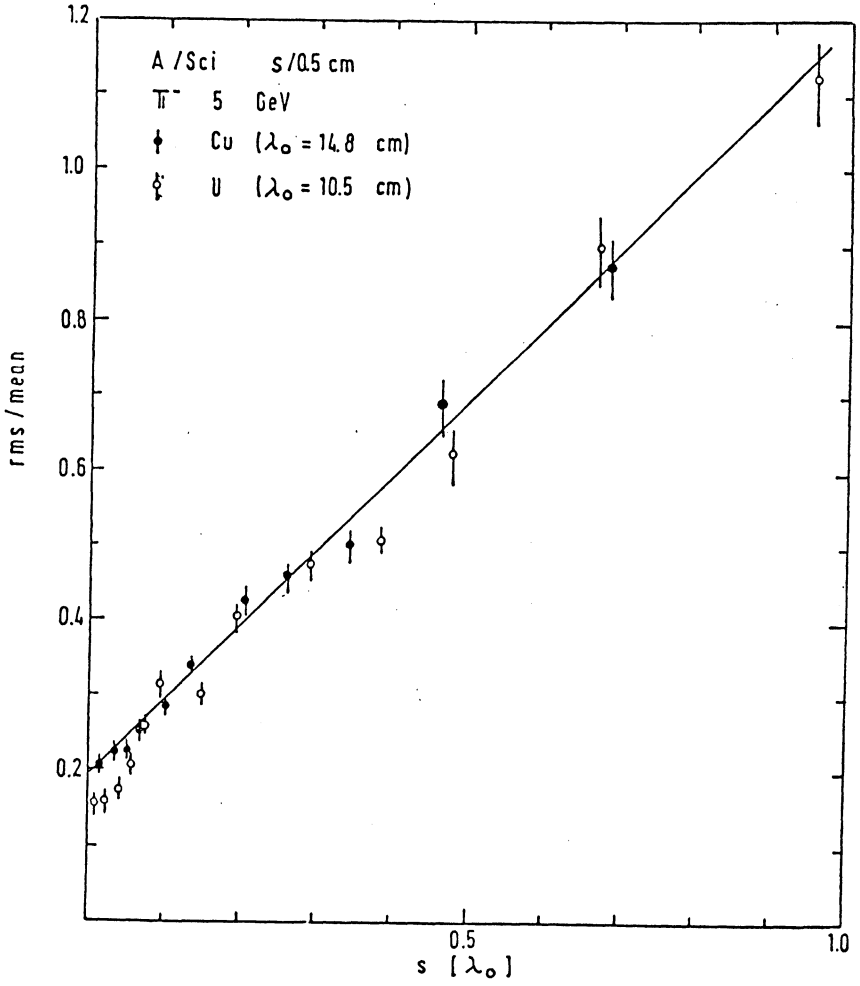

Figure 153. Comparison of copper and uranium sandwich calorimeter. Shown is the pulse height resolution as function of the sampling thickness s expressed in units of absorbtion lengths.

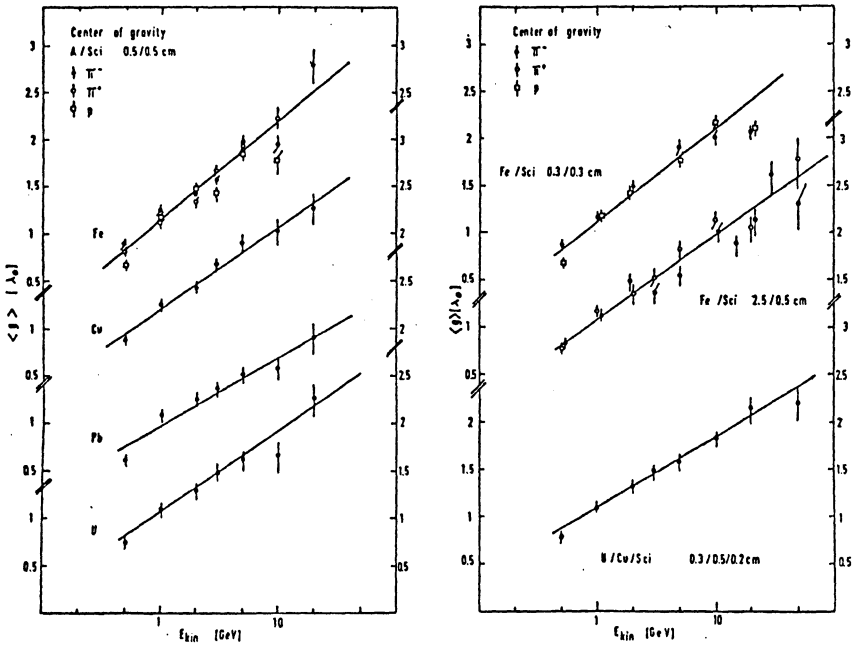

Figure 154. Center of gravity expressed in units of absorbtion lengths for various types of sandwich calorimeter as function of kinetic energy. The lines represent fits to the data, the results of which are summarized in table 15.

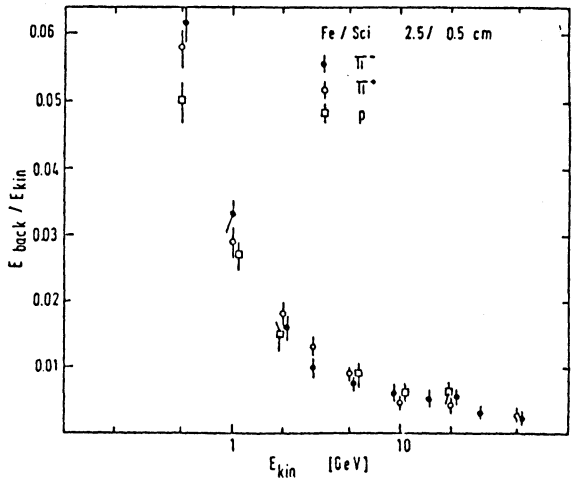

Figure 155. Fraction of energy scattered backward in iron scintilator sandwich calorimeter as function of kinetic energy.

5.4.1 Some selected test set-ups

Comparisons with experimental data have been carried out by a careful input of the geometries and a careful simulation of the read-outs as outlined in the respective publications. All trigger conditions, beam contaminations by other particles, beam momentum resolutions e.t.c have been taken into account. As a first step we normally simulated muons in the test set-up in order to calibrate amplifiers, ADC's and TDC's, the broadening of the Landau distribution by electron statistic of the phototubes, the saturation and statistic of the light output and the light attenuation as function of the pathlength in scintilators. The basic methods have already been discussed in chapter 5.2. We have checked then the digitization routines by simulation of the response to electrons. If the detector response to muons were not given in the publication, we have used the electrons directly for the calibration.

Unfortunatively the above calibration scheme could not passed through for all detector set-ups discussed in the following, since sometimes important informations were missing. Beside that authors of experimental papers like to improve the performance of their calorimeter by sophisticated hardware and tricky cuts in the off-line analysis. We are not always shure how accurate these cuts have been taken into account in our simulations.

We first study some experimental data of the total pulse height, then we continue with energy resolutions. The transverse and longitudinal shower shape will be studied as function of the energy of the incoming hadrons. Two special set-ups will be discussed in much more detail, a test set-up of the MARK J calorimeter and a test set-up of the CDHS calorimeter. They are somewhat complementary to each other in the sense, that the MARK J set-up has measured particles in the energy range of 0.5 - 10 GeV, whereas the CDHS people used particle energies from 15 to 140 GeV.

In fig.156 we compare the number of equivalent particles (nep), divided by the momentum of the incoming pion, as function of the momentum with experimental data from UA1 [132]. The reasons for the maximum at $\approx$ 0.5 GeV/c and the minimum at $\approx$ 2 GeV/c have been discussed in detail in the previous chapter. The same quantity, given in unnormalized form as (ADC-channel/GeV), is shown in fig.157 for an iron calorimeter with 2.5 cm sampling [133]. This test set-up consisted of an iron scintilator sandwich, which was viewed by plexiglas GS 218 wavelength shifters. Two different geometrical read-outs have been used (transversal read out and longitudinal read-out). The Monte Carlo results refer to the longitudinal read-out only.

Finally in fig.158 the ratio of the pulse heights for electrons and pions are shown for iron scintilator calorimeter and an uranium copper scintilator calorimeter ([134], [135] and [136]). In the experimental CDHS data some sophisticated off-line cuts have been applied, e.g.

a) an interaction should take place in the first 37.5 cm of iron, in order to assure adequate longitudinal containment;
b) events with backscatterings have been excluded.

Both cuts increase the average of the pion pulse heights. In the Monte Carlo simulations these cuts have not been applied.

From the last three figures we conclude that the total pulse height for hadron induced showers are well reproduced by the Monte Carlo simulation. The corresponding r.m.s. of the pulse heights from fig.157 are given in fig.159. The off-line cuts applied to the experimental CDHS data obviously improve also the resolutions. This is shown in fig.160, where the same cuts have also been applied to the Monte Carlo events.

The improvement of the resolution by use of uranium as absorber material is demonstrated in fig.161. The data are from ref. [136] and [137].

Shower profile measurements have been done by a lot of groups. For two detectors, a test set-up of the MARK J experiment and a test set-up of the CDHS experiment, this will be discussed later. Here we want to include only two figures, the center of gravity measurement for π^+ showers in the copper - streamer tube calorimeter of the L3 experiment in fig.162 and the transverse shower profile at different longitudinal thickness of iron for π^- shower at 10 GeV/c in fig.163 [138]. The Monte Carlo program seems to have no serious problems in describing these data.

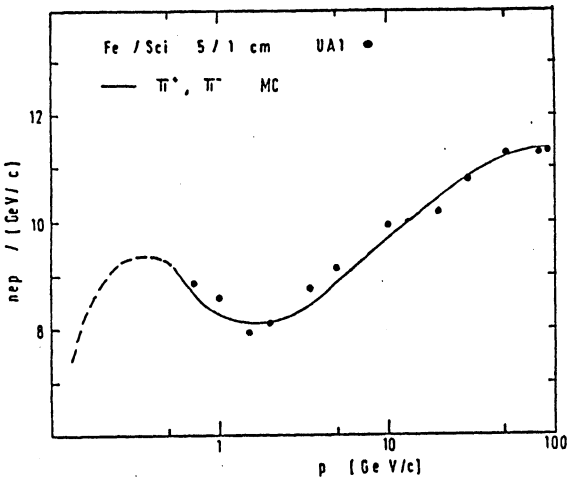

Figure 156. Pulse height expressed in number of equivalent particles divided by the momentum p as function of momentum. Shown are results for an iron scintilator calorimeter. For comparison data of the UA1 collaboration are given.

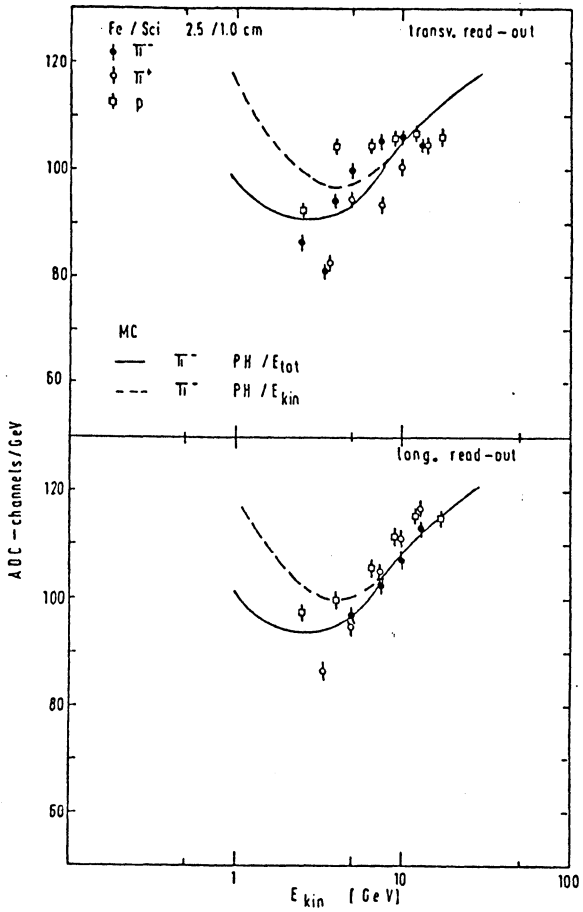

Figure 157. Pulse height expressed in ADC-channels divided by the total or kinetic energy as function of kinetic energy. The results are obtained for an iron scintilator calorimeter. For details see text.

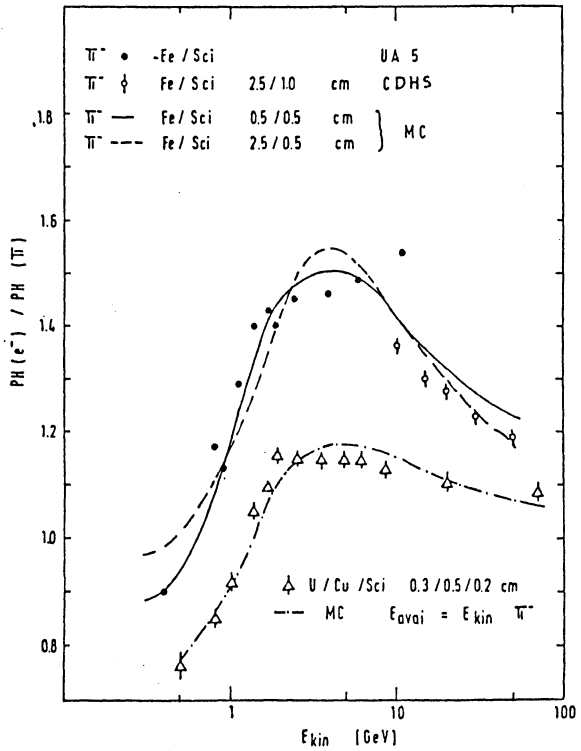

Figure 158. Pulse height ratio of electrons and pions as function of kinetic energy for iron scintilator calorimeter. Comparisons with experimental data are shown. For details see text.

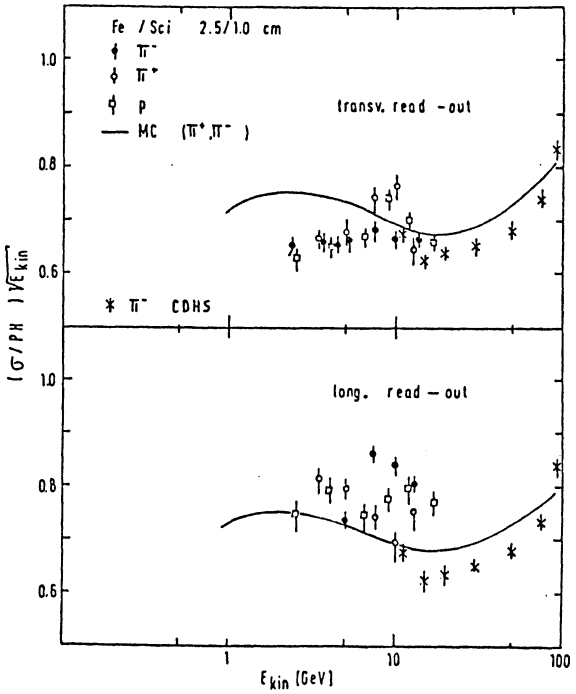

Figure 159. Pulse height resolution divided by the sqare root of the kinetic energy as function of kinetic energy for the data given in fig.157.

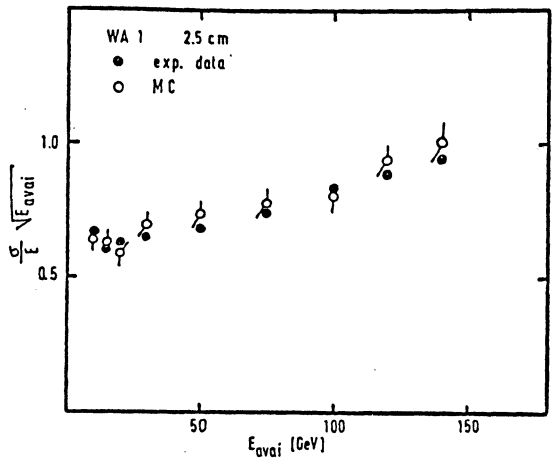

Figure 160. Same as fig.159, but for the WA1 test run results.

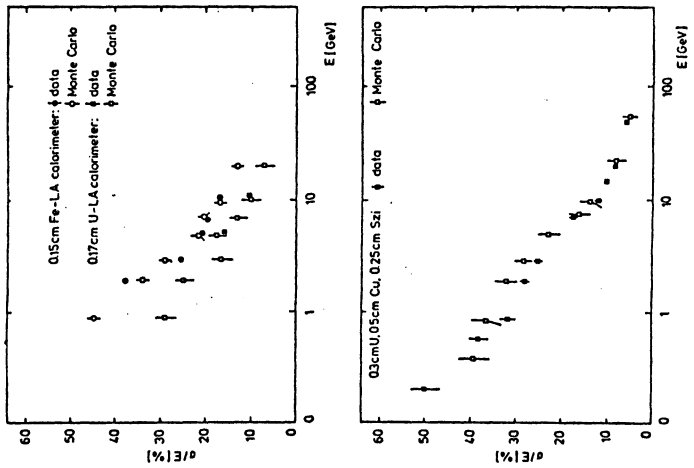

Figure 161. Pulse height resolution for Fe and U calorimeter (upper part) and a mixed U-Cu calorimeter (lower part) as function of kinetic energy.

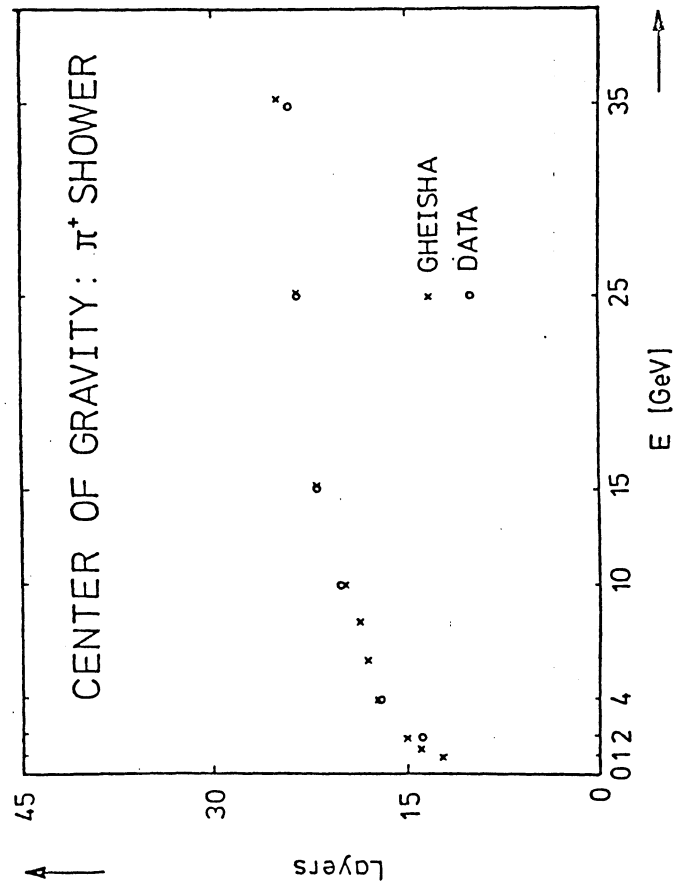

Figure 162. Center of gravity in units of layer number for the copper - streamer tube calorimeter of the L3 experiment as function of kinetic energy.

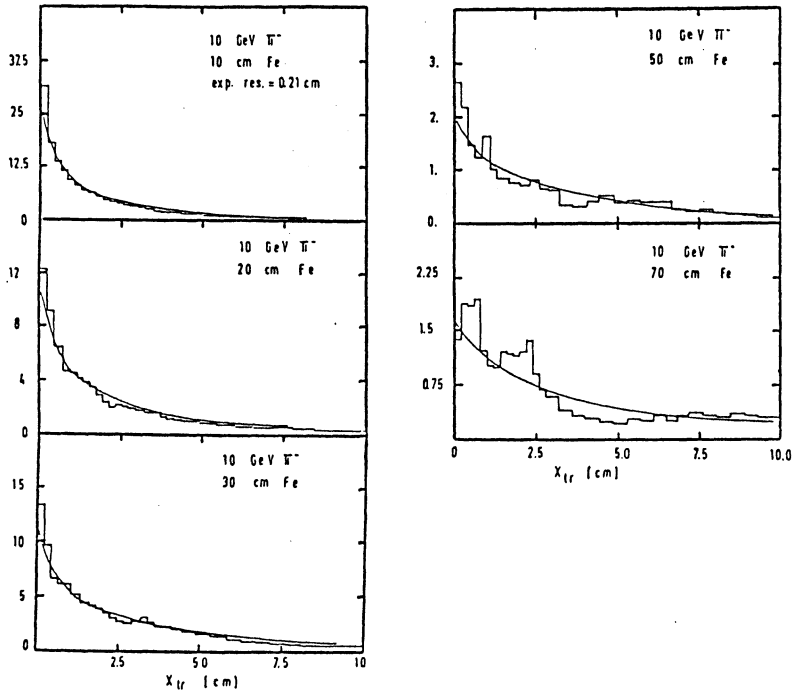

Figure 163. Transverse shower profile at different longitudinal thickness of iron for pion shower at 10 GeV/c. The experimental data are shown as lines. The histograms represent the Monte Carlo prediction.

5.4.2 Test run of the MARK J detector

The MARK J detector is shown in fig.164 and 165. It was designed to distinguish charged hadrons, electrons, muons, neutral hadrons and photons and to measure their directions and energies. It covers a solid angle of $\Phi = 2\pi$ and $\Theta = 12°$ to $168°$ (Θ is the polar and Φ is the azimuthal angle). The detector, which consists of five magnetized iron toroids built around a non-magnetic inner detector complemented by end caps, was designed to be insensitive to the effects of synchrotron radiation. The layer structure as seen by a particle emerging from the interaction point at a right angle to the beam axis is shown in fig.166.

Particles leaving the interaction region first pass through a five millimeter thick alluminium beam pipe, with an outer diameter of 190 mm. During the first nine months of operation, a ring of 2×16 lucite Cerenkov counters, each covering an azimuthal sector of 22.5° and a polar region of $9° < \Theta < 171°$, surrounded the beam pipe. In the later part of 1979 the lucite counter were replaced by a four-layer inner track detector composed of 992 drift tubes. Each tube is 300 mm long and 10 mm wide and has a spatial resolution of 300 microns. The tubes, which are arranged perpendicular to the beam line, distinguish charged from neutral particles in the angular range $30° < \Theta < 150°$ and reconstruct the position of the event vertex along the beam line to an accuracy of two millimeters. In a later stage of the experiment, this vertex detector has been improved and extended to 2616 drift tubes covering a polar angle $10° < \Theta < 180°$.

Particles then pass through 18 radiation lengthes of shower counters used to identify and measure the energy of electrons, photons, charged and neutral hadrons. This inner calorimeter is divided into three layers of shower counters (labelled A, B and C). Each counter is constructed of 0.5 cm thick pieces of scintilator alternated with lead plates of equal thickness. The A and B counters are each 3 radiation lengthes thick, while C is a total of 12 radiation lengthes thick. The 20 A shower counters are each 200 cm long and cover the angular region of $\Theta = 12°$ to $168°$. The 24 B shower counters are constructed identically to the A counters and cover an angular region from $\Theta = 16°$ to $164°$. Since every shower counter is viewed by one phototube at each end, the center of gravity in the lateral shower profile can be determined by comparing the relative pulse heights from each end of the counter. Timing information provides a measure of the spread of the transversal shower devellopment. The trajectory location determined by this method was found to be in excellent agreement with the data from the drift tubes.

Twelve planes of drift chambers (S,T) seperate the electromagnetic calorimeter from the hadron calorimeter K. 192 scintilation counters are

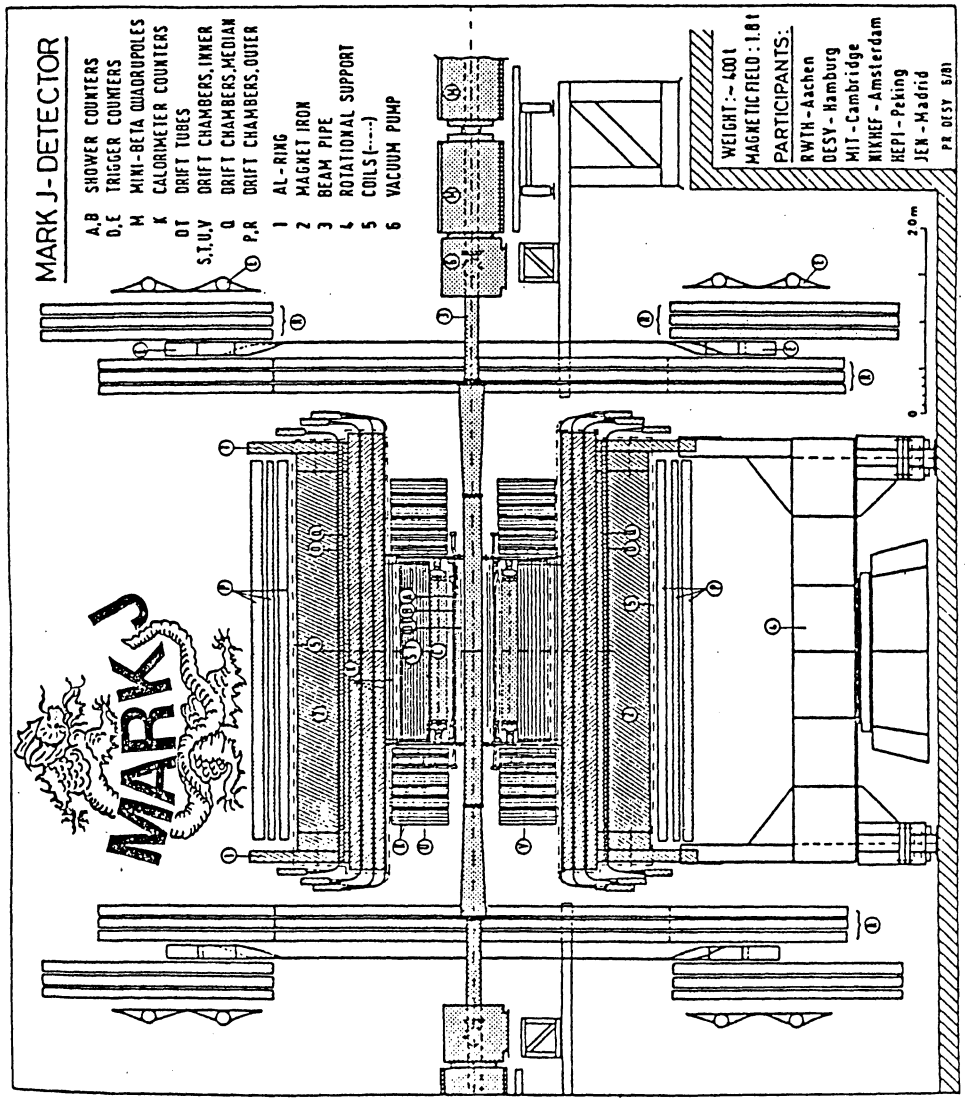

Figure 164. Layout of the Mark J detector. The beam direction is in the plane of the page.

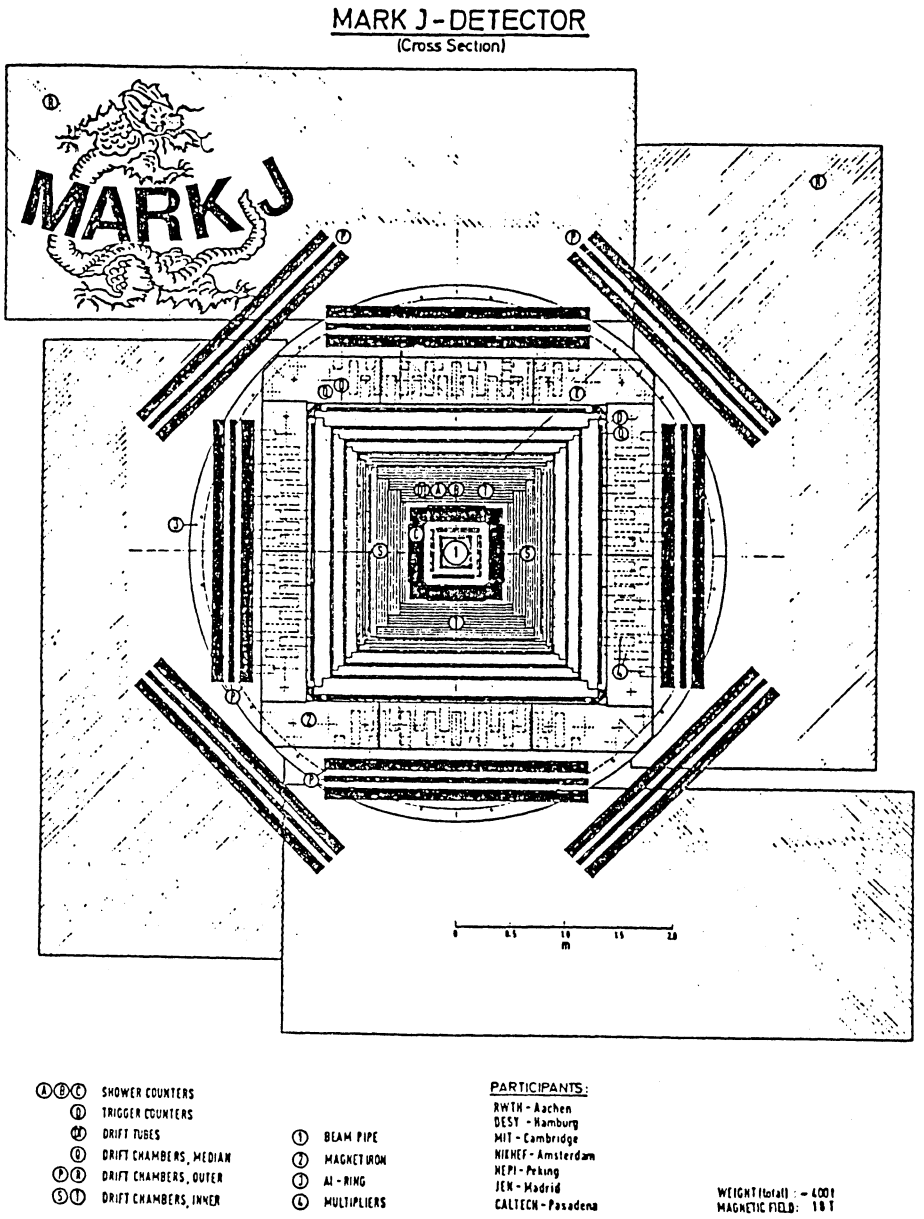

Figure 165. Layout of the Mark J detector. The beam direction is perpendicular to the page.

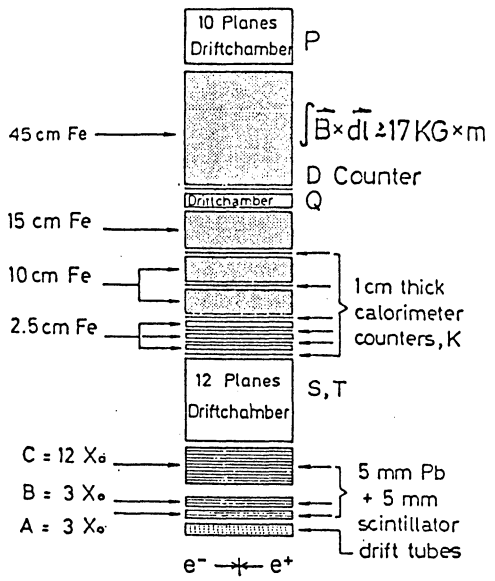

Figure 166. Schematic view of the layer structure of the Mark J detector.

arranged in four layers. The main body of the calorimeter is composed of the magnetized iron plates. These plates range in thickness from 2.5 to 15 cm.

Muons are identified by their ability to penetrate the iron of the hadron calorimeter. The momentum cut-off is about 1.3 GeV/c at normal incidence. The initial muon trajectory is measured in the S and T chambers and in the drift tubes. The bend angle and position of muons exiting from the calorimeter are measured in 10 planes of drift chambers, labelled R and P in fig.165. The total thickness of the iron is 87 cm and has a bending power of approximately 17 kG-meters. The typical bend angle for a 15 GeV muon is 30 mrad. An additional 2 layers of drift chambers (Q) are situated amidst the iron layers to measure the muon tracks in the bending plane. Adjacent to these chambers are the 32 muon trigger counter marked D used to trigger on single and multiple muon events and to reject cosmic rays. Beside that they may be used also as a part of the hadron

calorimeter. Covering each of the end cap regions are the E counter hodoscope.

In a detector of such a complicated structure it is essential that the behaviour of counter packages be investigated in particle beams of various types and energies. Thus, one quadrant of the compelete A, B, C and K assembly was reassembled at CERN and set up on a movable table in a test beam. The response of the counters to electrons, pions and muons of various energies, incident angles and positions was measured and compared with detailed shower Monte Carlo calculations. The analysis of this test beam data was fruitful for both, for the hardware people to find errors in the experimental technique and for the off-line people to find bugs in the Monte Carlo program.

A layout of the test set-up is shown in fig.167. Two Cerenkov counters were used to seperate muons, electrons and pions out of the beam. The counters have been adjusted in such a way that C_1 measures electrons only, whereas C_2 was sensitive for electrons and muons, but not for pions. Then we have the coincidence requirements: $C_1 \cdot C_2$ (electrons), $\bar{C}_1 \cdot C_2$ (muons) and $\bar{C}_1 \cdot \bar{C}_2$ (pions). These signals were used in coincidence with the beam defining trigger counters F (20×20×2.5 mm), T (120×120×6 mm) and O (10×10×2.5 mm) to start a gate of 100 nsec for the analog-digital converter. The main trigger $F \cdot T \cdot O \cdot \bar{C}_1 \cdot \bar{C}_2$ (for pions) was also used to start the TDC's.

Fig.168 shows a cross section through the electromagnetic calorimeter. It consisted of 2 A counter, 3 B counter and 3 C counter, mounted inside an alluminum box. The thickness of alluminum has been dimensioned in such a way, that it simulates the amount of material of the beam pipe and the lucite counters in front and the S and T chambers in the back. The missing S and T chambers were further simulated by an air-gap of 33 cm between the shower counter and the hadron calorimeter. The used set-up for the hadron calorimeter is shown in fig.169. Each scintilation counter was viewed by only one phototube. The pulse heights of the first two layers (K1) and the following two (K2) were added in order to simulate the performance of the real MARK J detector, where these layers are connected by a common light guide system and viewed by only one phototube. These light guides were no more available at the time of the test run. Note that PETRA came into operation half a year ahead of the schedule.

A CAVIAR system was used to read out the CAMAC controlled electronic and to drive a magnetic tape device.

All phototube gains were adjusted by normalizing the pulse height to that obtained from muons injected normally at the center of the counter. The peak position of the Landau distribution from muons will be called 'one

equivalent particle (ep)' or a 'minion'. For a detailed description of the analysis of this test run we refer to [139].

The pulse height distributions of negative pions at momenta from 1 to 10 GeV/c are shown in fig.170. We see the peak of the noninteracting particles (the calorimeter has a total length of only 2.6 λ_0) at all momenta. The distributions are quite well described by the Monte Carlo simulation.

The pulse height distributions at two selected longitudinal positions (A counter covering 0.06 - 0.14 λ_0 and K1 counter covering 0.91 - 1.08 λ_0) are shown in fig.171 for 1 GeV/c and 10 GeV/c momenta. One observes mainly the lines for one or two particles only. This must not be necessarily the lines for the noninteractiong particle. Also inside a shower there are only a very few charged particles crossing a longitudinal material boundary. The average values for the number of equivalent particles (minions) are summarized in fig.172 as function of momentum and as function of the longitudinal counter position. The dips at $t \approx 1\ \lambda_0$ show up just at the air gap between the lead scintilator shower counter and the iron scintilator hadron calorimeter.

The number of minions discussed so far is a very complicated quantity. Note that we have a calorimeter with different absorber materials and different samplings (18 layers lead with 0.5 cm, 4 layers iron with 2.5 cm and 2 layers with 10cm iron). The first 3 layers of scintilators (A counter) and the following 3 ones (B counter) are viewed by phototubes each at both ends, Then 12 layers (C counter) are connected to one phototube at both ends. In the hadron calorimeter the first 2 scintilator layers (K1 counter) and the following two ones (K2 counter) are connected to one phototube. Only the K3 and K4 counter are read out solely by one phototube. This complicated structure makes it necessary to introduce weighting factors for the pulse heights of each counter in order to determine a measure for the energy. The first approximation of this problem would lead to an expression of the form

$$E \sim ((1/6)P_A+(1/6)P_B+(4/6)P_C)+\alpha(P_{K1}+P_{K2}+2P_{K3}+2P_{K4}) \qquad (5.25)$$

where P_A, P_B, P_C, P_{K1},..... are the pulse heights in each layer, normalized to the muon line and the coefficients are determined by simple geometrical considerations. α should be roughly equal to 3.625 ($= \Delta\lambda_{K1}/\Delta\lambda_A$). This would lead to the weighting factors given in the first row of table 16.

Table 16: relative weighting factors for energy determination

counter	relative weighting factors	normalized to muon line	obtained by fits electrons	pions
A	0.167	0.032	0.032	0.080
B	0.167	0.032	0.042	0.059
C	0.667	0.128	0.114	0.140
K1	3.625	0.695		0.101
K2	3.625	0.695		0.167
K3	7.250	1.391		0.177
K4	7.250	1.391		0.181

If we use the actual factors for electrons, determined including the normalization to the muon line, we get the values in row 2. The energy resolution obtained in this way, may be improved. To this end we have fitted the pulse heights of each layer to an expression of the form

$$E_i = \sum_{k=1}^{7} f_k\ P_k \qquad (5.26)$$

The χ^2 condition reads

$$\chi^2 = \sum_{i=1}^{N} \frac{(E_{soll} - E_i(f_1,\ldots,f_7))^2}{w_i^2} = \text{Min.} \qquad (5.27)$$

The factors obtained with these fits are given in row 3 and 4 of table 16 for electrons and pions respectively. Comparing rows 2 to 4 one sees, that for electrons we get roughly the geometrical weights, but for pions the geometrical and fitted weighting factors are totally different. The factors for the electromagnetic shower counter are much higher for the fitted values ($\approx$ factor 2 for A counter, $\approx$ factor 1.1 for C counter), on the contrary the fitted factors for the hadron calorimeter counter are 2 to 8 times lower than the geometrical factors. The reason is simply that the electromagnetic π^0 component of the hadron shower can be measured much better in the lead scintilator shower counter than the hadronic part in the hadron calorimeter. With such fitted factors one measures essentially the π^0 energy within the hadronic shower.

In fig.173 energy distributions of pion induced shower are shown in the momentum range from 1 to 10 GeV/c. For the MC results we have used the same energy weighting factors (row 4 of table 16) as for the experimental

data. The average pulse heights and energies for electrons determined using the factors in row 3 of table 16 are shown in figs.174a and174b. The observed saturation with higher energies is partly a leakage effect, but may be also due to some noise in the electron data. This may be concluded from a comparison of experimental data and MC simulation for the pulse height distribution in fig.175c. There was no way to explain the low energy tail in the exp. data.

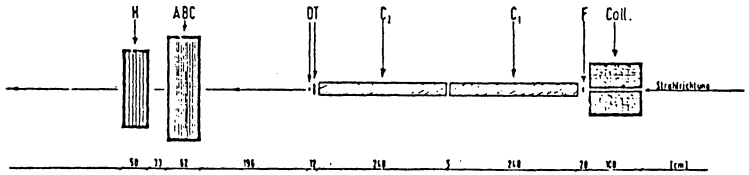

Lageplan des Versuchsaufbaus
Es bedeuten :
Coll.: Bleikollimator, Lochgröße 5 x 5 x 1000 mm
F,O,T: Triggerzähler, Größen: F: 20 x 20 x 2.5 mm
T: 120 x 120 x 6 mm
O: 10 x 10 x 2.5 mm
C_1, C_2 : Cerenkov-Zähler
ABC: Kalorimeter für elektromagnetische Schauer (A-,B-,C-Zähler)
H : Hadron-Kalorimeter (K-Zähler)

Figure 167. Layout of the test-run for the Mark J calorimeter.

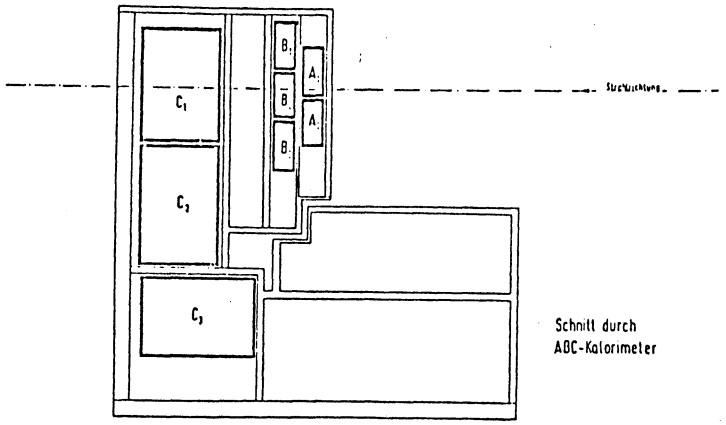

Figure 168. Cross section through the shower counter used in the test set-up of the Mark J calorimeter.

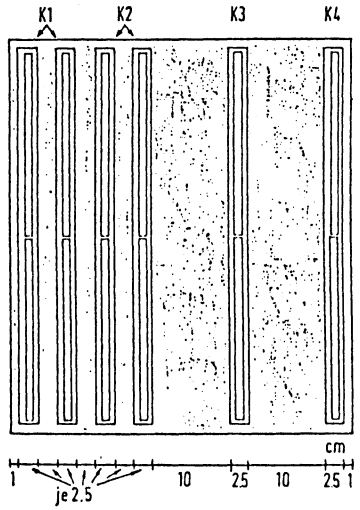

Figure 169. Cross section through the hadron calorimeter used in the test set-up of the Mark J calorimeter.

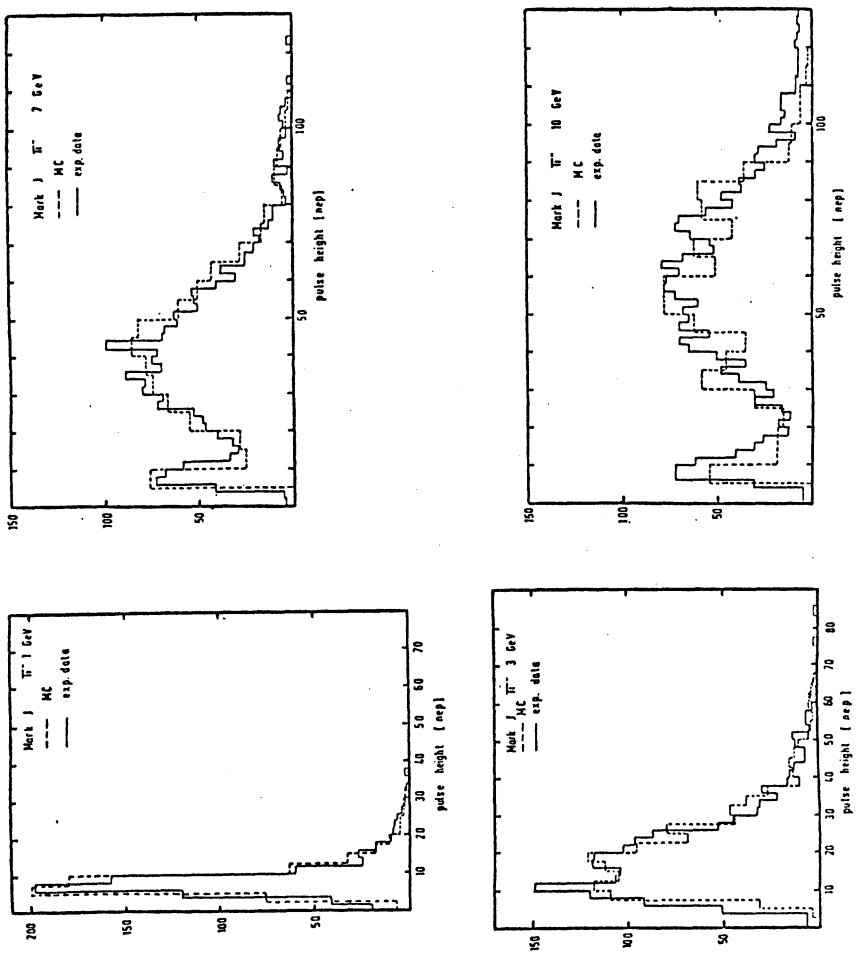

Figure 170. Pulse height distributions in units of equivalent particles for pions.

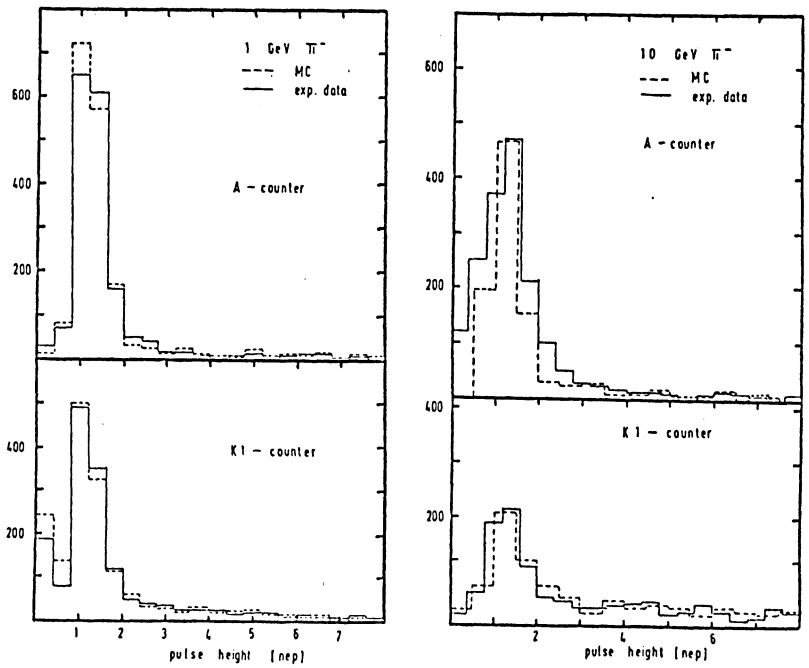

Figure 171. Pulse height distributions in units of equivalent particles for pions. Shown are results for the first layer of the shower counter (A) and the first layer of the hadron calorimeter (K1).

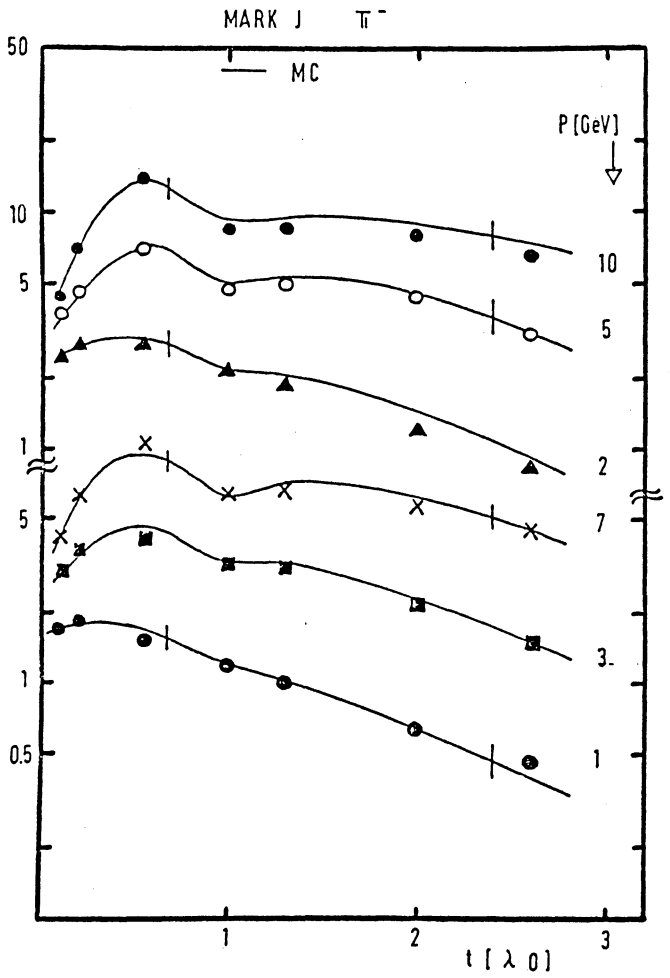

Figure 172. Average values for the number of equivalent particles as function of momentum p and as function of the longitudinal counter position.

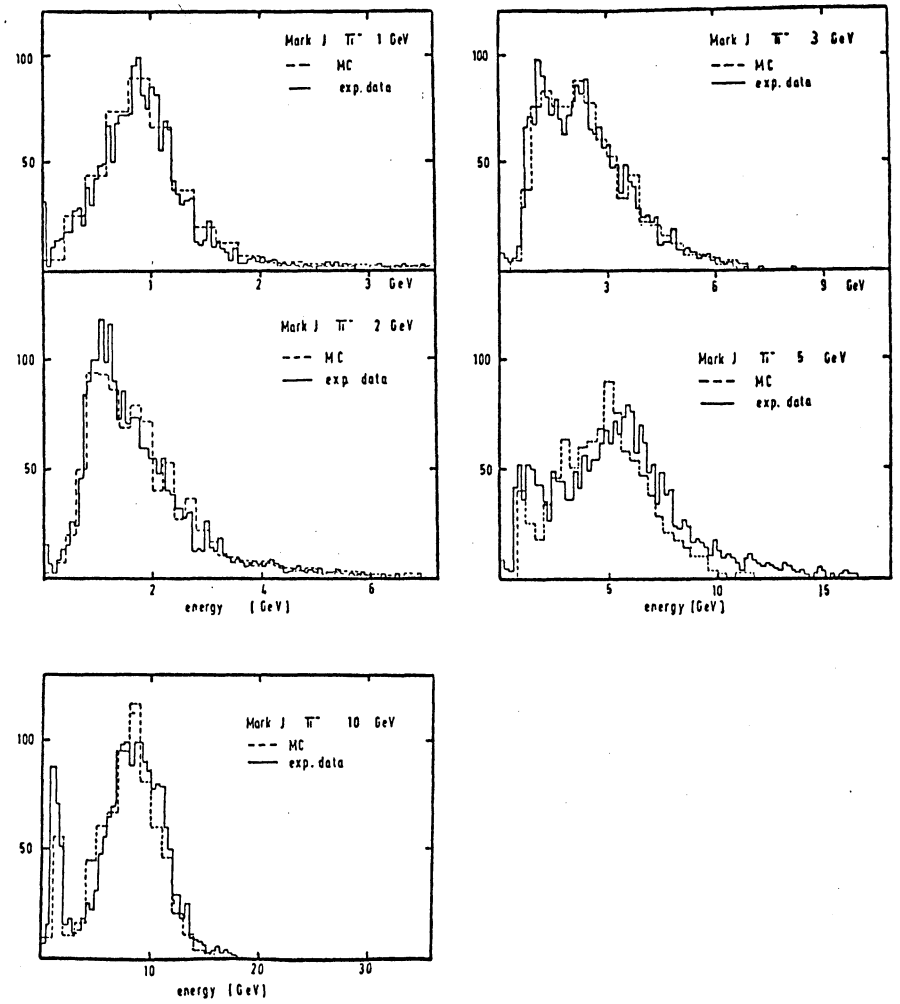

Figure 173. Pulse height distributions in units of weighted energy for pion induced shower in the momentum range from 1 to 10 GeV/c.

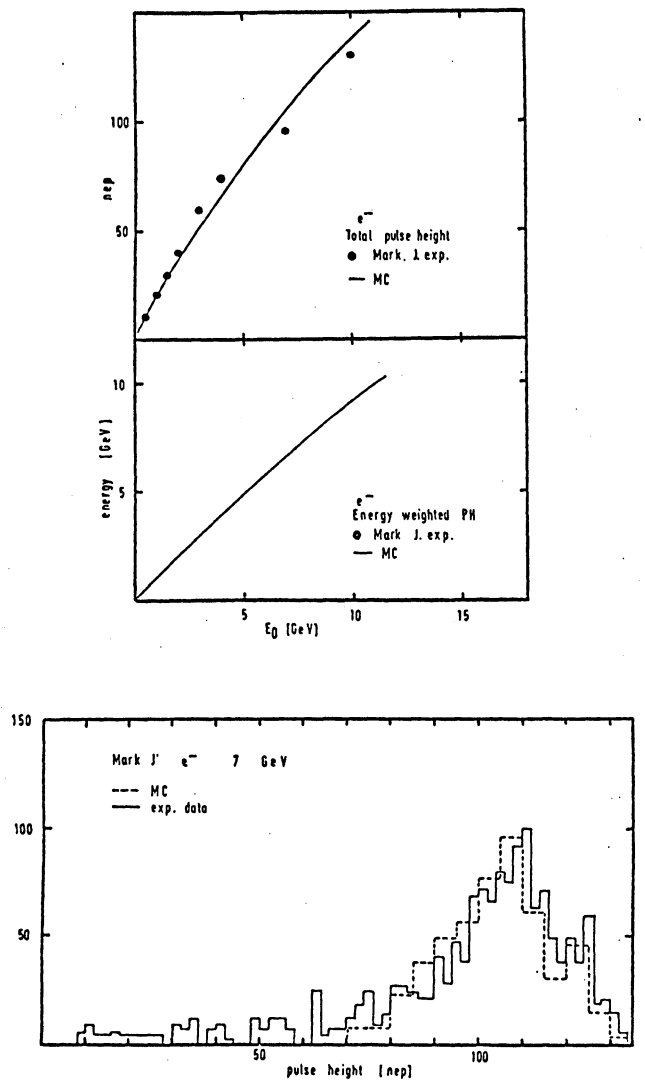

Figure 174. Average pulse heights and average weighted energies for electron induced shower. In the lower part of the figure the pulse height distribution for 7 GeV/c electrons is shown.

5.4.3 The CDHS iron scintilator calorimeter

A much simpler detector has been studied by the CDHS collaboration [140] We have chosen this experiment for our comparison with the Monte Carlo simulation, since the analysis has been reported in great detail. The experimental set-up consisted of 30 iron plates, each 120×120 cm^2 in area, sandwiched with 30 NE 110 plastic scintilation counters of dimensions 60×80×0.6 cm^3. The 3 cm thick iron plates were arranged in a periodic structure (6,3,6 cm thickness, repeated 10 times), which is equivalent to 5 cm Fe samplings on the average. A copper coil was mounted on the calorimeter in order to study the effect of magnetic fields on the energy calibration. The scintilation counters are each connected via a fan-shaped plexiglas light guide to a photomultiplier at one end. An alluminum plexiglas mirror is glued at the end opposite the phototube to improve light collection uniformity. Smaller NE 110 plastic scintilation counters (45×5×0.6 cm^3) were inserted at depths of 30, 60 and 90 cm of iron, in order to study the transverse shower devellopment in one radial direction. The beam line was defined by a serie of small scintilation counters before and behind the calorimeter. The counters behind the 1 m thick iron was used to tag for muons. Electrons are seperated from π^- by tagging with a differential Cerenkov counter located about 100 m upstream. The momentum acceptance of the beam was quoted to be ±1%.

Beam muons were used to calibrate the scintilation counter inside the calorimeter. It is clear that there is a background of hadron punch through in the muon sample, however this does not disturb the pulse height shape for the single particle line. A measured pulse height spectrum is compared in fig.175 with the MC simulation. The peak of the muon spectra, corresponding to the most probable energy loss, defines one equivalent particle (ep). This peak value is independent of the muon energy, since the most probable loss is not expected to vary with energy for energies above 1 GeV (see fig.1). The systematic uncertainty of the final energy calibration due to the definition of ep's and to the fitting of the ADC response was quoted to be about 3% in the experimental analysis.

As already mentioned, electrons were tagged at the lower energies (15 and 30 GeV) by means of a Cerenkov counter. At high energies electrons were seperated off-line by pulse height cuts on the first five shower counters. The data were usually taken with the magnet current switched on. Hadron showers were selected starting at a given depth in the calorimeter, listed in table 17. In addition hadrons are required to interact between the second and the sixth iron plate. An additional cut in minimum penetration of the shower was introduced to get rid of some low energy particles of short penetration.

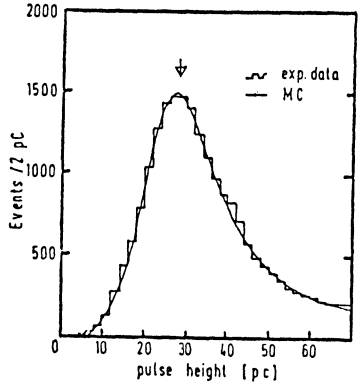

Figure 175. Pulse height spectrum for incident muons in the WA1 test run calorimeter.

Table 17: Cuts for shower selection (ph_i is the pulse height in scintilator i)

beam energy (GeV)	Cut for interaction in plate i	minimum number of counters with more than 3 ep.
15,30	ph_i, ph_{i+1} >2.5 ep	5
50,75	ph_i, ph_{i+1} >5.0 ep	7
100,140	ph_i, ph_{i+1} >10 ep	9

The geometry and off-line cuts have been applied to the Monte Carlo generated events too. The only unknown quantities were the relative amounts of electrons, pions and muons in the beam. We have used the ratio $e^-/\mu^-/\pi^- = 0.05/0.20/0.75$.

The mean number of equivalent particles is plotted in fig.176, the same quantity divided by the available energy in fig.177. If one reads out only every third layer, which correspond to 15 cm sampling, the results in fig.178 have been obtained. The energy resolutions, shown in fig.179, for 5

cm sampling, are fully compatible with our results, discussed already in chapter 5.3 for general classes of calorimeter.

The mean numbers of equivalent particles in each counter and the corresponding r.m.s. fluctuations are given in fig.180 for each energy. The non-exponentially falling down is due to the π^0 shower component near the maximum and a penetrating muon- and neutron- component at the tail of the distribution.

The transverse shower distribution is characterized in fig.181. Shown is the lateral dimension corresponding to 95% containment. This lateral dimension goes through a minimum at about 10 cm from the visible start of the shower. This is a significant effect at least in the MC results.

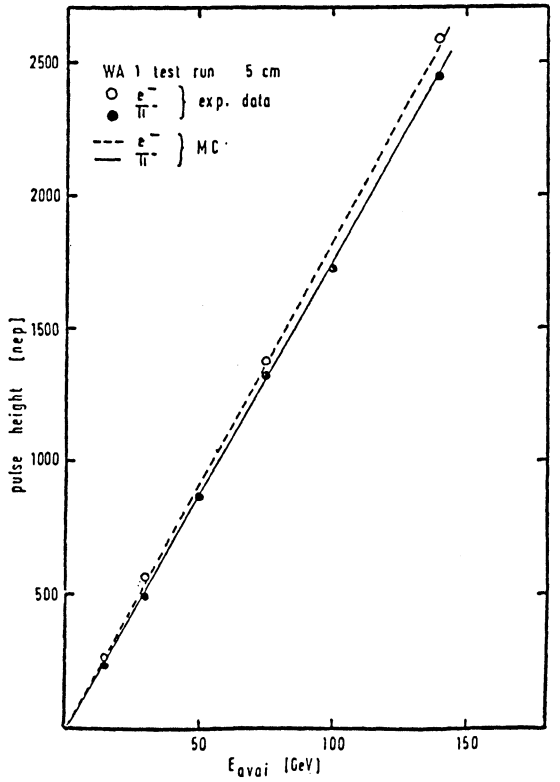

Figure 176. Total pulse height for electrons and pions as measured in the WA1 test run calorimeter. Off-line cuts are explained in the text.

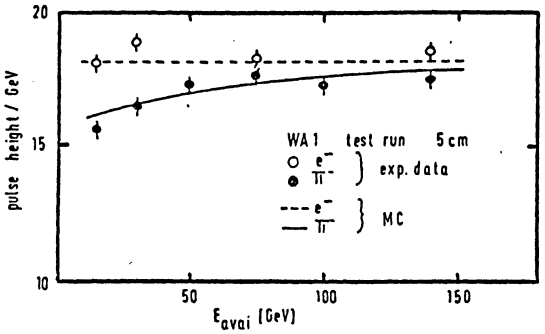

Figure 177. Total pulse height divided by the total energy as function of the energy for incident electrons and pions.

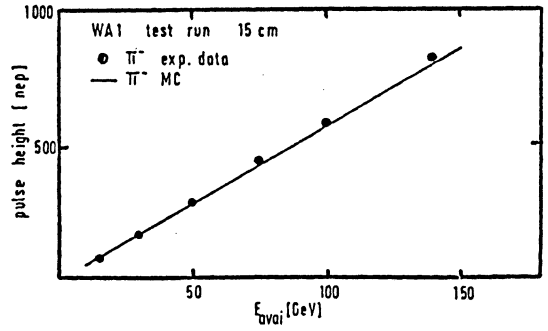

Figure 178. Total pulse height in units of equivalent particles as function of the energy for incident pions. Shown are results for 15 cm sampling instead of the 5 cm used otherwise.

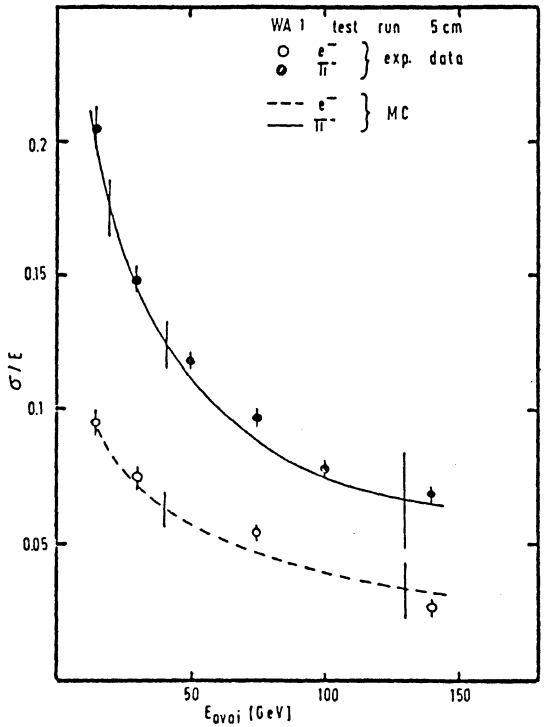

Figure 179. Energy resolution as function of energy for incident electrons and pions.

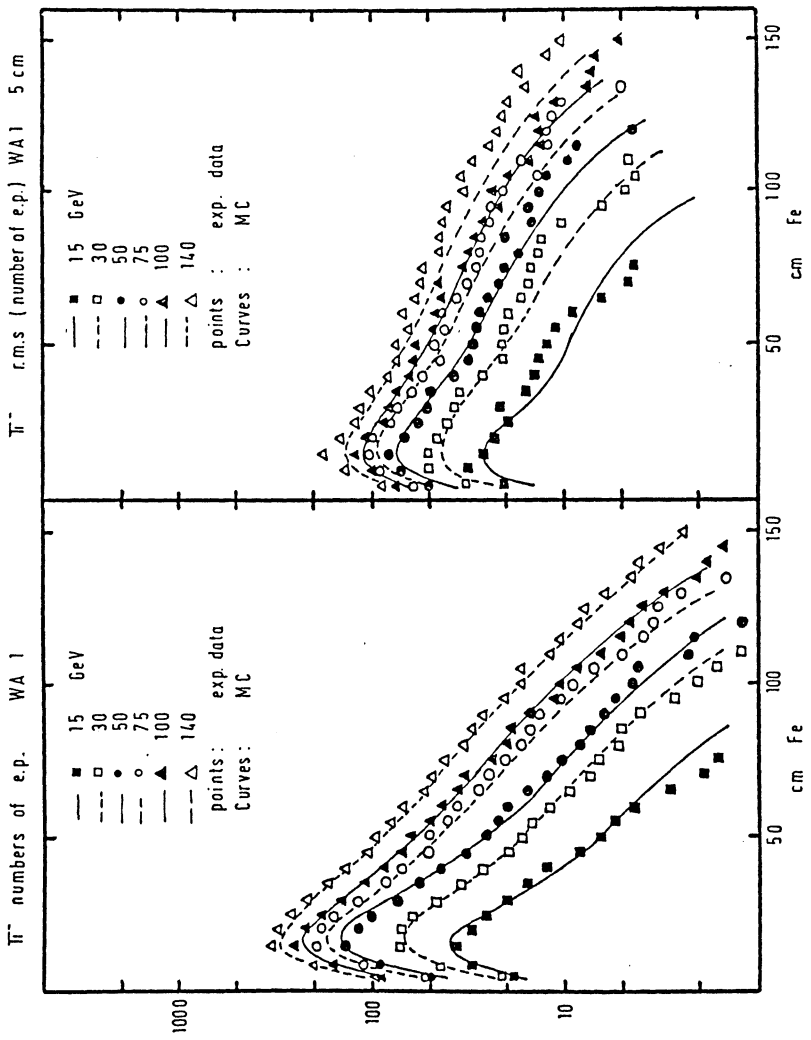

Figure 180. Mean number of equivalent particles and the corresponding r.m.s fluctuation as function of energy and as function of the longitudinal shower position.

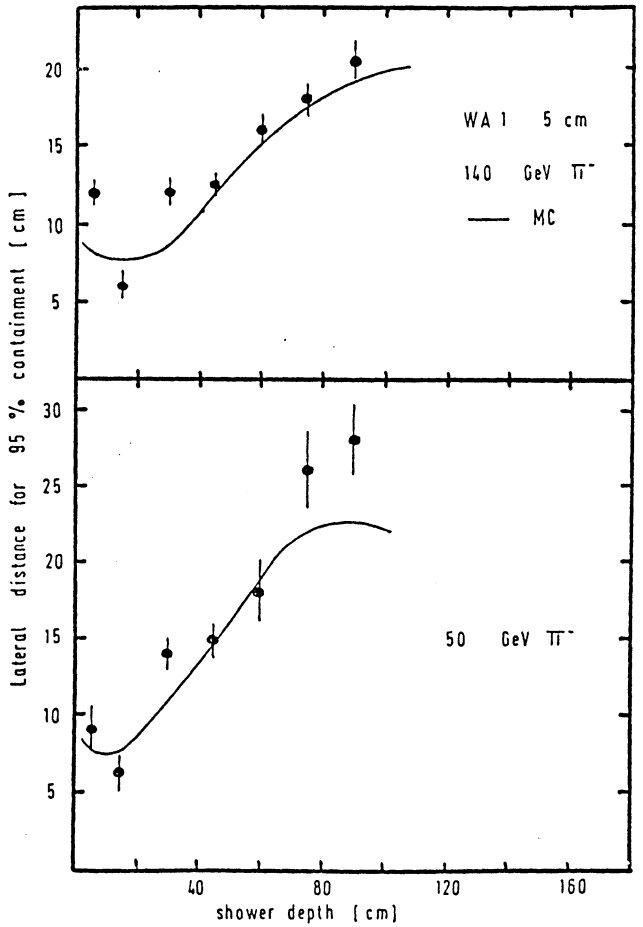

Figure 181. Transverse shower distribution given as the lateral dimension corresponding to 95% containment.

5.4.4 Calorimetric results of the MARK J detector at PETRA

The geometry of the MARK J detector has already been discussed in chapter 5.4.2. This section gives a brief description of the methods used to calculate the energy and direction of the particles seen by the detector and of the procedures used to select the events of interest. In this chapter we shall treat calorimetric measurements. The use of the muon spectrometer for inclusive muon measurements will be discribed in chapter 5.7.

The A, B, C and D counters have a phototube at each end (see fig.164 and 165). The position of a shower track along the z direction of the counter can thus be determined by use of the pulse height (ADC) and time (TDC) differences measured by these tubes. Combined with the position of the interaction vertex, calculated from the tracks in the drift tube vertex chamber, this gives the polar angle Θ of the track. The attanuation lengthes of the counters, which is needed for the ADC position measurement, was measured in the test beam as described in section 5.4.2. It is $\sim$ 100 cm for the A, B and C counter, $\sim$ 180 cm for the D counter and $\sim$ 400 cm for the K counter. The K counters are read out by only one phototube. Here the position measurement is done by a single TDC measurement, from which a resolution of 20 cm has been achieved. This value may be compared with a resolution of 15 cm obtained under perfect conditions (see section 5.2 for the discussion).

The position deduced from the TDC measurement uses a light propagation speed of $\sim$ 16 cm/nsec. This was also determined from test beam data. Corrections for the dependence of the TDC output signal on input pulse height (time slewing correction) and for the time of flight from the beam trigger counter to the calorimeter counter are applied. A weighted average of the two position measurements is then taken. The azimuthal angle Φ is determined by the position of the counters in space. The segmentation of the counter layers corresponds to a resolution of $\sim 7°$ in Φ for an individual hit.

The energy corresponding to the pulse height recorded in the shower counters and calorimeter counters is computed by taking a weighted sum of the ADC values. The appropriate weight for each layer of counters has been determined in first approximation from the analysis of the test beam data described in section 5.4.2, and has been adjusted later to minimize the total measured energy for hadronic e^+e^- events at $\sqrt{s} = 30$ GeV.

So called 'counter tracks' are constructed with a vector energy flow computed from the energy and position information of the groups of hits occuring within a cone of 20° opening angle, emanating from the interaction point. From this counter tracks the total missing energies in the directions parallel and perpendicular to the beam may be computed. The observed distributions of these quantities are shown in fig.182 for hadron events with 30 GeV $\leq \sqrt{s} \leq$ 36 GeV.

Physics results of the MARK J detector have been collected in two summary reports ([141] and [142]). Jet analysis is one of the main research domain of the MARK J detector. For each counter hit, a vector $\vec{E}_i$ is constructed, whose direction is given by the position of the signal in the counter, and whose magnitude is given by the corresponding energy. A parameter T (thrust) is defined as

$$T = \max \sum_i |\vec{E}_i \cdot \vec{e}_1| / \sum_i |\vec{E}_i| \quad , \tag{5.28}$$

where $\vec{E}_i \cdot \vec{e}_1$ is the parallel component of $\vec{E}_i$ along a given axis $\vec{e}_1$, and the maximum is found by varying the direction of this axis. The resultant direction is thus the direction along which the projected energy flow is maximized. To investigate the energy distribution in the plane perpendicular to the thrust axis $\vec{e}_1$, a second direction $\vec{e}_2$ is defined perpendicular to $\vec{e}_1$:

$$F_{major} = \max \sum_i |\vec{E}_i \cdot \vec{e}_2| / \sum_i |\vec{E}_i| \tag{5.29}$$

with $\vec{e}_1 \cdot \vec{e}_2 = 0$.

The third axis $\vec{e}_3$ is orthogonal to both $\vec{e}_1$ and $\vec{e}_2$. The projected energy flow along this axis is given by

$$F_{minor} = \sum_i |\vec{E}_i \cdot \vec{e}_3| / \sum_i |\vec{E}_i| \quad . \tag{5.30}$$

If hadrons were produced according to a $q\bar{q}$ two jet distribution, then the energy distribution in the plane as defined by the major and minor axes $\vec{e}_2$ and $\vec{e}_3$ would be isotropic. Alternatively, if hadrons were produced via three body intermediate states such as $q\bar{q}g$, and if each of the three partons fragments into a jet of particles, the energy distribution of these events would be oblate. This leads to the definition of the oblateness,

$$O = F_{major} - F_{minor} \quad . \tag{5.31}$$

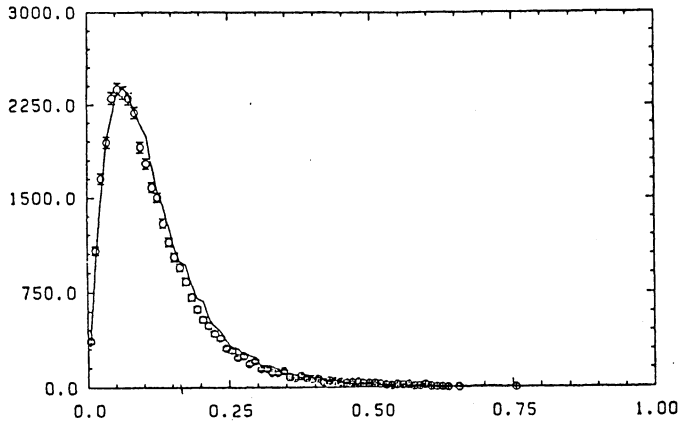

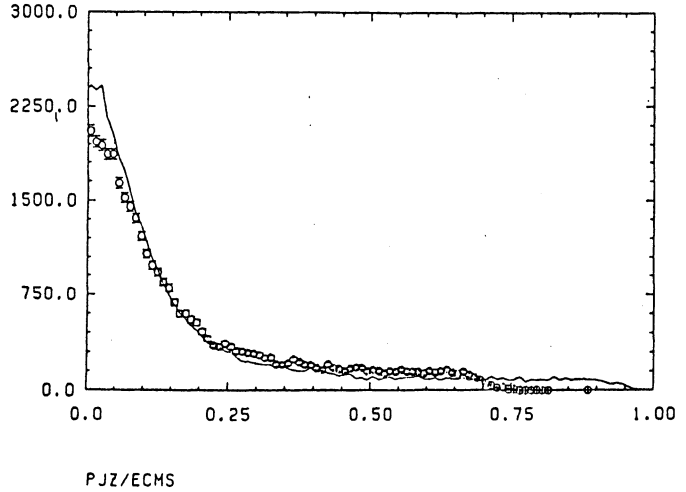

Figure 182. Total missing energies in the directions perpendicular(PJT) and parallel(PJZ) to the beam. The energies are normalized to the CMS energy, which is between 30 GeV ≦ $\sqrt{s}$ ≦ 36 GeV. The lines show the MC results.

One expects $O \approx 0$ for two jet events and

$$O \approx 2\, P_t^{gluon}/\sqrt{s} \tag{5.32}$$

for three jet final states. The oblateness is an extremely useful quantity to find three jet final states in e^+e^- interactions [143].

In the Monte Carlo simulation hadron production by e^+e^- annihilation is treated in the framework of quantum chromodynamics (QCD), where the final state hadrons are viewed as composite particles made up of quarks and antiquarks bound by a force mediated by gluons. The process proceeds through the production of a $q\bar{q}$ pair, accompanied by the possible final state radiation of one or two gluons. The quarks and gluons then fragment, forming jets of hadrons.

$$e^+e^- \rightarrow q\bar{q} \rightarrow \text{hadrons} \tag{5.33}$$

$$e^+e^- \rightarrow q\bar{q}g \rightarrow \text{hadrons} \tag{5.34}$$

$$e^+e^- \rightarrow q\bar{q}gg \rightarrow \text{hadrons} \tag{5.35}$$

$$e^+e^- \rightarrow q\bar{q}q\bar{q} \rightarrow \text{hadrons} \tag{5.36}$$

The event generator used is that of Ali et al.[78]. In general, $q\bar{q}$ pairs are produced in fractions proportional to the square of the quark charges for flavors up, down, strange, charm and bottom (u, d, s, c and b respectively). The fragmentation procedure used to transform quarks into hadrons is similar to that used by Feynman and Field [75]. The fragmentation functions used are $zD(z) = (1 - z)^2$ for u, d and s quarks and $zD(z) = c$ for c and b quarks. Heavy quarks (c and b) are allowed to decay weakly according to the six quark model [79]. Since gluon fragmentation functions are yet unknown, gluons simply decay to quark pairs which in turn fragment according to the normal procedure (see also chapter 2.6.8 for a discussion of parton fragmentation).

The distribution of the thrust and the oblateness are shown in fig.183. In the present report we want to study the longitudinal and transverse shower devellopment for jets. Consequently we have to cut out the three and four parton final states $q\bar{q}g$, $q\bar{q}gg$ and $q\bar{q}q\bar{q}$. This is achieved by rejecting all events with $O > 0.3$. In order to have a sample of $q\bar{q}$ events clear from other backgrounds, we additionally rejected all events with $E_{vis}/\sqrt{s} < 0.7$, $E_t/E_{vis} > 0.5$ and $E_z/\sqrt{s} > 0.5$ (see fig.182). The Mark J calorimeter has a

poor acceptance in the very forward and backward direction. In order to have a well defined event sample we cut out all events with a thrust direction corresponding to $|\cos\Theta| > 0.71$, Θ beeing the polar angle of the thrust axis with respect to the beam line. For this sample of two jet events we show in fig.184 the missing energies corresponding to fig.182 and in fig.185 the distributions of the thrust and the oblateness. The distribution of the total measured energy normalized to the center of mass energy $\sqrt{s}$, shown in fig.186, shows that the Monte Carlo prediction peaks exactly at 1, whereas the experimental distribution is shifted slightly to a higher value.

In order to investigate the longitudinal shower devellopment for quark jet initiated showers we show in fig.187 the normalized energy distributions for all counter layers. Some disagreement between exp. data and MC seems to show up in the D counter, placed at $\approx$ 3 absorbtion lengthes. This is exactly at the place, where the Q chambers are located, which are used for μ identification. So we come back to this problem in chapter 5.7, where we are going to study the measurement of inclusive muons in more detail.

In fig.188 we compare the absorbed energies in the electromagnetic shower counter and in the hadron calorimeter. As can be seen the ABC counter energy is in general as twice as much as the KD counter energy. From that we can not conclude anything about the π^0 component in jets. Note that we used energy weighting factors, which overestimate in general the shower counter energy (see the discussion in chapter 5.4.2). The weighting factors have been determined by minimizing the resolution of the total measured energy. This method favours the shower counters ABC due to the much smaller sampling and due to the large amount of π^0 energy within the shower of a single hadron.

The correlation of the measured energies in the ABC and KD counters is shown in fig.189. We have plotted the KD counter energy for four bins of the ABC counter energy distribution. The agreement between exp. data and MC is in general satisfactorily.

The transverse energy profile of jet initiated showers is studied in fig.190 in terms of the variable $\lambda = \text{cotg}\,\Theta/E_{jet}$. Θ is the angle of the energy flow vector with respect to the jet axis (see also chapter 2.6.7 ff for a discussion of this variable). Plotted is the quantity $d\varepsilon/d\lambda$ with $d\varepsilon = dE(\Delta\Theta)/E_{jet}$, $dE(\Delta\Theta)$ beeing the energy fraction emitted into the angular interval $(\Theta,\Theta+\Delta\Theta)$. The variable λ projects the energy flow perpendicular to the jet axis to $\lambda = 0$ and accordingly the energy flow parallel to the jet axis to $\lambda = \infty$ or $1/\lambda = 0$. In fig.190 the angular energy flow is shown for each counter seperately. There is apparantly no major problem to describe the longitudinal and transverse energy profile of jet initiated hadron shower.

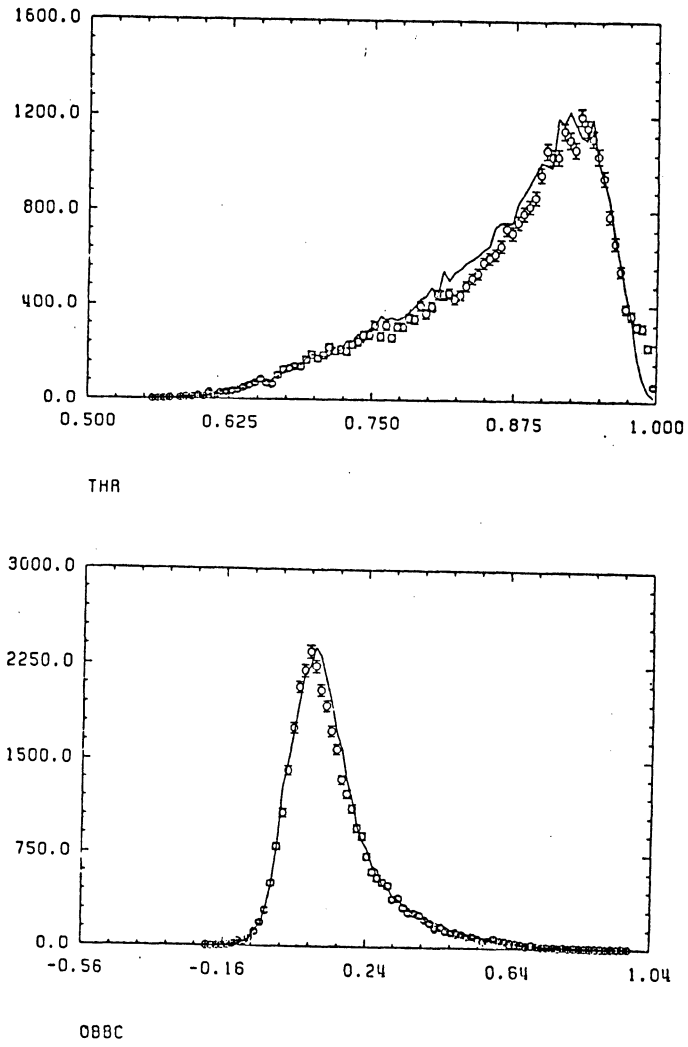

Figure 183. Distributions of thrust(THR) and oblateness(OBBC) as measured in the Mark J experiment at cms energies around 35 GeV. The lines show the MC results.

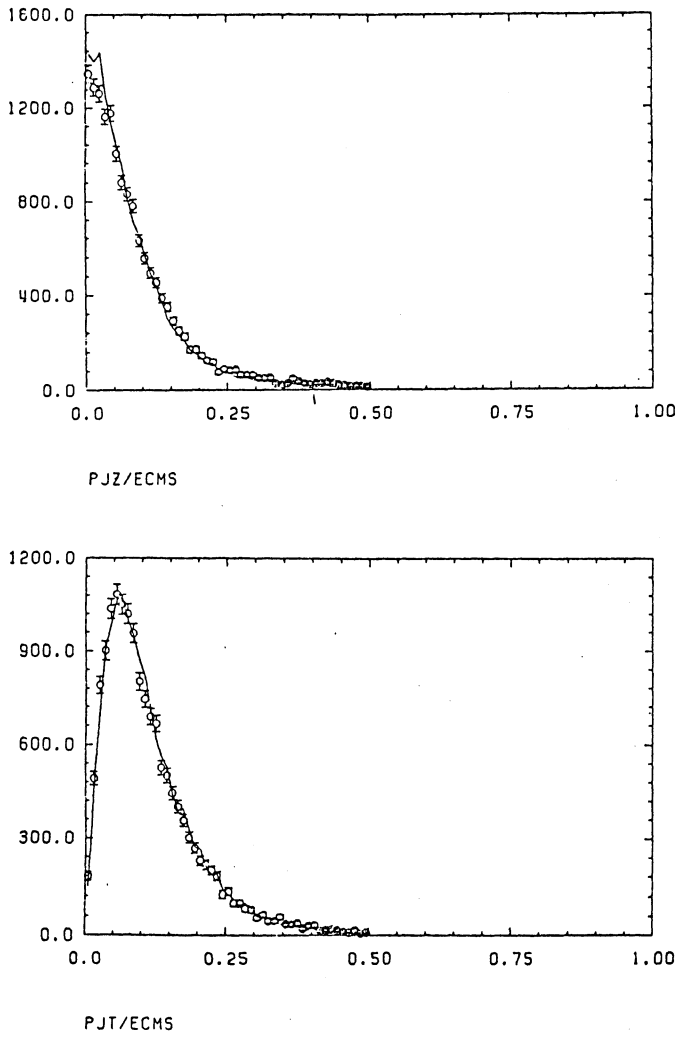

Figure 184. Same as fig.182, but for two jet events. The cuts are explained in the text.

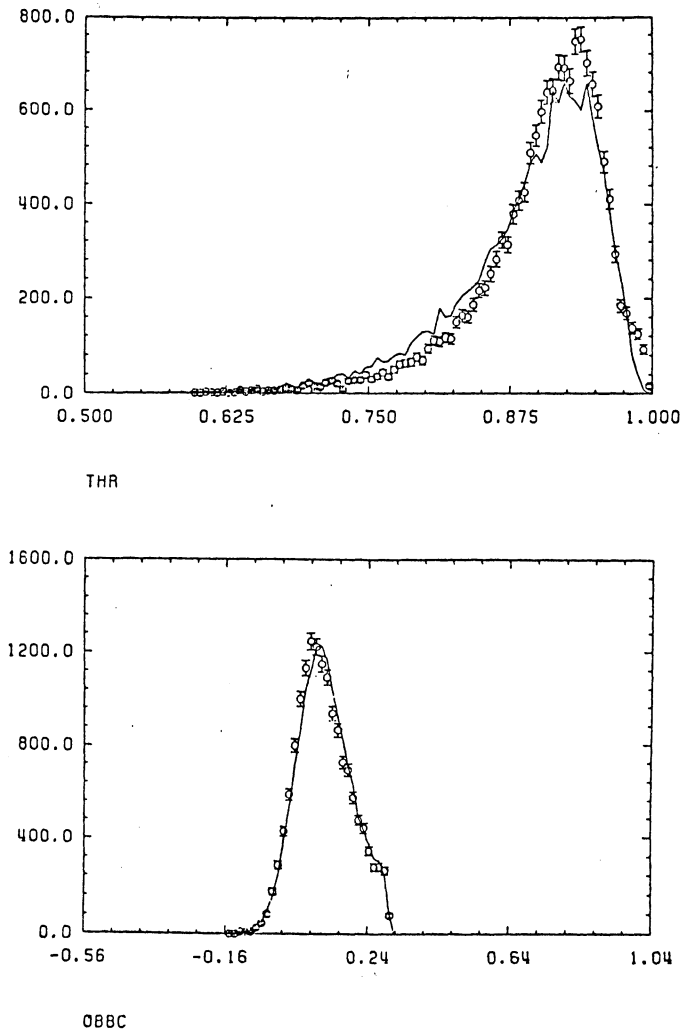

Figure 185. Same as fig.183, but for two jet events. The cuts are explained in the text.

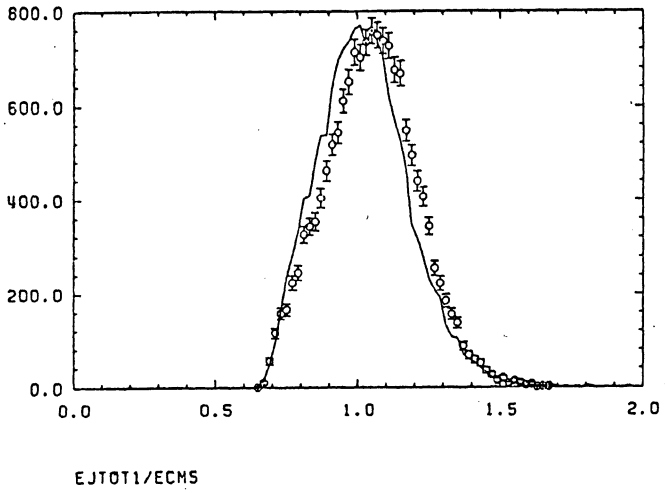

Figure 186. Distribution of the measured CMS energy normalized to the two times the beam energy for two jet events. The cuts are explained in the text. The line shows the MC results.

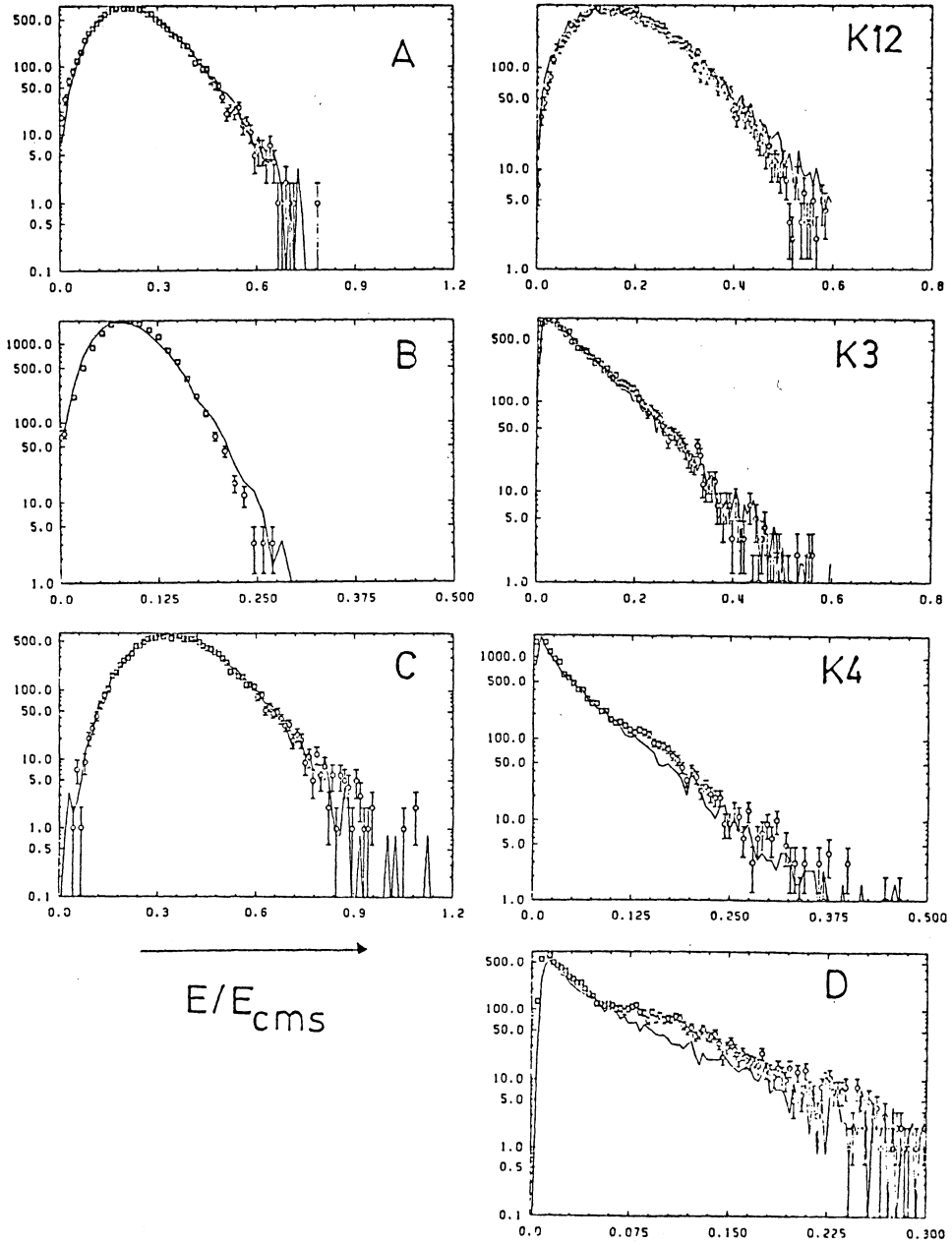

Figure 187. Longitudinal shower devellopment for two jet events. Shown are the distributions for the normalized energy as measured in the various counter layers of the Mark J experiment. The lines show the MC results. For further details see text.

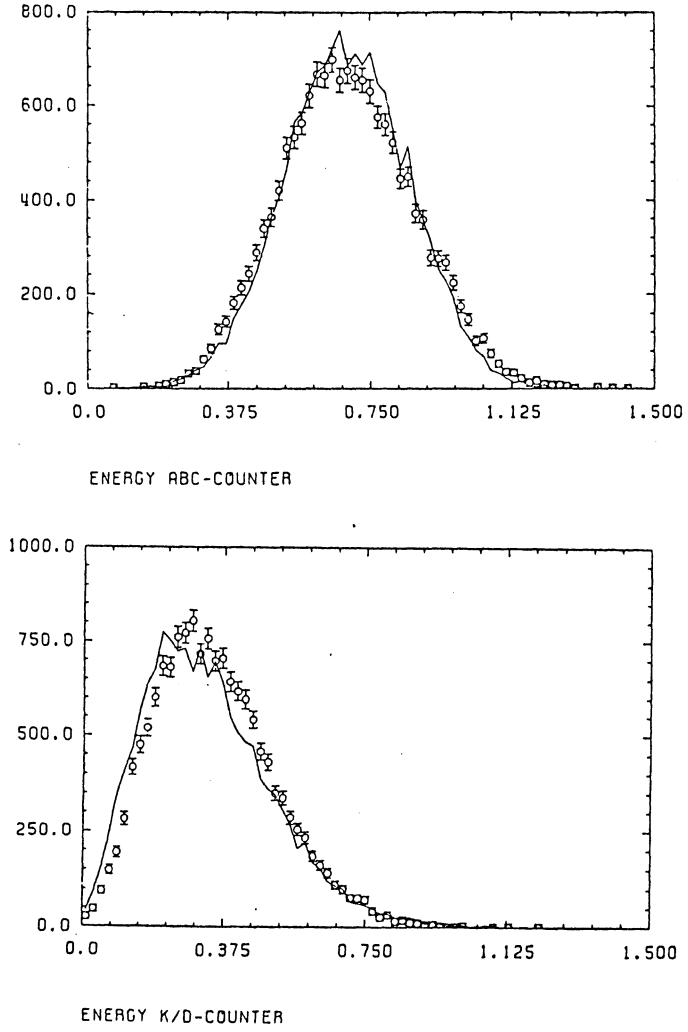

Figure 188. Comparison of the total energy as measured in the shower counter (ABC) and in the hadron calorimeter (K/D) for two jet events.

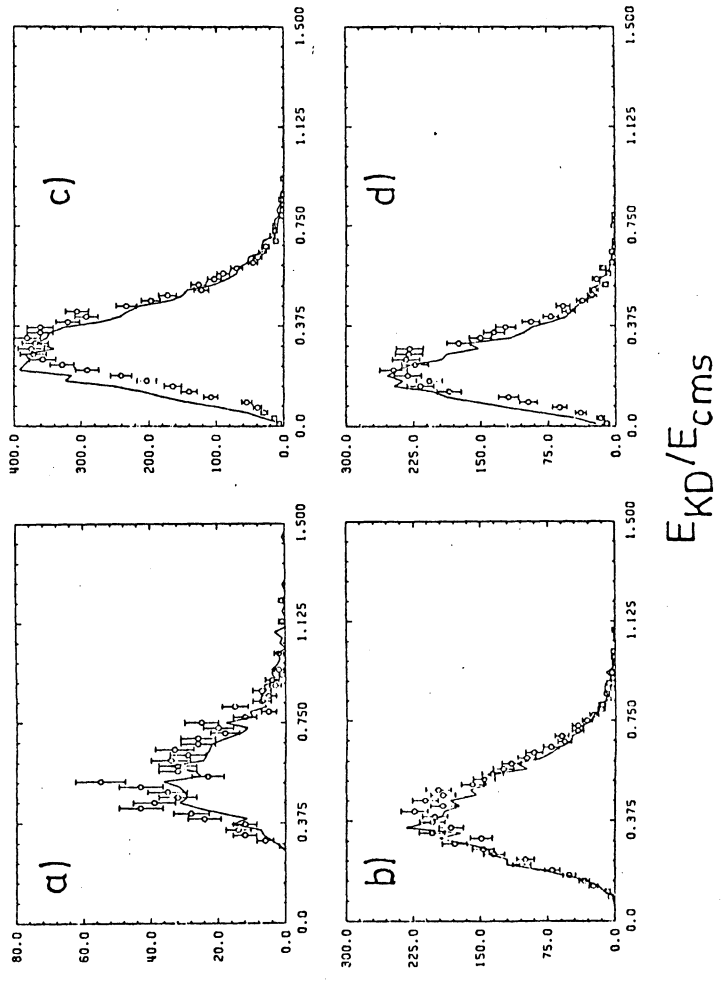

Figure 189. Distributions for the energy in the hadron calorimeter for different measured energies in the shower counter: E_{ABC}/E_{CMS} = 0 - 0.25 (a), 0.25 - 0.5 (b), 0.5 - 0.75 (c) and 0.75 - 1.0 (d).

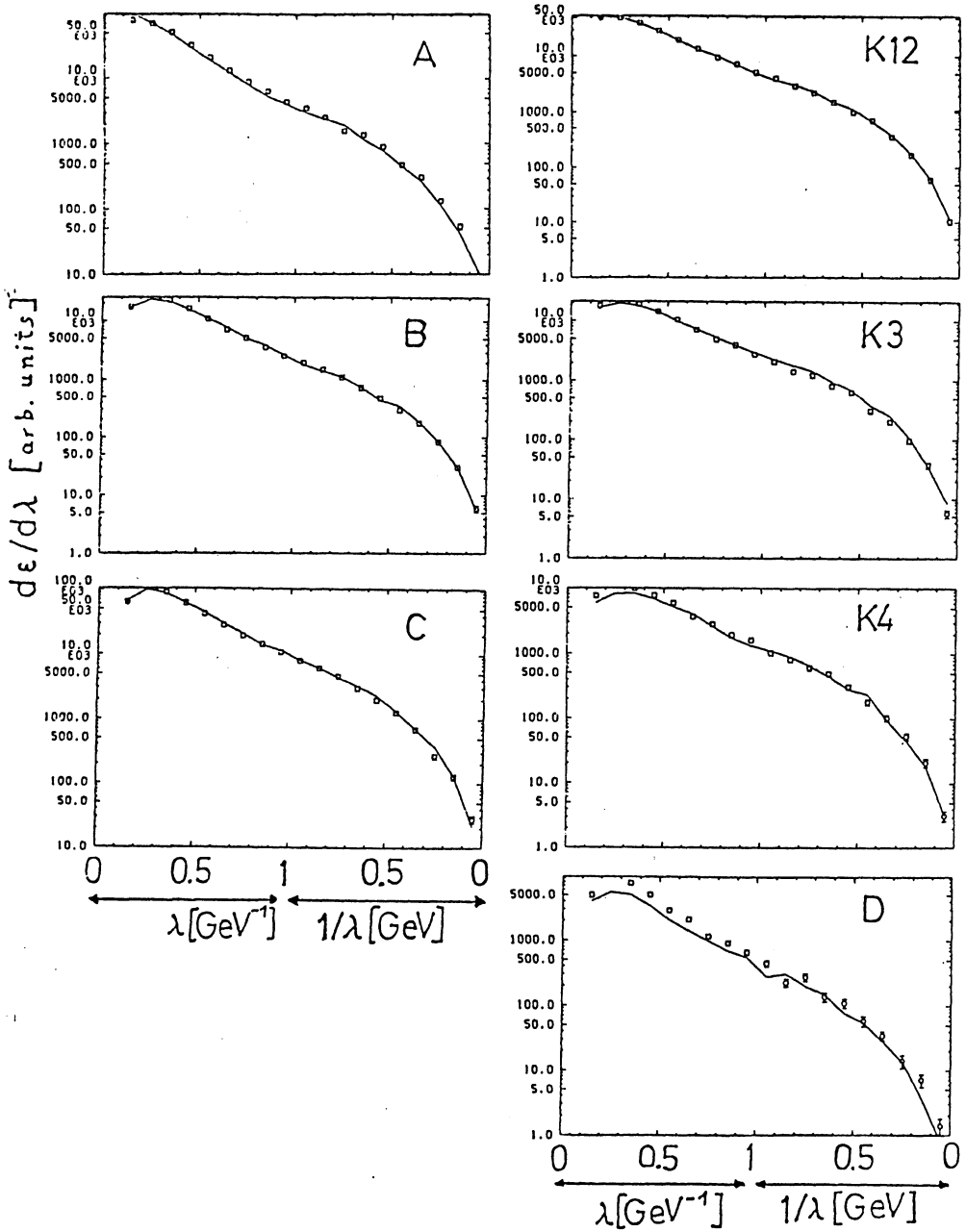

Figure 190. Transverse energy shower profile expressed by the distributions of the variable $\lambda = \cot g\ \Theta/E_{jet}$. The lines represent the MC results. For further details see text.

5.5 POSITION RECONSTRUCTION FROM THE SHOWER SHAPE

In addition to the accurate measurement of energy, which was discussed in the last four sections, calorimeters may yield detailed information on the longitudinal and transverse shower devellopment. This may be used to measure the energy flow. One example of such sophisticated calorimeters, the Mark J detector at PETRA, has already been described in the previous section. In this section we want to extend the analysis of position reconstruction and angle resolution in segmented calorimeters for a more general class of detectors. Comparisons of the longitudinal and transverse shower devellopment between exp. data and Monte Carlo simulation have already been presented in figs. 163, 172, 180, 181 and 187 - 190. A qualitative good agreement could be concluded.

In order to set the discussion on a more quantitative basis, we discuss first the r.m.s. of the lateral shower profile as a function of longitudinal position. In fig.191 we quote the data of Bollini et al. [144]. They have used the CDHS calorimeter of ref. [140] (see section 5.4.3). Two of the scintilator planes have been replaced by finely segmented scintilator hodoscopes, each of them are made of NE110 plastic scintilator strips : the inner 17 of dimensions 49×2×0.5 cm^3 and the outer 2 of dimensions 49×7.5×0.5 cm^3. One of these planes has horizontal strips and the other one vertical strips, both can be inserted at any depth inside the calorimeter. The r.m.s. of the lateral distributions is plotted as a function of the distance from the shower vertex. The definition of the shower vertex may introduce some biases. Thus we have adopted for the MC studies the same vertex selection algorithm as was done for the exp. data. To avoid ionization fluctuations the shower vertex is defined by an energy release larger than a few equivalent particles (ep) in two subsequent calorimeter planes (see table 17 of section 5.4.3). This type of vertex selection allows the derivation of a calorimetric absorbtion length (19.8 ± 0.6 cm) of π^- in iron, in good agreement with the value derived from absorbtion cross sections.

Since this test calorimeter has only two segmented planes it can not measure the angular resolution. An upper limit can be set based on the measurement in one plane. To this end we define the barycenter,

$$\bar{x} = \sum_i ph_i\ x_i \Big/ \sum_i ph_i \qquad (5.37)$$

where ph_i is the pulse height in the i-th strip and x_i the coordinate of the center of the i-th strip. The r.m.s. of the lateral barycenter distribution are shown in fig.192 as function of the longitudinal distance from the shower vertex. $\sigma(\bar{x})$ is in general proportional to the distance from the shower apex in the region between 15 and 55 cm iron. For very small dis-

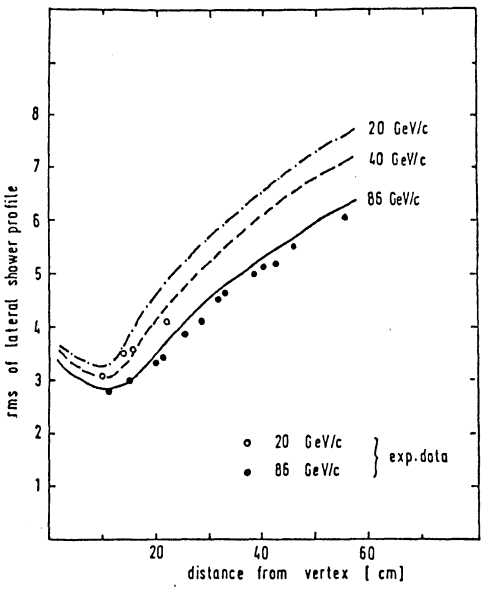

Figure 191. R.m.s. of the lateral shower profile as function of the longitudinal position in an iron scintilator calorimeter. The curves are the results of the MC.

tances $\sigma(\bar{x})$ flattens and becomes ≈ 1.8 cm near the shower apex independent of energy. An interpolation yields, for one lateral sampling and energies above 20 GeV,

$$\sigma_\theta \approx \frac{\sigma(\bar{x})}{z} \approx \frac{490}{\sqrt{E}} \quad [\text{mrad}] \qquad (5.38)$$

For more lateral samplings we expect an improvement by $\sqrt{n}$, where n is the number of planes. This gives roughly (for 5 cm sampling and E > 20 GeV):

$$\sigma_\theta \approx \frac{490}{\sqrt{n\,E}} \quad [\text{mrad}] \qquad (5.39)$$

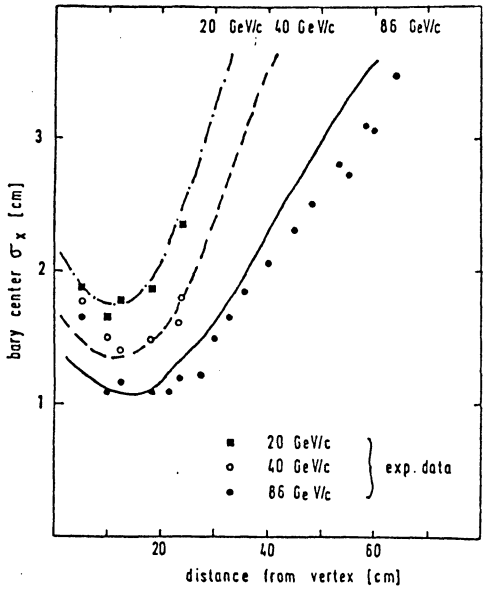

Figure 192. R.m.s. of the lateral barycenter distribution as function of the longitudinal distance from the shower vertex. For details see text.

or $\sigma_\theta \approx 35$, 25 and 16 mrad for 20, 40 and 86 GeV respectively and n=10.

It is clear from the previous discussion that the exact value for the angle resolution depend on the number n of independent planes, on the segmentation of the lateral sampling in each plane and depend in a complicated way on the energy of the incoming particle. The simple law (5.39) can of course not be extended to lower energies. Here we want to study especially in more detail the low energy behaviour of the angle resolution.We have adopted a Cu calorimeter with variable longitudinal samplings (s = 0.5, 1, 2, 4 and 8 cm). All read-out planes are segmented in one lateral direction. The total length of the calorimeter is 7 absorbtion lengthes. In fig.193 we show the angular resolutions obtained for muons, electrons and pions in the energy range from 1 to 12 GeV. The segmentation has been assumed to

be infinite small ($\sigma_E = 0$). This we call the intrinsinc angular resolution. The values for finite segmentation can be simply calculated by statistical arguments. It is clear that muons give an intrinsinc resolution some order of magnitudes smaller than electrons or pions, determined only by multiple scattering (see also chapters 2.3 and 4.1). The barycenter for one plane is in general a factor 2-3 smaller for electrons compared to pions. On the other hand, at the same longitudinal sampling rate, the effective number of planes is much larger for pions than for electrons. As a total result, the intrinsinc resolution for electrons and pions are in the same order of magnitude. The peak in the pion resolution at ≈ 8 GeV is correlated with the inset of low energy quasi two body reactions. From pure phase space distributed final states in nuclear interactions one would not expect such a pronounced peak.

As can be seen from fig.193 there is a relatively smooth dependence on the longitudinal sampling rate. Our empirical formula (5.39) would suggest a dependence of $\sigma_\Theta \sim \sqrt{s}$. In fig.194 we show the intrinsinc angular resolution as function of s for pions at 5 GeV. Comparisons for absorber materials other than Cu are included. For $s \geq 2$ cm we observe a nearly linear dependence on E.

We have not tried to investigate the angular resolution for finite segmentation. For a segmentation smaller than the r.m.s. of the transverse shower profile we do not expect a dramatic change of the results. For much higher values of the lateral segmentation the angular resolution becomes a complicated function of the distribution of the lateral strips relative to the distribution in other planes. Such investigations are outside of the scope of this report.

5.6 ELECTRON/PION SHOWER SEPARATION

Showers caused by electrons and hadrons differ in 1.) longitudinal size, 2.) lateral size, 3.) visible fraction of primary energy and 4.) time development of the shower. The first and third seperation principles are normally realized by replacing the first absorbtion length of a hadron calorimeter with layers of lead sampled at every radiation length (see e.g. the Mark J detector). Alternatively, blocks of lead glass, NaI or BGO are in use. As an example we shall discuss here the electromagnetic BGO calorimeter proposed for the L3 detector at LEP [145]. Test runs with electrons, muons and pions have been started for BGO blocks of various dimensions. The results quoted in this report are preliminary.

The following energy resolution for electrons and photons is expected:

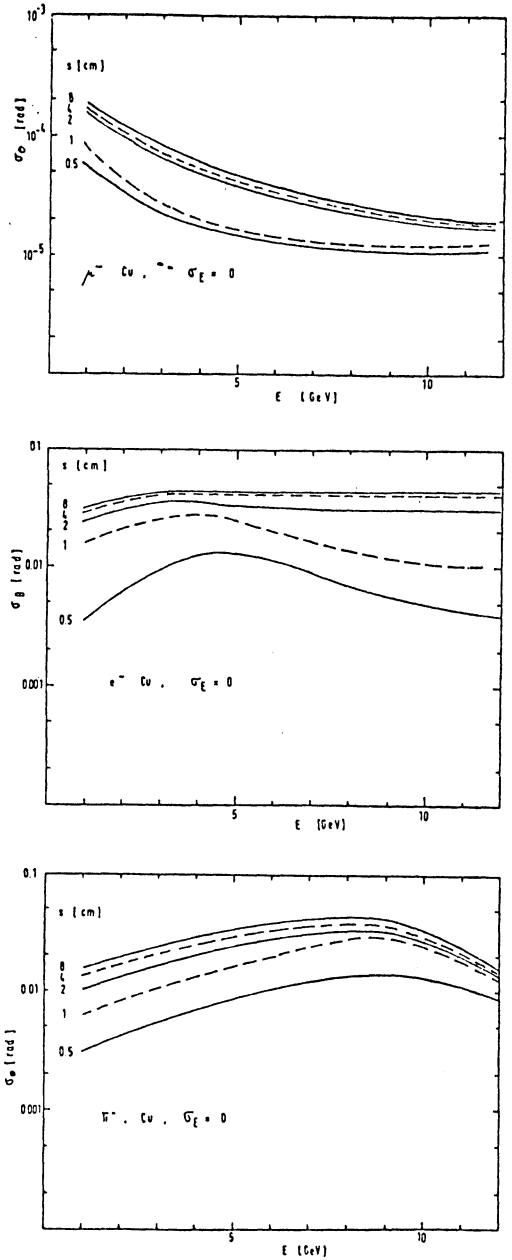

Figure 193. Angular resolution obtained for muons, electrons and pions in the energy range from 1 to 12 GeV. The segmentation in the lateral dimension has been assumed to be infinite small. For details see text.

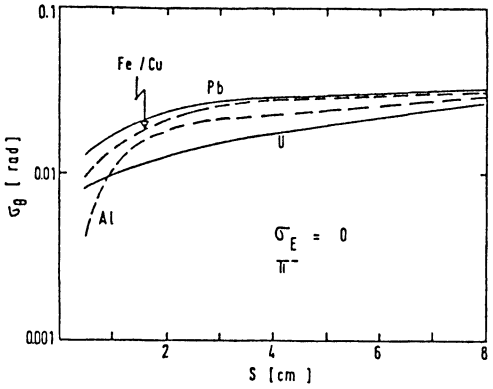

Figure 194. Intrinsinc angular resolution as function of sampling thickness s for pions at 5 GeV. Shown are results for various materials as absorber. The lateral segmentation of the read-out layers has been assumed to be indefinite small.

$$(\sigma/E) = \sqrt{(0.5\%/\sqrt{E} + 0.3\%)^2 + \sigma_{rl}^2 + \sigma_{noise}^2 + \sigma_{nc}^2} \qquad (5.40)$$

where E in GeV and σ_{rl}, σ_{noise} and σ_{nc} in %. The first term describes the dependence on the photon statistics and a constant contribution which represents systematic errors, such as non-uniformity of the crystals. The shower leakage term σ_{rl} can be calculated by Monte Carlo simulation. Fig.195 shows the leakage for a 9×9×23 cm^3 crystall. It amounts to roughly 5% in the energy range from 1 to 10 GeV. The effect of longitudinal leakage on energy resolution is shown in fig.196 for two blocks of BGO, 15×15×20 cm^3 and 15×15×24 cm^3 respectively. Leakage to the sides is studied in fig.197. Plotted is the energy resolution as a function of the lateral dimension of the fiducial volume.

σ_{noise} and σ_{nc} are the contributions due to photodiode and amplifier noise and due to fluctuations in the signal produced by charged particles passing through the photodiodes respectively. The use of photodiodes is a

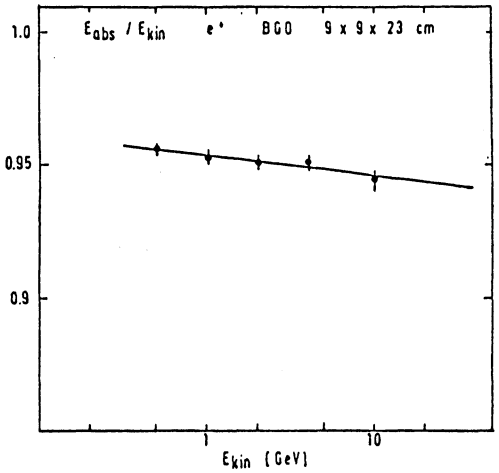

Figure 195. Shower leakage for electron induced showers in a 9×9×23 cm^3 BGO crystall. Shown are Monte Carlo results. The line is only to guide the eyes.

must, since phototubes are not expected to work in the magnetic field of 5 kG.

Pion runs have been made with a crystall size of 9×9×23 cm^3 The corresponding energy resolution for electrons using this dimensions of crystal size is given in fig.198, the average electron pulse height in fig.195. The measured pulse height distributions for positive pions at momenta of 2, 4 and 10 GeV/c [146] are compared in fig.199 with Monte Carlo simulations. In the simulation we have not tried to include any effect due to digitization, neither a light saturation due to quenching (see formula (5.3)), nor any electronic read-out statistic. As can be seen from the comparison, these effects must be small. Some broadening of the response is most clearly seen near the line for nonshowering particles. Together with the results for electrons from figs.195 and 198 we conclude that a rejection of better than 1:500 can be achieved, in agreement with the experimental

data. This value may be improved further by transverse shower shape analysis using a segmentation of the BGO blocks in both radial dimensions. An expected rejection rate of 10^{-3} has been quoted in the technical report of the L3 collaboration.

An interesting phenomena is the energy scaling of the pulse height distribution, as shown in fig.200. Plotted are the Monte Carlo results from fig.199 as function of E_{abs}/E_{kin} From this plots we see that the pion rejection should be a relatively smooth function on the energy of the imcoming particle. For energies below 2 GeV the pion rejection is expected to rise very steeply, approaching a maximum at ≈ 0.5 GeV. The reason is that the average of the pion pulse height distribution approach the average of the electron pulse height distribution for p ≈ 0.5 GeV (see also chapter 5.3). Pulse height distributions for pions at 0.5 and 1 GeV/c are shown in fig.201. For even lower values of the momentum we then expect a slightly better rejection, since the number of showering pions drop down. A comparison of pulse height distributions between exp. data and Monte Carlo for pions at 200 MeV/c is shown in fig.202. To explain the peak at ≈ 280 ADC-channels, we had to assume a muon contamination of

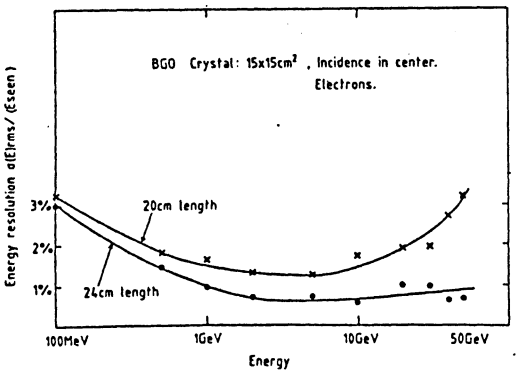

Figure 196. Energy resolution as function of energy for electron induced shower. Shown are the results for two longitudinal dimensions of the BGO crystal. The curves are only to guide the eyes.

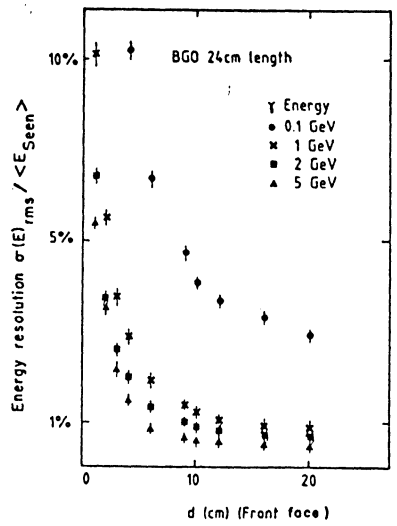

Figure 197. Energy resolution as function of the lateral dimension of the fiducial volume for γ induced shower.

5% with a momentum resolution of 0.5%. The momentum resolution for the pions has been quoted to be smaller than 0.1%. The width of the peak for noninteracting particles has been fitted by selecting a sensitive trigger time of the ADC's of 1 μsec. The signal for electrons of 200 MeV/c momentum would lie at ADC-channel ≈ 500.

Energy measurements of photons, electrons and positrons and also π/e rejection are only two of the main goals for the electromagnetic calorimeter. It acts also as a part of the hadron calorimeter. In fig.203 we show the longitudinal shower development for pions at 4, 10 and 20 GeV/c in a block of 20×9×24 cm^3 of BGO. This block consists of a total of 24 BGO pieces, each of dimensions of 3×3×20 cm^3. From this figure it is seen that the maximum of the longitudinal shower development lies well within the BGO block for pions even at energies above 10 GeV/c. It may be concluded that within an arrangement of an electromagnetic calorimeter in front of a hadron calorimeter the latter one must not be optimized for the energy measurement, but rather than should be well suited for μ - identification. This will be discussed in the next chapter.

Some comments have to be added to the results shown in fig.203. We had serious problems to describe these experimental measurements with the

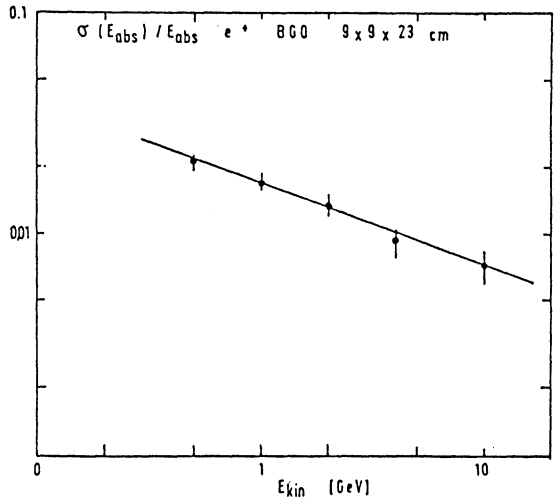

Figure 198. Energy resolution for electron induced shower in a 9×9×23 cm^3 BGO crystal. The line is only to guide the eyes. The points show MC results

GHEISHA6 version, especially at 20 GeV. The problem has been solved in the GHEISHA7 version by a careful adjustment of the energy spectrum of neutral pions produced in high energy scattering on heavy nuclei. The results for the three different contributions, the electromagnetic energy from neutral pions, the energy from charged pions and the energy from heavier particles, are shown in fig.203 for comparison.

Good discrimination of electrons against hadrons was one of the main objectives of the proposed ELECTRA detector at LEP [147]. To achieve this goal, a conventional lead liquid argon shower detector with high angular granularity, good energy resolution and longitudinal segmentation was proposed. In conjunction with a transition radiation detector an overall π/e discrimination of 10^{-4} can be achieved, a factor 10 better than was expected for the other detectors proposed for LEP. We shall quote here

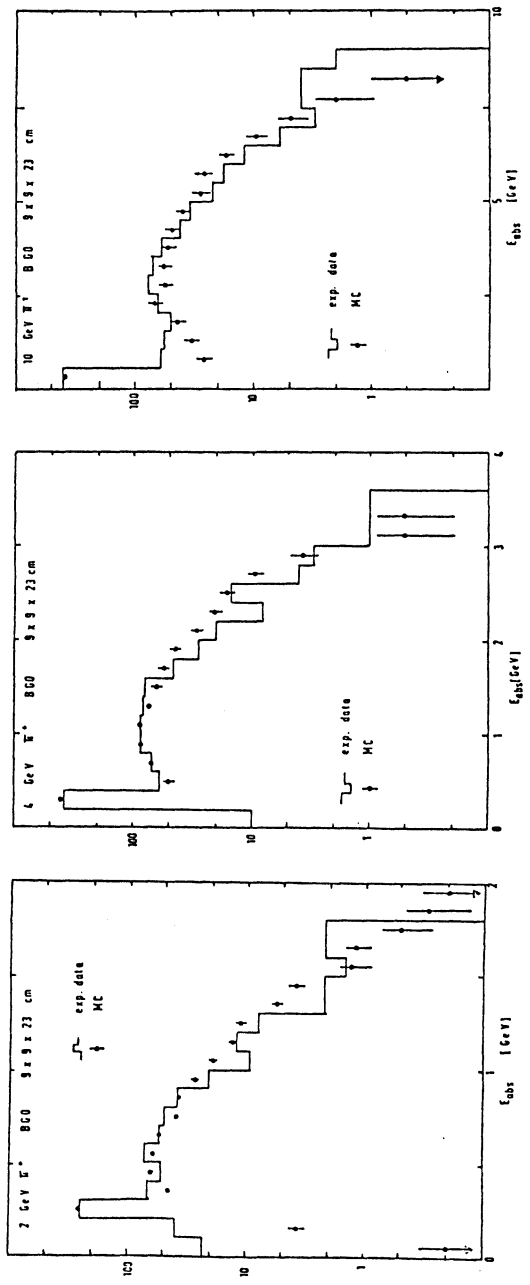

Figure 199. Pulse height distributions for pion induced showers in a 9×9×23 cm^3 BGO crystal. The histograms show experimental results, the points represent MC results.

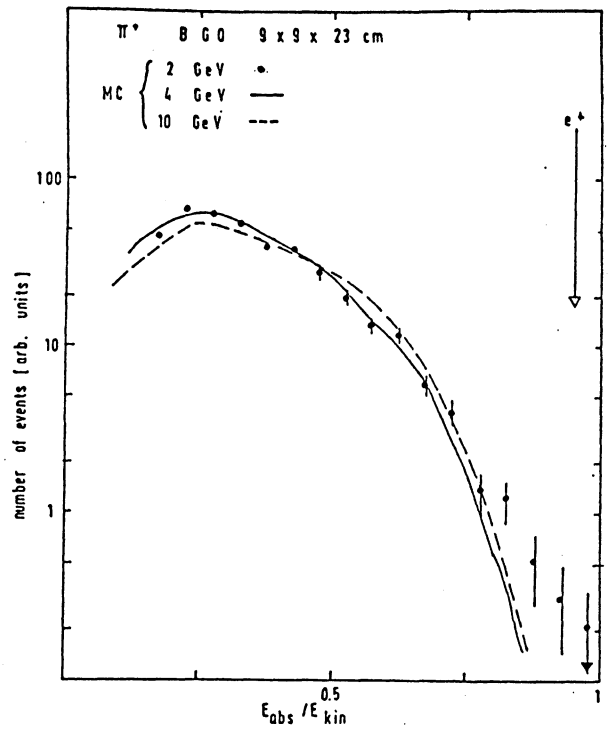

Figure 200. Pulse height distributions for pion induced showers in a 9×9×23 cm³ BGO crystal. Shown are the MC results from fig.199. The absorbed energy has been scaled by the kinetic energy of the incident pion.

some results for π/e rejection obtained with a test set-up of the lead liquid argon shower detector [148].

The test detector consisted of 16 modules, each covering an area of 8×8 cm². Each module, which is called a tower, is further subdivided into two longitudinal segments, a front tower of 5.3 r.l. and a back tower of 13.6 r.l.. The lead plates were 2 mm, the argon gaps 3 mm thick. In front of and behind the front towers there was a set of orthogonal strips, allowing a determination of the shower axis. For more details we refer to the original paper [147]. Measurements with electrons were done at DESY, data for pions and high energy electrons were taken at CERN. The following criteria have been used to tag on electrons:

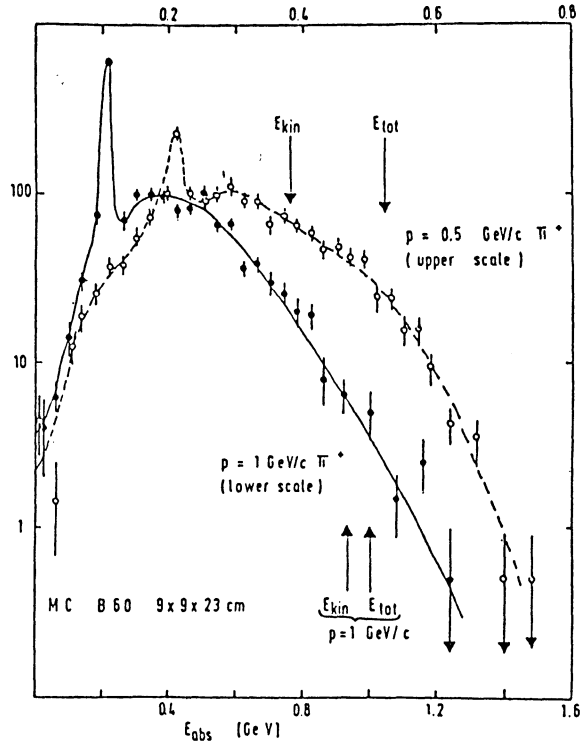

Figure 201. Pulse height distribution for pion induced showers in a 9×9×23 cm³ BGO crystall. Shown are MC results at low energies. The curves are only to guide the eyes.

1) a) The energy deposited in the central tower is no more than ± 3σ different from the mean energy deposited at the chosen beam momentum.
   b) The energy deposited in the front tower is larger than 25% of the total energy deposited.

2) From the center of gravity, determined by the system of strips the shower axis has been reconstructed. This axis is required to agree with the incoming beam within ± 25 mm.

3) An additional improvement can be achieved in the case of additional material in front of the detector by cutting on the pulse height in the first strip system. As electromagnetic showers start earlier than hadronic showers, pions will give small pulse heights in the first strip system.

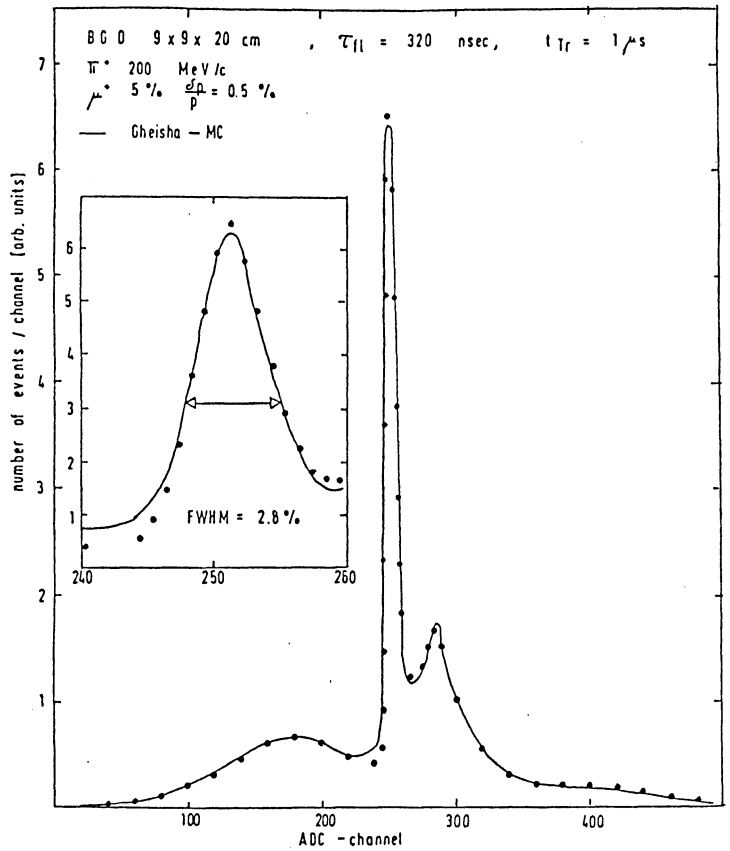

Figure 202. Pulse height distribution for pion induced showers in a 9×9×20 cm^3 BGO crystal. Shown are MC results at 200 MeV/c momentum. The points are experimental results. The lines represent the prediction of the Monte Carlo. For further details see text.

Table 18 summarizes the results obtained for the exp. data and the MC simulation applying the different cuts 1-3.

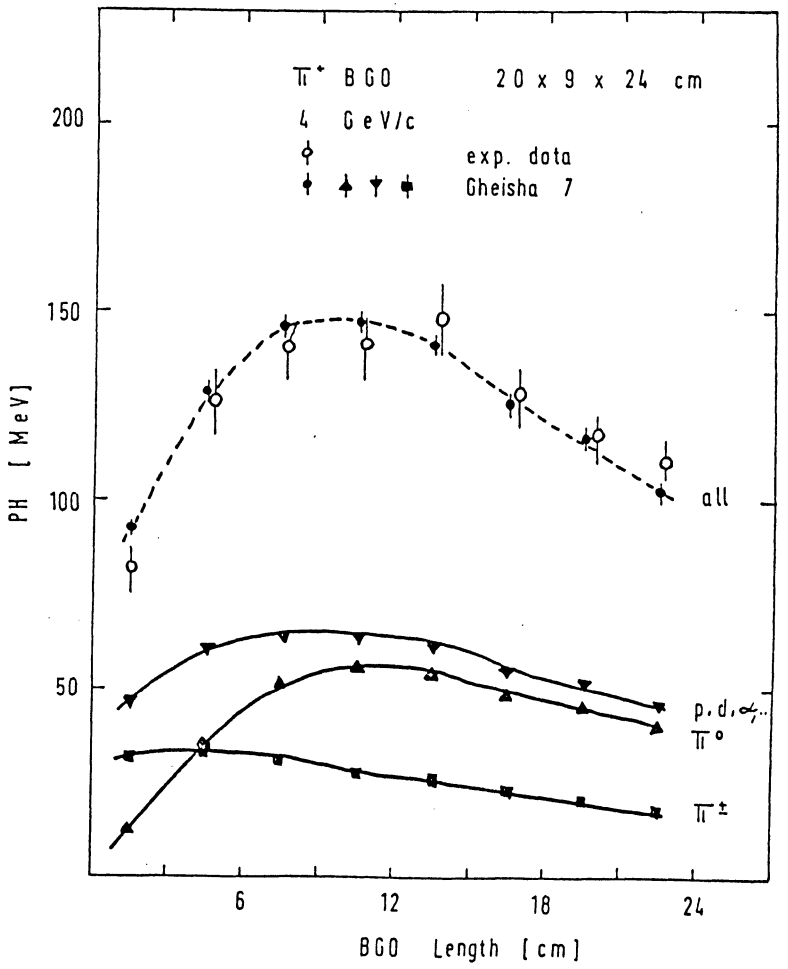

Figure 203. Average energy deposit as function of the longitudinal crystal position in 9×20 cm^2 BGO crystals for pion induced showers. For details see text.

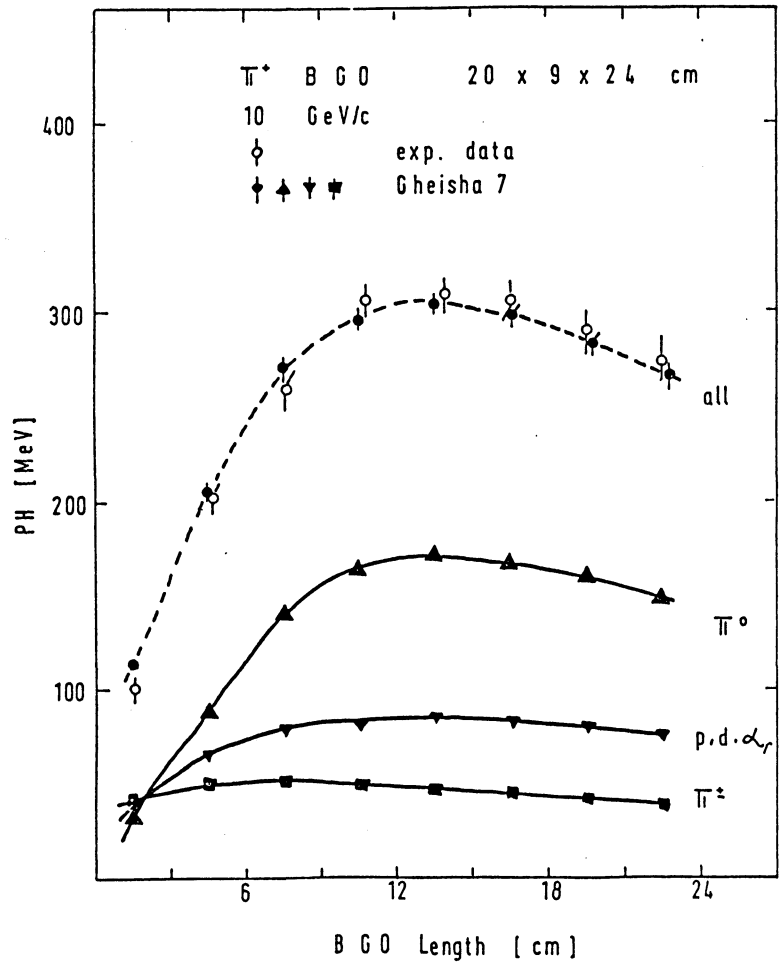

Figure 203. Average energy deposit as function of the longitudinal crystal position in 9×20 cm² BGO crystals for pion induced showers. For details see text.

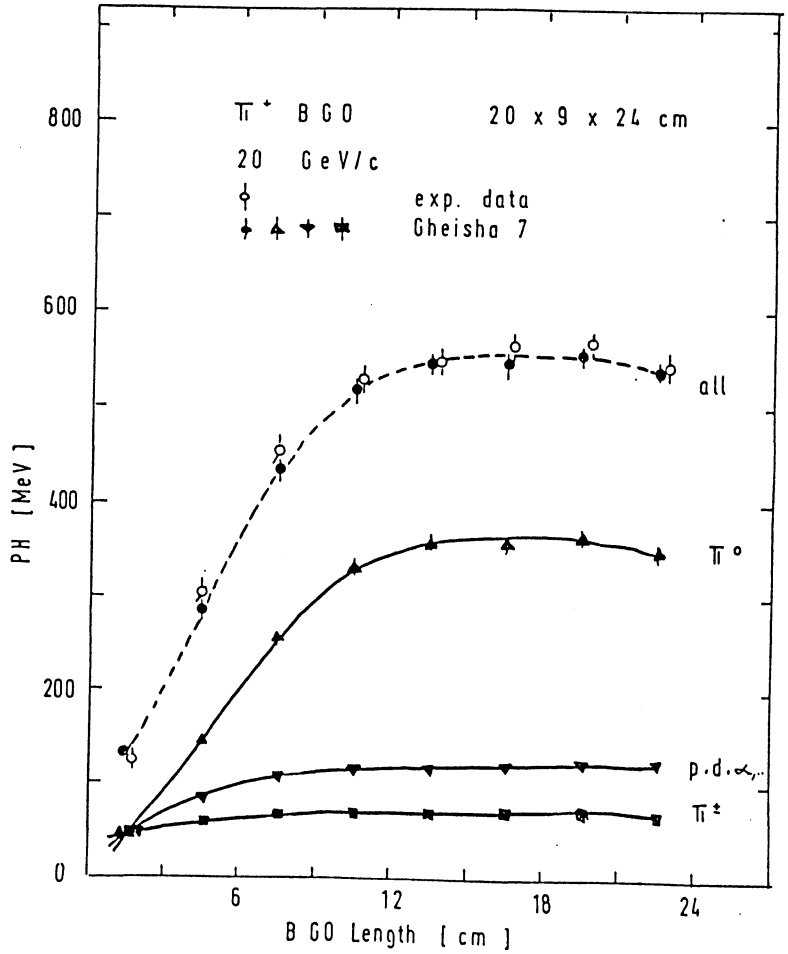

Figure 203. Average energy deposit as function of the longitudinal crystal position in 9×20 cm² BGO crystals for pion induced showers. For details see text.

Table 18: Summary of π/e discrimination in the ELECTRA liquid argon detector

E(GeV)	additional material in front	Cuts	electron efficiency		pion misidentification probability	
			data	MC	data	MC
2.0		1	0.975	0.968	0.020 ±0.006	0.015 ±0.005
2.0		1	0.975	0.968	0.016 ±0.006	
2.0	10 cm Al	1	0.968	0.988	0.026 ±0.006	0.026 ±0.004
2.0	10 cm Al	1+2	0.976	0.978	0.015 ±0.006	0.015 ±0.003
2.0	10 cm Al	1+3	0.966	0.950	0.012 ±0.006	
2.0	10 cm Al	1+2+3	0.957	0.950	0.007 ±0.003	0.008 ±0.003
5.0		1	0.975	0.968	0.020 ±0.003	
5.0	10 cm Al	1	0.986	0.988	0.011 ±0.007	0.007 ±0.002
5.0	10 cm Al	1+3	0.966	0.950	0.008 ±0.006	0.002 ±0.002
10.0		1	0.976	0.968	0.003 ±0.002	
10.0	10 cm Al	1	0.986	0.988	0.005 ±0.002	0.005 ±0.002
10.0	10 cm Al	1+3	0.966	0.950	0.004 ±0.002	0.001 ±0.001

As can be seen the π/e seperation is better than $7 \cdot 10^{-3}$ for 2 GeV/c. The electron efficiency is still large. This pion rejection has been reached using simple cuts taking advantage of the tower structure as well as of the strip system.

So far we have discussed two typical examples of π/e discrimination, which were based on the longitudinal and lateral shower size and on the visible fraction of primary energy. Additionally one can also use the different time development of electromagnetic and hadronic showers in order to distinguish between electrons and hadrons. This method has been mentioned already in chapter 5.2 in conjunction with muon/hadron seperation.

For our calculations we used a calorimeter of the Mark J type, namely a lead scintilator sandwich of 0.5 cm thickness for both the lead plates and scintilator plates. The longitudinal dimension corresponds to 22 r.l.. A segmentation in the lateral directions has however not been assumed. Cutting the pulse height distribution for pions on $\pm 2\sigma$ away from the corresponding signals for electrons, we arrive at the rejection rates shown in fig.203 as black points. If we now measure additionally the time dependence of the anode current of the photomultiplier, we would arrive at plots similar to those shown in figs.130 and 137. An analysis of the average time of the current pulse give plots as shown in fig.204. We observe a very narrow distribution for electrons. The distribution for pions, on the other

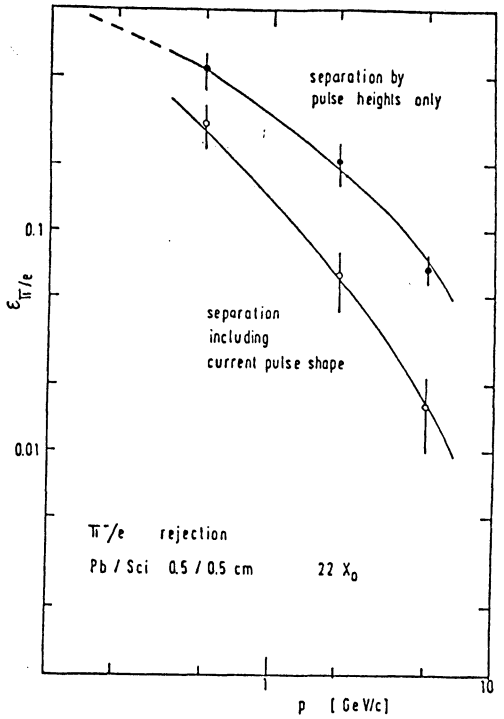

Figure 204. Electron/pion separation rate as function of momentum by means of pulse height separation only and by additional current pulse shape analysis. For details see text.

hand, consists of two contributions, one very similar to that for electrons, caused mainly by nonshowering pions, a second a delayed component, caused by showering pions. If we apply a pulse height selection the nonshowering pions are cutted out and the remaining showering pions can be clearly seperated from the electrons. The results obtained with this method are shown in fig.204 as open circles. An improvement by a factor 3-4 can be achieved.

Studies of electron/pion seperation were one of the most fruitful correlations between the simulation of nuclear interactions and experimental calorimeter data. The transverse shower development in the first absorbtion length of absorber material is directly correlated with the angular distribution of particles emitted in the first interaction. The total amount of absorbed energy is closely connected to the number of

produced particles, especially neutral pions and low energy grey-track and black-track particles. In general, electron/pion seperation problems are sensitive to the first interaction within a hadron shower and are thus an alternative way to study nuclear interactions. Multiplication effects play a minor role.

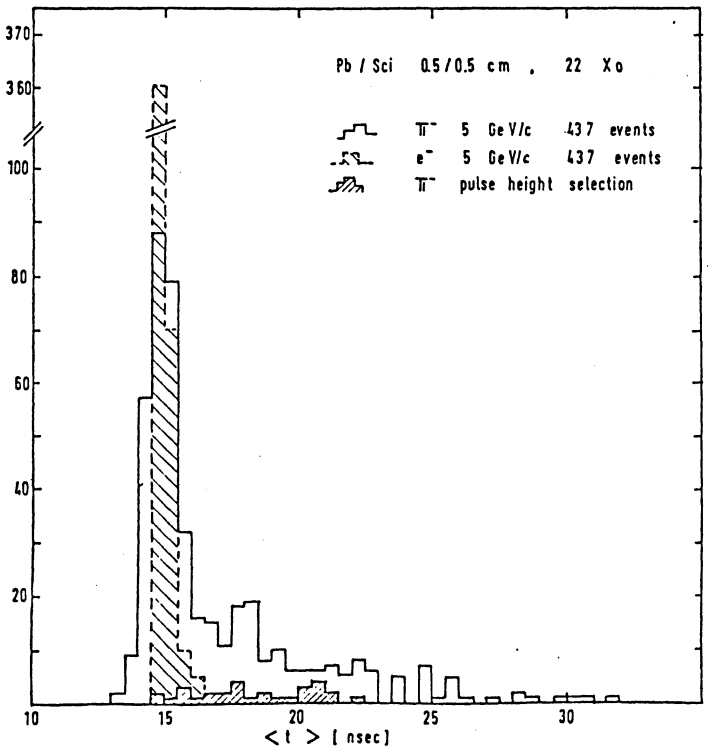

Figure 205. Distribution of the mean time of the current pulse for electron and pion induced shower in lead scintilator sandwich calorimeter. For details see text.

5.7 μ-IDENTIFICATION

5.7.1 General remarks

The muon loses its energy in the passage through matter by ionization. Only at energies much bigger than 10 GeV other processes such as electron pair production, bremsstrahlung and nuclear interactions become significant. The expected trajectory of a muon is well defined and its fluctuation is determined by multiple scattering and energy loss. The use of and limitations due to multiple scattering for the momentum measurement of muons have been discussed in detail in chapter 4.

The muon signature is thus a deep penetration through matter. To make use of this fact, the leakage of charged particles from a hadronic shower (punch through) should be suppressed and the muons coming from decays of primary mesons must be identified. The normal muon spectrometer in storage ring experiments consists of a central drift chamber, a calorimeter as absorber for hadrons and planes of drift chambers surrounding the hadron calorimeter. These outer drift chambers are used to measure the position and/or the angle of the muon leaving the absorber. The following signature can be used to identify decay- and punch through-background:

1.) A kink, larger than expected from multiple scattering, appears somewhere on the trajectory of the particle.

2.) A visible interaction in the calorimeter, detected either by an increase of the pulse height in case of scintilators or by identifying more than one track in a tracking calorimeter.

We shall discuss first the comparison of Monte Carlo simulations with some existing experimental data. In chapter 5.7.3 and 5.7.4 we continue with a short report on the identification of inclusive muons in hadronic events measured in the TASSO and MARK J detectors at PETRA. At the end we will present a general discussion about the optimization of a standard storage ring experiment in view of μ - identification.

5.7.2 The classic muon spectrometer

In a classic muon range detector, such as used in the SLAC 20 GeV spectrometer [149], muons are distinguished from hadrons purely on the basis of penetrating radiation. An absorber having a thickness of $\approx$ 15 absorbtion lengthes ($\approx$ 200 cm of iron) is sufficient to contain the pene-

trating secondaries in a hadron cascade. The data of the SLAC spectrometer are compared in fig.206 with MC calculations. For these simulations we have not used the geometry of the SLAC spectrometer, but the geometry of a high energy storage ring experimemt (ELECTRA, see chapter 5.7.5). This may cause the small deviations around 60 - 80 cm Fe.

To intercept a useful fraction of muons in a storage ring experiment, the identifier must cover a large area ($\approx 4\pi$ in stereo angle in a distance of $\approx$ 500 cm away from the interaction vertex, which results in an area of $\approx$ 300 m^2), and it must be able to distinguish muons in a sea of hadrons in which the energies vary by two orders of magnitudes and in which the hadrons originate in the same interaction as the muon beeing examined. The momentum spectrum of prompt muons in e^+e^- interactions peaks at a few GeV/c. The range for the penetration of a muon through an absorber is shown in fig.207 as function of the momentum. In order to have a sufficient acceptance for prompt muons we are thus restricted to an absorber thickness around 100 cm of iron.

The first detector, overcoming these limitations, has been discussed by Harris et al. [150]. The experimental apparatus is shown schematically in fig.206. It consists of two iron absorbers, A1 and A2, of variable thickness, a variable drift space d and x-y proportional chamber pairs, PC1 and PC2. A Cerenkov counter is located 20 m upstream and allows to distinguish π's and μ's from protons by velocity selection. Muons and pions are seperated by the conventional method. To this end counters S4 and S5 are located behind additional iron abosrbers A3 to A6. Counters S1 (not shown) and S2 serve for the definition of the beam.

Various configurations of absorber thickness (A1 and A2) and drift spaces have been used to measure μ/π rejection rates. The percent of pions detected inside a circle large enough to contain 96% of incident muons is compared in table 19 with Monte Carlo calculations. The momentum of the pions is 3 GeV/c. In fig.209 we have plotted these numbers as function of the effective absorber thickness. We get a good agreement between data and Monte Carlo.

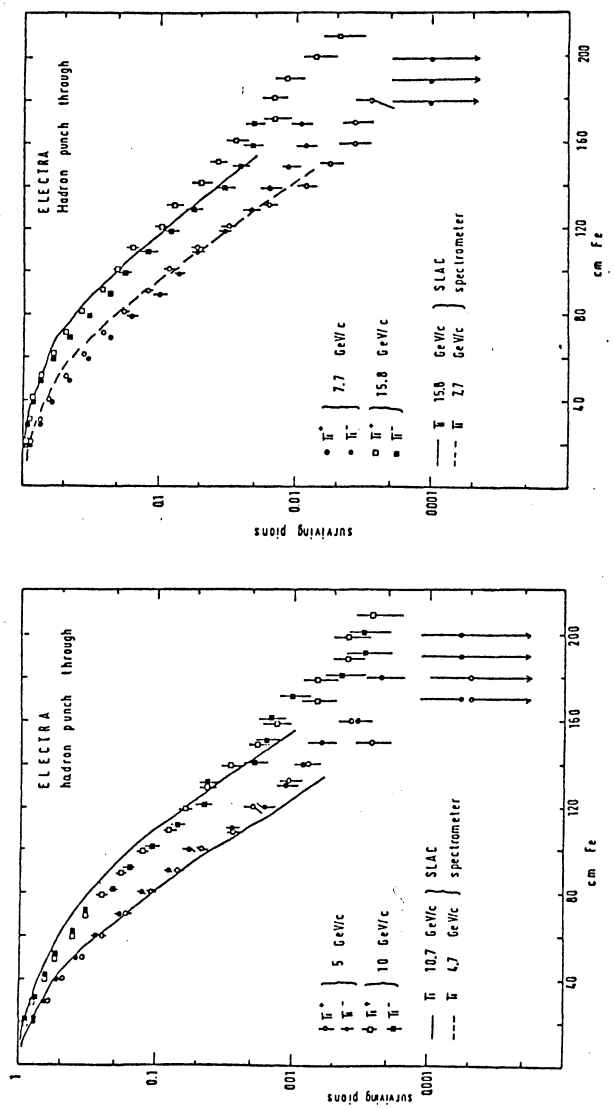

Figure 206. Percentage of surviving pions as function of the absorber thickness.

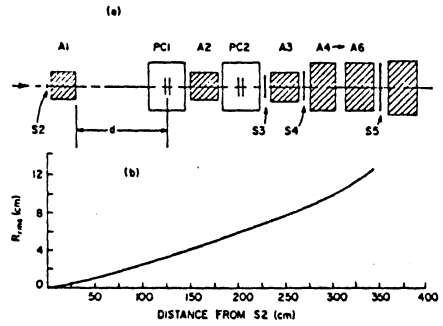

Figure 208. Layout of the classic muon spectrometer. For details see text.

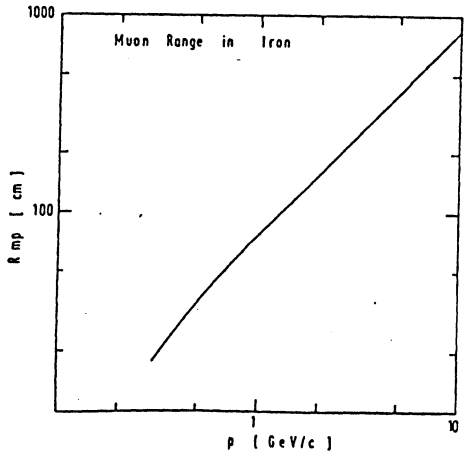

Figure 207. Muon range in iron.

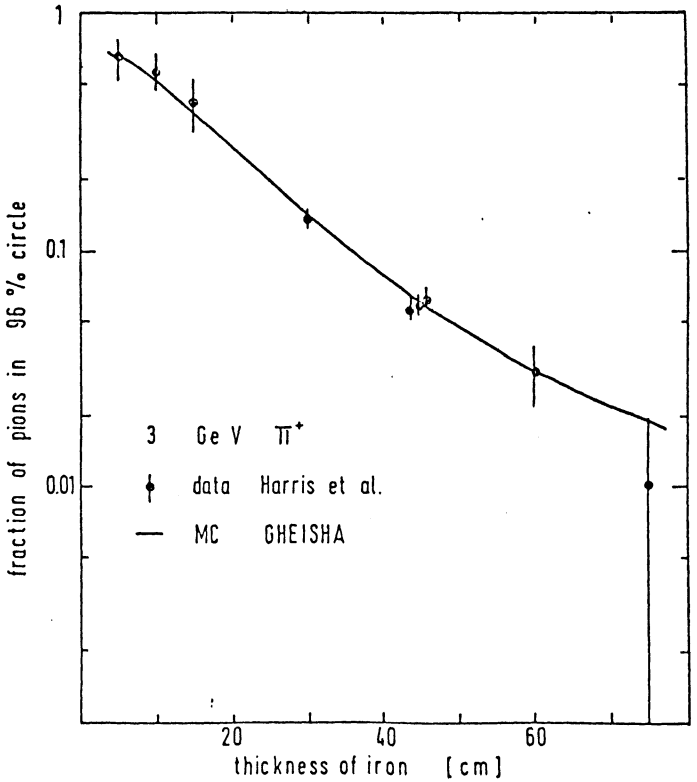

Figure 209. Percentage of pions detected inside a circle for 95% muon acceptance as function of the absorber thickness.

Table 19 Fraction of pions remaining in 96% muon circle for various run conditions. The momentum of the pions is 3 GeV/c. Unit for A1, A2 and d is [cm].

run	A1	A2	d	Chamber used as detector	total absorber thickness	percent π's remaining data	MC
1	5	0	19	PC1	5	67 ±12	65.8 ±0.5
2	10	0	19	PC1	10	57 ± 9	48.0 ±1.0
3	15	0	19	PC1	15	42 ±11	37.0 ±1.5
4	30	30	94	PC1	30	13.8 ± 0.9	15.1 ±0.5
5	45	30	19	PC1	45	6.1 ± 0.7	6.5 ±0.3
6	45	30	69	PC1	45	5.7 ± 0.6	6.3 ±0.3
7	45	30	79	PC1	45	5.9 ± 0.8	5.9 ±0.3
8	30	30	19	PC2	60	3.1 ± 0.8	3.2 ±0.2
9	45	30	19	PC2	75	1.0 ± 1.0	1.8 ±0.1

As can be seen an absorber thickness of ≈ 80 - 100 cm is sufficient to get a pion rejection of 1% by comparing the expected with the measured location after passage of the absorber. In principle the method of the drift space d combines both, the measurement of expected position and the measurement of expected angle. This may be demonstrated as follows. The mean squared radius of the radial distribution due to multiple scattering, after passage through an absorber of thickness t_0 and a drift space of distance d, is given by

$$\langle R_0^2 \rangle = \langle \Theta_0^2 \rangle \left(\tfrac{1}{3} t_0^2 + t_0 d + d^2\right) . \qquad (5.41)$$

$\langle \Theta_0^2 \rangle$ is the mean squared scattering angle. For an absorber thickness of t_0 = 25.6 r.l. (= 45 cm Fe) and a drift space d = 19, 69 and 79 cm (run 5, 6 and 7 respectively in table 19), we get $2\sqrt{\langle R_0^2 \rangle} \approx$ 2.28, 5.74 and 6.44 cm. The angular distribution for the pion punch through is not distributed in the same way. In fig.210 we show the radial distributions of muons and pions for drift spaces d = 19, 69 and 79 cm. The mean values of the pion distributions are 12.1, 27.0 and 29.0 cm respectively. We see that the increase in the lateral displacement for increasing drift space d is about the same for the pion punch through as for the muons. Thus the rejection rates are approximately the same (see table 19 and fig.209). Only a very little improvement is obserbed when going to longer drift spaces.

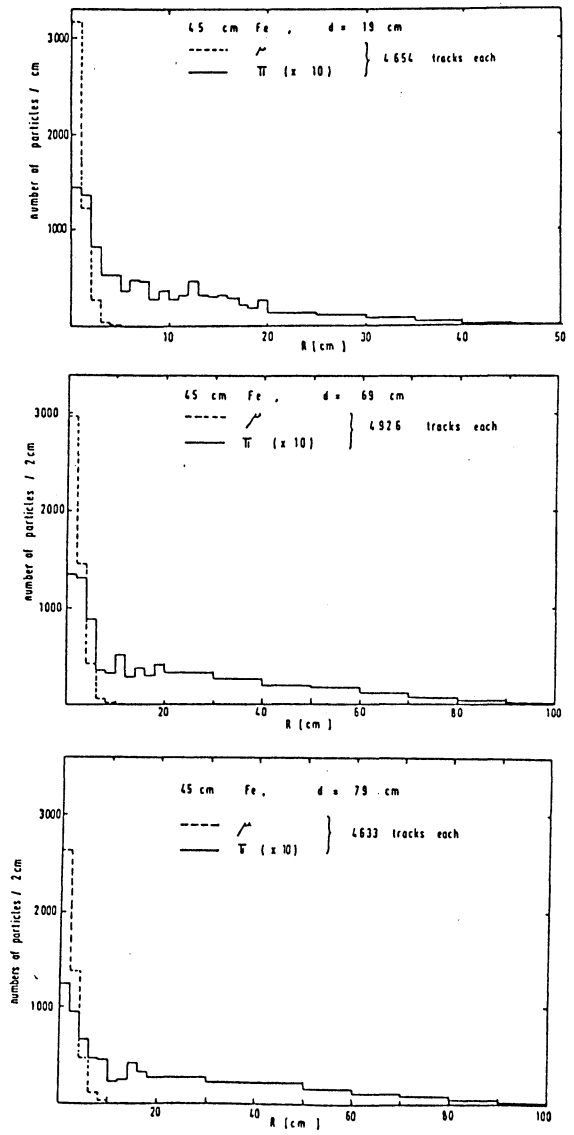

Figure 210. Radial distributions of muons and pions for drift spaces d = 19, 69 and 79 cm in the classic muon spectrometer of fig.208.

5.7.3 The TASSO spectrometer

An example of such a classic muon spectrometer has been realized in the TASSO detector at PETRA (see ref. [151] for more informations concerning the detector). The TASSO detector consists of a cylindrical central detector of radius 1.35 m within a magnetic field of 5 kG (see fig.211). The return yoke for the magnetic field is an iron box with open sides, with a thickness of 80 cm above and below the solenoid and 50 cm of iron capping the ends of the solenoid. Lead liquid argon shower calorimeter are installed between the solenoid and the iron yoke. Muon detection chambers are installed 30 cm above and below the iron yoke in the horizontal plane, and in the vertical plane both above and below the beam pipe 70 cm from the end cap iron. The open sides of the yoke box give access to two transverse arms for hadron identification. At the far ends, 5.5 m from the interaction point, are lead scintilator shower counters followed by iron 87 cm thick. 20 cm behind this iron are muon detection chambers. In the analysis of prompt muon production, information from only the central detector and the muon detection chambers has been used once an event has been accepted as hadron event [152].

The precision of the central detector is important in this experiment. The cylindrical drift chamber has a momentum resolution of $\sigma_p/p = 0.016 \sqrt{1+p^2}$, where p is the momentum transverse to the magnetic field in units of GeV/c.

The muon chambers consisted of four layers of tubes with two layers offset by 2 cm in each of the orthogonal directions. The structure is illustrated as insert in fig.211. The yoke chambers covered a solid angle of $0.17\times4\pi$, the arm chambers $0.13\times4\pi$ and the end cap chambers $0.13\times4\pi$ steradians. This result in a total geometrical acceptance of 43%. The muon spectrometer of the TASSO detector is very similar to the classic muon detector discussed in the privious chapter. Thus we expect a rejection rate of $\approx$ 2% for single tracks of 3 GeV/c momentum.

For a detailed description of the selection of muon candidates we refer to [152]. The prompt muon signal due to semileptonic decays of particles carrying c and b quarks is diluted by muons from π and K mesons decaying within the central detector (internal decay), by muons from decays outside the central detector (external decay) and by charged hadrons penetrating with or without interaction to the muon chambers (punch through). The yoke, arm and end cap detectors have different susceptibility to these different sources of background and their relative contribution is also highly momentum dependent. Nevertheless we quote here only the results combined for all three detector components. More detailed numbers can be found in the original publication.

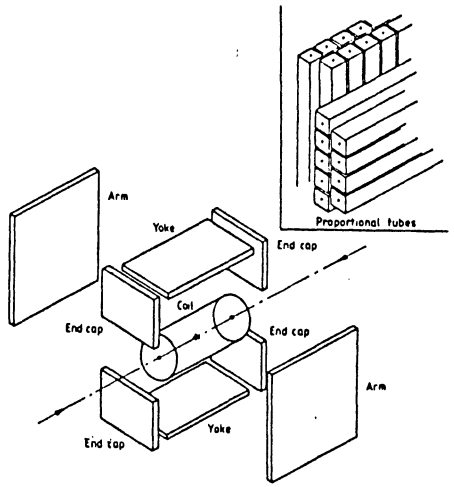

Figure 211. Disposition of the muon chambers in the TASSO detector. For details see text.

The GHEISHA Monte Carlo program was used to calculate for both pions and kaons the probability of penetration of the coil, counters and iron absorber by decay muons or secondary hadrons for each of the yoke, arm and end cap detecors. Both the probability and the radial distribution of tracks in the plane of the muon chambers were parametrized as a function of hadron type and momentum for yoke, arms and end caps. A detailed description can be found in ref. [153]. These parametrizations are used then in the general TASSO Monte Carlo program to assign coordinates in the plane of the muon chambers [154].

The Monte Carlo results for both good muon candidates and bad muon candidates are compared in table 20 and 21 respectively with experimental data. In this tables we have combined the contributions from internal and external decays and also the different prompt muon contributions.

Table 20 number of good muon candidates in each of the nine regions of the p_L-p_T [GeV/c] grid fitted.
Also shown are the predictions for punch through (PTHRU), internal and external decay (DECAY) and prompt muons (PROMPT).

	PTHRU	DECAY	PROMPT	Total	Data
$p_L<2$, $p_T<0.6$	40.3	99.3	39.4	179.0	157
$p_L<2$, $0.6<p_T<1.2$	16.3	58.0	32.2	106.5	89
$p_L<2$, $1.2<p_T$	9.9	28.9	21.3	60.0	43

	PTHRU	DECAY	PROMPT	Total	Data
$2<p_L<4$, $p_T<0.6$	59.3	104.5	87.7	251.7	271
$2<p_L<4$, $0.6<p_T<1.2$	32.6	62.8	59.6	154.9	164
$2<p_L<4$, $1.2<p_T$	13.1	19.7	31.1	64.1	73

	PTHRU	DECAY	PROMPT	Total	Data
$p_L>4$, $p_T<0.6$	38.3	29.7	61.8	129.8	132
$p_L>4$, $0.6<p_T<1.2$	38.3	27.1	59.6	125.0	127
$p_L>4$, $1.2<p_T$	21.6	15.4	41.2	78.2	79
Total	269.6	445.3	434.1	1149.0	1135

Table 20 number of bad muon candidates in each of the nine regions of the p_L-p_T [GeV/c] grid fitted.
Also shown are the predictions for punch through (PTHRU), internal and external decay (DECAY) and prompt muons (PROMPT).

	PTHRU	DECAY	PROMPT	Total	Data
$p_L<2$, $p_T<0.6$	112.9	20.2	2.3	135.3	172
$p_L<2$, $0.6<p_T<1.2$	34.1	14.8	1.7	50.6	57
$p_L<2$, $1.2<p_T$	17.9	10.2	1.1	29.2	33

	PTHRU	DECAY	PROMPT	Total	Data
$2<p_L<4$, $p_T<0.6$	148.6	50.4	4.1	203.0	220
$2<p_L<4$, $0.6<p_T<1.2$	75.0	35.7	2.8	113.5	102
$2<p_L<4$, $1.2<p_T$	29.3	15.0	1.3	45.5	34

	PTHRU	DECAY	PROMPT	Total	Data
$p_L>4$, $p_T<0.6$	91.6	22.3	1.4	115.2	100
$p_L>4$, $0.6<p_T<1.2$	88.2	24.2	1.2	113.6	105
$p_L>4$, $1.2<p_T$	51.5	20.3	1.2	72.9	66
Total	648.9	213.0	17.0	878.9	889

The p_T distribution of the good muon candidates is shown in fig.212, the corresponding p_L distribution in fig.213. p_L and p_T are the longitudinal and transverse momentum components with respect to the jet axis (thrust axis). In general a good agreement between Monte Carlo and experimental data is observed. As can be seen from table 20, the background (decays and punch through combined) amounts to ≈ 60% of the good muon candidates. Since the TASSO spectrometer is very similar to the classic spectrometer of Harris et al., this number corressponds to a rejection rate of ≈ 2% for a single pion at 3 GeV/c momentum.

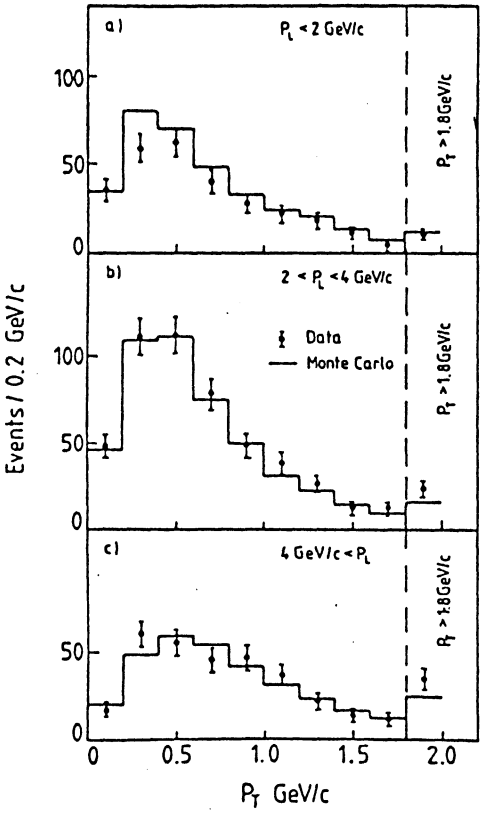

Figure 212. p_T distributions of good muon candidates in TASSO. The points are the data. The histograms show MC results.

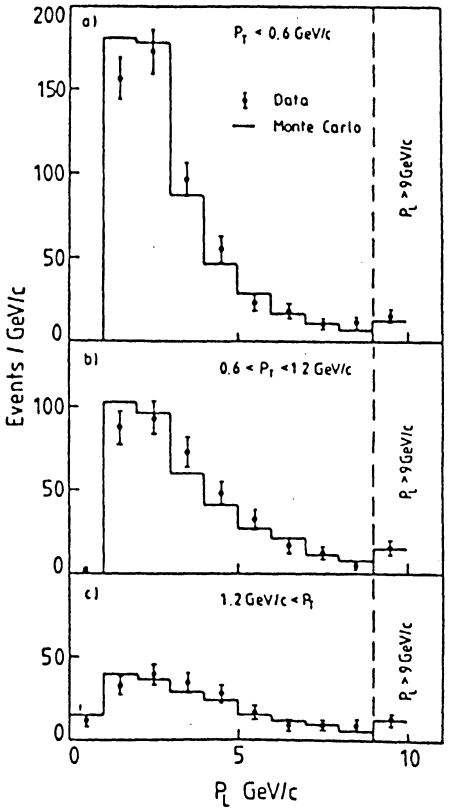

Figure 213. p_L distributions of good muon candidates in TASSO. The points are the data. The histograms show MC results.

5.7.4 The MARK J spectrometer

A slightly better muon identification has been achieved in the MARK J detector, namely 32% background, both decays and punch trough combined [155]. The general set-up of the MARK J detector has already been described in chapters 5.4.2 and 5.4.4. Here we shall discuss in some more detail the μ-spectrometer (see also figs. 164, 165 and 166). A graphic display of an inclusive muon event is shown in both projections in fig.214.

The event vertex in z-direction (along the colliding beams) is reconstructed from all charged particles measured in the drift tube array. The trajectories of particles emerging from the inner shower detector are recorded upon entrance into the muon spectrometer by twelve planes of drift chambers (S,T). Both end caps regions are covered by additional ten planes of drift chambers (U,V) of similar construction. Particles then enter into the momentum analyzing toroidal magnet which consists of iron plates magnetized to saturation, the scintilation counters (K) of the outer calorimeter and the TOF trigger counters (D). The magnet provides a minimum bending power of 17 kG-m and a minimum total material thickness of 5.4 hadronic interaction lengthes to filter out hadrons. Muons are identified by their ability to penetrate the magnet iron. Upon exit, their angles and coordinates are measured by ten or twelve planes of large area drift chambers (P,P' and R). Another coordinate on the muon trajectory in the bending direction is recorded halfway through the iron by a set of two plane drift chambers (Q).

All drift chambers consist of 10 cm cells formed by two field-shaping I-beams (which provide the structural strength) glued with insulators between two aluminum ground plates (see fig.215). A coordinate is measured by a double layer of such cells, with the second layer displaced by half a cell width from the first to resolve the left-right ambiguity. Because the electric field in the drift chamber cell is non-uniform, and the relation between time and position is not linear for inclined tracks, the positions must be corrected for angle during track reconstruction.

Individual cells have been tested to give a resolution of 0.4 mm for perpendicular tracks. In the system of 5000 wires with individually calibrated TDC's it is found that for all angles of incidence the average resolution is about 0.6 mm. This is much smaller than the spread resulting from multiple scattering in the iron.

As has been mentioned already, the toroidal magnetic field has an integrated field strength of $\int \vec{B} \cdot d\vec{l} \sim 17$ kG·m. The field is contained within the iron plates hence the muon will undergo multiple scattering in traversing the field. Similar set-ups have already been descibed in detail in chapter 4.

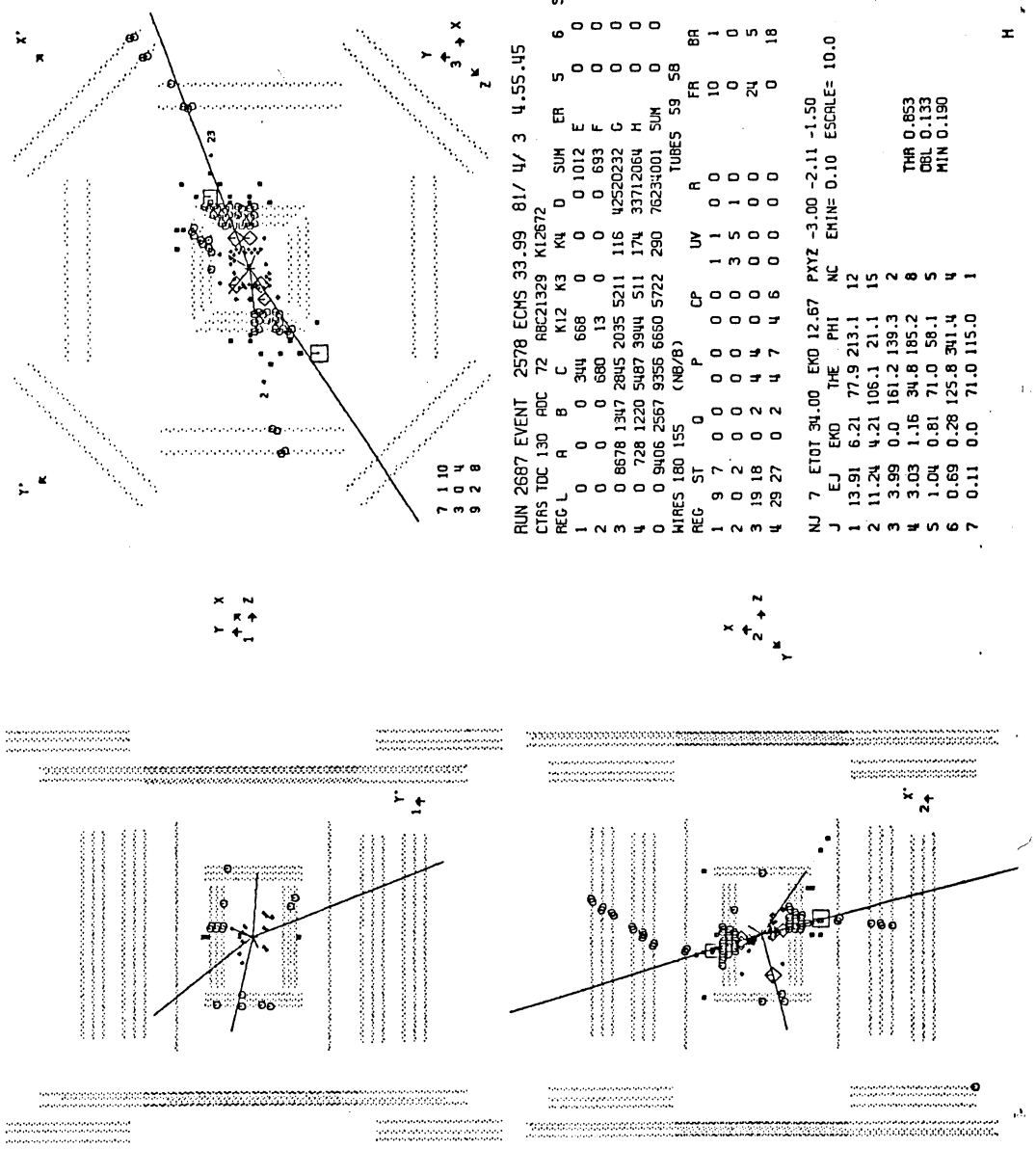

Figure 214. Graphic display of an inclusive muon event in the Mark J detector.

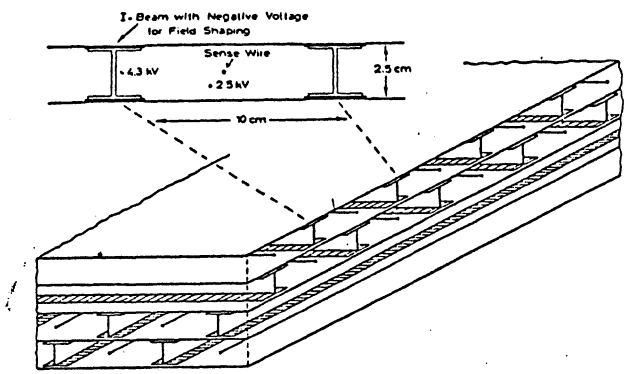

Figure 215. Mechanical assembly of the large Mark J drift chambers.

The average angular deviation due to multiple scattering is proportional to 1/p, p is the muon momentum. The position and direction of the muon is measured in the drift chambers S,T,Q and P or U,V and R traversing the barrel or the end caps respectively. For such an arrangement we expect a momentum independent resolution in the order of 25%. In practice measurement and survey errors in the drift chambers cause an additional momentum independent contribution. For momenta of ≈ 15 - 17 GeV/c the total fractional inverse momentum error is about 30%. In fig.216 we show the variation of $\sigma_{1/p}$ with polar angle Θ, both data and Monte Carlo.

The advantages of the MARK J muon spectrometer compared to the classic spectrometer are threefold:

1.) Due to the very short decay length (≈ 20 cm) in front of the shower detector the rate of decay muons from pions and kaons is strongly suppressed.

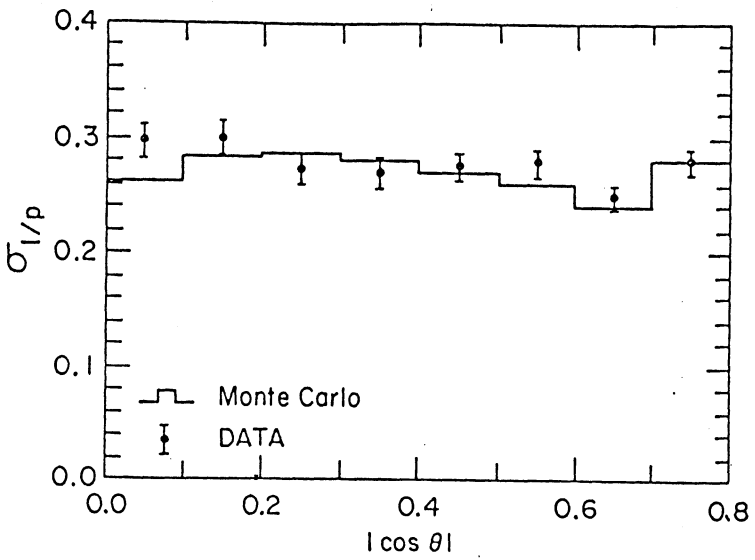

Figure 216. Momentum resolution for 17 GeV muons as measured in the Mark J spectrometer as function of the angle with respect to the beam axis.

2.) The MARK J detector measures the trajectory of the muon at various positions inside the calorimeter (S,T - chambers, U,V - chambers, Q - chambers).

3.) Outside the hadron absorber the stereo angle and the position of the penetrating particles are recorded.

The GHEISHA program has been used to establish a detailed detector simulation program for the MARK J experiment. Because of the tremendeous computer time needed to simulate a total hadronic event at PETRA - energies, some simplifications have been introduced. The cut-off parameters for hadrons have been adjusted to 20 MeV for both neutral and charged hadrons. This reduces the number of tracks to be followed by roughly a factor 2. Use has been made of the simplified treatment of electromagnetic showers as was discussed in chapter 2.5. On the other

hand the digitization of the scintilation counter output has been simulated as careful as possible. The methods were oulined in chapter 5.2 and the results were compared with experimental measurements in chapter 5.4.4. The chamber performance has been simulated in detail including background, inefficiencies, multiple hits, cross talks and δ-rays. The full chamber survey information has been used as was provided on an input file. The somewhat complicated drift time vs drift distance function has been obtained by inversing the drift distance vs drift time function as used in the analysis programs. All the detector informations have been coded into a form that resembles the raw data format. A flag in the event format has been introduced in order to distinguish experimental from Monte Carlo simulated events. For each Monte Carlo generated event a shower history data block has been added.

Details of the data analysis of inclusive muon candidates may be found elsewhere [156] In principle inclusive muon events are selected requiring a track in the outer drift chambers. A momentum fit is performed using additionally the information of the event vertex as measured by the drift tube array. By comparing the position of the reconstructed trajectory with the coordinate measured by the Q - chambers inside the hadron calorimeter, the background from punch through and decay can be determined. The quantity

$$\Delta Q = (z_Q - z_{flt}) \qquad (5.42)$$

is used. z_Q and z_{flt} are the measured and fitted z - coordinates respectively in the Q - chamber. In fig.217 ΔQ is compared for the exp. data and the MC. In the lower part of the figure we show the distributions for prompt muons, decays from pions and kaons and for hadron punch through separately. All tracks with $|\Delta Q| < 5$ cm have been accepted as good muon candidates. This cut results in a background of 13% for hadron punch through and 19% for decays.

For further physics analysis we show in figs. 218 and 219 the distributions of muon candidates as function of the longitudinal and transverse momentum component both with respect to the jet axis. Again a good agreement between exp. data and MC is observed. The contributions of prompt muons, of muons from decays and of the hadron punch through are shown in figs. 220 and 221.

The Monte Carlo calculations just shown include radiative corrections and the assumption that B decays via B → C X. Fig. 222 shows the differential cross section in p_T^2 compared with pion distributions. The muon p_T^2 distribution is distinctly different from the pion distribution, with the shoulder in the range $2 \leq p_T^2 \leq 5$ (GeV/c)^2 which is indicative of the decay of a

particle of mass around 5 GeV. Fig. 222b shows the data compared with the Monte Carlo prediction for the total μ rate and its two components B → μX and C → μX. The shoulder is well explained by B decays and the Monte Carlo prediction agrees with the data. A p_T cut is used to divide the data into B-enriched and C-enriched samples for further physics analysis. The B-enriched sample ($p_T > 1.2$ GeV/c, see also fig. 221) has a composition, according to Monte Carlo and after backgroundsubtraction, of 64% B decays, while the expected composition of the C-enriched sample ($p_T < 1.2$ GeV/c) is 85% C decays.

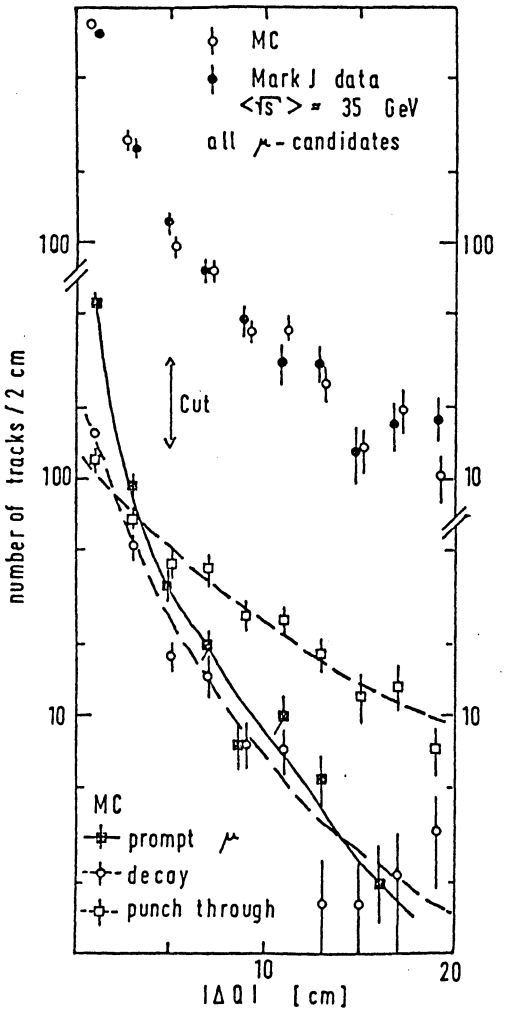

Figure 217. Distribution of the displacement in the Q-chamber for all muon candidates. In the lower part of the figure the MC results for the various contributions are shown.

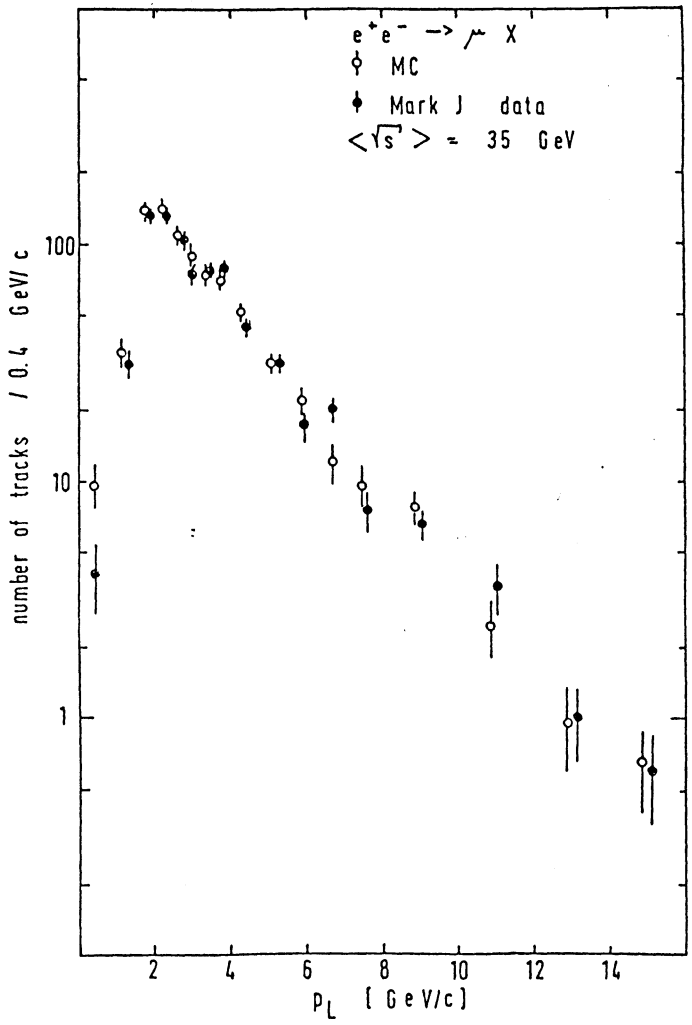

Figure 218. p_L distribution for good muon candidates in the Mark J detector.

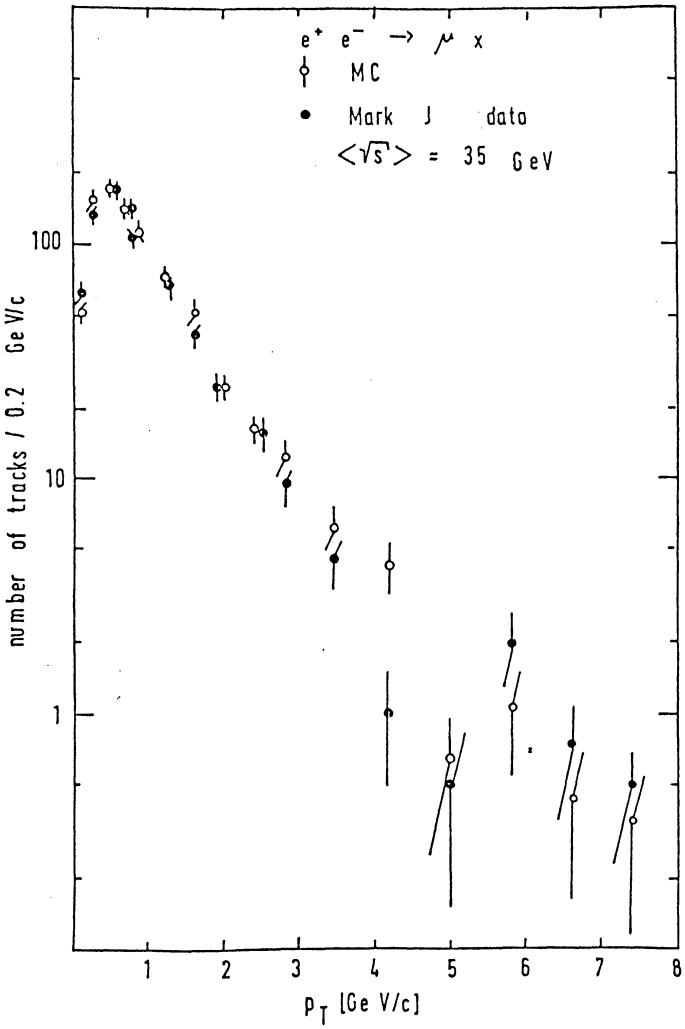

Figure 219. p_T distribution for good muon candidates in the Mark J detector.

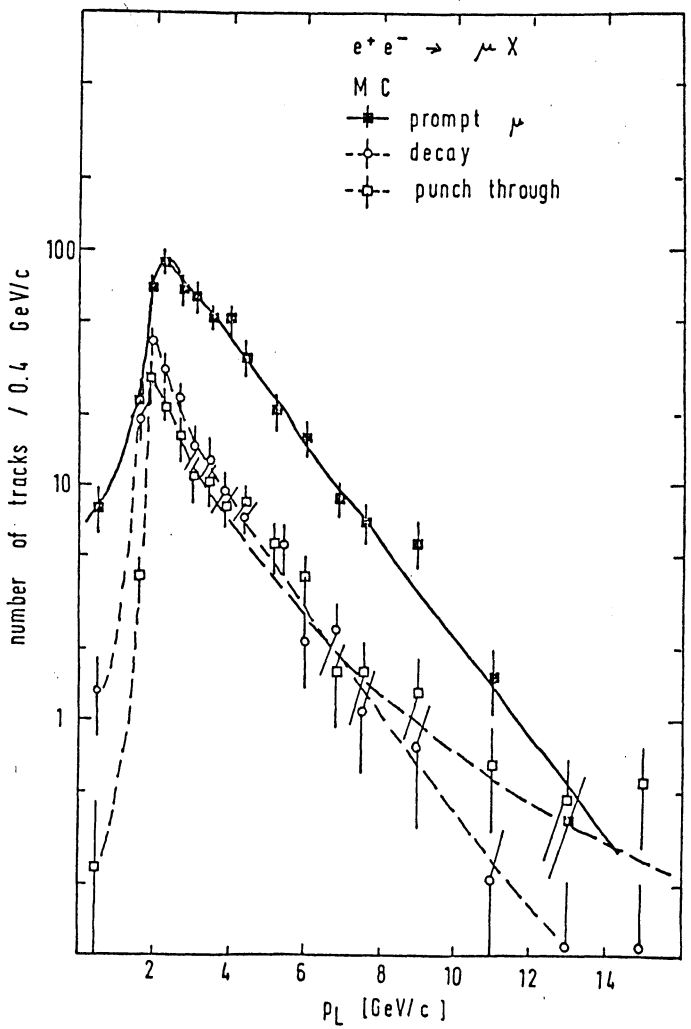

Figure 220. p_L distributions for the three contributions to the good inclusive muon sample.

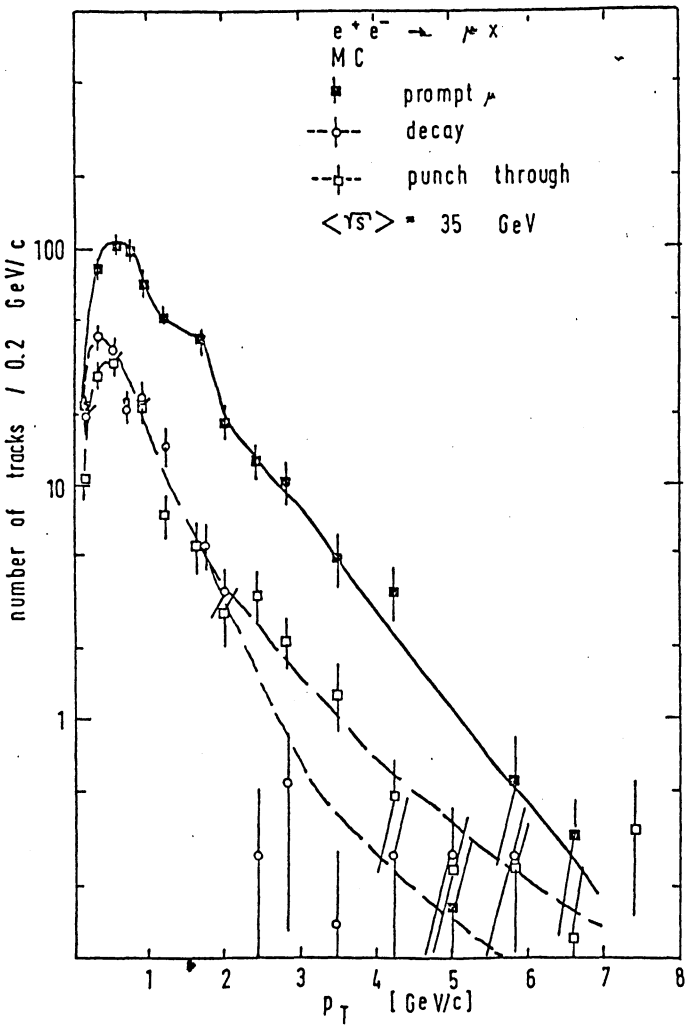

Figure 221. p_T distributions for the three contributions to the good inclusive muon sample.

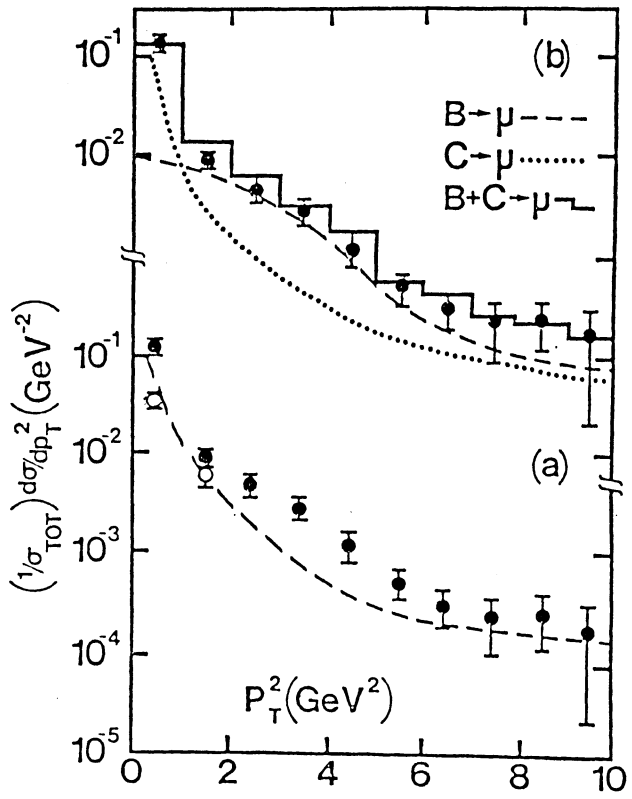

Figure 222. p_T^2 distributions for good muon candidates in the Mark J detector (a). The open circles are the cross sections with $p > 2$ GeV/c. The solid points are the cross sections extrapolated to all p. The dashed curve represent the inclusive pion spectrum. In the upper part of the figure (b) the data are compared with the Monte Carlo.

5.7.5 Optimization of μ-identification

Good lepton identification is one main point of all detectors proposed for LEP. In this study Monte Carlo calculations for the ELECTRA detector are presented. The detector set-up is shown in fig. 223. In order to save computer time and not to complicate the analysis the geometry is slightly simplified compared to that proposed in the letter of intend. But this should not have any influence on our conclusions.

The detector consists of a high precision vertex chamber (HPC) inside a conventional main drift chamber. The transition radiation detector together with the liquid argon calorimeter is used to identify electrons with high accuracy. The superconducting coil provides a magnetic field of 7.5 kG. At entrance to the iron yoke particles emitted under 90° with respect to the beam axis have passed 23.6 r.l. or 1.35 absorbtion lengthes in total. The yoke provides the return for the magnetic flux and acts also as a calorimeter and muon identifier. To this end it is segmented in 20 layers of iron, 5 cm each, and layers of streamer tubes between them. Muons will then be detected as non-interacting tracks in the tracking calorimeter which emerge from the iron into the muon chambers. As can be imagined this is a standard general purpose detector highly optimized for lepton identification.

In the first step of the analysis we have generated tracks of single particles (π^+, π^-, K^+ and K^-) at momeda of 2, 3, 4, 5, 10 and 15 GeV/c and also total jet events for e^+e^- interactions at $\sqrt{s}$ = 80 GeV. The jet generator was provided by H.G. Sander [157]. All particles are followed through the HPC and the main chamber. The directions and momenta of charged particles are recorded upon leaving the HPC and the Mainchamber. After the showering process in the calorimeter some particles may emerge the iron yoke and are recorded as tracks in the outer muon chambers. Graphic displays of some jet events are shown in fig. 224. We have selected 4 pictures, two events with prompt muons (a and b) and two events with punch trough (c with hadron punch through and d with decay punch trough).

In the second step of the analysis all charged particles, recorded before as leaving the HPC, are treated as muons through the detector without beeing subjected to multiple scattering. Due to energy loss they may stop before reaching the outer muon chambers. If a track recorded in the first step coincides within the limits of multiple scattering with the position and/or direction of the track simulated in the second step, it was identified as good muon candidate.

For momenta below 2 GeV/c the acceptance decreases rapidly for about 100 cm of iron. This was concluded from fig. 207 in chapter 5.7.2. The upper

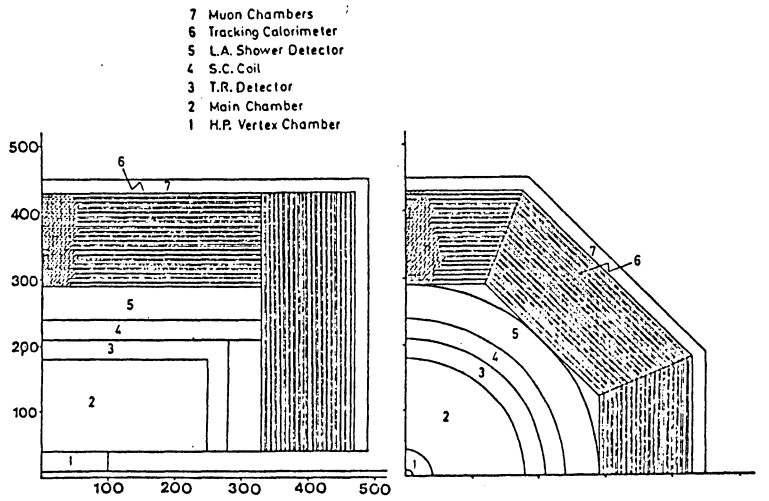

Figure 223. Layout of the ELECTRA detector used for optimization of muon detection

limit of the iron thickness is thus around 120 cm of iron. The optimization of the absorber thickness may be achieved by studying the following three contributions separately:

1) Muons from pion or kaons decaying inside the HPC or Main chamber (internal decay).

2) Muons from the decay of the primary particle between the Main chamber and the Muon chamber (external decay).

3) Other charged particles emerging the iron yoke, mainly low energy electrons and protons as well as fast pions and kaons (hadron punch through).

The three contributions are shown in fig. 225 for pions and kaons at 2, 5 and 10 GeV as curves labelled by (1). If we measure the displacement of the

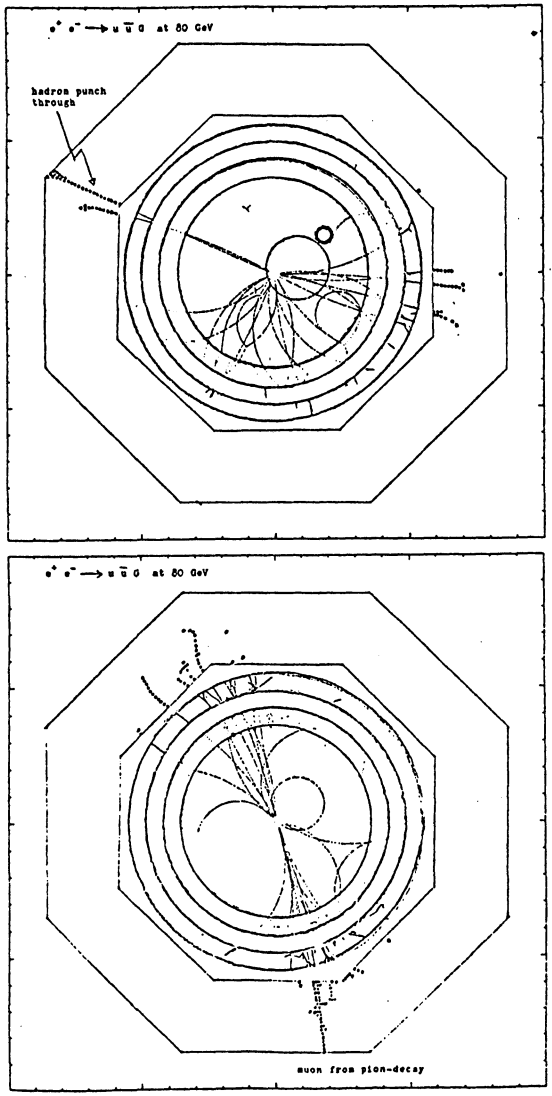

Figure 224. Graphic displays of different types of events as expected for the ELECTRA detector.

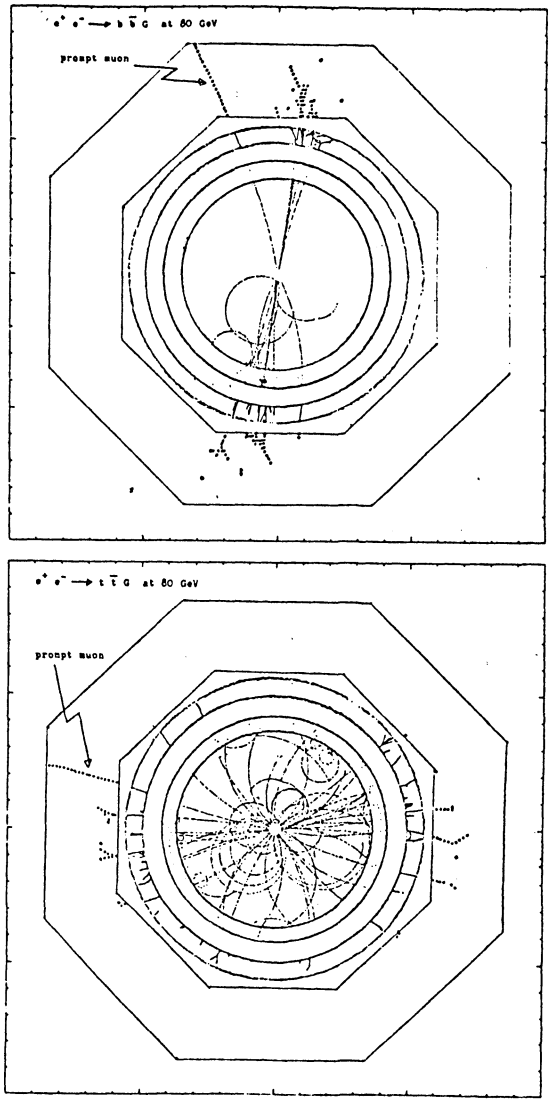

Figure 224. Graphic displays of different types of events as expected for the ELECTRA detector.

Calorimetry 354

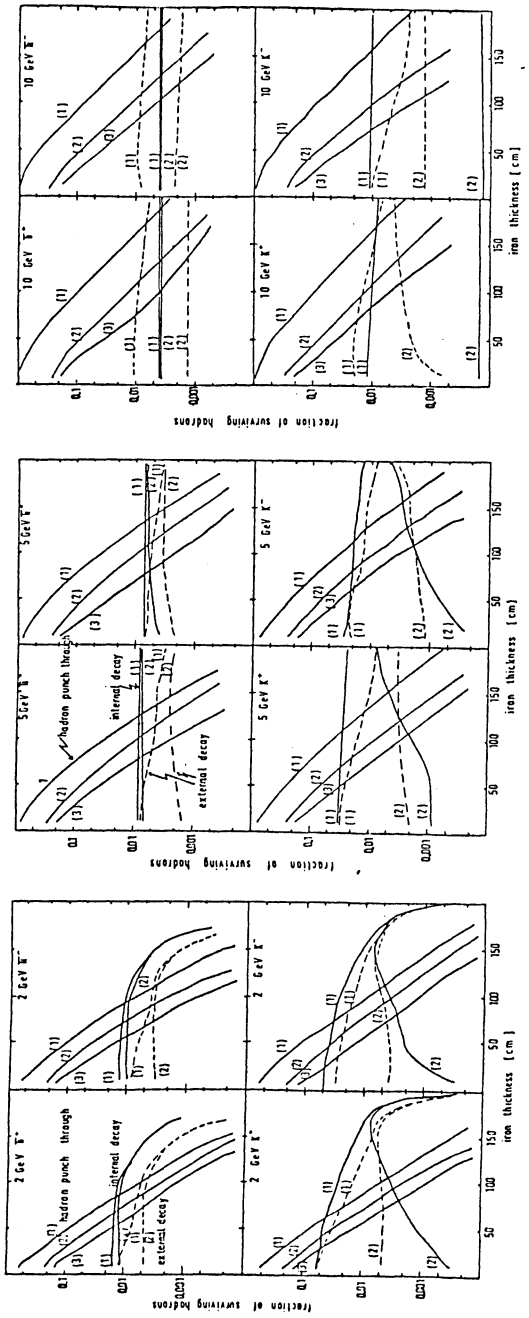

Figure 225. Fractions of surviving hadrons as function of iron thickness for hadron punch through, external and internal decay. For further details see text.

tracks outside the absorber compared to that expected for prompt muons and require the tracks to be inside a circle of $2R_0$ (corresponding to 96% acceptance for prompt muons), we arrive at the curves labelled by (2). If we require additionally the direction of the emitted particles to be in agreement with the expectation for a prompt muon, the curves labelled by (3) have been obtained. For muons from decays the latter curves are only slightly smaller as those labelled by (2). Thus they have been omitted. The curves obtained by cut (2) are certainly only lower limits for the decay punch through. In our calculations we have assumed perfect performances of the high precision vertex chamber and the muon chambers. Under these circumstances it is evident that the decay punch through can be measured the better the smaller the absorber thickness. The reason is simply that the overlap of the multiple scattering circles for prompt muons and decay muons increases with increasing absorber thickness. This effect is much more evident in case of kaons due to the larger laboratory decay angle compared to pions.

The optimal absorber thickness for the classic muon identifier may be determined now requiring the probability for hadron punch through to be in the same order of magnitude as the decay punch through.

In fig. 226 we show the absorber thickness as function of the momentum of the primary particle, determined by the requirement that the hadron punch through is as half as much as the decay punch through. Four different cases are given. In fig. 226a we assume the hadron punch through to be measured by the displacement only, whereas decays can not be distinguished from prompt muons. Including a measurement of the direction we arrive at the values given in fig. 226b. Additional measurements of the displacement and direction of the decay muons lead to the values given in fig. 226c and 226d respectively. But none of these solutions have a hadron punch through rejection of much less than 0.02, a number which was already met for the classic muon spectrometer as realized by e.g. the TASSO detector.

A further improvement may be obtained by the measurement of the momentum for all particles leaving the absorber. In fig. 227 we show the momentum spectrum of the total punch through, decay and hadron punch through combined, for incoming charged pions at 3 GeV/c. Both cuts for displacement and direction have already been applied for the decay- as well as for the hadron punch through. The spectrum is actually plotted as function of the difference p_0-p_f of the momentum p_0 of the incoming particle and the momentum p_f of the punch through particle. An absorber thickness of 100 cm has been chosen. this corresponds to an offset of ≈ 1.3 GeV/c in the distribution. Comparing these spectra with the corresponding spectra for prompt muons, we arrive at the rejection rates given

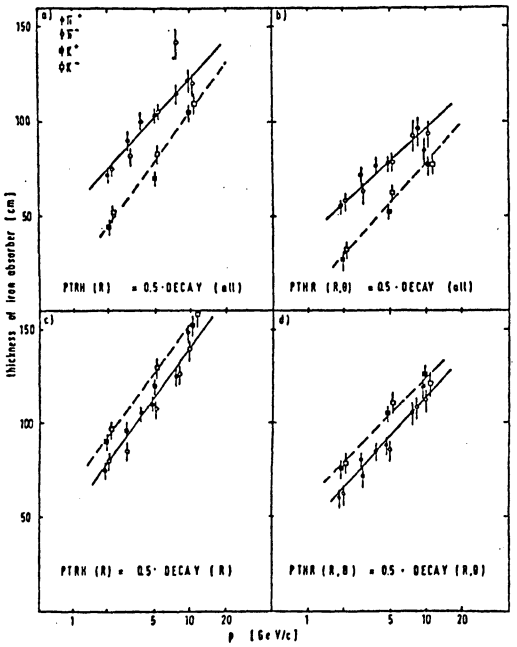

Figure 226. Optimal choice of the absorber thickness as function of the muon momentum. For further details see text.

in fig. 228. Hadron rejection by the measurement of the momentum is undoubtly the most powerful method. We have proven that all muon candidates left fullfil all requirements for prompt muons on the total pathlength through the detector. The punch through consists only of a small sail through (non-interactiong hadrons) contribution and decays with very small decay angles. This method will be used by the L3 detector at LEP. In fig. 229 we show a Monte Carlo event display for a two-jet event at 80 GeV center of mass energy.

If momentum measurement outside of the absorber can not be achieved by financial reasons, we propose to build the following μ-identifier (see fig. 230):

1) A high precision vertex chamber to measure the direction of the primary particle as accurate as possible.

2) A Main chamber to measure the momentum of the primary particle.

3) A Muon chamber 1, located near to the Main chamber, but at a position, where nearly all hadrons have already interact or decayed. An absorber thickness of 3 λ_0 may be an optimal choice. This chamber acts mainly to reject the decay punch through, but can also be used as a conventional muon identifier down to 0.5 GeV/c.

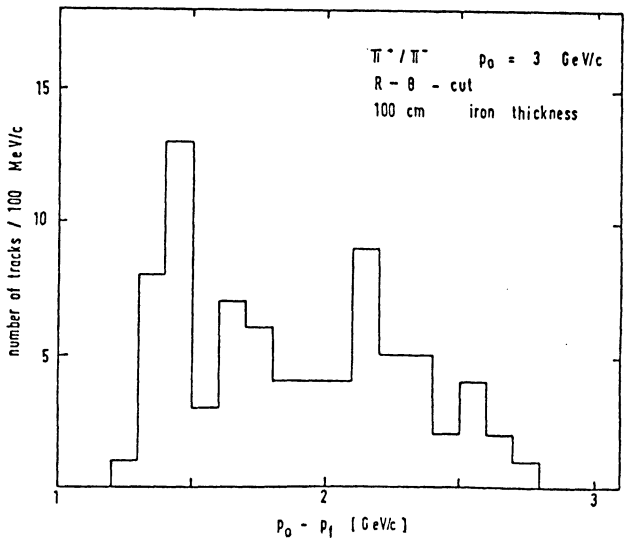

Figure 227. Momentum distribution of total punch through for pions penetrating 100 cm of iron. For details see text.

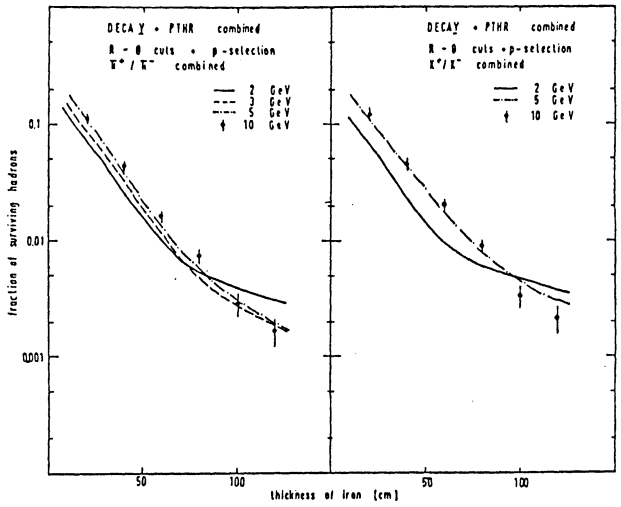

Figure 228. Total punch through as function of iron thickness applying displacement and angle cuts as well as momentum selection outside the absorber.

4) Muon chambers 2 outside of an additional absorber of $\approx 4\ \lambda_0$. Both the Muon chamber 1 and the Muon chamber 2 should be able to measure the displacement and the direction of the tracks.

With such a detector we got the π/K- rejection rates given in fig. 231 as function of the momentum. Shown are results with and without additional momentum measurement in the Muon chamber 2. This detector gives an improvement of a factor 100 in e identification (10^{-4}) and a factor 10 in μ-identification ($2 \cdot 10^{-3}$) compared to existing detectors. In spite of the fact that nearly all important discoveries in the last 20 years have been made using leptonic decay modes, one can expect such a detector to be very powerful for unexpected physics.

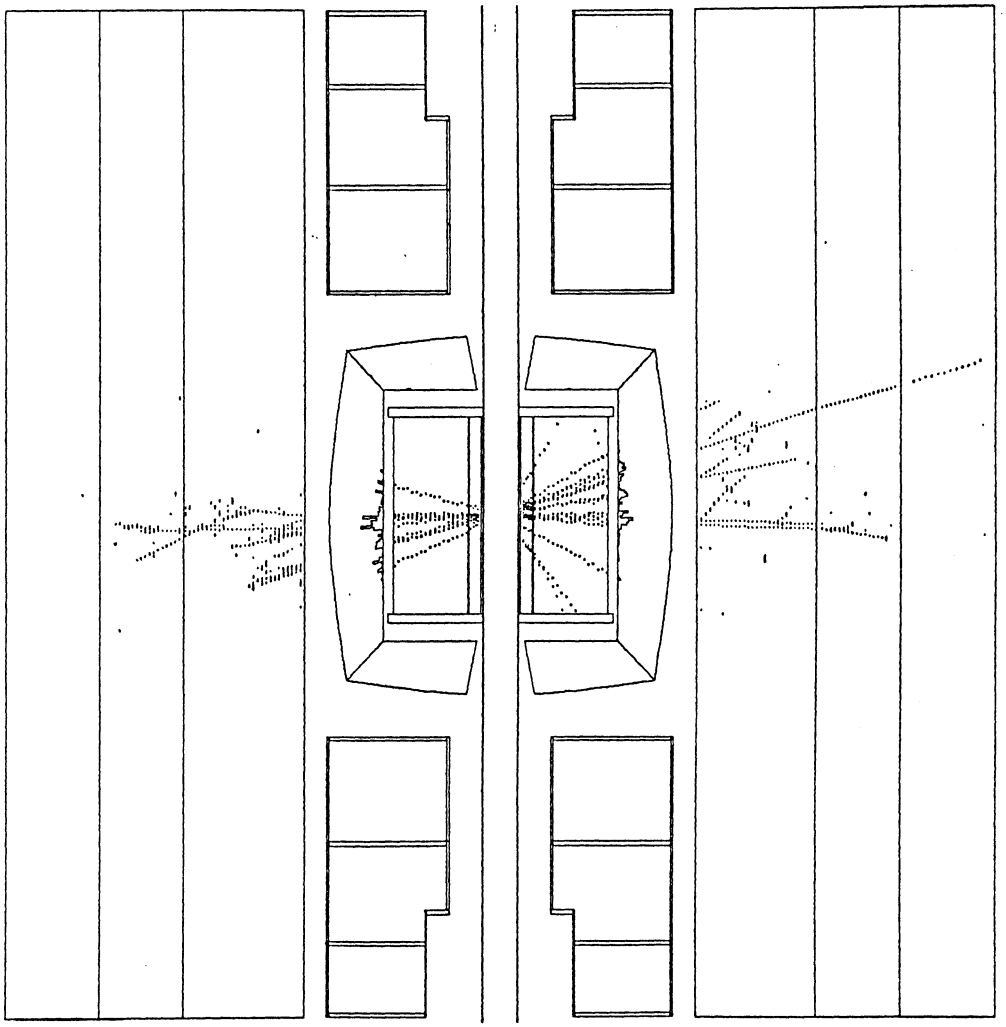

Figure 229. Graphic display of an event in the L3 detector. The big outer muon chambers have been omitted.

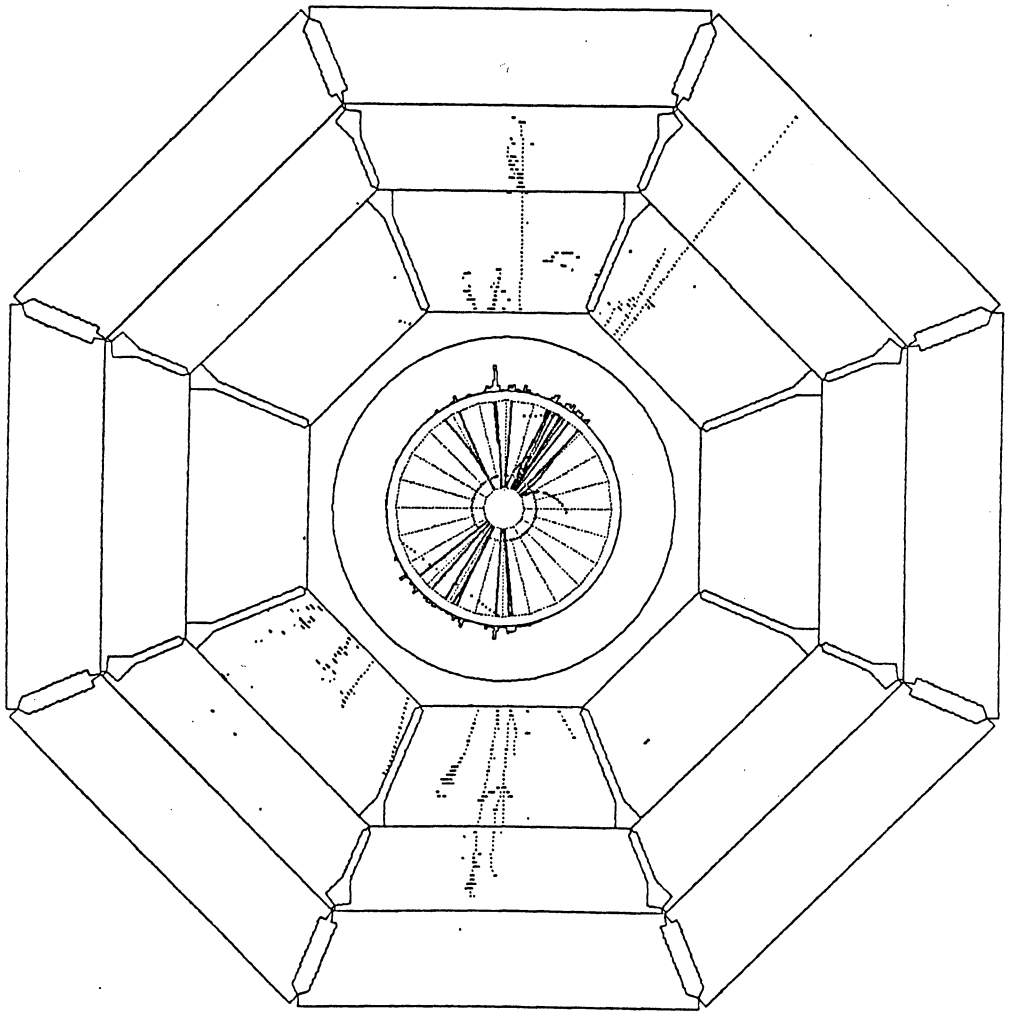

Figure 229. Graphic display of an event in the L3 detector. The big outer muon chambers have been omitted.

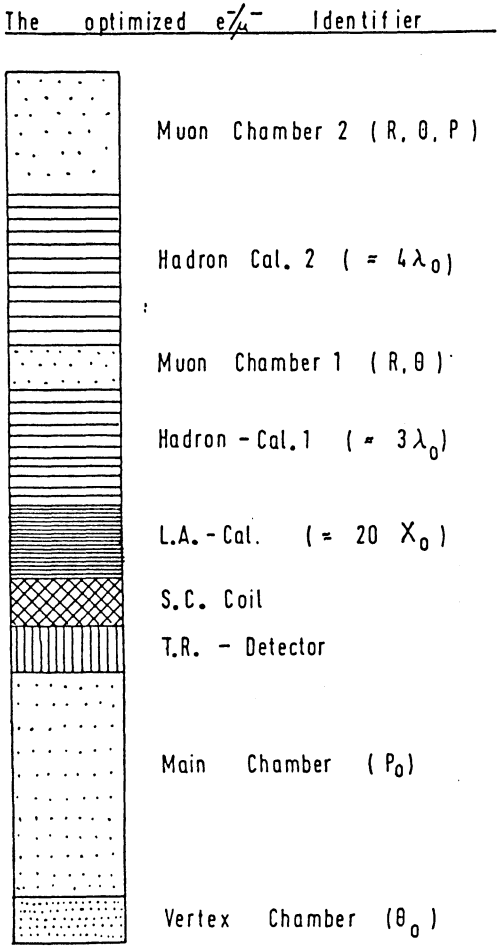

Figure 230. Schematic view of an optimized μ spectrometer.

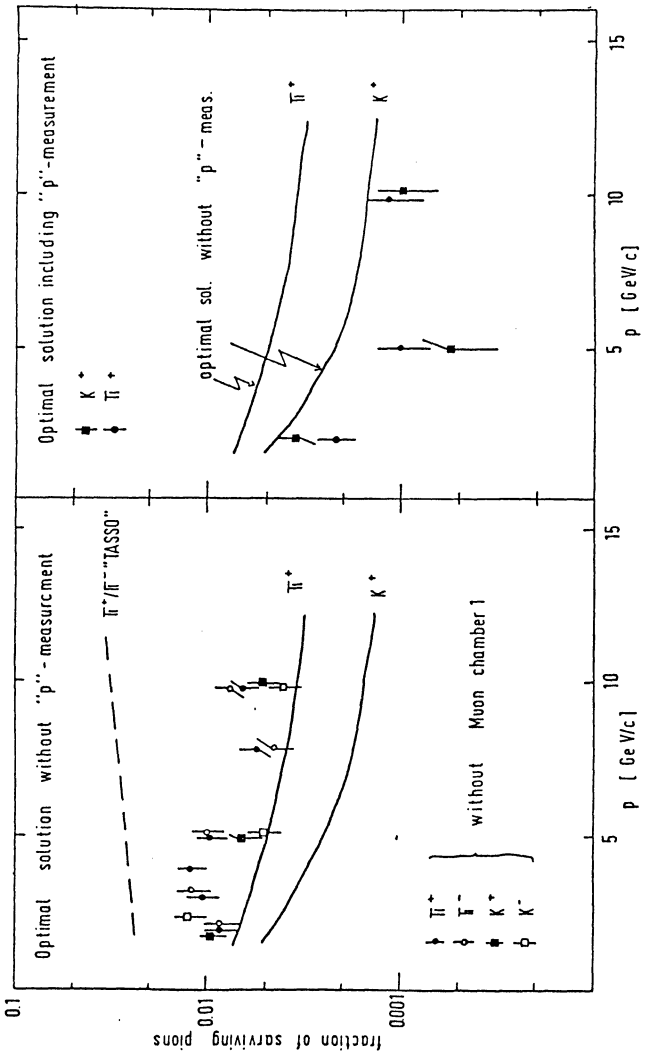

Figure 231. Punch through rejection rates for the optimized μ identifier as shown in fig.230, with and without momentum measurement outside the absorber. In the left part the improvement using additionally the inner muon chambers is demonstrated. The right shows the improvement by the momentum measurement.

6.0 ACKNOWLEDGEMENTS

I would like to thank Prof.A.Böhm and Dr.W.Krenz for their continous interest in this work, for many discussions and the good understanding, far beyond scientific questions.

The Mark J group at PETRA has initiated this work. I appreciate especially the excellent leadership of the group by Prof.S.C.C.Ting. For many discussions and helps I wish to thank H.Benda, G.Berghoff, Prof.J.Branson, Prof.M.Chen, Dr.M.Fukushima, T.Hebbeker, Dr.G.Massaro, Prof.H.Newman, Dr.F.P.Poschmann, Dr.J.Salicio and D.Teuchert.

The last version of the Gheisha program is a product of the Aachen Monte Carlo group of the L3 collaboration. Thus this work would not have been finished without the many contributions by D.Braun, T.Haeck, Ch.Helmrath, Prof.K.Lübelsmeyer, Dr.H.U.Martyn, Dr.U.Micke, Dr.M.Pohl, Dr.H.G.Sander, Prof.D.Schmitz, J.Schug and Dr.W.Wallraff.

I wish to thank the DESY-directorate, Prof.V.Soergel and Prof.P.Söding, for the financial support during my stay at DESY and the R1 group for the good performance of the IBM computers.

7.0 REFERENCES

1) D.Zerby and H.S.Moran, ORNL-TM-422 (1962);

2) J.C.Butcher and H.Messel, Phys.Rev.112 (1958)2096;

3) H.H.Nagel, Z.f.Physik 186 (1965) 319;

4) R.L.Ford and W.R.Nelson, SLAC Report 210 (1978);

5) W.V.Jones, Phys.Rev.D1 (1970) 2201;

6) J.Ranft, NIM 81 (1970) 29;

7) K.C.Chandler and T.W.Armstrong, ORNL-4744 (1972);

8) A.Grant, NIM 131 (1975) 167;

9) A.Crispin and G.N.Fowler, Rev.Mod.Phys.42 (1970) 290;

10) R.M.Sternheimer and R.F.Peierls, Phys.Rev.B3 (1971) 3681;

11) W.W.M.Allison, Phys.Script.23 (1981) 348;

12) A.H.Walenta, Phys.Script.23 (1981) 354;

13) D.M.Ritson, Techniques of High Energy Physics,
Interscience Publishers, New York (1961);

14) P.Rice-Evans, Spark-,Streamer-,Proportional- and Drift-Chambers,
Richelieu Press, London (1970);

15) K.A.Ispirian, A.T.Margarian and A.M.Zverev, NIM 117 (1974) 125;

16) L.Janossy, Theory and Practice of the Evaluation of Measurements,
University Press Oxford (1962);

17) J.D.Jackson, Classical Electrodynamics 2nd.ed.,
John Wiley and Sons (1975);

18) V.L.Highland, NIM 129 (1975) 497;

19) B.Rossi, High Energy Particles, Prentice Hall (1952);

20) G.Shen et al.,Phys.Rev.D20 (1979) 1584;

21) H.W.Koch and J.W.Motz, Rev.Mod.Phys.31 (1959) 920;

22) J.W.Motz, H.A.Olsen and H.W.Koch, Rev.Mod.Phys.41 (1969) 581;

23) E.Longo and I.Sestili, NIM 128 (1975) 283;

24) G.Bathow et al., Nucl.Phys. B20 (1970) 592;

25) W.Flaminio et al., CERN-HERA 79-02 and CERN-HERA 79-03 (1979)
and further references therein;

26) F.Uchiyama, Particle Data Group LBL-55 (1972)
and further references therein;

27) J.G.Rushbrooke and B.R.Webber, Phys.Rev.44 (1978) 1
and further references therein;

28) G.W.Brandenburg et al.,Phys.Rev.D9 (1974) 1939;

29) A.Engler et al., Phys.Rev.D18 (1978) 3061;

30) W.E.Cleland et al., Phys.Rev.D12 (1975) 1247;

31) G.Alexander et al., Phys.Lett. 58B (1975) 484;

32) A.Engler et al., Phys.Lett. 63B (1976) 231;

33) J.C.M.Armitage et al., Nucl.Phys. B123 (1977) 11;

34) W.Cameron et al., Nucl.Phys. B132 (1978) 189;

35) S.Cittolin et al., Nucl.Phys. B142 (1978) 410;

36) M.Mugge et al., Phys.Rev. D20 (1979) 2105;

37) B.T.Feld, Models of Elementary Particles,
Blaisdell Publishing Company (1969);

38) S.P.Denisov et al., Nucl.Phys. B61 (1973) 62;

39) M.J.Longo and B.J.Moyer, Phys.Rev.125 (1962) 701;

40) B.W.Allardyce et al., Nucl.Phys. A209 (1973) 1;

41) A.W.Thomas and R.H.Landau, Phys.Rep. 58 (1980) 121;

42) F.Binon et al., Nucl.Phys. B17 (1970) 168;

43) M.Crozon et al., Nucl.Phys. 64 (1965) 567;

44) J.W.Cronin et al., Phys.Rev. 107 (1957) 1121;

45) T.Bowen et al., Nuovo Cimento IX (1958) 908;

46) G.J.Igo et al., Nucl.Phys. B3 (1967) 181;

47) A.Gsponer et al., Phys.Rev.Lett. 42 (1979) 9;

48) A.Gsponer et al., Phys.Rev.Lett. 42 (1979) 13;

49) J.Beil et al., Phys.Rev.Lett. 36 (1976) 1104;

50) L.J.Cook et al., Phys.Rev. 75 (1949) 7;

51) R.Fox et al., Phys.Rev.80 (1950) 23;

52) J. De Juren, Phys.Rev.80 (1950) 27;

53) R.H.Hildebrand and C.E.Leith, Phys.Rev.80 (1950) 842;

54) J. De Juren and N.Knable, Phys.Rev.77 (1950) 606;

55) T.Corr et al., Phys.Rev. 98 (1955) 1369;

56) V.A.Nedzel, Phys.Rev.94 (1954) 174;

57) J.Froyland and O.Skontorp, Nucl.Phys.B68 (1974) 93;

58) K. von Holt et al., Nucl.Phys.B103 (1976) 221;

59) Z.Koba et al., Nucl.Phys.B40 (1972) 317;

60) Z.Koba, Proc. of the 1973 CERN-JINR School of Physics, Ebeltoft (1974) 171;

61) H.Fesefeldt et al., Nucl.Phys. B147 (1979) 317;

62) J.Whitmore, Phys.Rep.10 (1974) 273;

63) H.Fesefeldt, DESY internal report F1-73/11 (1973);

64) J.G.Rushbrooke and B.R.Webber, Phys.Rep.44 (1978) 1;

65) W.Ochs and L.Stodolsky, Phys.Lett.69B (1977) 225;

66) H.Fesefeldt, W.Ochs and L.Stodolsky, Phys.Lett.74B (1978) 389;

67) W.Ochs and T.Shimada, Z.Phys.C4 (1980) 141;

68) G.Sternman and S.Weinberg, Phys.Rev.Lett.39 (1977) 1436;

69) V.Blobel et al.,Nucl.Phys.B69 (1974) 454;

70) V.Blobel et al.,Nucl.Phys.B135 (1978) 379;

71) H.Fesefeldt and W.Ochs, unpublished, part of this work has been presented by W.Ochs at the Jet-Conference, Copenhagen(1978),Phys.Script.19(1979) 127;

72) A.Bialas and L.Stodolsky, Phys.Rev.D13 (1976) 1199;

73) D.C.Carey et al., Phys.Rev.Lett. 33 (1974) 327;

74) P.Chapiluppi et al., Nucl.Phys. B70 (1974) 1;

75) R.P.Feynman and R.D.Field, Nucl.Phys. B136 (1978) 1;

76) B.Andersson et al., Z.f.Phys. C1 (1979) 105;

77) B.Andersson and G.Gustafson, Phys.Lett. 84B (1979) 483;

78) A.Ali et al., DESY 79/86 (1979);

79) M.Kobayashi and M.Maskawa, Progr.Theor.Phys. 49 (1973) 652;

80) A.Ali et al., DESY 79/63 (1979);

81) B.Andersson et al., Phys.Lett. 69B (1977) 221 and Phys.Lett. 71B (1977) 337;

82) A.Capella et al., Phys Lett. 81B (1979) 68; and further references therein;

83) J.Dias de Deus and S Jadach, Acta.Phys.Polonica B9 (1978) 249;

84) A.C.Melissinos et al., Phys.Rev.Lett. 7 (1961) 454;

85) E.Gellert, LRL preprint 784 (1972) and
M.A.Abolins et al., Phys.Rev.Lett. 25 (1970) 126;

86) M.Alston-Garnjost et al., Phys.Lett. 39B (1972) 402;

87) J.V.Beaupre et al., Phys.Lett 37B (1971) 432;

88) M.Deutschmann et al., Nucl.Phys. B39 (1972) 133;

89) J.V.Beaupre et al., Nucl.Phys. B30 (1972) 381;

90) J.Bartsch et al., Nucl.Phys. B40 (1972) 103;

91) W.Ko and R.L.lander, Phys.Rev.Lett.26 (1971) 1064;

92) S.Barshay and Y.A.Chao, Phys.Lett. 38B (1972) 225;

93) A.Capella, Partons in Soft Hadronic Collisions,
Proc of the Europhysics Study Conference Erice,
March 1981, p. 199 ff;

94) K.Gottfried, Phys.Rev.Lett. 32 (1974) 957;

95) J.Ranft, Particle Accelerators 3 (1972) 129;

96) H.Winzeler, Nucl.Phys. 69 (1965) 661;

97) J.Hebert et al., Phys.Lett. 48B (1974) 467;

98) J.Babecki et al., Phys.Lett. 47B (1973) 268;

99) A.Gurtu et al., Phys.Lett. 50B (1974) 391;

100) I.Otterlund et al., Nucl.Phys. B142 (1978) 445;

101) T.Nakamura et al., Hiroshima University preprint HUPD-8019(1980);

102) W.Busza et al., Phys.Rev. D22 (1980) 13;

103) J.B.Marion and J.L.Fowler, Fast Neutron Physics, part I and II,
Wiley and Sons, New York-London (1963);

104) N.A.Perfilov and V.P.Eismont (ed.), Physics of Nuclear Fission,
Israel Program for Scientific Translations Ltd.,
Jerusalem (1965);
R.Vandenbosch and J.R.Huizenga, Nuclear Fission,
Academic Press New York - London (1973);

105) M.Nagano, INSJ-120, Institute for Nuclear Study,
University Tokyo (1970);

106) F.E.Close, An Introduction to Quarks and Partons,
Academic Press (1979), p. 181 ff;

107) H.Muirhead, The Physics of Elementary Particles,
Pergamon Press (1965), p.544 ff;

108) V.Blobel, DESY R-Info 79/C (1979) p.34 ff;

109) D.Braun, I.Physikalisches Institut, RWTH Aachen,
private communication (1983);

110) V.Blobel, private communication (1974);

111) P.Laurikainen et al., NIM 98 (1972) 349;

112) L.Lamanna et al.,NIM 187 (1981) 367;

113) H.Grote and P.Zanella, NIM 176 (1980) 43;
H.Eichinger and M.Regler, CERN 81-06 (1981);

114) D.Drijard et al., NIM 176 (1980) 389;

115) G.Flügge et al., KfK-Report Karlsruhe 3040B (1980);

116) D.P.Barber et al., Phys.Rep.63 (1980) 337;

117) H.Drum et al., DESY-Report 80/38 (1980);

118) S.Iwata, DPNU-13-80 (1980);

119) U.Amaldi, CERN-EP/80-212 (1980);

120) G.T.Wright, Phys.Rev.Lett.(1953) 1282;

121) J.B.Birks, Scintilation counters, Pergamon-Press London (1953);

122) Taylor et al., Phys.Rev. 84 (1951) 1034;

123) Frey et al., Phys.Rev. 82 (1951) 372;

124) W.E.Mott and R.B.Sutton, Scintilation and Cerenkov Counters, in: Handbuch der Physik (ed. S.Flügge), Vol.LXV p.86, Springer Verlag Berlin-Göttingen-Heidelberg (1958);

125) R.B.Murray, Scintilation Counters, in: Nuclear Instruments and their Use (ed. A.H.Snell), Vol.1, p.82, John Wiley & Sons, New York (1962);

126) E.Schramm, Organic Scintilation detectors, Elsevier Publ. Comp., Amsterdam (1963);

127) J.H.Neiler and P.R.Bell, The scintilation method, in: Alpha-, Beta- and Gamma-Ray Spectroscopy (ed. K.Siegbahn), p.245, Amsterdam (1965);

128) J.B.Birks, The Theory and Practice of Scintilation Counting, Pergamon Press London (1964);

129) V.Eckardt et al., NIM 155 (1978) 389;

130) W.Paulus, Dipl.-Thesis, RWTH Aachen, unpublished (1981);

131) M.Pohl, D.Phil.Thesis RWTH Aachen, unpublished (1979);

132) A.Astbury, Phys.Scripta 23 (1981) 397;

133) K.Jansen, Dipl.-Thesis, RWTH Aachen, AC Intern 82/04 (1982);

134) UA5-Collaboration, private communication (1983);

135) H.Abramovicz et al., CERN-EP/80-188 (1980);

136) O.Botner et al., IEEE Trans.Nucl.Sci. NS-28 (1981) 510;

137) C.W.Fabjan et al., NIM 141 (1977) 61;

138) B.Friend et al., NIM 136 (1976) 505;

139) H.Benda, Dipl.-Thesis, RWTH Aachen, unpublished (1980);

140) M.Holder et al., NIM 151 (1978) 69;

141) Mark J Collaboration, Phys.Rep.63 (1980) 337;

142) Mark J Collaboration, MIT-Report 131 (1983);

143) D.P.Barber et al., Phys.Rev.Lett. 43 (1979) 830;

144) D.Bollini et al., NIM 171 (1980) 237;

145) L3 Collaboration, Technical Proposal (1983);

146) D.Braun and U.Micke, private communication (1984);

147) ELECTRA Collaboration, CERN-LEPC/82-54 and CERN-LEPC/15 Add 1;

148) U.Micke et al., NIM 221 (1984) 495;
G.Schild, Dipl.-Thesis, RWTH Aachen AC-Intern 83/02 (1983);
C.Declercq et al., ELECTRA PHY-ACT 1982-1 (1982);

149) A.Boyarski, SLAC-Pub-559 (1969);

150) F.A.Harris et al., NIM 103 (1972) 345;

151) R.Brandelik et al., Phys.Lett.83B (1978) 261;
R.Brandelik et al., Phys.Lett.92B (1980) 199;
R.Brandelik et al., Phys.Lett.113B (1982) 499;
H.Boerner et al., NIM 176 (1980) 151;

152) M.Althoff et al., Z.Phys.C 22 (1984) 219;

153) P.Grossmann, Oxford University Report OUNP 74/83 (1983);

154) J.Thomas, D.Phil.Thesis Oxford, unpublished (1983);

155) B.Adeva et al., Phys.Rev.Lett. 51 (1983) 443;

156) G.Berghoff, Dipl.Thesis RWTH Aachen, unpublished (1982);
T.Hebbeker, Dipl.Thesis RWTH Aachen, unpublished (1983);
F.P.Poschmann, D.Phil.Thesis RWTH Aachen, unpublished (1985);

157) P.Hoyer et al., DESY 79/21 (1979);

158) for data published earlier than 1970 see e.g.
K.Kleinknecht, K-decay, Proc.of Daresbury Study Weekend (1971);
A.Gsponer et al., Phys.Rev.Lett. 42 (1979) 13;
D.Birnbaum et al., Phys.Rev. D9 (1974) 1242;
G.J.Bock et al., Phys.Rev.Lett. 42 (1979) 350;
W.C.Carithers et al., Phys.Rev.Lett. 34 (1975) 1240;
D.Freytag et al., Phys.Rev.Lett. 35 (1975) 412;
K.F.Albrecht et al., Nucl.Phys. B93 (1975) 237;

159) F.Perey and B.Buck, Nucl.Phys. 32 (1962) 353;

160) F.D.Bechetti and G.W.Greenless, Phys.Rev. 182 (1969) 1190;